Integrated Modular Microfluidic Systems for the Affinity Selection and Comprehensive Analysis of Rare Liquid Biopsy Biomarkers

By
Thilanga Nandana Pahattuge

Submitted to the graduate degree program in Department of Chemistry and the Graduate Faculty of the University of Kansas in partial fulfillment of the requirements for the degree of Doctor of Philosophy.

Chair: Steven A. Soper, Ph.D.

Susan M. Lunte, Ph.D.

Robert C. Dunn, Ph.D.

Krzysztof Kuczera, Ph.D.

Sara Wilson, Ph.D.

Date Defended: 13 April 2021

The dissertation committee for Thilanga Nandana Pahattuge certifies that this is the approved version of the following dissertation:

Integrated Modular Microfluidic Systems for the Affinity Selection and Comprehensive Analysis of Rare Liquid Biopsy Biomarkers

Chair: Steven A. Soper, Ph.D.

Date Approved: 07 May 2021

Abstract

Liquid biopsy is a less invasive sampling technique and is especially beneficial for diseased organs that are anatomically inaccessible for solid tissue biopsy such as the brain, lungs and pancreas. This sampling technique can be analytically challenging due to the multiple processing steps involved to complete the assay and also the mass limits imposed by liquid biopsy markers, such as circulating tumor cells (CTCs), extracellular vesicles (EVs), and cell-free DNA (cfDNA). New microfluidic-based technologies are rapidly evolving and have significantly improved the clinical sensitivity of liquid biopsy assays compared to their benchtop counterparts. Unfortunately, many of these assays are only semi-automated and require extensive sample handling, skilled operators, number of cold-storage reagents and centralized laboratories to perform the experiment which generated difficulties when translating the assay into the point of care testing (POCT).

Here, we are introducing an integrated modular microfluidic system for the comprehensive analysis of CTCs. The microsystem consists of a CTC selection module, impedance module and an imaging module to isolate, enumerate and immunophenotypic identification of CTCs, respectively. The three individual modules are integrated into a fluidic motherboard that is populated with membrane valves for fluidic directional control. The valving operation is automated to minimize the operator involvement. The individual modules and the motherboard are fabricated in plastics using low-cost replication techniques enabling the use of the system as inexpensive disposables in clinical testing. The individual modules can be easily replaced to reconfigure the system to analyze a different biomarker. We have introduced a 7-aminocoumarin photocleavable (PC) linker strategy to covalently attach the affinity agent (mAb) into the CTC selection module. The PC linker contains a central coumarin moiety and a primary amine group in one end and a carboxylic acid group in the other end. Primary amine group facilitating the surface conjugation and carboxylic acid group enables the covalent attachment of

the antibody following EDC/NHS reactions. PC linker cleaves at visible blue light (400-450 nm) obviating the oxidative DNA damage and mRNA expression changes in the desired biomarker. The affinity selected biomarkers were released rapidly (2 min) and efficiently (>90%) using the PC linker strategy. The photo-released CTCs were directed towards the impedance module and finally to the imaging module for the cell enumeration, cell viability assessment and for the immunophenotypic identification. The clinical utility of the system was demonstrated by processing blood samples secured from colorectal cancer (CRC) and pancreatic adenocarcinoma (PDAC) patients.

PC linker strategy is employed to covalently attach an aptamer specific to SARS-CoV-2 spike (S) protein. The viral particle selection chip was used to affinity select SARS-CoV-2 viral particles using saliva as the specimen. The selected viral particles were photo-released and directed towards the nano coulter counter (nCC) for enumeration. The PC linker-aptamer system could affinity select SARS-CoV-2 viral particles with a high recovery (94 %) and low non-specific attachments (<4 %). The nCC device is able to detect viral particles in 10^3-10^8/mL range. The system was validated by processing 20 clinical samples. We are currently in a process of integrating these two devices into a single chip and develop a hand-held instrument for the early detection of SARS-CoV-2.

Acknowledgments

I would like to offer my sincere gratefulness to my Ph.D. advisor Prof. Steven A. Soper for accepting me to the Soper group and providing his continuous support and guidance throughout my research. You guided me in every possible aspect to become a better scientist. You have been a great inspiration, and I am honored to have an advisor like you. I would also like to thank Dr. Mateusz Hupert, Dr. Maggie Witek, Dr. Matt Jackson and Dr. Kumuditha Rathnayake in our group for the help and guidance given by them for my projects, especially when I was new to the group.

I would also like to extend my deepest gratitude to our collaborators, especially Dr. Richard Givens, Dr. Blake Peterson, Dr. Chamani Perera and Dr. Digamber Rane for coming up with synthesis strategies and synthesizing the photocleavable linker for my experiments. I would like to thank Dr. Prem Thapa in Microscopy and Analytical imaging lab for training me SEM and TEM imaging.

I also would like to thank all the past Soper group members especially Dr. Camila Campos and Dr. Nicholas Larkey for their valuable support and guidance. I appreciate all the help and courage given by the present group members Uditha Athapattu, Swarnagowri Vaidyanathan, Ian Freed, Chathurika Rathnayake, Katie Childers and Dr. Menjia Hu.

I appreciate the support given by my Ph.D. dissertation committee for all their valuable comments and time. I am deeply grateful to Dr. Mario Rivera, Dr. Michael A. Johnson, Dr John Karanicolas and Dr. Joanna S. G. Slusky for their enormous support on recommending me for the KU Chemistry Ph.D. program. My honest gratitude is offered to the University of Kansas and the Department of Chemistry for providing me this opportunity to pursue my graduate studies in the United States. I want to thank all the lecturers at the Department of Chemistry, the University

of Kelaniya, Sri Lanka. My sincere gratitude goes to all my teachers at St' Thomas College, Matara, Sri Lanka.

I want to thank my loving wife, Achala, for the support and courage she gave me during the hard times especially when we were distance learning for 2 years. My heartiest gratitude goes to my mother and father, brothers and sister for their support and encouraging words. I am privileged to have a family like you.

Table of Contents

Table of Figures

Chapter 1 – Introduction

1.1 Integrated microfluidic systems

Microfluidics is now going through a transition in which devices geared toward research endeavors are being transitioned into clinical applications. For a successful clinical transition, the following requirements are necessary: (1) Devices must be fabricated reproducibly in a high-scale production modality with tight tolerances at low cost. High-scale production is important for clinical applications because the devices should be disposable to eliminate carry-over contaminants from one measurement to the next that could result in false-positives. (2) The ability to utilize the device/assay in point-of-care (POC) settings. POC testing has many advantages such as making sophisticated tests more accessible to the general population. For example, the recent SARS CoV-2 pandemic utilizes a real-time RT-qPCR assay that requires sophisticated instruments and trained personnel to perform the measurements and interpret the results. Xpert Xpress system developed by Cepheid allows carrying this same assay into physician's offices[1] permitting rapid detection and faster clinical decisions. (3) The device must be fully automated to minimize operator involvement and clinical sample loss and contamination. In many cases, clinical samples contain biomarkers that are rare, especially in the early stages of the disease. In such situations, marker loss or contamination cannot be accommodated as it may result in false negatives/positives.

Integrated microfluidic systems can meet many if not all these clinical transition requirements by employing a single platform to carry out complex multi-step assays in a fully automated fashion requiring minimal operator expertise.

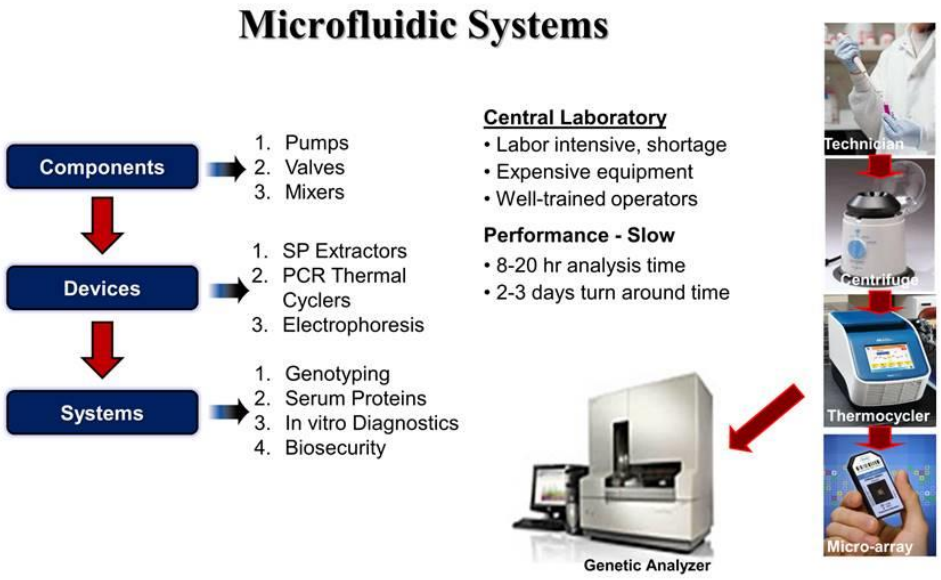

Figure 1.1. Integrated microfluidic systems. Microfluidic devices are made with different components and these task specific devices are integrated to build a single system that can perform a complex assay without requiring bench-top instruments.

So, what is a microfluidic system and how does it differ from a microfluidic device? Inspection of **Figure 1-1** helps to define this difference. For this discussion, we define a microfluidic device that performs a single function, such as solid-phase extractions, PCR thermal cycling, or electrophoresis. To perform this specific function, the device may be comprised of various components, such as mixers, valves, or pumps. Finally, microfluidic systems consist of 2 or more devices that are required to carry out a complete assay, for example genotyping as well as others. In the case of genotyping, the following processing steps are typically required: (1) acceptance of a clinical sample and the isolation of the relevant biological cells carrying the genome of interest; (2) lysis of the biological cells and solid-phase extraction of the genomic DNA; (3) PCR amplification of the isolated genomic DNA; (4) analysis of the PCR products using as an example electrophoresis. A successful microfluidic system can accept a clinical sample and perform all the aforementioned steps directly on-chip.

Integrated systems can be broadly categorized into three formats: (1) centrifugal systems, (2) monolithic systems, and (3) modular systems. This chapter describes the three systems in detail with some of their recent biomedical applications.

1.2 Centrifugal microfluidics

Centrifugal microfluidics, also known as Lab-on a disk, has developed as an advanced diagnostics platform during the last few years.[2] These systems integrate multiple processes such as valving, loading, mixing, reaction, and detection in one disc to perform complex biological assays. The technology promotes point-of-care (POC) testing due to the system's portability and the requirement of minimally trained personnel for its operation.[3] These systems typically contain a compact disc (CD) with fluidic channels and chambers. The CD is connected to a motor that generates forces required to manipulate the fluids within the system.[4-5] The pseudo-forces generated by the rotation of the CD can be utilized for fluidic pumping,[6-7] mixing[8-9], and metering.[10-11]

Centrifugal microfluidics has multiple advantages: (i) External pumps are not required to control the fluid flow. Once the sample is introduced into the sample loading chamber, centrifugal force acts as a pump and directs the fluid flow. (ii) Actuation forces can be easily scaled as per assay requirements. For example, different spinning speeds (50-80 Hz) can be utilized in different stages of a single assay for nucleic acid analysis of foodborne pathogens.[12] The fluid flow rate depends on the type of fluid, dimensions of the disc, and the rotational speed. It can vary from 10 nL/s to 100 μL/s.[13] (iii) Trapped air bubbles, and un-swept volumes can be easily removed from the system by changing the motor's rotational speed.[3] (iv) Reduced assay time and low cost associated with the system enable its potential use in POC testing as a disposable microfluidic. Unidirectional fluid flow caused by centrifugal forces is a limitation of the system. So, additional actuation forces are required for multi-dimensional liquid manipulation.[14]

Centrifugal microfluidics have widespread biological applications such as cell lysis,[15] nucleic acid purification,[3, 12] CTCs[16], proteins[17], and EV isolation.[18] Major diagnostic companies have already developed and commercialized centrifugal microfluidic-based products for primary care applications. For example, Roche has developed a Cobas b 101 system to analyze HbA1c (glycated hemoglobin), lipids, and CRP (C-reactive protein) in blood.[19]

This following section will describe the fundamental physics of centrifugal microfluidics and unit operations such as sample and reagent pre-storage, valving and switching, metering and aliquoting, and reagent mixing. Finally, we will describe typical biomedical applications of centrifugal microfluidic systems.

1.2.1 **Physics of centrifugal microfluidics**

Centrifugal microfluidics utilize three forces to direct the flow of fluids (**Figure 1.2**), centrifugal (Fc), Coriolis (Fco), and Euler (F_E). These pseudo forces are generated due to the rotor's centripetal acceleration, and the forces acting on fluids or particles in a rotating system. These forces are easily controlled by changing the rotating speed of the rotor. The centrifugal force (F_C)acting on a particle with the mass of *m* in radius *r* is given by equation (1);

$$F_C = -m\omega \times (\omega \times r) - - - - - (1)$$

where ω is the angular rotational frequency. Centrifugal force is the main driving force in lab on a disc system, and it pushes liquid radially outward from the center of the disc.

The Coriolis force (F_{CO}) is perpendicular to the velocity of a moving mass and is given by equation (2);

$$F_{CO} = -2m\omega \times \frac{dr}{dt} - - - - - (2)$$

where $\frac{dr}{dt}$ is the velocity of the particle moving in the system. Coriolis force is applied when a sample is mixing, flow switching, and a sample directed to a specific channel.[20]

The Euler force (F_E)is given by equation (3);

$$F_E = -m\frac{d\omega}{dt} \times r \text{ ----- } (3)$$

where $\frac{d\omega}{dt}$ is the change in angular rotational frequency per unit time. As per equation (3), the Euler force is only generated when there is angular momentum. The force is perpendicular to the centrifugal force and opposite to the direction of angular acceleration/de-acceleration. The Euler force is essential for sample homogenization.

Hydrostatic pressure induced by centrifugation depends on the radially inward, and radially outward locations of a liquid column (density ρ), with the pressure difference given by equation (4);

$$\Delta\rho_C = \frac{1}{2}\,\rho\omega^2(r_2^2 - r_1^2) \text{ ----- } (4)$$

where r_1 and r_2 are the inner and outer radius, respectively.

In addition to these three major forces, non-pseudo forces such as viscous, capillary, and fluidic inertia forces are also important in centrifugal microfluidics even though they do not depend on rotation. The differential pressures corresponding to these three forces Δp_{vi}, Δp_{ca}, and Δp_{in} are given by;

$$\Delta p_{vi} = -R_{hyd}q$$

$$\Delta p_{ca} = \sigma\kappa$$

$$\Delta p_{in} = -\rho la$$

where R_{hyd} is the hydraulic resistance, and q is the volumetric flow rate, σ is the surface tension of a processed liquid, κ denotes the curvature of its meniscus, l is the length of a fluidic channel filled with the liquid, and a is the acceleration of the liquid.[21-22] When particles are moving through fluids, a viscous force also known as the drag force (F_d) is applied. This is given by;

$$F_d = C_d \frac{\rho_{fluid}}{2} u^2 A_{particle}$$

where C_d is the drag coefficient, ρ_{fluid} is the density of the fluid, u is the velocity of the fluid relative to a particle, and $A_{particle}$ is the cross-sectional area of the particle.[21]

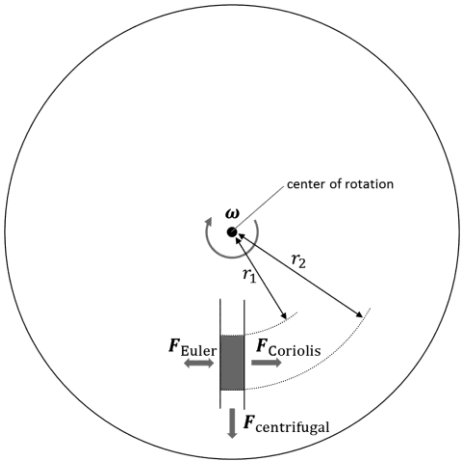

Figure 1.2. Pseudo-forces that drive reagents and particles in centrifugal microfluidics. Centrifugal force acts radially outward from the center of the disc. Coriolis force is perpendicular to the velocity of the moving mass while the Euler force is opposite to the direction of angular acceleration/de-acceleration (Adapted with permission from reference 21 (**https://doi.org/10.1039/C4CS00371C**)-Published by The Royal Society of Chemistry).

1.2.2 **Unit operations in Centrifugal microfluidics**

Unit operations, which are typically carried out using components and/or devices are the primary functions integrated into any system to complete a complex assay. This section will briefly describe sample and reagent pre-storage, release, valving and switching, metering and aliquoting, and mixing as unit operations.

1.2.2.1 Reagent pre-storage and release

On-disc reagent pre-storage is essential to facilitate ease of use, minimizes operator intervention, and sample contamination. Various strategies like stick packages,[23-24] glass ampoules,[25] and elastic membrane micro-dispensers[26] have been reported for reagent pre-

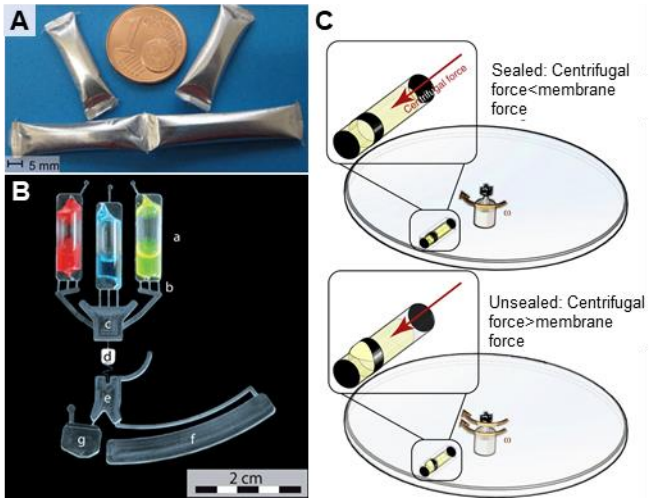

Figure 1.3. Reagent pre-storage and release **(A)** Composite foil was used as stick packs to store reagents and buffers. Seals were peeled off at defined burst pressure (Adapted from reference 23 (https://doi.org/10.1039/C3LC50404B)–with permission from The Royal Society of Chemistry). **(B)** Three glass ampoules were connected to the device to store buffer reagents and reagent release was achieved by manually rupturing (Adapted from reference 25 (https://doi.org/10.1039/B926139G)–with permission from The Royal Society of Chemistry). **(C)** An elastic membrane was used as a sealer to store reagents. Membrane stretched towards the direction of centrifugal force when the centrifugal force> membrane force and as a result, reagents were released (Adapted from reference 26 (https://doi.org/10.1038/s41467-018-08091-z).

storage. The pre-stored reagents require either a controlled release or rehydration of dry reagents to perform the assay.

Stick-packs fabricated using vapor-tight aluminum/polyethylene composite foil were reported for long-term storage of reagents (**Figure 1.3A**). The peelable seals were opened at defined burst pressures to release the stored reagents.[23] Glass ampoules (**Figure 1.3B**) were used to store buffer for DNA extraction and manually ruptured through the elastic lid to release the liquids. Ethanol and water were stored using this technique for 300 days at room temperature

without any noticeable loss.[25] Highly reactive bromine water was stored in inert Teflon or glass by using ferrowax plugs. The solution was released by exposing the wax plugs to laser irradiation.[27-28] Wax that have different melting temperatures were used to connect pre-stored liquids to fluidic channels, and infra-red heating was then utilized for the sequential release of reagents.[29] Micro-dispenser is comprised of a hole, and the elastic membrane was reported for long-term reagent storage (**Figure 1.3C**). The reagents were released when the centrifugal force was increased to stretch the membrane. Different membranes with different elastic properties were used to release different liquids at different rotational speeds. [26] Enzymes were stored in lyophilized form and rehydrated when processing during a DNA amplification assay.[30]

1.2.2.2 Liquid transport

Liquid transport in a centrifugal microfluidic system is typically governed by the centrifugal force and directed from a radially inward position to a radially outward position. This unidirectional fluid flow limits the number of processes that can be integrated into a centrifugal microfluidic platform. Alternative forces may be thus required to drive liquid transport in alternative directions. Fluid flow from a radially outward position to a radially inward position was achieved by expanding[31] or contracting[32] a trapped gas. This was achieved by altering the temperature. Besides, capillary priming,[33] pneumatic pumping,[34] and suction-enhanced siphon priming[35] were also reported for fluid transport.

1.2.2.3 Valves and Switches

The incorporation of valves into fluidic channels is vital to control and manipulate fluid delivery. Centrifugal systems have used both passive and active valves. Passive valves are normally closed and actuated by exceeding the spinning speed. Capillary valves are passive and, the valve is connected to a reservoir through a straight channel. When the disc is not rotating, the fluid flow stops due to capillary pressure. The liquid can only pass through the valve when the centrifugal force is high enough to break the capillary barrier pressure.[36] Hydrophobic surface

coatings such as fluorinated polymer solutions and printed toner spots were reported as passive valves to prevent liquid passage.[37-38] Burstable seal valves utilizing sealing foil or PDMS membranes were used as vapor-tight valves.[39] Siphoning valves depend on the capillary priming of a liquid into a siphon channel. High spinning rates prevent the capillary primming and stop the liquid flow. Lower spinning rates facilitate the capillary primming and pass the liquid. Siphon valves such as capillary siphon,[40] overflow siphon, and pneumatic siphon[34] were also used as passive valves to control the fluid passage.

Valves controlled by an external source are known as active valves. Active valves can be configured to be either normally open or normally closed. Optically addressable single-use valves utilizing a solid-state laser to melt the substrate and actuate valves were reported.[41] Paraffin wax and iron-oxide nanoparticles were used to build ferrowax valving systems in centrifugal microfluidics. The channel was blocked using a wax, and it can be opened by melting the wax using an infrared source. Low power lasers (1.5 W)[11] or heat guns[42] were used to actuate the paraffin wax valves. A novel magnetically actuated membrane (PDMS) valving system was proposed. At low spinning frequency, the valve was closed by the membrane's deformation due to the magnetic force. At high spinning rates, the centrifugal force pulled the bottom-side magnet, disrupting the magnetic force, and opened the valve.[43] Reversible thermo-pneumatic valves for real-time fluid manipulation were also reported. The valve actuation was based on latex film deflection triggered by heating or cooling of a trapped air chamber.[44]

Flow switches were used to change the fluidic direction. Flow switching was achieved by incorporating a Y-shaped channel and applying different centrifugal forces. When the centrifugal force was low, the fluid was equally distributed into the two outlet channels. The fluid flow was limited to one outlet channel when the centrifugal force was increased. This flow deviation occurred as a result of transversal Coriolis force.[45] A regulated stream of a compact gas (pneumatic flow switching) was also used to control the flow switching in a T-shaped junction.[46]

1.2.2.4 Metering and Aliquoting

Metering/measuring of defined liquid volumes is essential to obtain a reproducible analytical result. The most straightforward metering technique contains a metering chamber that has a defined volume and a waste chamber. The metering chamber's outlet channel opens to the waste chamber that collects the overflow volume of the metering chamber. Aliquoting is known as splitting an input volume into multiple sub-volumes, which requires multiple parallel metering steps. The metering chamber can be connected to valves for further fluidic processing.[47]

1.2.2.5 Mixing

Mixing solutions and reagents are necessary to obtain a homogenized sample, and to perform an efficient chemical reaction. Benchtop mixing strategies such as vortexing, stirring, or shaking cannot be performed in a centrifugal microfluidic, and fluidic mixing in a miniaturized system is challenging due to the low Reynolds numbers (1-10).[48]

Shake mode mixing based on acceleration and deacceleration of the microfluidic cartridge was demonstrated. The angular momentum caused by changes of the spinning speed induced Euler forces and resulted in an advective current within the liquid. This current reduced the mixing time from 7 min to 3 s for a 25 μl volume. A combination of shake mode mixing with pre-filled magnetic beads achieved mixing within 0.5 s. For the combination shake mode, magnetic beads were deflected inbound and outbound periodically by a set of magnets positioned in the frame.[8]

A microfluidic mixer utilizing centrifugal force and pneumatic pressure to reciprocate the fluid flow was introduced as a mixing strategy. A centrifugal acceleration field acting upon a liquid generates and stores pneumatic energy that can be used later when centrifugal deacceleration occurred. This resulted in a reverse direction of fluid flow. So, continuous acceleration and deacceleration can be used to reciprocate a fluid that facilitates mixing.[49] Centrifugal force and active pneumatic pumping was used to mix and agitate liquids rapidly (~0.1 s) and efficiently. The

mixing was based on the rising of air bubbles at the bottom of a microfluidic reservoir.[50] Gas generated by an internal reaction was used to generate bubbles without using an external source. As an example, oxygen air bubbles generated by decomposing hydrogen peroxide was used to induce vigorous mixing of blood and lysing reagents to extract DNA.[51]

1.2.3 Biomedical applications of centrifugal microfluidic systems

Centrifugal microfluidic systems have gained attention within the biomedical community during the last two decades due to the portability, decreased sample volume and reagent requirements, reduced processing time, the ability for parallel processing, and automation. In this section, we will cover several examples of biomedical applications that have employed the use of centrifugal microfluidic systems.

1.2.3.1 Nucleic acid (NA) analysis

Nucleic acid analysis requires three processes, extraction/purification, amplification, and detection. These processes are often time-consuming and require skilled operators. Centrifugal microfluidic systems can integrate all of the aforementioned processes required for NA analysis into a lab on a disk platform that can result in reducing the assay complexity, laboratory time, and amount of reagents. The operation requires minimal operator intervention without special laboratory training that can facilitate POC testing.

1.2.3.1.1 Nucleic acid extraction/purification

Mechanical cell lysis was achieved by introducing spherical particles (beads) into a microchamber fabricated in a CD. Bead-cells interactions were maximized by rotating the CD in forwarding and backward directions at high spinning rates. Cells were lysed by friction and collision. Lysis efficiency was determined using a microscope or measuring the DNA concentration after lysing.[52] Mechanical impaction and shear forces generated by oscillating ferromagnetic blades were reported to disrupt cells. Cell debris was eliminated by centrifugation,

and the supernatant was directed to a collection chamber via siphoning.[53] Thermal energy generated by magnetic beads after laser irradiation was also used to lyse cells.[54]

A silica extraction matrix was integrated into a COC cartridge to isolate DNA from a pre-lysed sample. Sample and the binding buffer were processed through the silica membrane followed by a post-selection wash. Finally, the bound DNA was released by an elution buffer.[25] Silica-sol-gel matrix was used to isolate RNA from an influenza virus. Lysed viral particle solution, washing buffer, and elution buffer were loaded to silica-sol-gel sequentially to bind, purify and elute viral RNA.[55] On-chip NA purification technique combining the centrifugal force with pneumatic actuation was reported. The method used commercial glass microfiber filters as the solid-phase extraction matrix, which allows for easy implementation. Pneumatic pumping was used to circulate air through the system before the elution to minimize the ethanol contamination in purified NA (1% (v/v)).[3]

Strohmeier *et al.* used silica-coated magnetic beads for DNA purification. Magnetic beads were transported between multiple microfluidic chambers using permanent magnets to bind, wash and elute DNA. Complete purification was achieved within 12.5 min.[56] Lab tube cartridges consisted of three stacked revolvers in a 50 mL centrifuge tube for automated DNA extraction from blood was reported. Revolver 1 contained cavities for reagent pre-storage and release. Revolver 2 includes a mixing system and solid-phase extraction matrix, while revolver 3 consisted of a detachable tube to collect the eluent. Reagent release and liquid routing were done by a centrifugally activated ball-pen mechanism.[57]

1.2.3.1.2 Nucleic acid amplification

Nucleic acid amplification is often used as a diagnostic technique to detect a few copies of biomarkers to identify diseases in early stages. Lab-on-a-CD DNA amplification systems using

conventional polymerase chain reaction and isothermal amplification are a few techniques that have been reported in the literature.

A Rotary PCR genetic analyzer that contained a PCR microchip and three thermal blocks to perform the PCR assay was developed (**Figure 1.4A**). The PCR chip was sequentially rotated on different thermal blocks to perform the PCR steps of denaturation (94 °C), annealing (58 °C), and extension (72 °C). The system was used to identify multiple influenza viral RNAs obtained from H3N2, H5N1, and H1N1.[58] Multiplex detection of SARS CoV-2, influenza A and B viruses were demonstrated with sixteen targets amplified and detected within 1.5 h (**Figure 1.4B**).[59] Digital polymerase chain reaction platform that provided 1000 nanoliter sized compartments for plasmid DNA amplification was introduced. A rapid thermal cycler was used to achieve 45 cycles in less than 25 min. A fluorimeter was mounted to a thermal cycler and used for real-time fluorescence reading.[60]

The challenges associated with PCR are the long time required to reach temperatures associated with the amplification reactions and substantial power consumption. An efficient heating and cooling system (2 °C/s) for bacterial lysis and PCR was introduced by changing the temperature in two steps.[61] Different temperature requirements for PCR can be replaced by isothermal amplification. Loop-mediated isothermal amplification (LAMP) was used for the simultaneous detection of hepatitis B, hepatitis C, and cytomegalovirus. The target gene amplification was monitored by employing a LED light and measure the turbidity.[62]

Whole-genome amplification (WGA) is essential for evaluating the genetic information in biology and medicine. Single-cell gene amplification was performed by a centrifugal-driven droplet generation method (Multiple Displacement Amplification, (MDA)) (**Figure 1.4C**). Fast and

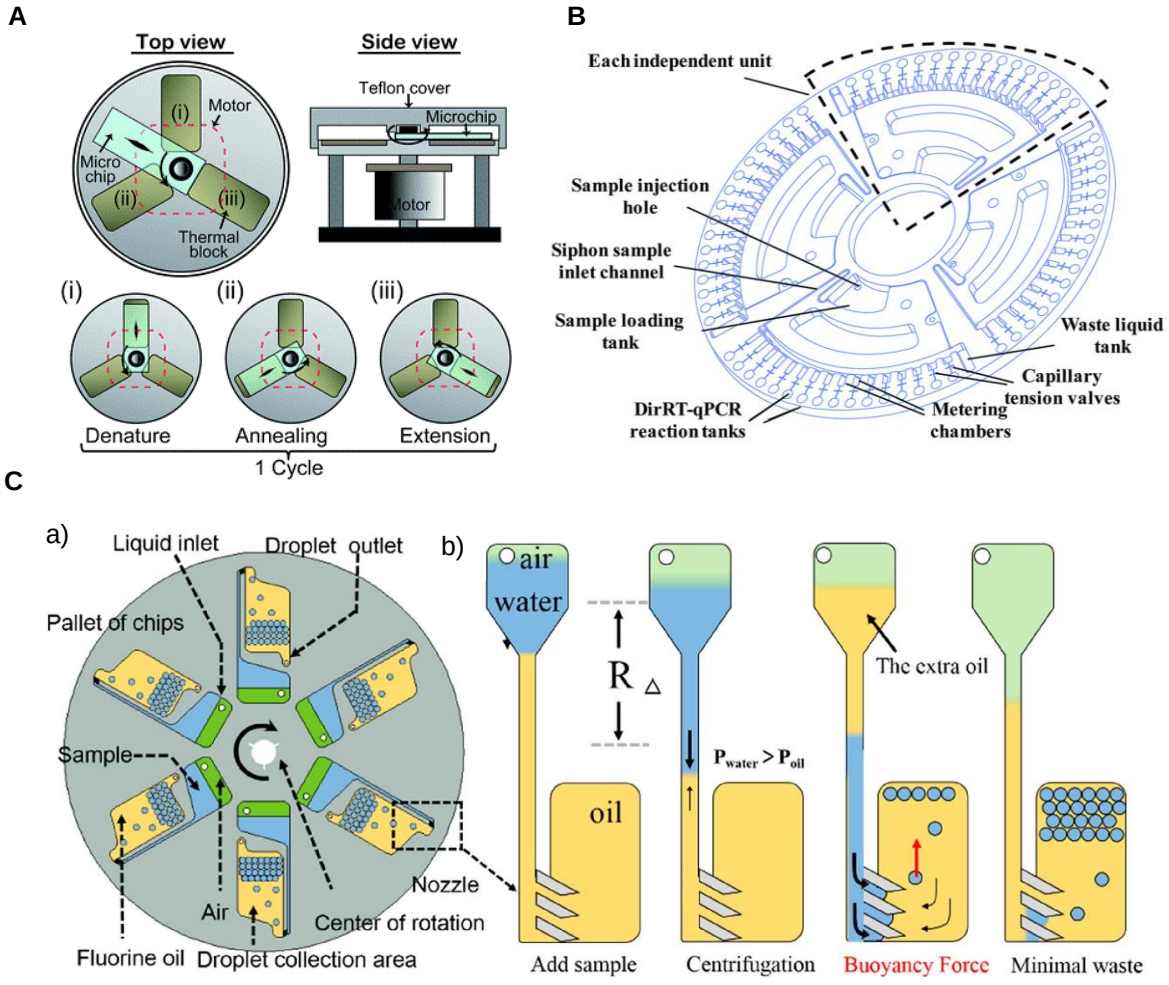

Figure 1.4. Centrifugal systems for genomic material amplification **(A)** Rotary PCR Genetic Analyzer that consists of a microchip and three heat blocks. PCR chip rotates into three heating blocks and they have different temperatures to (i) denature (94 °C), (ii) anneal (58 °C), and (iii) extend (72 °C) genomic material (Adapted from reference 58 (https://doi.org/10.1039/C2LC21269B) – with permission from The Royal Society of Chemistry). **(B)** Design of the direct RT-qPCR disc with four independent reaction units. The disc can simultaneously detect SARS CoV-2, influenza A and B viruses (Adapted with permission from reference 59 (https://doi.org/10.1039/D0RA04507A) – Published by The Royal Society of Chemistry). **(C)** (a) The schematic diagram of droplet generation chip. (b) The schematic diagram of the droplet generation process. The collection chamber was filled with high-density fluorine oil, and then an aqueous sample was added. Droplets are generated when the centrifugal force pushed the aqueous phase into the oil phase (Adapted with permission from reference 63 (https://doi.org/10.1021/acs.analchem.9b02786). Copyright (2019) American Chemical Society).

homogeneous droplet production was achieved by carefully controlled centrifugal emulsification. During the single-cell gene amplification, single cells were separated and lysed. The lysed solution was used to generate droplets. Each reaction samples (5 µL) was compartmentalized into droplets, and the MDA reaction was performed independently in each droplet.[63]

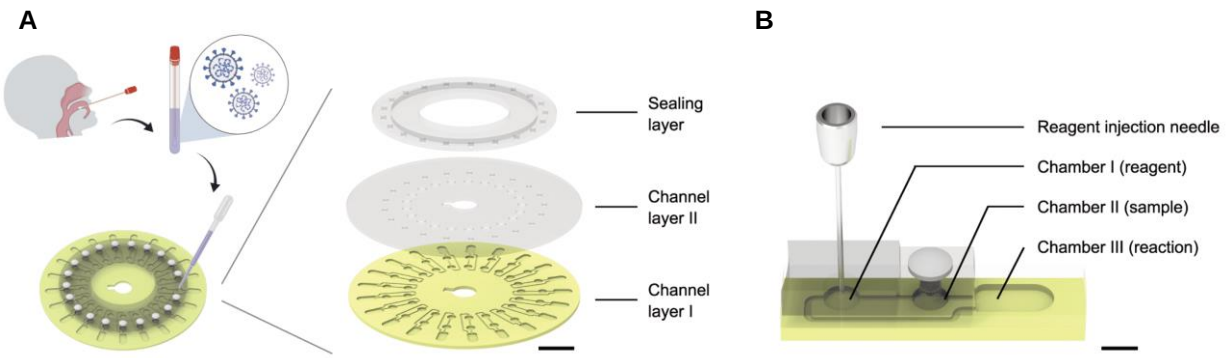

Figure 1.5. Centrifugal microfluidic system for the detection of SARS-CoV-2. **(A)** The device utilizes oropharyngeal swab samples to detect viral RNA. It contains three layers, two channel layers and a sealing layer. **(B)** Single reaction unit contains three chambers for reagent injection (chamber I), sample injection (chamber II), nucleic acid release and RT-LAMP reaction (chamber III) (Adapted with permission from reference 64 (https://doi.org/10.1007/s11426-020-9800-6)).

RT-LAMP technology in a centrifugal microfluidic system was used for the detection of SARS-CoV-2 from oropharyngeal swab samples (**Figure 1.5**). The microfluidic system consisted of a microfluidic disc and a customized instrument. The disc contained three layers, channel layer I, channel layer II and a sealing layer (**Figure 1.5A**). The disc was placed inside the instrument for the automated sample processing following sample loading into the chamber II. The instrument injects viral lysis buffer, RT-LAMP reagents and mineral oil into the chamber I to lyse the viral particles and release the genomic material. The RT-LAMP reaction is performed in chamber III. The system can provide results in less than 70 min.[64]

1.2.3.2 Immunoassays

Immunoassays are based on highly specific antibody-antigen interactions. Target analyte could be either the antibody or an antigen. Some immunoassays use a primary/capture antibody to binds the analyte first, and a secondary labeled antibody to binds next and make a sandwich-type structure with the analyte. After the bound/free separation, the quantification is performed. Competitive immunoassays are used when the analyte is small and expose only one binding site/epitope. In this case, a conjugated analyte competes with the target analyte in the sample to bind into the primary antibody. When the target analyte concentration is high, few conjugated

antigens will be bound and when the target analyte concentration is low more conjugated antigens will be bound. Immunoassays are widely utilized in securing biomarkers for biomedical diagnostics, biological and biochemical studies, drug and vaccine characterization, environmental analysis, and food safety.[21]

Conventional immunoassays need lengthy incubation periods, procedures, and trained operators. The integration of immunoassays on a centrifugal microfluidic platform and automation of the process is attractive because it can eliminate the operator involvement, reduce reaction times, diffusional distances, and cost while securing consistent results. The most common immunoassay format incorporated on centrifugal microfluidics is ELISA.

1.2.3.2.1 ELISA assays

ELISA (enzyme-linked immunosorbent assay) utilizes an enzyme-substrate reaction to quantify the desired analyte. After an incubation time, the enzymatic reaction is terminated by adding a stopping solution, and finally, the absorbance measured at a particular wavelength.

A fully automated lab on a disc ELISA assay system was developed for the detection of Hepatitis B. Buffers and reagents preloaded into specific chambers, and ferro wax microvalves used for sequential release of certain reagents. Capture antibodies were coated onto polystyrene beads. The assay's total processing time was 30 min.[65] The centrifugal system for quantifying botulinum neurotoxin from human blood in less than 30 min was developed (SpinDx). Beads coated with capture antibodies and fluorescent-tagged detection antibodies were incubated with the sample. The beads were separated from the sample by sedimentation through a density media following incubation. The bead pellet's fluorescent signal was used for the quantification.[66] Okamoto *et al.* demonstrated a lab on a disc ELISA assay using a PDMS device at a steady rotational frequency (**Figure 1.6A**). The device contains four reservoirs for sample/standard,

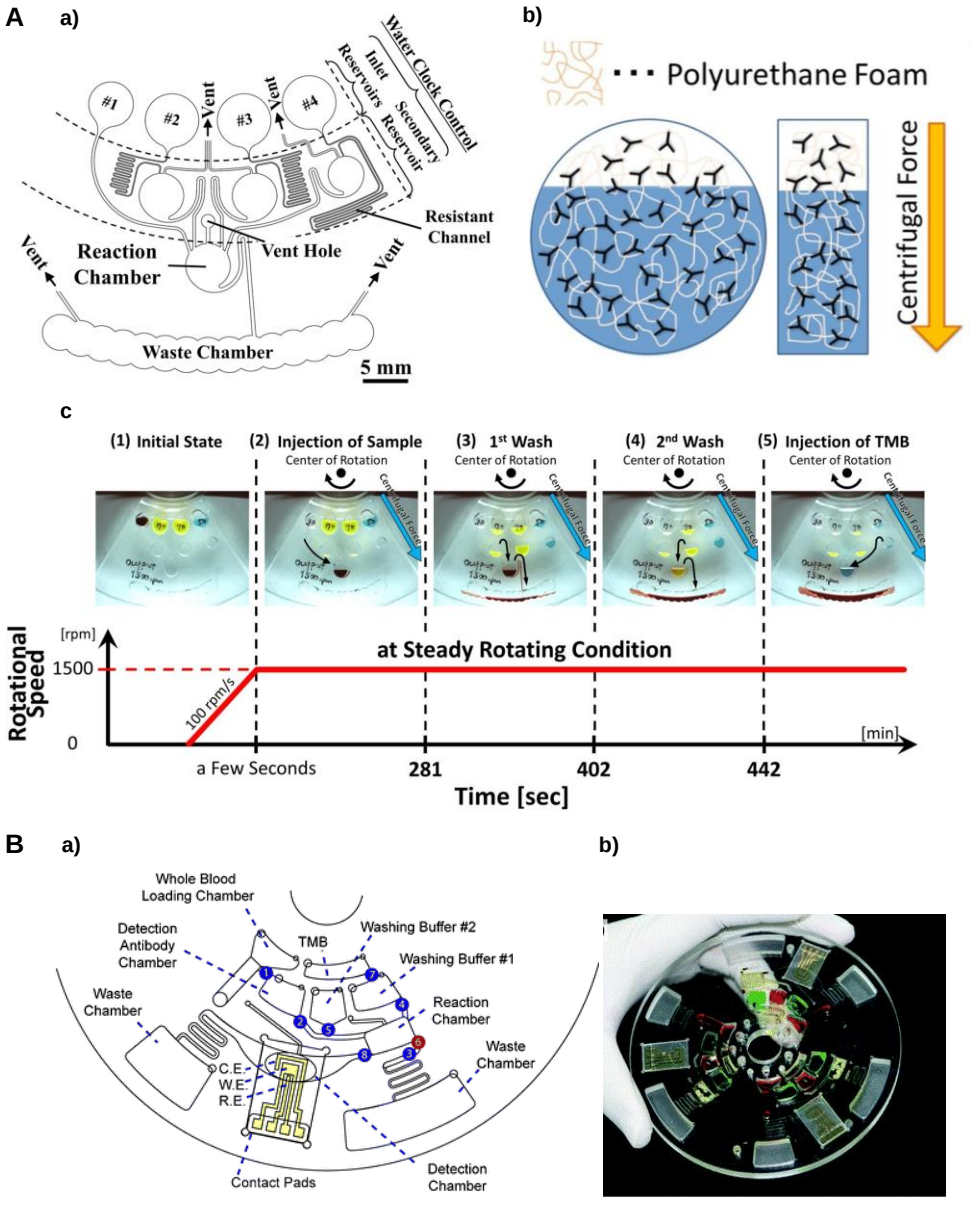

Figure 1.6. Centrifugal systems utilizing ELISA assays. **(A)** ELISA platform designed based on CLOCK concept. (a) Schematic drawing of the automated ELISA device. Four reservoirs to store sample/standard, washing buffer, and TMB substrate. Secondary chambers are designed to store reagents temporarily and inject them on time. (b) Antibody distribution of the polyurethane foam (c) Step-by-step operation of the disc at the steady rotating condition (Adapted with permission from reference 67 (https://doi.org/10.1016/j.snb.2018.01.150)) Copyright (2018), with permission from Elsevier). **(B)** Flow enhanced electrochemical detection of C-reactive protein. (a) Schematic representation of the microfluidic device that contains miniaturized gold electrodes. (b) Image of the fabricated disc loaded with colored solutions for visualization (Adapted from reference 28 (https://doi.org/10.1039/C3LC50374G) with permission from The Royal Society of Chemistry).

washing buffer, and TMB substrate and secondary chambers for temporary liquid storage (**Figure 1.6Aa**). The capture antibodies were immobilized in polyurethane foam (**Figure 1.6Ab)**, and the

foam was fit into the reaction chamber. Sequential release of the reagents was achieved by CLOCK (Control of Liquid Operation on Centrifugal hydroKinetics) (**Figure 1.6Ac)**. Human albumin was detected by the system in less than 18 min.[67]

The same group developed a small centrifugal microfluidic device driver (bento-box) and a centrifugal microfluidic device made of polypropylene to advance their previous device. The new device detected mouse IgG in 12 min.[68] A multiplexed ELISA assay was reported by Espulgar *et al.* Capture antibodies were immobilized on microbeads for the specific capture of IgA. The beads were partially filled in a ring structured channel, and the unfilled portion was used for colorimetric detection of the analyte. The system could perform four reactions in parallel within 30 min.[69] Electrochemical detections were used with ELISA to improve the sensitivity. A fully integrated microfluidic system for flow-enhanced electrochemical detection of C-reactive protein was demonstrated (**Figure 1.6B**). The technique was able to generate a LOD of 4.9 pg mL^{-1}, which was a 17-fold improvement from the LOD obtained via optical density measurements.[28]

1.2.3.3 Blood analysis

Blood is relatively a minimally invasive liquid biopsy sample and can provide a copious amount of information about a patient's health. Most diagnostic tests utilize blood as the sample. Diagnostic tests for glucose, lipids, electrolytes, and protein quantification require the plasma component of whole blood. Plasma separation from the formed components in blood (*i.e.*, blood cells) can be done in two steps, sedimentation of blood cells by centrifugation and decanting the separated plasma.

A Centrifugal Lab-on-a-CD system that can separate and direct blood cells and plasma into two different reservoirs was presented. After the initial separation, centrifugation frequency was increased and as a result, plasma flowed through a Y-shaped microchannel while dividing the sample into two smaller fractions of equal volume. Additional manipulation of the centrifugal

frequency decanted a portion of the plasma sample into a detection chamber for further analysis.[70] Quasi-isoradial channel was reported for the continuous separation of plasma. The device consists of a metering structure and a drain channel connected to two adjacent chambers. Blood cells sediment in the first chamber while decanting the purified plasma in to the second chamber for downstream analysis.[71]

A simple and robust system utilizing H_2O_2 production to detect desired analytes in whole blood was established. The electrochemical system had a catalyst and a nano porous thin film working electrode coated with an analyte-specific enzyme. Glucose, lactate, and uric acids were quantified within a few minutes using 16 µl of whole blood.[72] Roche provides a centrifugal microfluidic platform (Cobas b 101) for the analysis of HbA1c and lipids. The sample volume requirement was 2 mL to 19 mL, respectively, and the results were obtained within 6 min.

1.2.3.4 Circulating tumor cells (CTCs)

Centrifugal systems have been developed for the isolation and analysis of CTCs. Lee *et al.* developed a centrifugal platform to isolate CTCs. Target CTCs were trapped (61%) on a track-etched polycarbonate (PC) membrane filter while small blood cells passed through the pores towards the waste chamber. The disc had three chambers for the parallel analysis of three samples. Captured cells were immune-stained and identified by fluorescence microscopy.[73] The same group introduced fluid-assisted separation technology (FAST) to improve the cell recovery. Size-selective pores were filled with a stably held fluid during the entire filtration process, providing a reduced pressure drop. The continuous wetting of the membrane was achieved by placing a fluid assisted chamber underneath the membrane. This modification facilitated an uniform filtering throughout the membrane.[74] Integration of a micromixer unit with an inertial flow-focusing unit in a centrifugal system was first reported by Aguirre *et al.* The micromixer consisted of alternating sidewinding channels, which facilitated the mixing of anti-EpCAM coated beads with the blood sample. The inertial flow unit enabled the detection and separation. Both units have different

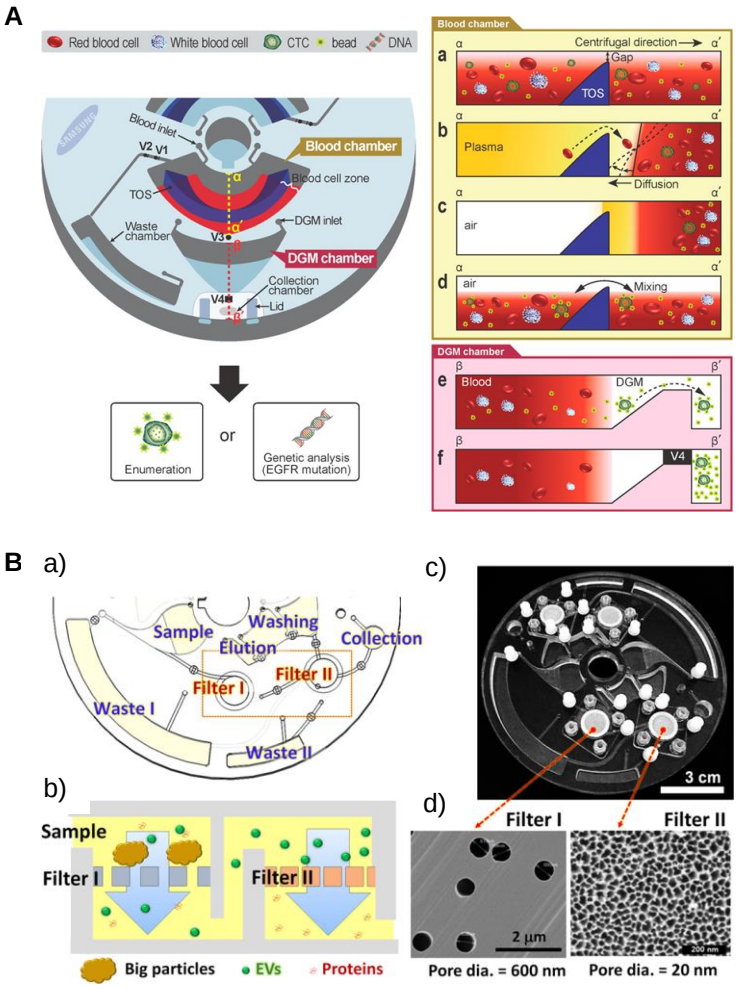

Figure 1.7. Centrifugal microfluidic systems for CTC and EV isolation. **(A)** CTC isolation device with a triangular obstacle structure (TOS) to facilitates the retention of blood cells. Affinity selected CTC-microbead complexes moved into the collection chamber through the DGM chamber (Adapted with permission from reference 16 (https://doi.org/10.1021/ac403456t). Copyright (2014) American Chemical Society). **(B)** Schematic diagram of Exodisc for rapid EV isolation. (a) Detailed features of the device. (b) A cross-sectional view of the filters. (c) A photograph of the dual-chamber Exodisc. (d) SEM images of two populations of EVs captured in both filters (Adapted with permission from reference 78 (https://doi.org/10.1021/acsnano.6b06131). Copyright (2017) American Chemical Society).

operational principles but could act at the same centrifugal force.[75] A lab on a disc platform for single-cell selection and imaging was reported. The microsystem comprised a central sample loading chamber and an array of funnel-shaped microtraps situated along the edge. When centrifugal force was applied, cells were directed towards micro traps, and individual cells were isolated while the rest of the fluid drained through the microchannel.[76] Some applications require handling a large sample volumes (ex- for drug susceptibility studies). A disc device that handled

a large blood volume to isolate CTCs for enumeration and genetic analysis was reported. The blood chamber contained a triangular obstacle structure (**Figure 1.7A**) and a valve to facilitate plasma removal from whole blood. Anti-EpCAM coated microbeads bound CTCs, and CTC-microbead complexes were separated in a density gradient medium. Isolated CTC-microbead complexes were directed to the collection chamber for enumeration and genetic analysis.[16]

1.2.3.5 Extracellular vesicles (EVs)

A centrifugal microfluidic device for the isolation of EV subpopulations was reported. The device (EV-Ident) contained three differently sized nanoporous membranes (200 nm, 100 nm, and 20 nm) for sequential separation of EVs. Captured EVs were labeled on the device and imaged.[77] Lab on a disc system (Exodisc) was used for rapid and size-selective isolation of EVs in a size range of 20-600 nm (**Figure 1.7B**). The device contained double filtration units. Filter one (600 nm) captured large debris and the second filter (20 nm) isolated EVs. The enriched EVs were directed for downstream molecular analysis, such as RT-qPCR or an on-disc ELISA.[78] The same group modified the Exodisc platform to perform EV isolation from whole blood by integrating a plasma separation unit. The dual filters used in this study were 600 nm and 100 nm. The 600 nm filter trapped large particles while residual proteins were removed from the 100 nm filter.[18]

1.2.3.6 Cell-free DNA (cfDNA)

Cell-free DNA extraction and purification using immiscible filtration-assisted surface tension (IFAST) was demonstrated by Hu *et al.*[79] The disc enables to perform plasma isolation, protein lysis, DNA binding, and elution using the centrifugal force in less than 15 min. The disc contained two chambers for plasma separation and cfDNA extraction. Magnetic beads were mixed with plasma and lysis/binding buffer for the solid-phase extraction of cfDNA by IFAST technique. The purified cfDNA was moved into the elution chamber by an external magnetic field followed by collecting the bead-free supernatant for downstream analysis.

Reversible and magnetically actuated diaphragm valves integrated into a disc system were used to isolate and purify cfDNA from peripheral blood. A table-top, custom-designed centrifuge system could isolate cfDNA within 30 min. After the initial plasma separation step, the plasma sample was directed to a separate chamber containing a preloaded lysis buffer, and proteinase K. Silica beads were used as the substrate for cfDNA binding. The elution buffer was added to the bead chamber, and the supernatant was removed by agitation. Extracted cfDNA was used to perform ddPCR for EGFR L858R mutational analysis.[80]

1.2.3.7 Bacterial and viral isolation

Lab disc platforms have also been used for the isolation and detection of bacteria and viruses. Methicillin-resistant *Staphylococcus aureus* (MRSA) was isolated using a CD by Schulz *et al.*[81] Nasal swabs were used as the specimen, and unit operations of swab uptake, reagent pre-storage, sample distribution, enzymatic lysis, and amplification of strain-specific markers were performed.

Salmonella enterica cells were isolated, and *Salmonella* specific *invA* gene was detected by on disc PCR. Bacterial cells were separated into single cells and thermally lysed, followed by PCR amplification of the target gene. The device consisted of 24 microchannels and each microchannel contained 313 microchambers and cells were separated into each microchamber during the centrifugation. Each microchamber consisted of 1.5 nL of PCR mixture. A custom made thermal cycler was used for the PCR amplification of the target gene.[82]

Centrifugal disc for the rapid detection of influenza virus subtypes (H1, H3, H5, H7, H9, and influenza B) has been demonstrated in a recent report. Fluidic manipulation was controlled using membrane-barrier valves. Enzymes (DNA polymerase and reverse transcriptase) required for the assay were preloaded into a chamber and the detection was performed by a colorimetric or fluorescent LAMP assay in less than 45 min.[83]

1.3 Monolithic systems

Monolithic microfluidic systems have different task-specific modules fabricated on the same platform. As a result, monolithic systems do not require interconnects to connect modules enabling them to tolerate high fluidic pressure conditions and external forces. Moreover, residual/unswept volume associated with the tubing and interconnects was negligible. Therefore applications that require high performance and reliability, monolithic systems are more appropriate.[84]

Monolithic systems have some limitations. Since the modules are fabricated in a single platform, a simple change or an upgrade of a module requires redesign and refabricate the whole system. This increases time and cost and limits the use of the system in different applications. Besides, monolithic systems restrict the material and fabrication choice for individual modules, affecting the overall performance of the system.

Monolithic microfluidic devices are fabricated using 3D printing, elastomeric casting, inkjet printing, cutting plotting, and micro-milling.

1.3.1 Biomedical applications of monolithic systems

This section of the chapter describes recent biomedical applications of monolithic systems in nucleic acid analysis, CTC and EV analysis, ELISA analysis, and single-cell analysis.[84]

1.3.1.1 Nucleic acid analysis

Integrated microfluidic systems for the genetic analysis should have faster processing times, reduced reagent volumes, automated sample processing, and prevent potential contamination.

PCR amplification typically requires a benchtop instrument and highly trained operators. Lagally *et al* developed a miniaturized integrated microsystem for the PCR amplification and capillary electrophoresis (CE). The device consisted of heaters, temperature sensors, and PCR

chambers. The PCR-CE system was equipped with membrane valves, a solid-state laser, and confocal fluorescence detection optics. Microfabricated heaters and temperature sensors achieved uniform heating during PCR amplification. The system could perform pathogen detection and genotype analysis in less than 10 min.[85] Easley *et al* demonstrated a glass and PDMS-based microsystem for genetic profiling. The device integrated more processes such as DNA extraction, amplification, target DNA separation, and detection into a single platform. An elastomeric membrane valving system was employed for the fluidic control. Samples with microliter volumes were processed, and genetic profiles were generated in less than 30 min.[86]

Short tandem repeat analysis (STR) is used in forensics for human genome identification. The analysis requires sophisticated bench-top instruments and highly trained operators to perform the steps such as DNA extraction, quantitation, PCR amplification, and CE. Roux et al developed a monolithic microsystem by combining enzymatic DNA preparation, PCR amplification, and high-resolution separation of amplified products. Non-contact IR-mediated PCR amplification was employed, and STR profiling was achieved in less than 2 h.[87] The same group has developed a valve-less microsystem with a single-base resolution and accurate allele identification for STR analysis (**Figure 1.8A**). The system integrated PCR and ME with a reduced separation length (7 cm) for multiplexed DNA analysis.[88]

On-chip PCR systems utilizing small volumes reduce the amount of PCR reagents and sample input. Low volumes also increase the thermocycling efficiency of the PCR reaction. The same group has developed an integrated microsystem that can process nanoliter-sized samples to extract and amplify DNA for STR analysis.[89] Burns *et al* also developed a microsystem for the processing of nano-liter-sized volumes. The microsystem consisted of a liquid injector, a sample mixing and positioning system, a temperature-controlled reaction chamber, an electrophoretic separation system, and a fluorescence detector.[90]

Pre-concentration of STR products is essential for increasing the efficiency of CE separation. Liu *et al* introduced a post-PCR sample enrichment step. The system combined sequence-specific DNA purification and post-PCR cleanup with inline injection into the CE system. Biotin-labeled oligonucleotide probes were used for the isolation of sequence-specific DNA fragments. STR amplification was performed in the PCR chamber, and biotinylated STR products were concentrated using streptavidin modified capture gel. The concentrated narrow band was injected into the CE separation after a thermal release.[91]

Lab-on-a-chip DNA sequencing can dramatically reduce the reagent consumption, analysis time, cost, and macroscale laboratory equipment. Blazej *et al* developed an integrated microsystem for DNA sequencing (**Figure 1.8B**). The device integrated three sanger sequencing steps, thermal cycling, sample purification, and capillary electrophoresis, into a single glass-PDMS wafer. Two separate sequencing devices were fabricated in a single wafer and could process 1 fmol DNA template providing read lengths up to 556 bases. PDMS pneumatic valves were used for the fluidic direction.[92]

DNA methylation has been identified as an essential epigenetic biomarker for the early detection of cancer. Different monolithic microfluidic systems have been developed for the identification and quantification of DNA methylation. A fluidic platform to streamline the methylation-specific PCR (MSP) assay was reported by Stark *et al*.[93] The device consists of a droplet magneto fluidic platform that integrated all necessary steps required for MSP assay, including genomic DNA isolation, bisulfite conversion, and qPCR. A thermal control unit consisting of two heating elements was used for bisulfite conversion and PCR thermal cycling. Fluorometer was employed for the real-time data acquisition. The entire assay was performed in less than 4.5 h.

Methylated DNA has an extremely low abundance in a clinical sample (pM). Therefore, sample pre-concentration is required. Hong et al developed an integrated device that can pre-

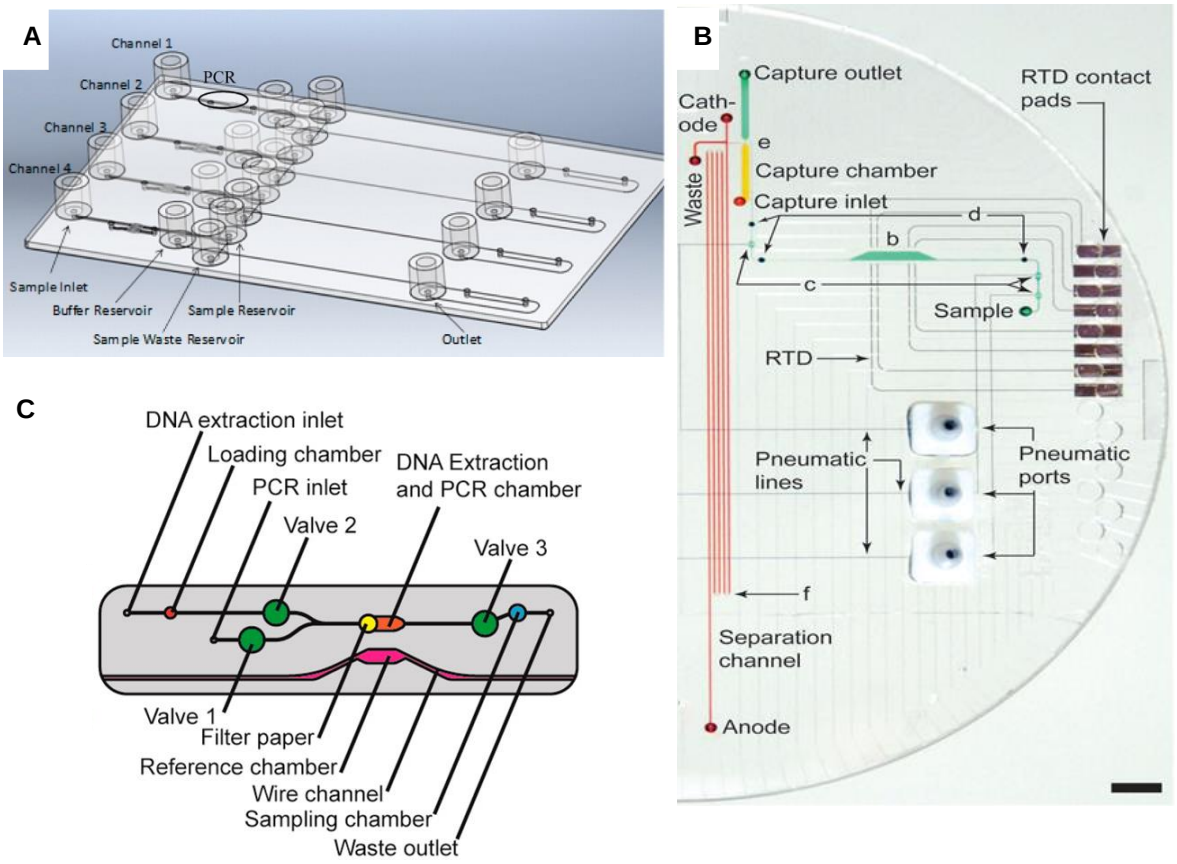

Figure 1.8. Integrated monolithic microsystems for the DNA analysis. **(A)** Integrated valve-less PCR-ME microchip containing PCR chambers in the middle of the microchannels. The detection region is at the outlet top of the microchannel (Adapted with permission from reference 88 (https://doi.org/10.1021/ac501666b). Copyright (2014) American Chemical Society). **(B)** Integrated bio-processor for the nano-scale sanger sequencing (Adapted with permission from reference 92 (https://doi.org/10.1073/pnas.0602476103). Copyright (2006) National Academy of Sciences). **(C)** Integrated device for the genetic testing of hereditary hearing loss. The microdevice contains DNA extraction and PCR amplification chambers (Adapted with permission from reference 95 (https://doi.org/10.1021/ac5039303). Copyright (2015) American Chemical Society).

concentrate methylated DNA for their electrochemical detection. The integrated system consists of an ion concentration polarization (ICP) module to enrich DNA and an electrochemical sensor for quantification. The device measures both methylated DNA concentration and the degree of methylation.[94]

Integration of DNA extraction and PCR amplification into a monolithic platform was also demonstrated by Zhuang *et al* (**Figure 1.8C**).[95] The microsystem was designed for the genetic

testing of hereditary hearing loss. DNA was extracted from whole blood using a filter paper-based DNA extraction structure and captured by a filter disc. PCR amplification was performed in the same extraction chamber, and the amplification of three muted genes was used to identify inherited hearing loss.

1.3.1.2 CTC analysis

Epithelial cancer cells can undergo epithelial to mesenchymal transition (EMT). During this transition, cells express different surface markers. Therefore, EpCAM based affinity selection is not sufficient to isolate a diverse tumor population. Toner group developed an integrated microsystem (CTC-iChip) to isolate CTCs either by positive selection (antigen-dependent) or negative depletion (antigen-independent) modes. The system housed three tasks into a single platform. (i) Deterministic lateral displacement (DLD) array to separate CTCs and some WBCs from red blood cells. (ii) Inertial focusing for the alignment of nucleated cells. (iii) Deflection of magnetically labeled cells by magnetophoresis. In the positive selection, beads were used for the CTC labeling (anti-EpCAM), [96], and in the negative selection, beads were used for the WBC labeling (anti-CD44, anti-CD 66b).[97]

Another DLD based CTC selection was reported for the deformability analysis (**Figure 1.9A**). The first module has a two mirrored DLD array facilitating the depletion of blood cells. The second module also contains another DLD array with an increased tilt angle facilitating the size-exclusion separation of CTCs. High throughput sample processing was achieved by integrating four DLD arrays for CTC enrichment.[98]

The same group has developed an integrated microsystem (IMS-Chip) to analyze the silent gene effect (**Figure 1.9B**). The microsystem consists of two modules. One module is for producing transient membrane holes as a result of membrane deformation and siRNA delivery.

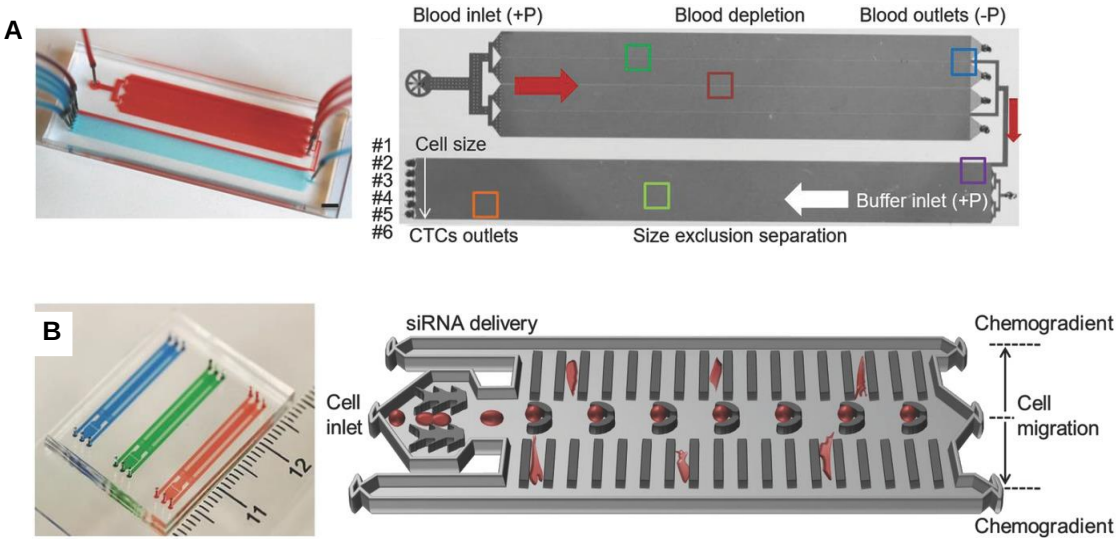

Figure 1.9. Monolithic microsystems for the CTCs isolation and analysis. **(A)** DLD based microfluidic device to enrich CTCs. Red solution indicates the blood sample, and the blue solution indicates the buffer. First module depletes blood while the second module enriches CTCs based on size exclusion ((https://doi.org/10.1002/adbi.201800200) Copyright Wiley-VCH GmbH. Reproduced with permission.) **(B)** Photograph of the IMS-Chip with a schematic illustration. IMS-Chip was used for the CTC deformation, siRNA delivery and cell migration evaluation through a chemotaxis gradient ((https://doi.org/10.1002/adbi.201700054) Copyright Wiley-VCH GmbH. Reproduced with permission.)

The second module is for cell capture, cell culture, and migration through a chemotaxis gradient. siRNA silenced a gene affecting the migration of CTCs.[99]

Soper group has developed a microsystem for the affinity isolation, enumeration, and preconcentration of CTCs. The device integrated a cell selection module, a conductivity sensor, and an electro-manipulation unit. The affinity captured cells were released from the capture device using trypsin and directed towards the conductivity sensor for counting. After then, the cells were introduced into the electromanipulation unit for enrichment. The enrichment occurred due to the intrinsic electrophoretic mobility of CTCs and the applied electric field. The device achieved an enrichment factor of 500, and the enriched cells were used to search point mutations.[100]

It has been hypothesized that CTCs can secrete proteolytic enzymes facilitating the CTC invasion into a tissue. Dhar *et al* developed a microsystem combining CTC isolation and CTC encapsulation. Following the CTC isolation and post-isolation wash, metalloprotease (MMP)

substrate was infused, and cells were directed towards a droplet generator to form microdroplets. Cell secreted proteases were determined by fluorescent product formation.[101]

1.3.1.3 Extracellular vesicles

Tumor-derived exosomes are used as biomarkers in cancer diagnosis and therapeutic efficacy determinations. Integrated systems based on the affinity isolation of exosomes were reported. He *et al* developed a microsystem for on-chip immune isolation of exosomes and *in situ* protein analysis (**Figure 1.10A**). Cascading microfluidic channels were incorporated into the system. The system could isolate EpCAM (+) exosomes, lyse, and immunoprecipitate target proteins. The sandwich immunoassay was used for the chemifluorescence detection and expression level analysis of insulin growth factor receptor (IGF-1R), a biomarker and a therapeutic target for non-small-cell lung cancer (NSCLC).[102] Shao *et al* demonstrated a microfluidic platform for immunomagnetic exosome RNA analysis (iMER). The system integrated three functions, enrich cancer-specific exosomes using anti-EGFR, on-chip RNA isolation, and mRNA expression analysis by on-chip RT-qPCR. The system was used to evaluate the mRNA expression levels of O^6-methylguanine DNA methyltransferase (MGMT) and alkylpurine-DNA-N-glycosylase (APNG), potential biomarkers for the determination of therapeutic efficacy in glioblastoma multiforme (GBM) patients.[103]

Size-based EV isolation systems are common in monolithic microsystems. An integrated double filtration system for the isolation, enrichment, and quantification of EVs was reported by Liang *et al*.[104] Two polycarbonate membranes with 200 nm, and 30 nm pore sizes were used for the separation of EVs. The separated fraction was quantified using on-chip ELISA. The ELISA result was imaged using a smartphone facilitating the use of the system in POC settings.[104] An acoustofluidic platform for the single-step on-chip isolation of exosomes was demonstrated by Wu *et al*.[105] The system had two sequential surface acoustic wave (SAW) microfluidic modules that contained tilted angle standing SAW field generated by interdigital transducers. The first

module removed large blood cells and separated plasma for the downstream analysis, and the second module separated exosomes from other EV subpopulations.[105]

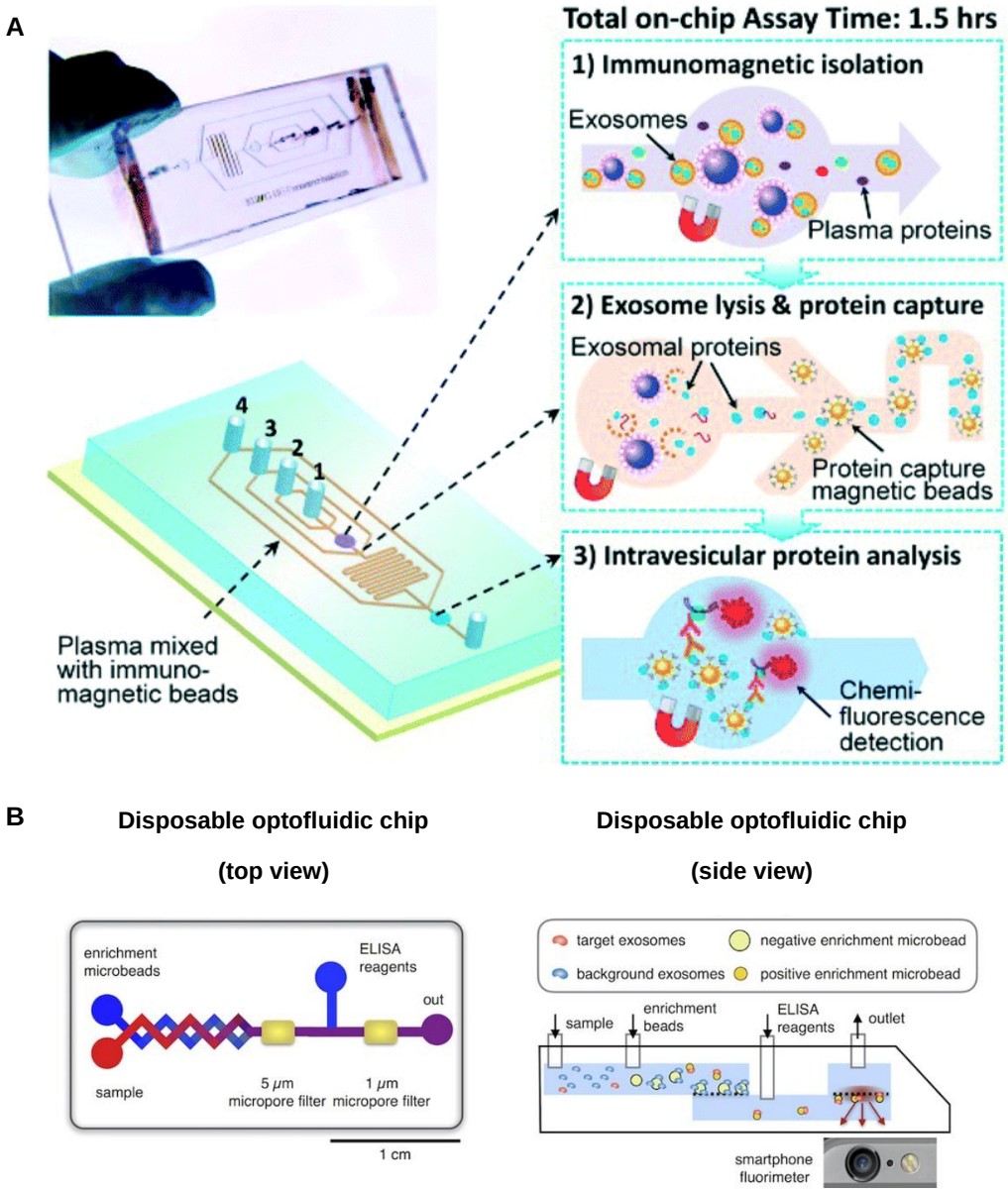

Figure 1.10. Integrated microfluidic systems for the analysis of exosomes. **(A)** PDMS device that contains a cascading microchannel circuit for the analysis of exosome specific protein biomarkers. The steps include the immunomagnetic separation of exosomes, chemical lysis, desired protein affinity selection and intravesicular protein analysis by chemifluorescence. #1–4 are the inlet for exosome capture beads, washing/lysis buffer, protein capture beads, and ELISA reagents, respectively (Adapted from reference 102 (https://doi.org/10.1039/C4LC00662C) - Published by the Royal Society of Chemistry). (**B)** Top and side views of the optofluidic chip (μMED) containing sample and bead inputs, two micropore filters for trapping beads and ELISA reagent input. Chaotic mixer rapidly mixes the microbeads with the sample and incubate on-chip for the affinity selection. Final readout was taken using a smart phone (Adapted from reference 106 (https://doi.org/10.1038/srep31215)).

A combination of Immunoaffinity based EV isolation and size-based separation was

demonstrated by Ko *et al* (**Figure 1.10B**).[106] Smartphone enabled optofluidic platform (μMED) was used for the isolation and quantification of brain-derived exosomes. The system consisted of enrichment channels and two micropore filter structures (5 μm and 1 μm). The serum sample was incubated with functionalized negative selection beads (7 μm) and positive selection beads (2.2 μm). Background exosomes were depleted using the negative selection beads, while the desired exosomes were positively selected and trapped on a 1 μm filter. Brain injury-specific surface markers were used for the quantification of exosomes using ELISA.

1.3.1.4 Single-cell analysis

Study a large number of single cells are essential to get more reliable information about a cell population. Multiplexed analysis of single cells was demonstrated by Valdes *et al*.[107] The device integrated 16 separate microchambers with microwells for single-cell cultivation. The microfluidic device consists of three layers, a control layer, a flow layer, and a microwell layer. Each microwell has an individual microenvironment and can hold 1-4 cells. The utility of the system was demonstrated by analyzing neutrophil extracellular traps.[107] The same group has developed a microsystem consisted of an array of cell culture modules and biosensor chambers for secretory analysis of interleukin-8 (IL-8) and tumor necrosis factor-alpha (TNF-α) from neutrophils and monocytes. Cells were trapped in the microwells and chemically stimulated to quantify their secretions using a sandwich ELISA.[108]

Leukocytes also secrete proteases for regulating inflammatory responses. An integrated continuous flow microsystem was developed to detect secretory protease activity of individual leukocytes (**Figure 1.11**). The microsystem consisted of a DLD module and a droplet generator module. DLD module washed Leukocytes with a substrate buffer and directed them towards the droplet generator module that compartmentalizes single leukocytes into droplets. The protease activity was measured using fluorescence.[109]

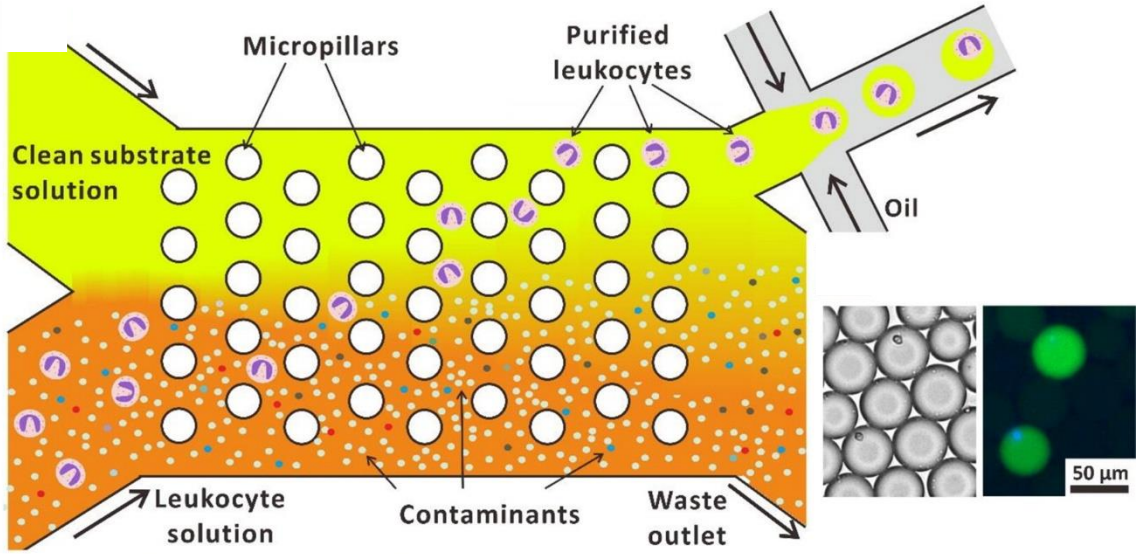

Figure 1.11. Integrated microsystem for the single cell analysis of leukocyte protease activity. Schematic drawing showing the Leukocyte purification by deterministic lateral displacement (DLD) and single cell encapsulation by the droplet generator. Fluorescent image shows two leukocytes in droplets (blue, Hoechst nuclear staining; green, protease signal) (Adapted with permission from reference 109 (**https://doi.org/10.1021/acs.analchem.6b03370**). Copyright (2016) American Chemical Society).

1.3.1.5 ELISA-assays

Quantification of low abundance proteins is essential in biological and clinical applications. An integrated microsystem for quantifying disease-associated protein biomarkers in resource-limited settings was introduced by Liu *et al*.[110] The system integrated ELISA and platinum nanoparticles (PtNP) catalyzed oxygen distance readout into a single device (ELISA-Chip). The fluidic manipulation was performed using a permanent magnet. Human C reactive protein was quantified in less than 2 h using the system.[110] Integrated microfluidic solid-phase ELISA platform that combines a microwell patterned assay chamber with micropumps for fluidic manipulation was reported. The assay chamber can be pneumatically actuated to minimize the volume requirement for the chemifluorescent reaction. Low volume improved the assay sensitivity as well as the speed assay speed. The utility of the system was demonstrated by quantifying insulin-like growth factor (IGF-1R) with the detection limit of 21.8 aM.[111] Immunoassay platform that uses microparticles for labeling was demonstrated by Kim *et al*.[112] Microfluidic pumps, and PDMS membrane valves were incorporated into the system for the programable fluid and bead delivery. APTES patterning

was used to derivatize capture antibodies into the glass surface, and magnetic microparticles conjugated with the detection antibody were used for the sandwich ELISA assay. Multiple samples can be processed through the system, and the utility was demonstrated by screening for IgG, and PSA.[112] CD4(+) T lymphocytes were enumerated using a single bead-based high throughput integrated microsystem. The system contained multiple reaction chambers allowing the functionalized bead (anti-CD4) to react with sample lysate, wash buffer, horseradish peroxidase (HRP) enzyme, and mixed substrate buffers. An external magnetic force was used to move the single bead in different compartments, and a sandwich chemiluminescent assay was used for the indirect enumeration of CD4 (+) T lymphocytes in a lysed blood sample.[113]

1.3.1.6 Other biomedical applications

An integrated system for the viral detection was published by Lee *et al*.[114] The antibody-conjugated magnetic beads were used to isolate viral particles and then subjected to thermal lysis, RNA extraction, and RT-qPCR. The dengue virus was detected with a sensitivity of 10-100 PFU using this method.[114] An integrated slidable microfluidic system was developed for the detection of foodborne pathogens. The system consisted of modules for solid-phase DNA extraction, PCR amplification, and immunochromatographic strip detection. Slidable chambers were incorporated into the system to transport liquid from module to module without having microvalves.[115] Genetic analysis system for subtyping influenza viral strain was reported by Pal et al. The device consisted of biochemical reactors, heaters, temperature sensors, valves, and a gel electrophoresis section. The utility of the system was demonstrated by identifying hemagglutinin A subtype of the A/LA/1/87 strain of influenza virus.[116] Huang *et al* reported a microsystem for the automated immunohistochemistry (IHC) staining of clinical tissue samples. Ten tissue samples were stained simultaneously using an aptamer-based IHC assay.[117] Sickel cells were detected using a label-free impedance sensing technique. The microfluidic device consisted of an on-chip oxygen control unit and an electrical impedance sensing unit for the

hematological analysis.[118] Controlled drug delivery is essential for the efficacy of molecular therapeutics. Integrated microsystems for the controlled delivery of drug compounds were reviewed.[119]

1.4 Modular Systems

In modular systems, task-specific units are fabricated separately and then connected to form an integrated system. The significant advantage of modular design is the ability to reconfigure the system quickly for a different application or when there is a need to upgrade the system. This requires the replacement/upgrade of an individual module without changing the entire system. For example, Kamande *et al* developed a modular microsystem to analyze CTCs by integrating a cell selection device, cell counting device, and a cell imaging device.[120] This setup can be easily reconfigured to analyze extracellular vesicles. Since each task-specific unit is designed and fabricated separately, the material and fabrication method can be selected to improve the system's performance.

The major challenge in modular systems is designing interconnects that guarantee perfect module alignment while having a minimum dead volume. Interconnects are used to make a leak-free connection between two consecutive modules even in high fluidic pressure. Unswept volumes associated with the interconnects add an extra volume to the final device. However, the selection between a monolithic or a modular system depends on the cost, application, and flexibility associated with the system.[121]

This section will describe common fabrication methods of modular systems, interconnects, and their biomedical applications.

1.4.1 Fabrication methods and modular assembly

Major fabrication methods of modular microfluidic systems are photolithography, injection molding, laser ablation, hot embossing, micro/nanoimprinting, and 3D printing. The 3D printing

technology is widely used due to the low cost, rapidity, and relatively high throughput.[122] Besides, the bonding process can be eliminated by enclosing the microchannels during the printing.[123]

Different methods were used to connect task-specific units in modular microfluidics. The techniques should guarantee a reversible, low extra volume, leak-free connection with perfect modular alignment. Lego-like building blocks (**Figure 1.12A**) were reported to use as individual modules to build an integrated system. The microfluidic channels were imprinted on the bottoms and lateral surfaces.[124] The fluidic connection between the individual units was based on the compression sealing of the Legos.[125] Another lego-like plug-and-play system (μOrgano) was demonstrated to use as a multi-organ chip. The plug-and-play connectors (**Figure 1.12B**) contain a microfluidic channel and two cylindrical inlet and outlet channels to connect two modules.[126] 3D printed microfluidic devices containing male and female parts to connect individual modules were reported. The microsystem was used to make an integrated droplet generator. The 3D-printed interconnects were smoothed to achieve a leak-free connection.[127]

Grodzinski *et al* used barbed connectors as an approach to connect individual modules. Although the connectors provide a reusable, easy connection with a tight seal, the increased internal fluidic volume (39 μL) associated with the connectors was a disadvantage.[128] Microgaskets and O-rings were used to interconnect individual modules. The connection could hold > 200 psi pressure with a minimal unswept volume (1 nL).[121] Lee *et al* used rubber O-rings and metal pins to interconnect 3D printed modules. The performance of the interconnects was improved by applying silicone grease around the O-ring.[129] Magnetic interconnects that have ring magnets and sealing gaskets were used to build larger integrated systems.[125] Magnetic clamping structures that contain neodymium disc magnets combined with PDMS gaskets were used to connect consecutive modules with a negligible dead volume.[130] Tubing-based interconnections were also reported. Kamande *et al* used capillary tubing to integrate modules.[120] The major disadvantage of using capillary tubing is that the tubing add an extra volume to the system. This

limitation was overcome by introducing semi-rigid Tefzel tubing. The tubing had an unswept volume of ~20 nL.[131]

1.4.2 Applications of modular microfluidics

Modular microfluidic systems were used in different biomedical applications. This section will briefly describe the recent use of modular systems in nucleic acid analysis, biomarker isolation and analysis (CTC, EV, and proteins), organ-on-a-chip systems, and single-cell analysis.

1.4.2.1 Nucleic acid analysis

Integrated modular microsystems were used in forensic DNA analysis. Reedy et al demonstrated a rapid, short tandem repeat (STR) analysis system. Three devices, solid-phase extraction (SPE) device, PCR device, and microfluidic electrophoresis (ME) device, were integrated into the STR analysis system. Non-contact IR thermal source was employed for the PCR amplification reaction, and a ~ 2-fold decrease in analysis time was achieved. The

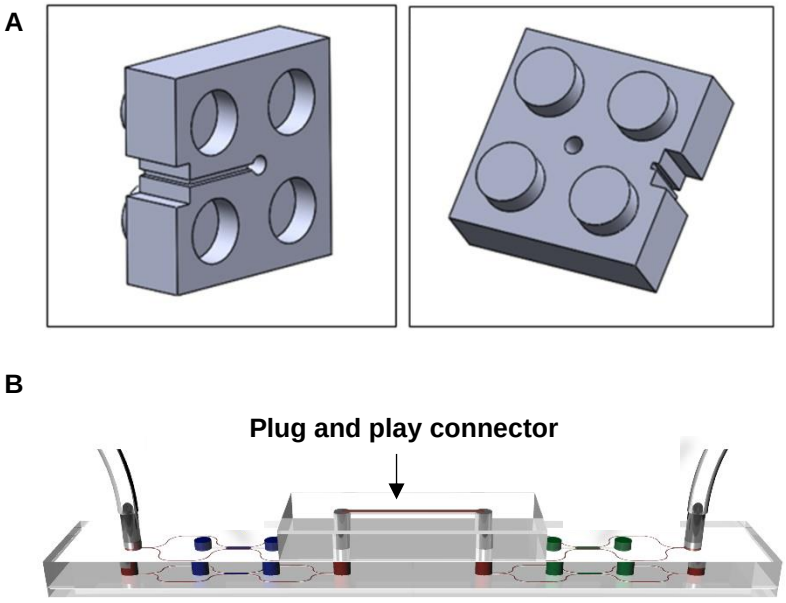

Figure 1.12. Integration of modular systems. **(A)** Lego-like microfluidic building block. Microfluidic channels are imprinted on the bottom and lateral surfaces (Adapted with permission from reference 124 (https://doi-org.www2.lib.ku.edu/10.1088/1361-6439/aa53ed); permission conveyed through Copyright Clearance Center, Inc). (B) Plug and play fluidic interconnect use in µOrgano-system to connect two modules (Adapted with permission from reference 126 (https://doi.org/10.1371/journal.pone.0139587)).

microsystem was able to perform a complete STR analysis in less than 2.5 h using DNA extracted from a buccal swab sample.[132] A microfluidic system that can employ a wide range of sample types for STR was reported by Han *et al*.[133] The system contains a DNA extraction and amplification chip and a capillary array electrophoresis chip (CAE). The extraction chip has a chitosan-modified quartz filter paper with *in situ* PCR capability to extract DNA in high efficiency and perform PCR amplification in a single chamber. The CAE chip has two long separation channels (16 cm) for the separation of STR products. The products were detected by a four-color confocal fluorescence microscope in less than 2 h.[133] The same group developed a more advanced sample-in-answer-out format to analyze a wide range of sample types for forensic analysis (**Figure 1.13A**). The system consists of two types of sample preparation modules (SPMs) to analyze different samples, a CAE module and a plastic chip cartridge with injection electrodes for device assembly. A direct SPM module was used to analyze samples without a DNA extraction step, and more complex samples were analyzed using the extraction SPM module. The CAE chip contained three separation channels (19 cm), two channels for samples, and one channel for the ladder. The sample analysis time was close to 2 h as previously.[134]

The Soper group developed a polymer-based continuous flow thermal cycler (CFTC) device for Sanger sequencing. The device consisted of a spiral microchannel for 20 thermal cycles and contained defined temperature zones for denaturation, renaturation, and DNA extension. The thermal cycler was integrated with a solid-phase reversible immobilization (SPRI) chip to remove excess dye-labeled terminators facilitating the subsequent gel electrophoresis. The two devices were coupled using capillaries and a Micro Tee. The system could read >600 bp in less than 15 min.[135]

PCR/ligase detection reaction (LDR)/universal array assay was used for the multiplexed analysis of unique DNA signatures.[136] The technique was used in a modular microfluidic processor for the identification of multi-drug resistant tuberculosis by looking for point mutations

in the *rPoB* gene (**Figure 1.13B**). The fluidic motherboard integrated cell lysis, solid-phase DNA extraction, thermal reactors, and microarray with micromixers, pumps, heaters, and optical detection systems. Individual modules were fabricated separately using thermoplastics and integrated into a fluidic motherboard to build the final system. The fluidic motherboard was populated with membrane valves for automated sample processing. The single-base variations of the multi-drug-resistant bacterium were detected in less than 30 min.[137] The microsystem utilized a sputum sample that typically contains a high load of bacterial cells. Therefore, an enrichment step was not incorporated, but when analyzing a water sample, an enrichment step is required before the analysis due to the presence of a low cell number. Chen et al developed an integrated system for the detection of bacterial pathogens in water. The device integrated affinity

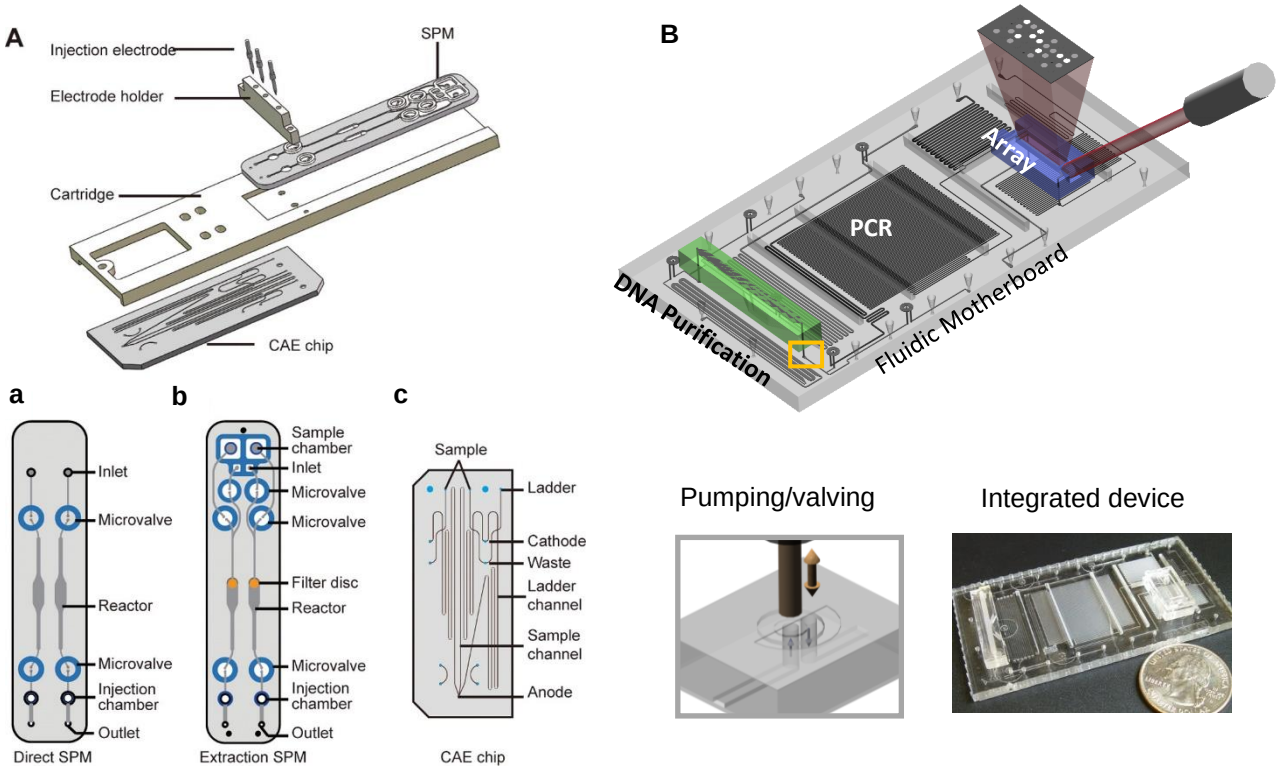

Figure 1.13. Modular microfluidic systems for DNA analysis. **(A)** Schematic diagram of individual components of the STR analysis microsystem. Structures of **(a)** the direct SPM, **(b)** extraction SPM, and **(c)** capillary array electrophoresis chip (Adapted with permission from reference 134 (**https://doi.org/10.1021/acs.analchem.9b01560**). Copyright (2019) American Chemical Society). **(B)** Modular microfluidic system for the identification of multi-drug resistant tuberculosis. Polycarbonate based membrane valving system was used for the fluidic manipulation (Adapted with permission from reference 137 (**https://doi.org/10.1002/anie.201200732**)).

isolation, cell lysis, solid-phase extraction, continuous flow (CF)-PCR, CF LDR, and a universal zip-code array. Motherboard-module assembly was achieved using semi-rigid Tefzel tubing and conical receiving ports. The system could identify *E.Coli* and *Salmonella* bacterial pathogens in less than 40 min.[131]

An integrated system consisted of DNA extraction and PCR-based amplification module, and capillary electrophoresis (CE) module was used in pharmacogenetic testing. The amplified DNA was injected into the CE chip for the separation and detection of single-nucleotide polymorphisms.[138] A Plug-less clamp-based modular system was introduced for the parallel purification of four genome segments. The purification provided better results than the conventional methods.[139]

1.4.2.2 CTC analysis

Integrated modular systems were used for the negative selection of CTCs. A modular system (μ MixMACS) for the selection of CTCs was introduced by Lee et al. The device consisted of two modules, a multi-vortex mixing module, and a magnetic-activated cell sorting module. Blood was mixed with anti CD45 conjugated magnetic beads in the multi-vortex mixing module to deplete WBCs from the fraction. In the module, sudden expansion microchannels and incubation chambers were designed to facilitate mixing and increase the Ab-Ag interactions. Magnetically activated cell sorting module depletes the magnetically labeled WBCs in the sample while CTCs were enriched for the downstream analysis.[140] Rapid and high sensitivity CTC detection was achieved by integrating a deterministic lateral displacement (DLD) module, magnetic purifying module, and CTC capture platform. DLD module contains micro-posts and larger cells like CTCs, and some WBCs were directed towards the center of the channel. This partially enriched sample was directed to the purifying chip for further depletion of WBCs. Purifying chip contains CD45 coated dynabeads, and affinity captured WBCs were removed using a permanent magnet. Finally, CTCs were arrested in a CTC capture platform coated with rat-tail collagen.[141]

CTC positive selection system was demonstrated by Sun et at. Cell replicated PDMS modules (CellRePDMS) coated with anti-EpCAM antibodies were used as individual modules tobuild an integrated system. CellRepPDMS film was modified with C18, biotinylated BSA, and streptavidin. Biotinylated anti-EpCAM antibodies were conjugated into the surface after the modification. These modules were stacked together using silicone washers to form a CTC chamber. The device was able to capture EpCAM (+) cancer cells as well as EpCAM (-) cancer cells.[142] Kamande *et al* developed a microsystem for the affinity isolation of CTCs and their downstream analysis. Three individual task modules, a CTC selection module, impedance module, and an imaging module, were connected via capillary tubing (**Figure 1.14A**). CTC selection module consisted of sinusoidal-shaped microchannels for high CTC recovery. Anti-EpCAM antibodies were covalently attached to the device surface, and after the affinity isolation of CTCs, trypsin was used to release them. The released CTC fraction was directed to the impedance module for label-free counting and the imaging module for immunophenotyping. The imaging module consisted of micropore structures to physically trap CTCs within a common imaging plane. The utility of the system was demonstrated by analyzing EpCAM (+) CTCs from pancreatic ductal adenocarcinoma (PDAC) patients.[120]

An automated single-cell analysis system was reported to separate, concentrate, and trap cells in a single cell array format (**Figure 1.14B**). Two individual modules, an acoustic chip and a dielectrophoretic chip were interconnected following plasma treatment. Cancer cells were pre-aligned, separated, and concentrated using the acoustic chip, and the single cells were actively trapped into microwells using dielectrophoresis.[143]

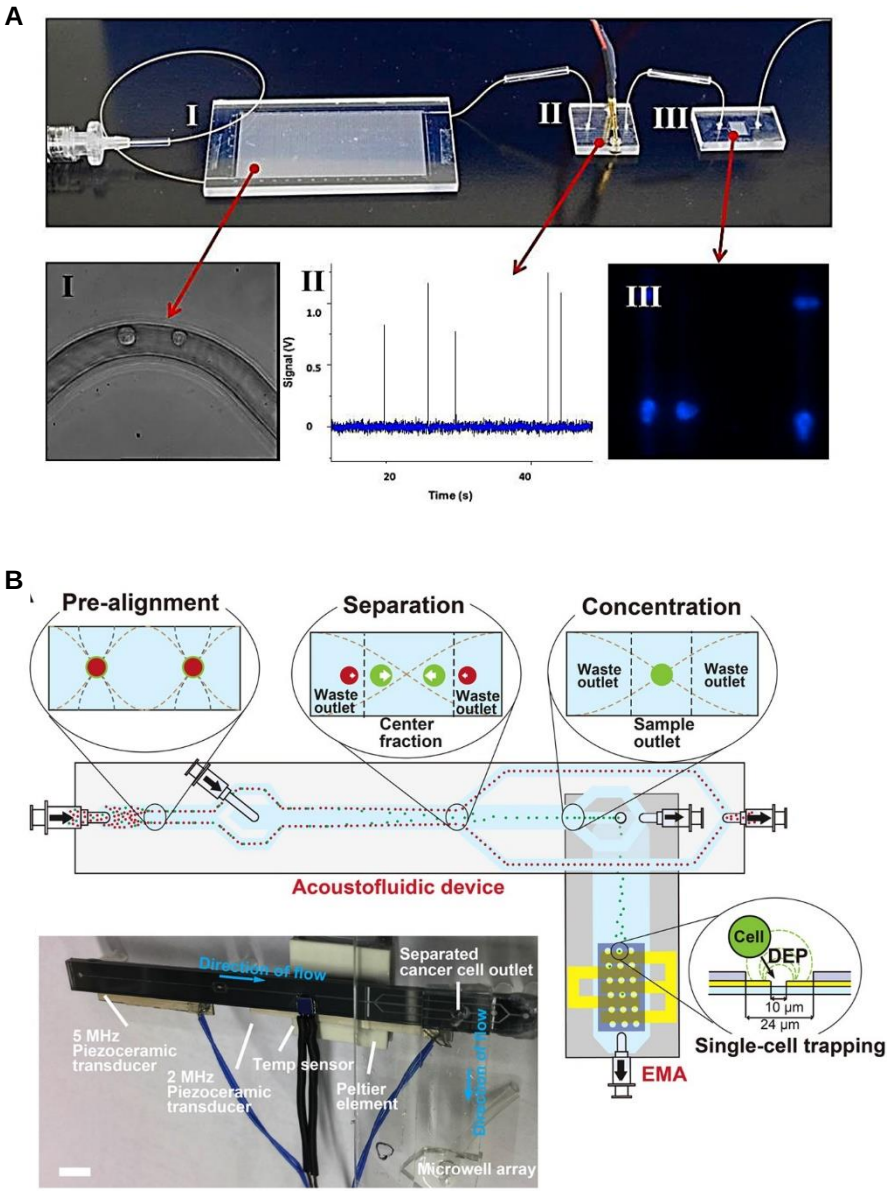

Figure 1.14. Integrated modular platforms for the isolation and analysis of CTCs. (**A**) Integrated system for the affinity isolation, enumeration and immunophenotypic identification of CTCs. Individual modules were connected using capillary tubing (Adapted with permission from reference 120 (https://doi.org/10.1021/ac401720k). Copyright (2013) American Chemical Society). **(B)** Schematic diagram of the integrated device that contains an acoustic module and a dielectrophoretic module. The acoustic module pre-aligns, separates, and concentrates the CTCs. Single CTCs were trapped in the microwells due to the dielectrophoresis (Adapted with permission from reference 143 (https://doi.org/10.1038/srep46507)).

1.4.2.3 Extracellular vesicle (EV) analysis

An integrated microfluidic system was developed by Chen et al for on-chip enrichment and quantification of extracellular vesicles. Three modules were integrated into the system and

could perform plasma separation from whole blood, affinity enrichment of EVs, and EV quantification. A stirring-enhanced filtration module has a membrane filter (0.2 μm), and vortex flow facilitates plasma separation. Vortex flow agitates blood cells minimizing the cell clogging during the filtration process. Antibody (anti-CD63) coated magnetic beads were used in the EV enrichment module to capture EVs from the plasma. EV quantification module consists of micro-chambers, pumps, and valves to perform on-chip ELISA to quantify EVs using tyramide signal amplification (TSA). The modules were integrated using double-sided tape.[144]

A microfluidic cartridge was reported for erythrocyte-derived microvesicle (MV) isolation and labeling. The system consisted of two modules, an MV filtration module and an affinity selection and labeling module. The filtration module contains a membrane filter (~1 μm) and, underneath the membrane, a capillary layer for the direction of filtered MVs towards the collection channel. The filtered MVs were captured by antibody-coated beads and magnetically labeled using target-specific magnetic nanoparticles. MV quantification and the detection of molecular markers were performed using a miniaturized nuclear magnetic resonance system. The entire process required less than 30 min. The modules were connected using two ring magnets.[145]

1.4.2.4 Protein analysis

A miniaturized modular microfluidic chromatography device for POC protein enrichment and purification was presented by Millet *et al.*[146] *E. Coli* cell lysate was processed through an immobilized metal affinity chromatography (IMAC) column followed by a size exclusion column to purify overexpressed His-tagged green fluorescent protein (eGFP). Two modules were interconnected by a 3D fluidic bridge that also permitted the desalting of the product. The system achieved performance comparable to conventional column approaches.[146]

Individual microfluidic breadboards (FBB) were used to build multiple chip modular platforms for the high sensitivity detection of prostate-specific antigen (PSA). The two modules

include an FBB module and a detection module. PSA was captured using monoclonal anti-PSA coated magnetic microparticles and sandwiched using polyclonal anti-PSA antibodies immobilized in gold nanoparticles. Released bar code molecules were directed to the detection module and attached, followed by sandwiching with gold nanoparticles giving an optical readout. Ato molar concentrations of PSA were detected using this technique. Channels in micromachined connecting pieces achieved the fluidic connection between two modules.[147]

1.4.2.5 Organ-on a chip systems

In vitro tissue culture microsystems, also known as organs-on-a-chip systems, were developed to create miniaturized tissue mimics for modeling diseases, predicting human responses to different therapeutics, and determining drug efficacy and side effects.[148] These systems can be used as an alternative to animal models.

A PDMS-based multisensor integrated modular platform was developed to monitor microenvironmental parameters (pH, O_2, and temperature), measure biomarkers, and observe organoid morphologies in human tissue and organ models. This organ-on-a-chip system contained individual modules, including micro bioreactors, a physical and chemical sensing module, bubble trap, and bio-electrochemical sensing module. All these modules were integrated into a flow control breadboard that was populated with pneumatic valves allowing automated valve operation. The system's utility was demonstrated by monitoring the drug-induced organ toxicity in a dual-organ human liver-and-heart-on-a-chip platform and a dual-organ human liver-cancer-and-heart-on-a-chip platform.[149]

Another PDMS-based Tetris-Like (TILE) modular microfluidic platform was developed as a microfluidic perfusion device for bioimaging and analytical measurements (**Figure 1.15A**). The interconnection of the modules was achieved by incorporating self-aligning magnetic

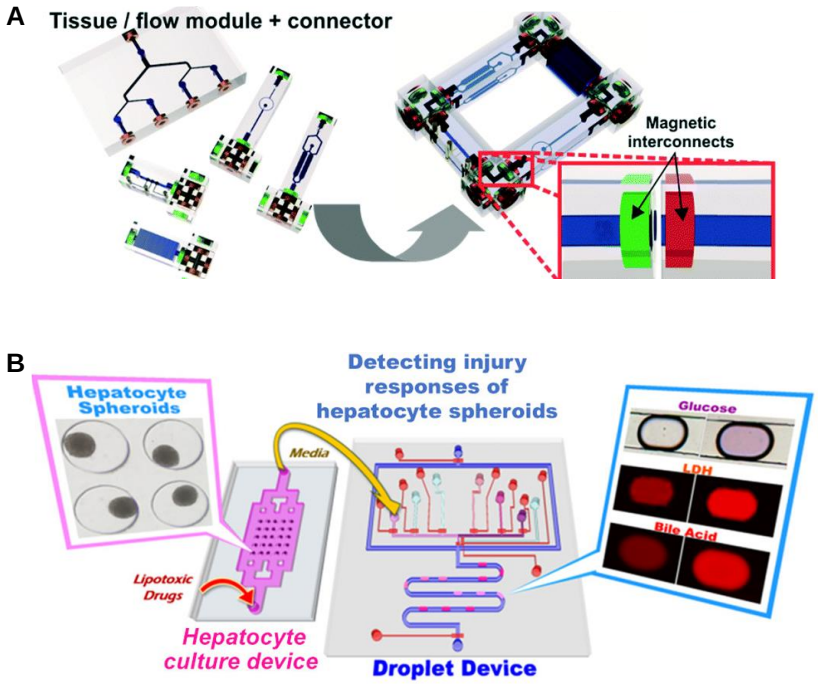

Figure 1.15. Modular microsystems as organ-on-chips. **(A)** PDMS-based Tetris-like (TILE) modular microfluidic perfusion system that contains magnetic interconnects for modular integration (Adapted n from reference 150 (https://doi.org/10.1039/C9LC00160C) with permission from The Royal Society of Chemistry). **(B)** Droplet-based modular system for the multiplexed analysis of glucose, LDH, and bile acid in a hepatocyte conditioned medium (Adapted with permission from reference 151 (https://doi.org/10.1021/acs.analchem.8b05689). Copyright (2019) American Chemical Society).

interconnects at lateral walls enabling the stick and play mode of operation. The applicability of the system was demonstrated by assembling 2 or 3 tissue perfusion circuits to evaluate the liver-mediated bioactivation of a nutraceutical compound (quecertin) and a cancer prodrug (cyclophosphamide).[150]

Customizable Lego-like system (μOrgano) to connect multiple organ-on-a-chip devices were demonstrated by Loskill *et al*.[126] Different master organ chips were used to culture different cells and finally combined using plug & play connectors for drug screening purposes. The utility of the system was demonstrated by combining two heart-on-chips.

A droplet-based modular microfluidic system was introduced for the multiplexed analysis of biochemical markers in a microliter volume (**Figure 1.15B**). An organ-on-a-chip device was

connected to a droplet device to form the integrated system to detect injury responses. Hepatocyte spheroids were cultured in a cell culture device, and cell-conditioned media was directed into a droplet device for the multiplexed analysis of LDH, glucose, and total bile acids that are used for the biomarkers for injured hepatocyte spheroids. Both colorimetric and fluorescent detections were used to quantify the analytes.[151]

Besides the organ-on-a-chip approach, the tumor microenvironment was mimicked to analyze oxygen-dependent cytotoxicity and genotoxicity of an anti-cancer drug using an integrated modular system. The device consisted of a single cell culturing chamber and a chemical reaction channel. A thin PDMS membrane (100 μm) was used to separate the two modules. The oxygen gradient was achieved by chemical scavenging of oxygen in the culture chamber. The cytotoxicity was measured by evaluating the cell viability, and genotoxicity was evaluated by a comet assay.[152] Qiu *et al* demonstrated a similar cell culture system developed using different functional PDMS slices and a PET membrane.[153]

Munshi et al connected a series of 3D printed microfluidic modules for the electrochemical detection of ATP-mediated nitric oxide (NO) release from endothelial cells. The three functional modules were for cell culture, sample injection, and detection.[154] A 3D printed Lego-like modular system based on capillary driving was proposed to use in stent degradation and cell culture.[155] Xie *et al* developed a lego-like modular system to cultivate two types of cells for drug toxicity evaluation.[156]

1.4.2.6 Other biomedical applications

An integrated modular system was reported to analyze the effect of external chemical signals on intracellular signaling. The system consists of two modules, a linear-gradient generator and a single cell analysis microwell platform. The linear gradient generator generated chemical waveforms that have different amplitudes. The cells trapped in the microwells received these

different amplitude signals, and the response of each cell was measured by fluorescent time-lapse microscopy.[157]

1.4.2.7 Sensor integrated systems

Modular microfluidic systems integrating different sensors as individual modules to analyze/detect analytes were also reported. A portable Coulter counter module for a label-free counting of single particles,[158] separate sensor modular systems for conductivity, amperometric and pH measurements,[130] electrochemical sensor modules for salivary cotinine detection,[159] and enzymatic activity detection[160], and a conductivity sensor module for the label-free counting of single-cells were reported in this category.[161]

1.4.3 Summary of thesis chapters

1.4.3.1 Chapter 2: Photo-cleavable linker for the release of rare liquid biopsy markers after microfluidic affinity enrichment

Liquid biopsy markers such as circulating tumor cells (CTCs) and extracellular vesicles (EVs) provide a good source of information for disease diagnosis and prognosis. These markers can be selected from blood using an affinity approach where antibodies or other affinity agents are used. Following affinity enrichment, the release of the isolated liquid biopsy markers from the device's surface is essential for downstream enumeration and molecular profiling. In this chapter, we detail a heterobifunctional, 7-aminocoumarin photocleavable (PC) linker to covalently attach Abs to carboxylated surfaces. After enrichment, we selectively cleaved the PC linker by exposing the microfluidic device to visible light (400 – 450 nm) and efficiently released captured liquid biopsy markers from the device's surface for downstream analysis. The use of visible light minimized physical damage to the marker and UV damage to the molecular cargo. The PC linker was used to enrich CTCs from blood and rapidly (2 min) and efficiently (>90%) released them for subsequent enumeration, culturing, and mRNA expression profiling with more than 85% of purity. PC linker was also used to enrich EVs from CD8(+) T-cell line and rapidly (2 min) and efficiently

(>90%) released them for nanoparticle tracking analysis (NTA) and transmission electron microscopy (TEM).

1.4.3.2 Chapter 3: Integrated modular microfluidic system (SMART-Chip) for the comprehensive analysis of circulating tumor cells

In this chapter, we report a system modularity chip for the analysis of rare targets (SMART chip) comprised of three task-specific modules that can fully automate the processing of CTCs. The modules were used for affinity selection of the CTCs from peripheral blood with subsequent photorelease, simultaneous counting and viability determinations of the CTCs, and staining/imaging of the CTCs for immunophenotyping. The modules were interconnected to a fluidic motherboard populated with valves, interconnects, pneumatic control channels, and a fluidic network. The SMART chip components were made from thermoplastics via micro-replication, which significantly lowered the cost of production, making it amenable to clinical implementation. The utility of the SMART chip was demonstrated by processing blood samples secured from colorectal cancer (CRC) and pancreatic ductal adenocarcinoma (PDAC) patients. We were able to affinity select EpCAM expressing CTCs with high purity (0-3 white blood cell contaminants/mL of blood), enumerate the selected cells, determine their viability and immunophenotype. The assay could be completed in <4 h, while manual processing required >8 h.

1.4.3.3 Chapter 4: Microfluidic approach for the detection of SARS-CoV-2 from saliva

In this chapter, we describe a microfluidic system that can accept saliva samples and selectively enrich viral particles (VPs) and then count the number of VPs using a label-free, nano-Coulter Counter. The VP selection chip affinity selected SARS-CoV-2 VPs using an aptamer surface-immobilized to pillar structures contained within the chip that was directed against the SARS-CoV-2 Spike protein. Following selection, the VPs were released from the capture surface using a photocleavable linker discussed in chapter 2. Following and subsequent release from the

VP selection chip, the VPs were counted using the nCC chip. For high throughput VP counting, 5 nCCs were placed in parallel and offered 100% detection efficiency for VPs traveling through a 200 nm pore. The entire assay could be completed in ~15 min. Besides, the enriched particles were available for analysis of their RNA content using RT-qPCR. Because the chip can be programmed for a specific target by simply changing the identity of the affinity agent, it will find a plethora of additional applications, for example, selection and counting of exosomes for health-related scenarios as well as addressing future viral pandemics.

1.4.3.4 Chapter 5: Future directions

The integrated modular microfluidic system that we described in chapter 3 will be reconfigured to analyze extracellular vesicles. The new system will integrate EV selection, enumeration, lysis, reverse transcription, solid-phase ligase detection (LDR), and mRNA profiling into a single motherboard. We have recently shown that mRNA expression analysis of CD8 (+) EVs can be used for the diagnosis of acute ischemic stroke (AIS).[162] Some processing steps required off-chip benchtop instrumental analysis minimizing the assay use in point of care applications. The integrated system describes in this chapter can mitigate the limitations of our previous work.

An integrated system will be developed for the detection of SARS-CoV-2. The individual modules, a viral selection module, and an nCC module will be integrated using superhydrophobic seals. The final device will be housed in a cartridge to form a hand-held instrument for at-home testing.

1.5 References

1. Loeffelholz, M. J.; Tang, Y.-W., Laboratory Diagnosis of Emerging Human Coronavirus Infections—The State of the Art. *Emerging Microbes & Infections* **2020,** (just-accepted), 1-26.
2. Kong, L. X.; Perebikovsky, A.; Moebius, J.; Kulinsky, L.; Madou, M., Lab-on-a-CD: A Fully Integrated Molecular Diagnostic System. *J Lab Autom* **2016,** *21* (3), 323-55.
3. Brassard, D.; Geissler, M.; Descarreaux, M.; Tremblay, D.; Daoud, J.; Clime, L.; Mounier, M.; Charlebois, D.; Veres, T., Extraction of nucleic acids from blood: unveiling the potential of

active pneumatic pumping in centrifugal microfluidics for integration and automation of sample preparation processes. *Lab Chip* **2019,** *19* (11), 1941-1952.
4. Morelli, L.; Serioli, L.; Centorbi, F. A.; Jendresen, C. B.; Matteucci, M.; Ilchenko, O.; Demarchi, D.; Nielsen, A. T.; Zor, K.; Boisen, A., Injection molded lab-on-a-disc platform for screening of genetically modified E. coli using liquid-liquid extraction and surface enhanced Raman scattering. *Lab Chip* **2018,** *18* (6), 869-877.
5. Gorkin, R.; Park, J.; Siegrist, J.; Amasia, M.; Lee, B. S.; Park, J.-M.; Kim, J.; Kim, H.; Madou, M.; Cho, Y.-K., Centrifugal microfluidics for biomedical applications. *Lab on a Chip* **2010,** *10* (14), 1758-1773.
6. Madou, M.; Zoval, J.; Jia, G.; Kido, H.; Kim, J.; Kim, N., Lab on a CD. *Annu. Rev. Biomed. Eng.* **2006,** *8*, 601-628.
7. Zoval, J. V.; Madou, M. J., Centrifuge-based fluidic platforms. *Proceedings of the IEEE* **2004,** *92* (1), 140-153.
8. Grumann, M.; Geipel, A.; Riegger, L.; Zengerle, R.; Ducrée, J., Batch-mode mixing on centrifugal microfluidic platforms. *Lab on a Chip* **2005,** *5* (5), 560-565.
9. Haeberle, S.; Brenner, T.; Schlosser, H. P.; Zengerle, R.; Ducrée, J., Centrifugal micromixery. *Chemical Engineering & Technology: Industrial Chemistry‐Plant Equipment‐Process Engineering‐Biotechnology* **2005,** *28* (5), 613-616.
10. Steigert, J.; Grumann, M.; Brenner, T.; Riegger, L.; Harter, J.; Zengerle, R.; Ducrée, J., Fully integrated whole blood testing by real-time absorption measurement on a centrifugal platform. *Lab on a Chip* **2006,** *6* (8), 1040-1044.
11. Park, J.-M.; Cho, Y.-K.; Lee, B.-S.; Lee, J.-G.; Ko, C., Multifunctional microvalves control by optical illumination on nanoheaters and its application in centrifugal microfluidic devices. *Lab on a Chip* **2007,** *7* (5), 557-564.
12. Kim, T. H.; Park, J.; Kim, C. J.; Cho, Y. K., Fully integrated lab-on-a-disc for nucleic acid analysis of food-borne pathogens. *Anal Chem* **2014,** *86* (8), 3841-8.
13. Madadelahi, M.; Acosta-Soto, L. F.; Hosseini, S.; Martinez-Chapa, S. O.; Madou, M. J., Mathematical modeling and computational analysis of centrifugal microfluidic platforms: a review. *Lab Chip* **2020,** *20* (8), 1318-1357.
14. Hess, J. F.; Zehnle, S.; Juelg, P.; Hutzenlaub, T.; Zengerle, R.; Paust, N., Review on pneumatic operations in centrifugal microfluidics. *Lab Chip* **2019,** *19* (22), 3745-3770.
15. Jahromi, A. K.; Saadatmand, M.; Eghbal, M.; Yeganeh, L. P., Development of simple and efficient Lab-on-a-Disc platforms for automated chemical cell lysis. *Sci Rep* **2020,** *10* (1), 11039.
16. Park, J.-M.; Kim, M. S.; Moon, H.-S.; Yoo, C. E.; Park, D.; Kim, Y. J.; Han, K.-Y.; Lee, J.-Y.; Oh, J. H.; Kim, S. S., Fully automated circulating tumor cell isolation platform with large-volume capacity based on lab-on-a-disc. *Analytical chemistry* **2014,** *86* (8), 3735-3742.
17. Schwemmer, F.; Blanchet, C. E.; Spilotros, A.; Kosse, D.; Zehnle, S.; Mertens, H. D.; Graewert, M. A.; Rossle, M.; Paust, N.; Svergun, D. I.; von Stetten, F.; Zengerle, R.; Mark, D., LabDisk for SAXS: a centrifugal microfluidic sample preparation platform for small-angle X-ray scattering. *Lab Chip* **2016,** *16* (7), 1161-70.
18. Sunkara, V.; Kim, C. J.; Park, J.; Woo, H. K.; Kim, D.; Ha, H. K.; Kim, M. H.; Son, Y.; Kim, J. R.; Cho, Y. K., Fully Automated, Label-Free Isolation of Extracellular Vesicles from Whole Blood for Cancer Diagnosis and Monitoring. *Theranostics* **2019,** *9* (7), 1851-1863.
19. Criel, M.; Jonckheere, S.; Langlois, M., Evaluation of three hemoglobin A1c point-of-care instruments. *Clin Lab* **2016,** *62* (3), 285-291.
20. Hugo, S.; Land, K.; Madou, M.; Kido, H., A centrifugal microfluidic platform for point-of-care diagnostic applications. *South African Journal of Science* **2014,** *110* (1-2), 1-7.
21. Strohmeier, O.; Keller, M.; Schwemmer, F.; Zehnle, S.; Mark, D.; von Stetten, F.; Zengerle, R.; Paust, N., Centrifugal microfluidic platforms: advanced unit operations and applications. *Chem Soc Rev* **2015,** *44* (17), 6187-229.

22. Tang, M.; Wang, G.; Kong, S. K.; Ho, H. P., A Review of Biomedical Centrifugal Microfluidic Platforms. *Micromachines (Basel)* **2016,** *7* (2).
23. van Oordt, T.; Barb, Y.; Smetana, J.; Zengerle, R.; von Stetten, F., Miniature stick-packaging–an industrial technology for pre-storage and release of reagents in lab-on-a-chip systems. *Lab on a Chip* **2013,** *13* (15), 2888-2892.
24. Stumpf, F.; Schwemmer, F.; Hutzenlaub, T.; Baumann, D.; Strohmeier, O.; Dingemanns, G.; Simons, G.; Sager, C.; Plobner, L.; von Stetten, F.; Zengerle, R.; Mark, D., LabDisk with complete reagent prestorage for sample-to-answer nucleic acid based detection of respiratory pathogens verified with influenza A H3N2 virus. *Lab Chip* **2016,** *16* (1), 199-207.
25. Hoffmann, J.; Mark, D.; Lutz, S.; Zengerle, R.; von Stetten, F., Pre-storage of liquid reagents in glass ampoules for DNA extraction on a fully integrated lab-on-a-chip cartridge. *Lab on a Chip* **2010,** *10* (11), 1480-1484.
26. Kazemzadeh, A.; Eriksson, A.; Madou, M.; Russom, A., A micro-dispenser for long-term storage and controlled release of liquids. *Nature communications* **2019,** *10* (1), 1-11.
27. Hwang, H.; Kim, Y.; Cho, J.; Lee, J.-y.; Choi, M.-S.; Cho, Y.-K., Lab-on-a-disc for simultaneous determination of nutrients in water. *Analytical chemistry* **2013,** *85* (5), 2954-2960.
28. Kim, T.-H.; Abi-Samra, K.; Sunkara, V.; Park, D.-K.; Amasia, M.; Kim, N.; Kim, J.; Kim, H.; Madou, M.; Cho, Y.-K., Flow-enhanced electrochemical immunosensors on centrifugal microfluidic platforms. *Lab on a Chip* **2013,** *13* (18), 3747-3754.
29. Abi-Samra, K.; Hanson, R.; Madou, M.; Gorkin III, R. A., Infrared controlled waxes for liquid handling and storage on a CD-microfluidic platform. *Lab on a Chip* **2011,** *11* (4), 723-726.
30. Lutz, S.; Weber, P.; Focke, M.; Faltin, B.; Hoffmann, J.; Müller, C.; Mark, D.; Roth, G.; Munday, P.; Armes, N., Microfluidic lab-on-a-foil for nucleic acid analysis based on isothermal recombinase polymerase amplification (RPA). *Lab on a Chip* **2010,** *10* (7), 887-893.
31. Abi-Samra, K.; Clime, L.; Kong, L.; Gorkin, R.; Kim, T.-H.; Cho, Y.-K.; Madou, M., Thermo-pneumatic pumping in centrifugal microfluidic platforms. *Microfluidics and nanofluidics* **2011,** *11* (5), 643-652.
32. Thio, T. H. G.; Ibrahim, F.; Al-Faqheri, W.; Moebius, J.; Khalid, N. S.; Soin, N.; Kahar, M. K. B. A.; Madou, M., Push pull microfluidics on a multi-level 3D CD. *Lab on a Chip* **2013,** *13* (16), 3199-3209.
33. Garcia-Cordero, J. L.; Basabe-Desmonts, L.; Ducrée, J.; Ricco, A. J., Liquid recirculation in microfluidic channels by the interplay of capillary and centrifugal forces. *Microfluidics and nanofluidics* **2010,** *9* (4-5), 695-703.
34. Gorkin, R.; Clime, L.; Madou, M.; Kido, H., Pneumatic pumping in centrifugal microfluidic platforms. *Microfluidics and nanofluidics* **2010,** *9* (2-3), 541-549.
35. Gorkin, R.; Soroori, S.; Southard, W.; Clime, L.; Veres, T.; Kido, H.; Kulinsky, L.; Madou, M., Suction-enhanced siphon valves for centrifugal microfluidic platforms. *Microfluidics and nanofluidics* **2012,** *12* (1-4), 345-354.
36. Chen, J. M.; Huang, P.-C.; Lin, M.-G., Analysis and experiment of capillary valves for microfluidics on a rotating disk. *Microfluidics and Nanofluidics* **2008,** *4* (5), 427-437.
37. Honda, N.; Lindberg, U.; Andersson, P.; Hoffmann, S.; Takei, H., Simultaneous multiple immunoassays in a compact disc–shaped microfluidic device based on centrifugal force. *Clinical chemistry* **2005,** *51* (10), 1955-1961.
38. Ouyang, Y.; Wang, S.; Li, J.; Riehl, P. S.; Begley, M.; Landers, J. P., Rapid patterning of 'tunable'hydrophobic valves on disposable microchips by laser printer lithography. *Lab on a Chip* **2013,** *13* (9), 1762-1771.
39. Hwang, H.; Kim, H.-H.; Cho, Y.-K., Elastomeric membrane valves in a disc. *Lab on a Chip* **2011,** *11* (8), 1434-1436.
40. Schembri, C.; Burd, T.; Kopf-Sill, A.; Shea, L.; Braynin, B., Centrifugation and capillarity integrated into a multiple analyte whole blood analyser. *Journal of Automatic Chemistry* **1995,** *17*.

41. Garcia-Cordero, J. L.; Kurzbuch, D.; Benito-Lopez, F.; Diamond, D.; Lee, L. P.; Ricco, A. J., Optically addressable single-use microfluidic valves by laser printer lithography. *Lab on a Chip* **2010,** *10* (20), 2680-2687.
42. Schaff, U. Y.; Sommer, G. J., Whole blood immunoassay based on centrifugal bead sedimentation. *Clinical chemistry* **2011,** *57* (5), 753-761.
43. Cai, Z.; Xiang, J.; Zhang, B.; Wang, W., A magnetically actuated valve for centrifugal microfluidic applications. *Sensors and Actuators B: Chemical* **2015,** *206*, 22-29.
44. Aeinehvand, M. M.; Ibrahim, F.; Harun, S. W.; Kazemzadeh, A.; Rothan, H. A.; Yusof, R.; Madou, M., Reversible thermo-pneumatic valves on centrifugal microfluidic platforms. *Lab on a Chip* **2015,** *15* (16), 3358-3369.
45. Brenner, T.; Glatzel, T.; Zengerle, R.; Ducrée, J., Frequency-dependent transversal flow control in centrifugal microfluidics. *Lab on a Chip* **2005,** *5* (2), 146-150.
46. Kong, M. C.; Salin, E. D., Pneumatic flow switching on centrifugal microfluidic platforms in motion. *Analytical chemistry* **2011,** *83* (3), 1148-1151.
47. Mark, D.; Weber, P.; Lutz, S.; Focke, M.; Zengerle, R.; von Stetten, F., Aliquoting on the centrifugal microfluidic platform based on centrifugo-pneumatic valves. *Microfluidics and Nanofluidics* **2011,** *10* (6), 1279-1288.
48. Stone, H. A.; Stroock, A. D.; Ajdari, A., Engineering flows in small devices: microfluidics toward a lab-on-a-chip. *Annu. Rev. Fluid Mech.* **2004,** *36*, 381-411.
49. Noroozi, Z.; Kido, H.; Peytavi, R.; Nakajima-Sasaki, R.; Jasinskas, A.; Micic, M.; Felgner, P. L.; Madou, M. J., A multiplexed immunoassay system based upon reciprocating centrifugal microfluidics. *Review of Scientific Instruments* **2011,** *82* (6), 064303.
50. Clime, L.; Brassard, D.; Geissler, M.; Veres, T., Active pneumatic control of centrifugal microfluidic flows for lab-on-a-chip applications. *Lab on a Chip* **2015,** *15* (11), 2400-2411.
51. Burger, S.; Schulz, M.; von Stetten, F.; Zengerle, R.; Paust, N., Rigorous buoyancy driven bubble mixing for centrifugal microfluidics. *Lab on a Chip* **2016,** *16* (2), 261-268.
52. Kim, J.; Jang, S. H.; Jia, G.; Zoval, J. V.; Da Silva, N. A.; Madou, M. J., Cell lysis on a microfluidic CD (compact disc). *Lab on a Chip* **2004,** *4* (5), 516-522.
53. Kido, H.; Micic, M.; Smith, D.; Zoval, J.; Norton, J.; Madou, M., A novel, compact disk-like centrifugal microfluidics system for cell lysis and sample homogenization. *Colloids and Surfaces B: Biointerfaces* **2007,** *58* (1), 44-51.
54. Cho, Y.-K.; Lee, J.-G.; Park, J.-M.; Lee, B.-S.; Lee, Y.; Ko, C., One-step pathogen specific DNA extraction from whole blood on a centrifugal microfluidic device. *Lab on a Chip* **2007,** *7* (5), 565-573.
55. Park, B. H.; Jung, J. H.; Zhang, H.; Lee, N. Y.; Seo, T. S., A rotary microsystem for simple, rapid and automatic RNA purification. *Lab on a Chip* **2012,** *12* (20), 3875-3881.
56. Strohmeier, O.; Emperle, A.; Roth, G.; Mark, D.; Zengerle, R.; von Stetten, F., Centrifugal gas-phase transition magnetophoresis (GTM)–a generic method for automation of magnetic bead based assays on the centrifugal microfluidic platform and application to DNA purification. *Lab on a Chip* **2013,** *13* (1), 146-155.
57. Kloke, A.; Fiebach, A.; Zhang, S.; Drechsel, L.; Niekrawietz, S.; Hoehl, M.; Kneusel, R.; Panthel, K.; Steigert, J.; von Stetten, F., The LabTube–a novel microfluidic platform for assay automation in laboratory centrifuges. *Lab on a Chip* **2014,** *14* (9), 1527-1537.
58. Jung, J. H.; Choi, S. J.; Park, B. H.; Choi, Y. K.; Seo, T. S., Ultrafast rotary PCR system for multiple influenza viral RNA detection. *Lab on a Chip* **2012,** *12* (9), 1598-1600.
59. Ji, M.; Xia, Y.; Loo, J. F.-C.; Li, L.; Ho, H.-P.; He, J.; Gu, D., Automated multiplex nucleic acid tests for rapid detection of SARS-CoV-2, influenza A and B infection with direct reverse-transcription quantitative PCR (dirRT-qPCR) assay in a centrifugal microfluidic platform. *Rsc Advances* **2020,** *10* (56), 34088-34098.
60. Sundberg, S. O.; Wittwer, C. T.; Gao, C.; Gale, B. K., Spinning disk platform for microfluidic digital polymerase chain reaction. *Analytical chemistry* **2010,** *82* (4), 1546-1550.

61. Geissler, M.; Brassard, D.; Clime, L.; Pilar, A. V. C.; Malic, L.; Daoud, J.; Barrère, V.; Luebbert, C.; Blais, B. W.; Corneau, N., Centrifugal microfluidic lab-on-a-chip system with automated sample lysis, DNA amplification and microarray hybridization for identification of enterohemorrhagic Escherichia coli culture isolates. *Analyst* **2020,** *145* (21), 6831-6845.
62. Chang, H.-C.; Chao, Y.-T.; Yen, J.-Y.; Yu, Y.-L.; Lee, C.-N.; Ho, B.-C.; Liu, K.-C.; Fang, J.; Lin, C.-W.; Lee, J.-H., A turbidity test based centrifugal microfluidics diagnostic system for simultaneous detection of HBV, HCV, and CMV. *Advances in Materials Science and Engineering* **2015,** *2015*.
63. Li, X.; Zhang, D.; Ruan, W.; Liu, W.; Yin, K.; Tian, T.; Bi, Y.; Ruan, Q.; Zhao, Y.; Zhu, Z., Centrifugal-driven droplet generation method with minimal waste for single-cell whole genome amplification. *Analytical chemistry* **2019,** *91* (21), 13611-13619.
64. Tian, F.; Liu, C.; Deng, J.; Han, Z.; Zhang, L.; Chen, Q.; Sun, J., A fully automated centrifugal microfluidic system for sample-to-answer viral nucleic acid testing. *Science China Chemistry* **2020,** *63* (10), 1498-1506.
65. Lee, B. S.; Lee, J.-N.; Park, J.-M.; Lee, J.-G.; Kim, S.; Cho, Y.-K.; Ko, C., A fully automated immunoassay from whole blood on a disc. *Lab on a Chip* **2009,** *9* (11), 1548-1555.
66. Koh, C.-Y.; Schaff, U. Y.; Piccini, M. E.; Stanker, L. H.; Cheng, L. W.; Ravichandran, E.; Singh, B.-R.; Sommer, G. J.; Singh, A. K., Centrifugal microfluidic platform for ultrasensitive detection of botulinum toxin. *Analytical chemistry* **2015,** *87* (2), 922-928.
67. Okamoto, S.; Ukita, Y., Automatic microfluidic enzyme-linked immunosorbent assay based on CLOCK-controlled autonomous centrifugal microfluidics. *Sensors and Actuators B: Chemical* **2018,** *261*, 264-270.
68. Abe, T.; Okamoto, S.; Taniguchi, A.; Fukui, M.; Yamaguchi, A.; Utsumi, Y.; Ukita, Y., A lab in a bento box: an autonomous centrifugal microfluidic system for an enzyme-linked immunosorbent assay. *Analytical Methods* **2020,** *12* (40), 4858-4866.
69. Espulgar, W.; Tadokoro, T.; Tamiya, E.; Saito, M., Utility of Centrifugation-Controlled Convective (C3) Flow for Rapid On-chip ELISA. *Sci Rep* **2019,** *9* (1), 20150.
70. Kuo, J.-N.; Chen, X.-F., Plasma separation and preparation on centrifugal microfluidic disk for blood assays. *Microsystem Technologies* **2015,** *21* (11), 2485-2494.
71. Haeberle, S.; Brenner, T.; Zengerle, R.; Ducrée, J., Centrifugal extraction of plasma from whole blood on a rotating disk. *Lab on a Chip* **2006,** *6* (6), 776-781.
72. Li, T.; Fan, Y.; Cheng, Y.; Yang, J., An electrochemical Lab-on-a-CD system for parallel whole blood analysis. *Lab on a Chip* **2013,** *13* (13), 2634-2640.
73. Lee, A.; Park, J.; Lim, M.; Sunkara, V.; Kim, S. Y.; Kim, G. H.; Kim, M.-H.; Cho, Y.-K., All-in-one centrifugal microfluidic device for size-selective circulating tumor cell isolation with high purity. *Analytical chemistry* **2014,** *86* (22), 11349-11356.
74. Kim, T.-H.; Lim, M.; Park, J.; Oh, J. M.; Kim, H.; Jeong, H.; Lee, S. J.; Park, H. C.; Jung, S.; Kim, B. C., FAST: size-selective, clog-free isolation of rare cancer cells from whole blood at a liquid–liquid interface. *Analytical chemistry* **2017,** *89* (2), 1155-1162.
75. Aguirre, G. R.; Efremov, V.; Kitsara, M.; Ducrée, J., Integrated micromixer for incubation and separation of cancer cells on a centrifugal platform using inertial and dean forces. *Microfluidics and Nanofluidics* **2015,** *18* (3), 513-526.
76. Snider, A.; Pirozzi, I.; Tripathi, A., Centrifugal Microfluidics Traps for Parallel Isolation and Imaging of Single Cells. *Micromachines* **2020,** *11* (2), 149.
77. Kim, D.; Woo, H.-K.; Lee, C.; Min, Y.; Kumar, S.; Sunkara, V.; Jo, H.-G.; Lee, Y. J.; Kim, J.; Ha, H. K., EV-Ident: Identifying Tumor-Specific Extracellular Vesicles by Size Fractionation and Single-Vesicle Analysis. *Analytical chemistry* **2020,** *92* (8), 6010-6018.
78. Woo, H. K.; Sunkara, V.; Park, J.; Kim, T. H.; Han, J. R.; Kim, C. J.; Choi, H. I.; Kim, Y. K.; Cho, Y. K., Exodisc for Rapid, Size-Selective, and Efficient Isolation and Analysis of Nanoscale Extracellular Vesicles from Biological Samples. *ACS Nano* **2017,** *11* (2), 1360-1370.

79. Hu, F.; Li, J.; Peng, N.; Li, Z.; Zhang, Z.; Zhao, S.; Duan, M.; Tian, H.; Li, L.; Zhang, P., Rapid isolation of cfDNA from large-volume whole blood on a centrifugal microfluidic chip based on immiscible phase filtration. *Analyst* **2019,** *144* (14), 4162-4174.
80. Kim, C.-J.; Park, J.; Sunkara, V.; Kim, T.-H.; Lee, Y.; Lee, K.; Kim, M.-H.; Cho, Y.-K., Fully automated, on-site isolation of cfDNA from whole blood for cancer therapy monitoring. *Lab on a Chip* **2018,** *18* (9), 1320-1329.
81. Schulz, M.; Calabrese, S.; Hausladen, F.; Wurm, H.; Drossart, D.; Stock, K.; Sobieraj, A. M.; Eichenseher, F.; Loessner, M. J.; Schmelcher, M.; Gerhardts, A.; Goetz, U.; Handel, M.; Serr, A.; Haecker, G.; Li, J.; Specht, M.; Koch, P.; Meyer, M.; Tepper, P.; Rother, R.; Jehle, M.; Wadle, S.; Zengerle, R.; von Stetten, F.; Paust, N.; Borst, N., Point-of-care testing system for digital single cell detection of MRSA directly from nasal swabs. *Lab Chip* **2020,** *20* (14), 2549-2561.
82. Furutani, S.; Nagai, H.; Takamura, Y.; Kubo, I., Compact disk (CD)-shaped device for single cell isolation and PCR of a specific gene in the isolated cell. *Analytical and bioanalytical chemistry* **2010,** *398* (7), 2997-3004.
83. Yao, Y.; Chen, X.; Zhang, X.; Liu, Q.; Zhu, J.; Zhao, W.; Liu, S.; Sui, G., Rapid Detection of Influenza Virus Subtypes Based on an Integrated Centrifugal Disc. *ACS sensors* **2020,** *5* (5), 1354-1362.
84. Lai, X.; Lu, B.; Zhang, P.; Zhang, X.; Pu, Z.; Yu, H.; Li, D., Sticker Microfluidics: A Method for Fabrication of Customized Monolithic Microfluidics. *ACS Biomater Sci Eng* **2019,** *5* (12), 6801-6810.
85. Lagally, E.; Scherer, J.; Blazej, R.; Toriello, N.; Diep, B.; Ramchandani, M.; Sensabaugh, G.; Riley, L.; Mathies, R., Integrated portable genetic analysis microsystem for pathogen/infectious disease detection. *Analytical chemistry* **2004,** *76* (11), 3162-3170.
86. Easley, C. J.; Karlinsey, J. M.; Bienvenue, J. M.; Legendre, L. A.; Roper, M. G.; Feldman, S. H.; Hughes, M. A.; Hewlett, E. L.; Merkel, T. J.; Ferrance, J. P., A fully integrated microfluidic genetic analysis system with sample-in–answer-out capability. *Proceedings of the National Academy of Sciences* **2006,** *103* (51), 19272-19277.
87. Le Roux, D.; Root, B. E.; Hickey, J. A.; Scott, O. N.; Tsuei, A.; Li, J.; Saul, D. J.; Chassagne, L.; Landers, J. P.; De Mazancourt, P., An integrated sample-in-answer-out microfluidic chip for rapid human identification by STR analysis. *Lab on a Chip* **2014,** *14* (22), 4415-4425.
88. Le Roux, D.; Root, B. E.; Reedy, C. R.; Hickey, J. A.; Scott, O. N.; Bienvenue, J. M.; Landers, J. P.; Chassagne, L.; de Mazancourt, P., DNA analysis using an integrated microchip for multiplex PCR amplification and electrophoresis for reference samples. *Analytical chemistry* **2014,** *86* (16), 8192-8199.
89. Legendre, L. A.; Bienvenue, J. M.; Roper, M. G.; Ferrance, J. P.; Landers, J. P., A simple, valveless microfluidic sample preparation device for extraction and amplification of DNA from nanoliter-volume samples. *Analytical chemistry* **2006,** *78* (5), 1444-1451.
90. Burns, M. A.; Johnson, B. N.; Brahmasandra, S. N.; Handique, K.; Webster, J. R.; Krishnan, M.; Sammarco, T. S.; Man, P. M.; Jones, D.; Heldsinger, D., An integrated nanoliter DNA analysis device. *Science* **1998,** *282* (5388), 484-487.
91. Liu, P.; Li, X.; Greenspoon, S. A.; Scherer, J. R.; Mathies, R. A., Integrated DNA purification, PCR, sample cleanup, and capillary electrophoresis microchip for forensic human identification. *Lab on a Chip* **2011,** *11* (6), 1041-1048.
92. Blazej, R. G.; Kumaresan, P.; Mathies, R. A., Microfabricated bioprocessor for integrated nanoliter-scale Sanger DNA sequencing. *Proceedings of the National Academy of Sciences* **2006,** *103* (19), 7240-7245.
93. Stark, A.; Shin, D. J.; Wang, T. H., A sample-to-answer droplet magnetofluidic assay platform for quantitative methylation-specific PCR. *Biomed Microdevices* **2018,** *20* (2), 31.

94. Hong, S. A.; Kim, Y. J.; Kim, S. J.; Yang, S., Electrochemical detection of methylated DNA on a microfluidic chip with nanoelectrokinetic pre-concentration. *Biosens Bioelectron* **2018,** *107*, 103-110.
95. Zhuang, B.; Gan, W.; Wang, S.; Han, J.; Xiang, G.; Li, C. X.; Sun, J.; Liu, P., Fully automated sample preparation microsystem for genetic testing of hereditary hearing loss using two-color multiplex allele-specific PCR. *Anal Chem* **2015,** *87* (2), 1202-9.
96. Ozkumur, E.; Shah, A. M.; Ciciliano, J. C.; Emmink, B. L.; Miyamoto, D. T.; Brachtel, E.; Yu, M.; Chen, P.-i.; Morgan, B.; Trautwein, J., Inertial focusing for tumor antigen–dependent and–independent sorting of rare circulating tumor cells. *Science translational medicine* **2013,** *5* (179), 179ra47-179ra47.
97. Karabacak, N. M.; Spuhler, P. S.; Fachin, F.; Lim, E. J.; Pai, V.; Ozkumur, E.; Martel, J. M.; Kojic, N.; Smith, K.; Chen, P.-i., Microfluidic, marker-free isolation of circulating tumor cells from blood samples. *Nature protocols* **2014,** *9* (3), 694-710.
98. Liu, Z.; Chen, R.; Li, Y.; Liu, J.; Wang, P.; Xia, X.; Qin, L., Integrated Microfluidic Chip for Efficient Isolation and Deformability Analysis of Circulating Tumor Cells. *Advanced Biosystems* **2018,** *2* (10).
99. Liu, Z.; Han, X.; Zhou, Q.; Chen, R.; Fruge, S.; Jo, M. C.; Ma, Y.; Li, Z.; Yokoi, K.; Qin, L., Integrated Microfluidic System for Gene Silencing and Cell Migration. *Adv Biosyst* **2017,** *1* (6).
100. Dharmasiri, U.; Njoroge, S. K.; Witek, M. A.; Adebiyi, M. G.; Kamande, J. W.; Hupert, M. L.; Barany, F.; Soper, S. A., High-throughput selection, enumeration, electrokinetic manipulation, and molecular profiling of low-abundance circulating tumor cells using a microfluidic system. *Analytical chemistry* **2011,** *83* (6), 2301-2309.
101. Dhar, M.; Lam, J. N.; Walser, T.; Dubinett, S. M.; Rettig, M. B.; Di Carlo, D., Functional profiling of circulating tumor cells with an integrated vortex capture and single-cell protease activity assay. *Proc Natl Acad Sci U S A* **2018,** *115* (40), 9986-9991.
102. He, M.; Crow, J.; Roth, M.; Zeng, Y.; Godwin, A. K., Integrated immunoisolation and protein analysis of circulating exosomes using microfluidic technology. *Lab on a Chip* **2014,** *14* (19), 3773-3780.
103. Shao, H.; Chung, J.; Lee, K.; Balaj, L.; Min, C.; Carter, B. S.; Hochberg, F. H.; Breakefield, X. O.; Lee, H.; Weissleder, R., Chip-based analysis of exosomal mRNA mediating drug resistance in glioblastoma. *Nature communications* **2015,** *6* (1), 1-9.
104. Liang, L.-G.; Kong, M.-Q.; Zhou, S.; Sheng, Y.-F.; Wang, P.; Yu, T.; Inci, F.; Kuo, W. P.; Li, L.-J.; Demirci, U., An integrated double-filtration microfluidic device for isolation, enrichment and quantification of urinary extracellular vesicles for detection of bladder cancer. *Scientific reports* **2017,** *7* (1), 1-10.
105. Wu, M.; Ouyang, Y.; Wang, Z.; Zhang, R.; Huang, P.-H.; Chen, C.; Li, H.; Li, P.; Quinn, D.; Dao, M., Isolation of exosomes from whole blood by integrating acoustics and microfluidics. *Proceedings of the National Academy of Sciences* **2017,** *114* (40), 10584-10589.
106. Ko, J.; Hemphill, M. A.; Gabrieli, D.; Wu, L.; Yelleswarapu, V.; Lawrence, G.; Pennycooke, W.; Singh, A.; Meaney, D. F.; Issadore, D., Smartphone-enabled optofluidic exosome diagnostic for concussion recovery. *Scientific reports* **2016,** *6* (1), 1-12.
107. Jimenez-Valdes, R. J.; Rodriguez-Moncayo, R.; Cedillo-Alcantar, D. F.; Garcia-Cordero, J. L., Massive Parallel Analysis of Single Cells in an Integrated Microfluidic Platform. *Anal Chem* **2017,** *89* (10), 5210-5220.
108. Rodriguez-Moncayo, R.; Jimenez-Valdes, R. J.; Gonzalez-Suarez, A. M.; Garcia-Cordero, J. L., Integrated Microfluidic Device for Functional Secretory Immunophenotyping of Immune Cells. *ACS Sens* **2020,** *5* (2), 353-361.
109. Jing, T.; Lai, Z.; Wu, L.; Han, J.; Lim, C. T.; Chen, C. H., Single Cell Analysis of Leukocyte Protease Activity Using Integrated Continuous-Flow Microfluidics. *Anal Chem* **2016,** *88* (23), 11750-11757.

110. Liu, D.; Li, X.; Zhou, J.; Liu, S.; Tian, T.; Song, Y.; Zhu, Z.; Zhou, L.; Ji, T.; Yang, C., A fully integrated distance readout ELISA-Chip for point-of-care testing with sample-in-answer-out capability. *Biosens Bioelectron* **2017,** *96*, 332-338.
111. Wang, T.; Zhang, M.; Dreher, D. D.; Zeng, Y., Ultrasensitive microfluidic solid-phase ELISA using an actuatable microwell-patterned PDMS chip. *Lab on a Chip* **2013,** *13* (21), 4190-4197.
112. Kim, J.; Jensen, E. C.; Megens, M.; Boser, B.; Mathies, R. A., Integrated microfluidic bioprocessor for solid phase capture immunoassays. *Lab on a Chip* **2011,** *11* (18), 3106-3112.
113. Qiu, X.; Zhang, J.; Gong, S.; Wang, D.; Qiao, S.; Ge, S.; Xia, N.; Yu, D.; Qian, S., A single-bead-based, fully integrated microfluidic system for high-throughput CD4+ T lymphocyte enumeration. *SLAS TECHNOLOGY: Translating Life Sciences Innovation* **2018,** *23* (2), 134-143.
114. Lee, W.-C.; Lien, K.-Y.; Lee, G.-B.; Lei, H.-Y., An integrated microfluidic system using magnetic beads for virus detection. *Diagnostic microbiology and infectious disease* **2008,** *60* (1), 51-58.
115. Kim, Y. T.; Lee, D.; Heo, H. Y.; Kim, D. H.; Seo, T. S., An integrated slidable and valveless microdevice with solid phase extraction, polymerase chain reaction, and immunochromatographic strip parts for multiplex colorimetric pathogen detection. *Lab Chip* **2015,** *15* (21), 4148-55.
116. Pal, R.; Yang, M.; Lin, R.; Johnson, B.; Srivastava, N.; Razzacki, S.; Chomistek, K.; Heldsinger, D.; Haque, R.; Ugaz, V., An integrated microfluidic device for influenza and other genetic analyses. *Lab on a Chip* **2005,** *5* (10), 1024-1032.
117. Huang, S. P.; Chuang, Y. J.; Lee, W. B.; Tsai, Y. C.; Lin, C. N.; Hsu, K. F.; Lee, G. B., An integrated microfluidic system for rapid, automatic and high-throughput staining of clinical tissue samples for diagnosis of ovarian cancer. *Lab Chip* **2020,** *20* (6), 1103-1109.
118. Liu, J.; Qiang, Y.; Alvarez, O.; Du, E., Electrical impedance microflow cytometry with oxygen control for detection of sickle cells. *Sens Actuators B Chem* **2018,** *255* (Pt 2), 2392-2398.
119. Razzacki, S. Z.; Thwar, P. K.; Yang, M.; Ugaz, V. M.; Burns, M. A., Integrated microsystems for controlled drug delivery. *Advanced drug delivery reviews* **2004,** *56* (2), 185-198.
120. Kamande, J. W.; Hupert, M. L.; Witek, M. A.; Wang, H.; Torphy, R.; Dharmasiri, U.; Njoroge, S. K.; Jackson, J. M.; Aufforth, R.; Snavely, A., Modular microsystem for the isolation, enumeration, and phenotyping of circulating tumor cells in patients with pancreatic cancer. *Analytical chemistry* **2013,** *85* (19), 9092-9100.
121. Miserendino, S.; Tai, Y.-C., Modular microfluidic interconnects using photodefinable silicone microgaskets and MEMS O-rings. *Sensors and Actuators A: Physical* **2008,** *143* (1), 7-13.
122. Bhattacharjee, N.; Urrios, A.; Kang, S.; Folch, A., The upcoming 3D-printing revolution in microfluidics. *Lab on a Chip* **2016,** *16* (10), 1720-1742.
123. Yi-Qiang, F.; Hong-Liang, W.; Ke-Xin, G.; Jing-Ji, L.; Dong-Ping, C.; ZHANG, Y.-J., Applications of modular microfluidics technology. *Chinese Journal of Analytical Chemistry* **2018,** *46* (12), 1863-1871.
124. Vittayarukskul, K.; Lee, A. P., A truly Lego®-like modular microfluidics platform. *Journal of Micromechanics and Microengineering* **2017,** *27* (3).
125. Yuen, P. K., A reconfigurable stick-n-play modular microfluidic system using magnetic interconnects. *Lab Chip* **2016,** *16* (19), 3700-3707.
126. Loskill, P.; Marcus, S. G.; Mathur, A.; Reese, W. M.; Healy, K. E., muOrgano: A Lego(R)-Like Plug & Play System for Modular Multi-Organ-Chips. *PLoS One* **2015,** *10* (10), e0139587.
127. Tsuda, S.; Jaffery, H.; Doran, D.; Hezwani, M.; Robbins, P. J.; Yoshida, M.; Cronin, L., Customizable 3D Printed 'Plug and Play' Millifluidic Devices for Programmable Fluidics. *PLoS One* **2015,** *10* (11), e0141640.
128. Grodzinski, P.; Yang, J.; Liu, R.; Ward, M., A modular microfluidic system for cell pre-concentration and genetic sample preparation. *Biomedical Microdevices* **2003,** *5* (4), 303-310.

129. Lee, K. G.; Park, K. J.; Seok, S.; Shin, S.; Kim, D. H.; Park, J. Y.; Heo, Y. S.; Lee, S. J.; Lee, T. J., 3D printed modules for integrated microfluidic devices. *RSC Adv.* **2014,** *4* (62), 32876-32880.
130. Giménez-Gómez, P.; Fernández-Sánchez, C.; Baldi, A., Microfluidic Modules with Integrated Solid-State Sensors for Reconfigurable Miniaturized Analysis Systems. *ACS Omega* **2019,** *4* (4), 6192-6198.
131. Chen, Y.-W.; Wang, H.; Hupert, M.; Witek, M.; Dharmasiri, U.; Pingle, M. R.; Barany, F.; Soper, S. A., Modular microfluidic system fabricated in thermoplastics for the strain-specific detection of bacterial pathogens. *Lab on a Chip* **2012,** *12* (18), 3348-3355.
132. Reedy, C. R.; Hagan, K. A.; Marchiarullo, D. J.; Dewald, A. H.; Barron, A.; Bienvenue, J. M.; Landers, J. P., A modular microfluidic system for deoxyribonucleic acid identification by short tandem repeat analysis. *Analytica chimica acta* **2011,** *687* (2), 150-158.
133. Han, J.; Gan, W.; Zhuang, B.; Sun, J.; Zhao, L.; Ye, J.; Liu, Y.; Li, C. X.; Liu, P., A fully integrated microchip system for automated forensic short tandem repeat analysis. *Analyst* **2017,** *142* (11), 2004-2012.
134. Gu, Y.; Zhuang, B.; Han, J.; Li, Y.; Song, X.; Zhou, X.; Wang, L.; Liu, P., Modular-Based Integrated Microsystem with Multiple Sample Preparation Modules for Automated Forensic DNA Typing from Reference to Challenging Samples. *Anal Chem* **2019,** *91* (11), 7435-7443.
135. Wang, H.; Chen, J.; Zhu, L.; Shadpour, H.; Hupert, M. L.; Soper, S. A., Continuous flow thermal cycler microchip for DNA cycle sequencing. *Analytical chemistry* **2006,** *78* (17), 6223-6231.
136. Hashimoto, M.; Barany, F.; Xu, F.; Soper, S. A., Serial processing of biological reactions using flow-through microfluidic devices: coupled PCR/LDR for the detection of low-abundant DNA point mutations. *Analyst* **2007,** *132* (9), 913-921.
137. Wang, H.; Chen, H. W.; Hupert, M. L.; Chen, P. C.; Datta, P.; Pittman, T. L.; Goettert, J.; Murphy, M. C.; Williams, D.; Barany, F., Fully Integrated Thermoplastic Genosensor for the Highly Sensitive Detection and Identification of Multi-Drug-Resistant Tuberculosis. *Angewandte Chemie International Edition* **2012,** *51* (18), 4349-4353.
138. Zhuang, B.; Han, J.; Xiang, G.; Gan, W.; Wang, S.; Wang, D.; Wang, L.; Sun, J.; Li, C. X.; Liu, P., A fully integrated and automated microsystem for rapid pharmacogenetic typing of multiple warfarin-related single-nucleotide polymorphisms. *Lab Chip* **2016,** *16* (1), 86-95.
139. Kersaudy-Kerhoas, M.; Amalou, F.; Che, A.; Kelly, J.; Liu, Y.; Desmulliez, M. P.; Shu, W., Validation of a fully integrated platform and disposable microfluidic chips enabling parallel purification of genome segments for assembly. *Biotechnol Bioeng* **2014,** *111* (8), 1627-37.
140. Lee, T. Y.; Hyun, K.-A.; Kim, S.-I.; Jung, H.-I., An integrated microfluidic chip for one-step isolation of circulating tumor cells. *Sensors and Actuators B: Chemical* **2017,** *238*, 1144-1150.
141. Jiang, J.; Zhao, H.; Shu, W.; Tian, J.; Huang, Y.; Song, Y.; Wang, R.; Li, E.; Slamon, D.; Hou, D.; Du, X.; Zhang, L.; Chen, Y.; Wang, Q., An integrated microfluidic device for rapid and high-sensitivity analysis of circulating tumor cells. *Sci Rep* **2017,** *7*, 42612.
142. Sun, H.; Han, L.; Yang, L.; Yang, Y.; Jiang, W.; Xu, T.; Jia, L., Modular Chamber Assembled with Cell-Replicated Surface for Capture of Cancer Cells. *ACS Biomater Sci Eng* **2019,** *5* (5), 2647-2656.
143. Antfolk, M.; Kim, S. H.; Koizumi, S.; Fujii, T.; Laurell, T., Label-free single-cell separation and imaging of cancer cells using an integrated microfluidic system. *Scientific reports* **2017,** *7* (1), 1-12.
144. Chen, Y. S.; Ma, Y. D.; Chen, C.; Shiesh, S. C.; Lee, G. B., An integrated microfluidic system for on-chip enrichment and quantification of circulating extracellular vesicles from whole blood. *Lab Chip* **2019,** *19* (19), 3305-3315.
145. Rho, J.; Chung, J.; Im, H.; Liong, M.; Shao, H.; Castro, C. M.; Weissleder, R.; Lee, H., Magnetic nanosensor for detection and profiling of erythrocyte-derived microvesicles. *ACS nano* **2013,** *7* (12), 11227-11233.

146. Millet, L. J.; Lucheon, J. D.; Standaert, R. F.; Retterer, S. T.; Doktycz, M. J., Modular microfluidics for point-of-care protein purifications. *Lab Chip* **2015,** *15* (8), 1799-811.
147. Shaikh, K. A.; Ryu, K. S.; Goluch, E. D.; Nam, J.-M.; Liu, J.; Thaxton, C. S.; Chiesl, T. N.; Barron, A. E.; Lu, Y.; Mirkin, C. A., A modular microfluidic architecture for integrated biochemical analysis. *Proceedings of the National Academy of Sciences* **2005,** *102* (28), 9745-9750.
148. Polini, A.; Prodanov, L.; Bhise, N. S.; Manoharan, V.; Dokmeci, M. R.; Khademhosseini, A., Organs-on-a-chip: a new tool for drug discovery. *Expert opinion on drug discovery* **2014,** *9* (4), 335-352.
149. Zhang, Y. S.; Aleman, J.; Shin, S. R.; Kilic, T.; Kim, D.; Mousavi Shaegh, S. A.; Massa, S.; Riahi, R.; Chae, S.; Hu, N.; Avci, H.; Zhang, W.; Silvestri, A.; Sanati Nezhad, A.; Manbohi, A.; De Ferrari, F.; Polini, A.; Calzone, G.; Shaikh, N.; Alerasool, P.; Budina, E.; Kang, J.; Bhise, N.; Ribas, J.; Pourmand, A.; Skardal, A.; Shupe, T.; Bishop, C. E.; Dokmeci, M. R.; Atala, A.; Khademhosseini, A., Multisensor-integrated organs-on-chips platform for automated and continual in situ monitoring of organoid behaviors. *Proc Natl Acad Sci U S A* **2017,** *114* (12), E2293-E2302.
150. Ong, L. J. Y.; Ching, T.; Chong, L. H.; Arora, S.; Li, H.; Hashimoto, M.; DasGupta, R.; Yuen, P. K.; Toh, Y. C., Self-aligning Tetris-Like (TILE) modular microfluidic platform for mimicking multi-organ interactions. *Lab Chip* **2019,** *19* (13), 2178-2191.
151. Cedillo-Alcantar, D. F.; Han, Y. D.; Choi, J.; Garcia-Cordero, J. L.; Revzin, A., Automated Droplet-Based Microfluidic Platform for Multiplexed Analysis of Biochemical Markers in Small Volumes. *Anal Chem* **2019,** *91* (8), 5133-5141.
152. Li, L.; Li, Y.; Shao, Z.; Luo, G.; Ding, M.; Liang, Q., Simultaneous Assay of Oxygen-Dependent Cytotoxicity and Genotoxicity of Anticancer Drugs on an Integrated Microchip. *Anal Chem* **2018,** *90* (20), 11899-11907.
153. Qiu, J.; Gao, Q.; Zhao, H.; Fu, J.; He, Y., Rapid Customization of 3D Integrated Microfluidic Chips via Modular Structure-Based Design. *ACS Biomater Sci Eng* **2017,** *3* (10), 2606-2616.
154. Munshi, A. S.; Chen, C.; Townsend, A. D.; Martin, R. S., Use of 3D Printing and Modular Microfluidics to Integrate Cell Culture, Injections and Electrochemical Analysis. *Anal Methods* **2018,** *10* (27), 3364-3374.
155. Nie, J.; Gao, Q.; Qiu, J. J.; Sun, M.; Liu, A.; Shao, L.; Fu, J. Z.; Zhao, P.; He, Y., 3D printed Lego((R))-like modular microfluidic devices based on capillary driving. *Biofabrication* **2018,** *10* (3), 035001.
156. Xie, X.; Maharjan, S.; Liu, S.; Zhang, Y. S.; Livermore, C., A Modular, Reconfigurable Microfabricated Assembly Platform for Microfluidic Transport and Multitype Cell Culture and Drug Testing. *Micromachines (Basel)* **2019,** *11* (1).
157. Gonzalez-Suarez, A. M.; Pena-Del Castillo, J. G.; Hernandez-Cruz, A.; Garcia-Cordero, J. L., Dynamic Generation of Concentration- and Temporal-Dependent Chemical Signals in an Integrated Microfluidic Device for Single-Cell Analysis. *Anal Chem* **2018,** *90* (14), 8331-8336.
158. Dekker, S.; Isgor, P. K.; Feijten, T.; Segerink, L. I.; Odijk, M., From chip-in-a-lab to lab-on-a-chip: a portable Coulter counter using a modular platform. *Microsyst Nanoeng* **2018,** *4*, 34.
159. Lee, K.; Yoon, T.; Yang, H. S.; Cha, S.; Cheon, Y. P.; Kashefi-Kheyrabadi, L.; Jung, H. I., All-in-one platform for salivary cotinine detection integrated with a microfluidic channel and an electrochemical biosensor. *Lab Chip* **2020,** *20* (2), 320-331.
160. Tan, S. N.; Ge, L.; Tan, H. Y.; Loke, W. K.; Gao, J.; Wang, W., Paper-based enzyme immobilization for flow injection electrochemical biosensor integrated with reagent-loaded cartridge toward portable modular device. *Anal Chem* **2012,** *84* (22), 10071-6.
161. Adams, A. A.; Okagbare, P. I.; Feng, J.; Hupert, M. L.; Patterson, D.; Göttert, J.; McCarley, R. L.; Nikitopoulos, D.; Murphy, M. C.; Soper, S. A., Highly efficient circulating tumor cell isolation from whole blood and label-free enumeration using polymer-based microfluidics with an integrated conductivity sensor. *Journal of the American Chemical Society* **2008,** *130* (27), 8633-8641.

162. Wijerathne, H.; Witek, M. A.; Jackson, J. M.; Brown, V.; Hupert, M. L.; Herrera, K.; Kramer, C.; Davidow, A. E.; Li, Y.; Baird, A. E., Affinity enrichment of extracellular vesicles from plasma reveals mRNA changes associated with acute ischemic stroke. *Communications biology* **2020,** *3* (1), 1-11.

Chapter 2 – Photocleavable linker for the release of rare liquid biopsy markers after microfluidic affinity enrichment

This chapter is based on the publication:

Pahattuge, T.N., Jackson, J.M., Digamber, R., Wijerathne, H., Brown, V., Witek, M.A., Perera, C., Givens, R.S., Peterson, B.R. and Soper, S.A., 2020. Visible photorelease of liquid biopsy markers following microfluidic affinity-enrichment. *Chemical Communications*, *56*(29), pp.4098-4101.

2.1 Introduction

Liquid biopsies consist of disease-associated markers harvested from body fluids in a minimally invasive manner that can provide information for guiding patient treatment (*i.e*., precision medicine) and securing molecular characteristics of the disease profiled from these markers.[1] Initially focused on epithelial cancers, liquid biopsies have been extended to other diseases such as blood cancers and stroke.[2, 3] Common liquid biopsy markers include, but are not limited to, nanometer-sized extracellular vesicles (EVs),[4] and cells (circulating tumor cells, CTCs,[2] or CD8(+) T-cells for stroke.)[5]

Microfluidics that use affinity-agents (e.g., Abs) attached to their surfaces can specifically enrich disease-associated EVs[1] or CTCs[2] from biological samples. Further, affinity-enrichment can fractionate different marker subsets, such as targeting epithelial CTCs via EpCAM (epithelial cell adhesion molecule) and mesenchymal CTCs via FAPα (fibroblast activation protein alpha).[6] While early studies focused on biomarker enumeration to indicate disease status, the Precision Medicine initiative now requires profiling the disease's molecular composition.[7] Thus, there is a need to integrate enrichment with advanced molecular profiling.[2, 5, 8] For nanometer-sized EVs, enumeration requires off-line nanoparticle tracking analysis (NTA) and transmission electron microscopy (TEM) for enumeration,[9] data critical for mRNA expression analyses.[10] Thus, it is necessary to release affinity-enriched markers without damaging the marker or its cargo.

New chemistries have been developed for "catch and release," where biomarkers are affinity-enriched on a solid-phase (*i.e*., microfluidic device) then released for analyses.[11-13]

Release has been accomplished using degraded polymer coatings, proteolytically digested Abs, or cleaved Ab linkers with enzymes or UV light.[2] Performance metrics for CTC catch and release strategies are: (i) Recovery (CTC yield/input); (ii) purity (CTCs/total cell count); (iii) release efficiency (CTCs released/recovered); (iv) cell viability; (v) preserving molecular cargo; and (vi) minimizing assay cost, workflow, and instrumentation.

Previously, we reported a single-stranded oligonucleotide linker for Ab immobilization and subsequent enzymatic release. Enzymatic cleavage of a dU nucleotide in the linker released >90% of CTCs, preserved viability (>85%), and enabled off-line immunophenotyping and cytogenetic analyses.[14] We incorporated the oligonucleotide linker into a sinusoidal microfluidic chip that achieved >75% CTC recovery from clinical samples, high purity (>90%), and 80-100% test positivity for several epithelial cancers.[2, 6] We also used the oligonucleotide linker to enrich leukemic cells[3] and immune cells responding to inflammatory processes associated with acute ischemic stroke (AIS).[5, 15, 16] However, the reaction time (~60 min) was prohibitively long for time-sensitive analyses such as required for AIS diagnosis, where the therapeutic time window for recombinant tissue plasminogen activator (r-tPA) treatment is only ~4.5 h from AIS onset.[5]

We report a photocleavable 7-amino coumarin Ab linker for specific biomarker enrichment and reagent-less release. 7- amino coumarin was used previously as a photolabile group to release different targets (drugs,[17, 18] thiol bearing proteins[19] and CTCs[20]) over a wide wavelength range (UV (365 nm), visible (400-450 nm), and near-IR (800 nm)), but UV induced DNA/RNA damage, low release efficiencies (50-80%) and lengthy release times (~120 min) limited their use. Here, we synthesized a 7-(diethylamino)coumaryl-4-methyl photo-release agent[19] that rapidly cleaves with visible light (400–450 nm,[21] quantum efficiency of coumarin dye is 0.25[19]) minimizing nucleic acid damage and little to no side reactions (**Figure 2.1**). Also, minimal changes in the UV/vis and fluorescence emission as a function of cleavage were observed. The PC linker is unique in its structure; the PC linker contains an amino and carboxy termini (*i.e.*, amino acid) to

allow for two EDC/NHS reactions to first covalently attach the linker to a carboxylated surface, and then to an Ab.

We sought to demonstrate efficient and rapid release with inexpensive LEDs (10^{18} photons/s) with minimal effects on the marker and its molecular cargo. Also, we show that the PC linker can be used for the catch and release of CTCs and EVs with no to minimal damage to the molecular cargo.

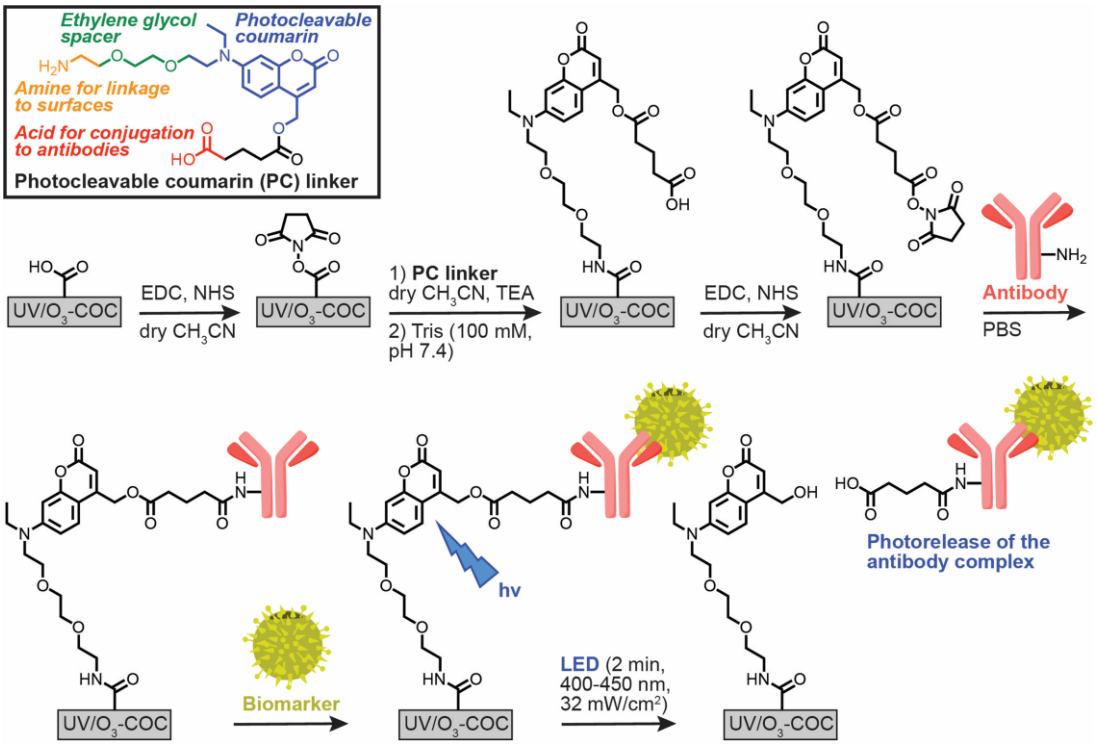

Figure 2.1. Structure of the heterobifunctional PC linker and immobilization strategy employing two EDC/NHS coupling reactions. The PC linker is immobilized to carboxylated (UV/O_3-oxidized) surfaces via the linker's primary amine group. Abs are then anchored to the linker's -COOH handle. After biomarker purification, a visible LED (400-450 nm) cleaves the PC linker. Immobilization reactions are conducted in organic solvent to mitigate NHS ester hydrolysis, which could lead to direct (and non-releasable) Ab conjugation to the -COOH surface. ((https://doi.org/10.1039/C9CC09598E) – Reproduced by permission of The Royal Society of Chemistry)

2.2 Experimental

2.2.1 **Reagents and materials**

Microfluidic devices were fabricated using 6013S-04 cyclic olefin copolymer (COC) substrates and 5013S-04 COC coverslips (250 µm, TOPAS Advanced polymers). Microfluidic devices were connected to syringe pumps (New Era) using Inner-Lok™ union capillary connectors (Polymicro Technologies) and barbed socket Luer Lock™ fittings (3/32″ ID, McMaster-Carr).

Reagents and materials included reagent-grade isopropyl alcohol (IPA), Micro 90®, 1-ethyl-3-[3-dimethylaminopropyl] carbodiimide hydrochloride (EDC), N-hydroxysuccinimide (NHS), anhydrous acetonitrile (ACN), anhydrous dimethylformamide (DMF), anhydrous dichloromethane (DCM), anhydrous triethyl amine (TEA), polyvinylpyrrolidone, 40 kDa (PVP-40), uranyl acetate (Sigma-Aldrich); toluidine blue O (TBO, Carolina Biological Supply); phosphate buffered saline (PBS, pH 7.4), sodium dodecyl sulfate (SDS, 10%), Hoechst 33342, SYTO® 82, LIVE/DEAD™ Cell Imaging Kit (Life Technologies); bovine serum albumin (BSA), acetic acid, hydrogen peroxide, sodium carbonate and bicarbonate, 2-(4-morpholino)-ethane sulfonic acid (MES), nuclease free water (Fisher Scientific); 10% (w/v) Tween-20, 10X Tris buffered saline (TBS), and SsoAdvanced™ Universal SYBR® Green Supermix (Bio-Rad); DNA Damage Competitive ELISA Kit (Invitrogen); 1 M Tris, pH 7.4 (KD Medical); Virkon S (Dupont); NEBuffer 2.1, Protoscript® II First Strand cDNA Synthesis Kit (New England Biolabs); phosphodiesterase I (Abnova); Novagen™ Benzonase® nuclease (EMD Millipore); FastAP Thermosensitive Alkaline Phosphatase (ThermoScientific); Cy5-oligonucleotide fluorescent reporter (5'-NH_2-C_{12}-T_8CCCTTCCTCACTTCCCTTTUT$_9$-Cy5-3', HPLC-purified, Integrated DNA technologies); Direct-zol RNA and Quick-DNA purification kits (Zymo Research). All solvents were reagent grade.

Monoclonal antibodies (mAbs) were mouse anti-human Fibroblast Activation Protein, FAPα (clone 427819), mouse anti-human EpCAM/TROP-1 (clone 158210), mouse IgG2A isotype

control (clone 133304), mouse anti-human CD8α (clone 37006), Human EpCAM/TROP1 Alexa Fluor® 488-conjugated antibody (clone 158206), Human Fibroblast Activation Protein α/FAP Alexa Fluor® 488-conjugated antibody (clone 427819), Mouse IgG 2B Alexa Fluor® 488-conjugated Isotype control (clone 133303), Mouse IgG1 Alexa Fluor® 488-conjugated Isotype control (clone 11711) all from R&D Systems. Cell lines were purchased from the American Type Culture Collection (ATCC). Culture reagents included fetal bovine serum (FBS, Performance, Gibco), McCoy's 5A (Corning), high glucose HyClone™ DMEM (GE Life Sciences), RPMI-1640 (ATCC), recombinant bovine insulin (Sigma), TrypLE express reagent (Thermo Fisher), and 25 cm^2 tissue culture flasks (Fisher Scientific). TEM grids (Carbon type B, 300 mesh) were purchased from Ted Pella Inc. Blocking, and washing buffers were filtered (0.2 µm, PTFE, Fisher Scientific) just prior to use. Nuclease-free microfuge tubes (Fisher Scientific) were used for the preparation and storage of all samples and reagents.

2.2.2 **Surface characterization of UV/O_3-activated COC exposed to organic solvents**

COC plates (6013S-04) were diced into 1″ square pieces, cleaned by rinsing with 10% Micro-90, IPA, and nanopure water, and dried at 60°C for >1 h. Substrates were UV/O_3-activated (16.1 min, 22 mW/cm^2 measured at 254 nm)[22] and either left in air or immersed in 100 mM MES buffer (pH = 4.8) or anhydrous solvents – ACN, DMF, or DCM – for 2 h. Treated substrates were rinsed with copious amounts of nanopure water and dried with N_2 before analysis. Water contact angles (WCAs) were measured by dispensing 2.0 µL of nanopure water onto the substrate using a VCA Optima instrument (AST Products). Three measurements were averaged per substrate.

Carboxylic acid (-COOH) surface densities were measured via toluidine blue O (TBO). The TBO assay[22] was performed using an *in situ* incubation chamber (Bio-Rad) and placing the chamber on substrate and covering the surface with 0.1% (w/v) TBO in 50 mM carbonate buffer (pH = 10.5). After 15 min, the substrate was submersed in the same buffer for 15 min then N_2-dried. TBO was desorbed using 40% acetic acid (d = 1.0196 g/mL) and collected in a pre-weighed

microfuge tube. TBO concentrations were determined with either a Shimadzu UV-1280 UV/Vis spectrophotometer or a BioTek Synergy H4 Hybrid plate reader against a calibration curve and a 40% acetic acid blank.

Attenuated total reflectance Fourier transform infrared (ATR-FTIR) spectra were secured using a Shimadzu IRAffinity-1S equipped with a Specac Quest ZnSe ATR accessory. Each scan (340-4700 cm^{-1}) was averaged 45 times and processed by a 3-point baseline correction (1500, 2000, and 4000 cm^{-1}) before integrating peak areas for carbonyls (1650-1850 cm^{-1}) and hydroxyls (3200-3700 cm^{-1}).

2.2.3 **Fabrication of microfluidic devices**

The microfluidic device used for CTC affinity-enrichment consisted of 50 sinusoidal high aspect ratio microchannels (25 µm × 150 µm, w × h) interconnected in a Z-configuration.[3, 22-29] EV affinity-enrichment used a microfluidic device with three, serially-connected beds populated with a total of 15,202 micropillars (110-120 µm pillar diameter, 10-20 µm pillar spacing).[30]

Mold masters were prepared in brass using high precision-micromilling (KERN 44, KERN Micro- und Feinwerktechnik GmbH & Co.KG; Murnau, Germany) with carbide bits (Performance Micro Tool). COC devices were fabricated from the brass mold masters by hot embossing.[27, 30] Hot embossing of the CTC affinity-enrichment device was performed at 155°C and 30 kN force for 120 s using a HEX03 embossing machine (Jenoptik Optical systems GmbH), and for EV affinity-enrichment device, devices were embossed at 162°C with 900 lb force using a precision press (Wabash MPI) followed by manual cooling and demolding at 150°C. Mold release agent (MoldWiz® F57-NC) was kindly gifted by Axel Plastics.

Measurements of the mold and replicated devices were made with a VK-X 3D laser scanning confocal microscope (Keyence). Embossed devices were taped, diced with a bandsaw, immediately cleaned of debris by sonicating in 10% Micro-90 and rinsing with IPA and nanopure

water, and finally dried at 60°C for ≥30 min. COC cover plates (250 µm thickness) were cut, rinsed with 10% Micro-90, IPA, and nanopure water, and similarly dried. Cleaned devices and 250 µm COC cover plates were UV/O_3-activated (15 min, 27 mW/cm^2 measured at 254 nm) in a Model 18 UVO-Cleaner® (Jelight Company).[31, 32] Devices were fitted with glass capillaries (365 µm OD, 150 µm ID) and an inverted UV/O_3-activated cover plate, and clamped between two glass plates for thermal fusion bonding (134°C, 1 h). Capillary fittings were sealed with epoxy after annealing.

2.2.4 **Immobilization of Cy5 oligonucleotide fluorescent reporter**

Flat substrates or thermal fusion bonded microfluidic devices were UV/O_3-activated and/or treated with solvents as described above. Surfaces or devices were then reacted with EDC (20 mg/mL) and NHS (2 mg/mL), either solubilized in 100 mM MES buffer (pH = 4.8) by pipetting or in anhydrous ACN by vigorous vortexing, for 25 min at room temperature. After air-drying, ssDNA oligonucleotides with 5'-NH_2, 3'-Cy5 functionalities were infused at 10-40 µM concentration in PBS. The reaction was carried out for 2 h at room temperature before rinsing with ~1 mL 0.1% SDS and finally PBS. Flat substrates were dried before imaging and sealed with tape. Imaging was conducted with a Zeiss Axiovert 200M microscope using a 10X objective (0.3 NA, Plan NeoFluar), an XBO 75 W lamp, Cy5 filter set (Omega Optical), a Cascade 1K EMCCD camera (Photometrics), and a MAC 5000 stage (Ludl Electronic Products), all of which were computer-controlled via Micro-Manager. Images were background subtracted, measured, and intensity-scaled for display in ImageJ.

2.2.5 **PC linker synthesis and characterization**

The Synthetic Chemical Biology Core facility at KU performed PC linker synthesis and characterization. All reactions were performed under an inert atmosphere of dry argon or nitrogen, and used either flame-dried or oven-dried glassware or in a glass microwave vial (Biotage, LLC). All anhydrous solvents were purchased from Sigma Aldrich and dried via passage through a glass contour solvent system (Pure Process Technology, LLC).

Thin-layer chromatography (TLC) was performed using commercial aluminum backed silica plates (TLC Silica gel 60 F254, Analytical Chromatography), and plates were visualized by UV irradiation. Flash chromatography used a normal-phase silica gel (230–400 mesh), normal-phase Combiflash purification system (gold silica column), or reverse-phase Combiflash purification system (50 g HP C18 gold column).

Nuclear magnetic resonance (NMR) spectra were recorded on either a 400 MHz or 500 MHz Bruker Avance spectrometer with a dual carbon/proton cryoprobe. NMRs were recorded in deuterated chloroform or methanol. Chemical shifts are reported in parts per million (ppm) and referenced to the center line of the solvent (δ 3.31 and 7.26 with respect to methanol-d_4 and chloroform-*d* for ^{1}H NMR, and δ 49.00 and 77.16 with respect to methanol-d_6 and chloroform-*d* for ^{13}C NMR). Coupling constants are given in Hertz (Hz). The spin multiplicities are reported as s = singlet, d = doublet, t = triplet, q = quartet, dd = doublet of doublet, td = doublet of triplet, and m = multiplet. NMR data was analyzed using MestReNova 14 software. High-resolution mass spectrometry (HRMS) data were collected on an LCT Premier (Waters Corporation) time-of-flight mass spectrometer.

The synthesized PC linker was dissolved in 1x PBS (2.1 μM) and exposed to visible light (400-450 nm, 34 ±4 mW/cm^2). Samples (50 μL) were withdrawn after 1 min, 2 min and 10 min light irradiation and analyzed by UPLC/HRMS (Waters Acquity UPLC with a photodiode array UV detector and an LCT Premiere TOF mass spectrometer). The gradient mobile phase consisted of water/acetonitrile (95:5 to 0:100 containing 0.05% TFA) over 2.7 min. The column was a Waters Acquity Atlantis T3 2.1x 50 mm, 1.7 μm column operated at a flow rate of 0.6 mL/min. The wavelength of detection was 247 nm and the volume injected onto the column was 2 μL.

2.2.6 **Immobilization of PC linker, Cy5 oligonucleotide fluorescent reporters or mAbs**

Devices were UV/O_3-activated then thermal fusion bonded to cover plates as described above. EDC (20 mg/mL) and NHS (2 mg/mL) were dissolved in dry ACN and infused into the device using all-plastic, Norm-Ject™ syringes (Air-Tite). Next, devices were wrapped in a protective Rubylith® film (Ulano) to prevent subsequent exposure of the PC linker to ambient light. After 25 min incubation at room temperature, reagents were displaced by air, and the PC linker (dissolved in dry ACN with a 2 molar excess of TEA) was infused into the device via a vacuum pump. After incubating 2 h at room temperature, reagents were displaced by air, and the device was infused with 100 mM Tris (pH 7.4) and incubated for 30 min at room temperature to inactivate any unreacted NHS ester groups on the device's surface. A second EDC/NHS reaction in dry ACN, as described above, was performed to activate the -COOH group at the end of the PC linker. Either Cy5 oligonucleotide reporters (40 µM) dissolved in PBS (pH 7.4) or mAbs (1 mg/mL) were incubated for 2 h at room temperature or overnight at 4°C, respectively. For Cy5 reporters, the device was washed with 0.1% SDS and finally PBS. When changing between anhydrous solvents and any buffered solution, devices were briefly flushed with nuclease free water (10-30 µL), then excess solvent or buffer as a preventative measure against salt precipitation.

2.2.7 **LED light exposure system and monitoring PC linker cleavage via Cy5 reporters**

An 885 mW LED (M420L3, ThorLabs) producing light from 385–470 nm (λ_{max} = 412 nm) was filtered through a 400 nm longpass colored glass filter (Edmund Optics) that was used to photocleave the PC linker. The LED's innate divergence (60°) illuminated a 90 mm diameter spot at 24 mm distance. The power distribution was measured with an 18 mm x 18 mm power sensor (ThorLabs) rastered beneath the LED spot. These measurements were then fit with a 2D Gaussian and integrated over the device's surface area in Matlab. For photocleavage reactions, the LED was mounted to a polished aluminum chamber with recesses that centered devices 24

mm beneath the LED, and the LED was triggered using an analog LED driver (Thorlabs) and a custom electronic timer.

For releasing Cy5 reporters immobilized via the PC linker, devices were first imaged by fluorescence microscopy as described above. Devices were then exposed to LED light for 1 min. Released Cy5 reporters were removed from the device by infusing PBS, collected into a pre-weighed microcentrifuge tube, and quantified against a calibration curve by fluorometry (Jobin-Yvon Fluorolog 3, λ_{ex} = 642 nm, λ_{em} = 664 nm). Devices were imaged by microscopy again after the photocleavage process was repeated for an additional 1 min (2 min total exposure) and a final 8 min LED exposure (10 min total) to investigate the efficiency of photocleavage as a function of dose.

2.2.8 **Cell culture, analysis of cellular antigen expression, cell enrichment, and release**

SKBR3, MCF7, and Hs578T (breast cancer) cell lines were cultured at 37°C under a 5% CO_2 atmosphere in 1x McCoy's 5A/10% FBS, 1x MEM alpha/10% FBS and 1.7 µM human insulin, or DMEM/10% FBS/ and 1.7 µM bovine insulin, respectively. Cells were harvested for experiments using TrypLE express reagent (5 min), centrifuged (300 g, 10 min), and resuspended in ice cold PBS.

For the analysis of cellular antigen expression levels, harvested cells were washed with ice cold PBS (three times) and fluorescently labeled primary antibody (Alexa Fluor 488, h-EpCAM or h-FAPα) was added (5-10 µl/10^6 cells in suspension). The suspension was mixed well and allowed to incubate for 30 min at room temperature in dark. Next, the cells were washed with 0.1% BSA (in PBS) three times to remove any unbound conjugated antibodies. After the final washing step, cells were resuspended in ice cold PBS, filtered (0.2 µm, PTFE) and analyzed by Flow cytometer (BD Accuri C6). Results were compared with a suitable isotype control (Alexa Fluor 488, IgG 2B or IgG1).

Healthy donor blood samples were obtained from the University of Kansas Medical Center (KUMC) from the IRB-approved Biospecimen Repository Core. Written informed consent was obtained from all patients included in the study before enrollment. Peripheral blood samples were drawn by venipuncture into Vacuette® containing EDTA (Greiner) tubes.

Prior to sample infusion, CTC devices modified with the PC linker and anti-EpCAM mAbs were infused with 2 mL of 0.5% BSA/PBS at 50 µL/min to remove unbound mAbs and block the surface to minimize nonspecific adsorption. SKBR3 cells were pre-stained with Hoechst 33342 (40 µg/mL, 15 min, RT), resuspended in PBS, then spiked into a 1 mL blood sample (69-269 SKBR3 cells/mL). The spiked blood was loaded into a 1-3 mL syringe (BD) and hydrodynamically infused through two devices in series at a flow rate of 25 µL/min (2 mm/s linear velocity). After blood processing, nonspecifically bound cells were removed by rinsing with 1 mL of 0.5%BSA/PBS at a flow rate of 50 µL/min (4 mm/s linear velocity). All captured cells were stained with SYTO 82 nucleic acid dye (5 µM, infused at 25 µL/min and incubated for 15 min). Excess dye was removed with 0.5% BSA/PBS (50 µL/min, 100 µL). Devices were exposed to the LED system (2 min, 32 ±4 mW cm^{-2}, described above), and released cells rinsed with 0.5% BSA/PBS (50 µL/min, 250 µL) and collected into a flat bottom 96-well plate for fluorescence microscopy (DAPI and Cy3 filters). Additionally, the microfluidic device was manually scanned to enumerate cells that were not released.

SKBR3 cells were identified as positive for both Hoechst 33342 and SYTO 82, whereas nonspecific leukocytes were positive for SYTO 82 only. Purity was calculated as the ratio of SKBR3 cells to total cell count (SKBR3 cells + leukocytes). Release efficiency was calculated as the ratio of released cells to the total cell count (released cells + cells on-chip). Capture efficiency was determined by self-referencing, where the SKBR3 cells captured in the first device was divided by the total cell count (first device + second device).[14, 29] Mouse IgG2A isotype control mAb was immobilized through the PC linker to evaluate nonspecifically bound SKBR3 cells. This

was undertaken to gauge the release efficiency of MCF7 and Hs578T cells spiked into PBS buffer using Hoechst 33342 staining only. In the case of Hs578T cell experiments, anti-FAPα mAbs were used.

2.2.9 **The effect of PC release on cell viability, cultivation, and oxidative DNA/RNA damage**

SKBR3 cells were spiked into PBS and affinity-enriched with anti-EpCAM mAbs. Cells were released by 2 min LED exposure, collected into a 96-well plate, and stained for viability using calcein AM and ethidium homodimer I (LIVE/DEAD Cell Imaging Kit) for 15 min at room temperature. The plate was centrifuged (300 rcf, 5 min), and staining reagents were aspirated and replaced with PBS for fluorescence microscopy. Viability measurements were taken from ~100 released cells (for other cell lines, the release step was omitted, and cells were directly exposed in a 96-well plate – for these viability measurements, several thousand cells were averaged). For monitoring cell cultivation after release, SKBR3 cells (180 cells) were seeded into the experiment and were then cultured (as described above) for up to 4 d.

LED-induced DNA/RNA damage was determined by measuring the oxidative product of DNA/RNA, 8-oxo guanine (8-oxo-G).[33, 34] Hs578T cells were grown in 35 mm diameter tissue culture dishes (Fisher Scientific) until ~80% confluency. The cells were washed with ice cold PBS, covered with 1 mL ice cold PBS, and the culture dish was irradiated in an ice bath in the LED exposure system for 2 min (18.47 J). In a control experiment, the cells were placed in the exposure system for 2 min without irradiation. To allow for comparison of LED exposure and UV exposure, this process was repeated with an equivalent dosage of UV light (18.47 J) using a UVP CL-1000 crosslinker chamber (Analytik Jena). Results from UV and LED irradiation were compared to results obtained from H_2O_2 treated cells. Briefly, the cells were washed twice with ice cold PBS, incubated in 10 mL H_2O_2 (300 µM in 1X PBS) for 30 min at 37°C and 5% CO_2, then washed twice with ice cold PBS.

DNA or RNA was immediately extracted following irradiation using Zymo Quick-DNA and Direct-zol RNA isolation kits according to the manufacturer's protocol. Extracted DNA/RNA was quantified by UV-Vis (Shimadzu BioSpec-nano) and High Sensitivity RNA or Genomic DNA Tapestation (Agilent) and diluted to 80 ng/µL, and 6 µg substrate was digested into mononucleotides using 18 mU phosphodiesterase I, 15 U benzonase nuclease, and 12 U alkaline phosphatase[35] in NEBuffer 2.1. 8-oxoG quantification was performed in triplicate using a DNA Damage Competitive ELISA Kit (Invitrogen) according to the manufacturer's protocol.

To establish the impact of RNA oxidative damage on the ability to conduct mRNA profiling, 1 µg non-digested RNA was reverse-transcribed into cDNA using Protoscript® II and poly(dT) primers at 42°C for 1 h followed by enzyme deactivation at 80°C for 5 min. cDNA was diluted 5-20× before being amplified by qPCR with gene-specific primers (200 nM for all genes except 125 nM for *MMP9*, **Table 2.1**), SsoAdvanced™ SYBR Green master mix, and a CFX Connect Real-Time System (BioRad). The PCR thermocycling protocol was 95°C for 5 min and 40 cycles of 95°C for 30 s, 50°C for 30 s, and 72°C for 1 min.

2.2.10 **The effect of attached Ab ligands on cell mRNA expression**

RT-qPCR was performed to investigate the molecular level changes caused by the remaining antibody ligands on the cell surface after photo release. For that, PC linker and anti-EpCAM Abs were immobilized to UV/O3-COC devices and rinsed with 0.5%BSA/PBS (50 µL/min, 2 mL). SKBR3 cells (~20,000) were spiked to PBS (pH 7.4) and infused (25 µL/min) into two devices connected as a series. Devices were washed with 0.5%BSA/PBS (50 µL/min, 250 µL) and exposed to 2 min LED blue light. Photo released cells were lysed, total RNA was extracted and quantified as described above (the time between the cell affinity selection and the cell lysis was ~1 h). Complementary DNA (cDNA) was synthesized by performing (RT) with the Protoscript® II cDNA synthesis Kit and anchored $d(T)_{23}$ VN primers (**Table 2.1**) for primer

sequences) according to New England Biolabs' protocol. q-PCR was performed as described above. SKBR3 cells in the culture for entire experimental time was used as the control.

Table 2.1. Gene-specific primers for evaluating Hs578T and SKBR3 gene expression by RT-qPCR.

Gene/cDNA	Forward 5'-3'	Reverse 5'-3'	Product size (bp)
Vim	AAT CTT GTG CTA GAA TAC TTT	TTT CCA AAG ATT TAT TGA AGC	112
CD44	ATT AAA CCC TGG ATC AGT C	TCG AAG AAG TAC AGA TAT TTA TTA T	107
CK19	CTT CTG CTG TCC TTT GG	CCC TTG GAC CAT AAA TTT TTA	108
MMP9	ACC GAG AGA AAG CCT ATT	GGG ATT TAC ATG GCA CTG	162
SMA	CAT TGT CCA CAG GAA GT	TAA GGC TTG TAG GTT TTA ATG	103
FAP v2	AAG GGA GTC ATG CAT TT	TAG CAC TTG AAC TTC TGA	87
IL8	TGA TAC TCC CAG TCT TGT C	AAG TTT CAA CCA GCA AGA A	131
HSP70	AGG TGA AAG CAA TGT TAA AG	CTT CCC AGG ATA ACT GAA G	122
CA4	AGC GCA CGG TGA TAA A	GAA GCC TGG AAC TTG GA	164
VCAN	AGA GCC ACA GAGCAT TT	TCT CAA AGA AAC AGA GTG ATA	156
GAPDH	TGG TTG AGC ACA GGG TA	TCA CAG TTG CCA TGT AGA C	93

2.2.11 **Anti-CD8 enrichment of MOLT-3-derived EVs**

MOLT-3 cells were cultured at 37°C and 5% CO_2 in RPMI-1640 with 10% FBS. FBS was depleted of background bovine EVs via ultracentrifugation (100,000 rcf, 18 h, 4°C) with an L8-80M ultracentrifuge, Type 45 Ti rotor, 38 mm × 102 mm (70 mL) polycarbonate tubes (Beckman Coulter), and a mechanical Harvard Trip balance (OHAUS). Tubes were sterilized with 10% hydrogen peroxide before use and disinfected with Virkon S when transferring between the centrifuge and culture hood. After ultracentrifugation, the FBS supernatant was decanted, mixed thoroughly to homogenize protein content, aliquoted, and stored at -20°C. Cells were transitioned

into EV-depleted FBS for 1 week before obtaining MOLT-3 conditioned media by centrifugation (2000 rcf, 10 min).

EV microfluidic affinity-purification devices were modified with the PC linker and a monoclonal anti-CD8 Ab as described above. Before affinity-enrichment, EV microfluidic devices were washed with 400 µL blocking buffer (1% BSA, 1% PVP-40 in PBS) at 10 µL/min. Conditioned media (500 µL) was infused at 5 µL/min, then the device was washed with 400 µL 0.2% Tween 20 in TBS buffer and then 50 µL PBS at 10 µL/min. After LED exposure, released EVs were collected in 400 µL PBS (20 µL/min) and stored at -80°C for subsequent analysis.

2.2.12 **Nanoparticle tracking analysis (NTA)**

Thawed samples were heavily vortexed, loaded into a 1 mL syringe (BD), and infused into the flow cell of a NanoSight LM10 NTA instrument (Malvern Panalytical) equipped with a 488 nm laser and NTA 2.3 software. In some cases, samples were diluted to ensure 10-100 EVs per frame. Imaging used a camera shutter setting of 1206, camera gain of 366, 90-160 s acquisition times, and 5 averaged replicates where the sample was advanced by ~25 µL while the camera was off to image a random portion of the sample for each replicate. Processing used the Detection Threshold 20 and all other automatic settings. Between each sample, the flow cell was slowly flushed with 1 mL PBS then air four times, and flushing was verified by manually monitoring the number of nanoparticles observed in 300 µL PBS (~0-1 per 100 µL). Nanoparticle concentrates were multiplied by each assay's elution volume to report the number of nanoparticles released.

2.2.13 **Transmission electron microscopy (TEM) imaging**

Samples were heavily vortexed and spotted onto TEM grids. After 20 min, excess buffer was blot dried, and the grids were washed three times with a drop of nanopure water for 10 s. Grids were blot dried and stained with 5 µL 2% (w/v) uranyl acetate (0.22 µm filtered) for 10 s.

Grids were blot dried, air dried for 15 min, and imaged with a Technai F20 XT Field Emission TEM (FEI).

2.2.14 **LED-induced mRNA damage of EVs**

A panel of genes *(MMP9*, *PLBD1*, *FOS*, *CA4* and *VCAN)* was previously identified for diagnosing acute ischemic stroke (AIS).[36] We used this gene panel to determine if there was LED-induced damage of EV mRNA that may affect their expression profiles. MOLT-3 conditioned media was obtained from culture as described above. Cells were removed by centrifugation (300 rcf for 10 min), and EVs were precipitated using the ExtraPEG procedure.[37] To 3 mL conditioned media, we spiked an equal volume of PEG and NaCl (final concentration of 12% and 0.5 M, respectively), mixed by pipetting, incubated overnight at 4°C, centrifuged the sample (4000 rcf for 1 h), removed the supernatant, washed the pellet with ice cold PBS, resuspended the pellet in PBS (6 mL) by pipetting and vortexing, and aliquoted 1 mL portions into 35 mm diameter tissue culture dishes. Culture dishes were placed in an ice bath, inserted in the LED chamber, and either not exposed (control) or exposed for 2 min (18.5 J) by the LED. The EV suspension was then removed from the culture dish, and 1 mL of TRI Reagent was added to lyse EVs. The RNA was extracted using Direct-zol RNA extraction kit according to Zymo's guidelines and analyzed with a 2200 TapeStation and High Sensitivity RNA reagents (Agilent).

2.2.15 **Reverse transcription and droplet digital PCR (RT-ddPCR)**

Complementary DNA (cDNA) was synthesized by performing RT with the Protoscript® II cDNA synthesis Kit and anchored $d(T)_{23}$ VN primers according to New England Biolabs' protocol. cDNA product was used to generate droplets with the QX200 droplet generator, EvaGreen® Supermix, and gene specific primers (**Table 2.2**, 125 nM) followed by PCR amplification with the BioRad C1000 thermal cycler and the above thermocycling protocol. Final cooling was carried out at 4°C. Droplets were read with a BioRad QX200 droplet reader, and data analyzed using QuantaSoft™ software. All data were normalized to the total RNA concentration.

Table 2.2. Gene-specific primers for MOLT-3 EV-mRNA profiling by RT-ddPCR.

Gene/cDNA	Forward 5'-3'	Reverse 5'-3'	Product size (bp)
PLBD1	GTA CTG AGA TGC TAG GTA GAT A	CAA GGG AAA GTG ACT GAT AC	189
FOS	TGC CAG GAA CAC AGT AG	TTC AGA GAG CTG GTA GTT AG	188
MMP9	GGG ATT TAC ATG GCA CTG	ACC GAG AGA AAG CCT ATT	162
CA4	GAA GCC TGG AAC TTG GA	AGC GCA CGG TGA TAA A	164
VCAN	TCT CAA AGA AAC AGA GTG ATA	AGA GCC ACA GAGCAT TT	156
IL8	AAG TTT CAA CCA GCA AGA A	TGA TAC TCC CAG TCT TGT C	131
CD8a	GCC ACT CAT AAC AGC ATA G	TGC CCA TTG GAG AGA AA	178
CD81	GGA GGG AAC AAG GTG AG	TGT AGG TGG CGT GTA TG	210

2.3 Results and Discussion

2.3.1 **Photocleavage of PC linker**

Photocleavage of 7- amino coumarin occurs from its meta carbon after excitation, which forms a tight ion pair (coumarinylmethyl cation and a leaving conjugate base) as key intermediates. Coumarinylmethyl cation reacts with a nucleophile resulting the bond cleavage and releasing the captured biomarker.[38] The PC linker was exposed to visible light (400-450 nm) and samples were taken at different time points (0, 1, 2, and 10 min total irradiation time). Photolysis products were monitored with UPLC (**Figure 2.2A**) and identified by mass spectrometry. The intact PC linker (**1**, 87%) concentration decreased with irradiation time and at 10 min, the chromatographic peak for the intact linker completely disappeared. Major photolysis product (**2**) was present in small amounts (5%) for the initial sample and that amount increased with the irradiation time up to 79%. In addition, UV-visible absorption (**Figure 2.2B**) and fluorescence measurements (**Figure 2.2C**) were used to monitor the photocleavage reaction. From the spectra shown in **Figure 2.2B**, very little changes in the absorption spectra were seen as a function of irradiation time. However, there was a slight increase in the fluorescence from the coumarin as a

function of photocleavage of the starting material (**1, Figure 2.2C**). This may be due to the increase of fluorescence quantum efficiency (ϕ) as a function of photocleavage from the meta carbon.

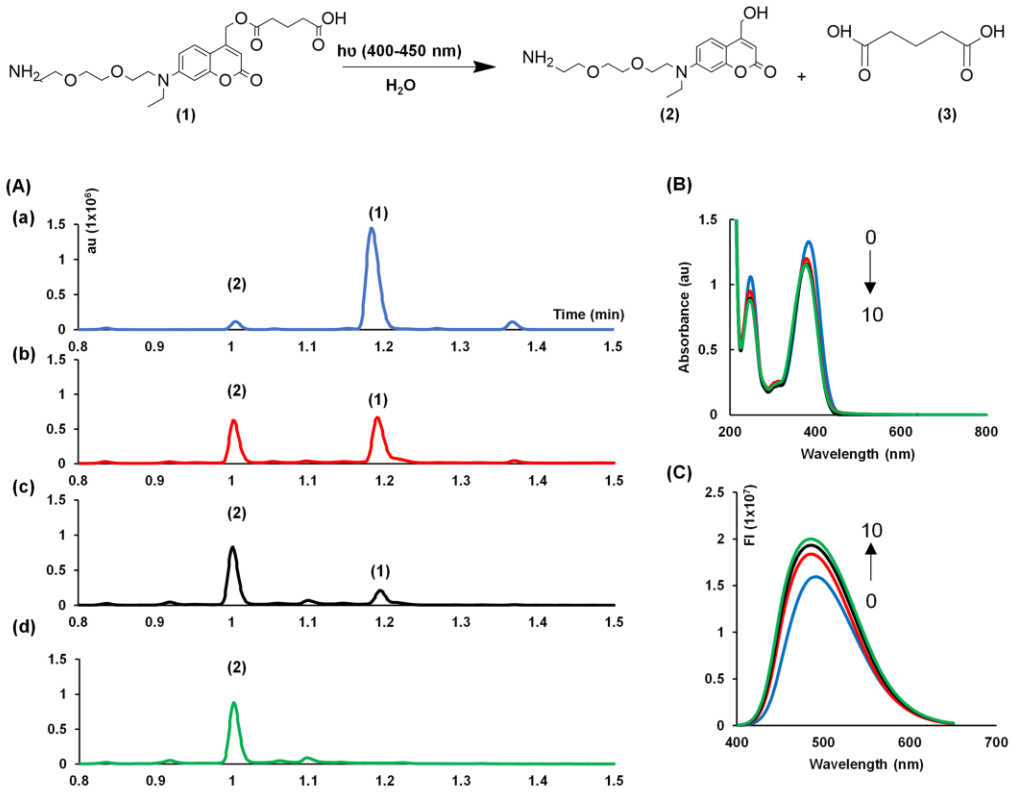

Figure 2.2. (A) Ultra-high performance liquid chromatography (UPLC) of the photocleavage of (**1**) using 400 – 450 nm light for exposure times of 0, 1, 2, and 10 min (a-d). The chromatography used a C18 column with an aqueous buffer and acetonitrile, ACN, as the mobile phase. (**B**) UV/vis spectra of the intact photolinker (**1**) as a function of exposure time. Same photo-irradiation conditions here as used in (**A**). (**C**) Fluorescence emission spectra of the photo-irradiated linker (**1**) as a function of time. ((https://doi.org/10.1039/C9CC09598E) – Reproduced by permission of The Royal Society of Chemistry)

2.3.2 **Stability of UV/O_3-activated COC in anhydrous solvents**

The immobilization chemistry was designed to allow for the facile surface attachment of a recognition element, for example an Ab, used in a microfluidic device fabricated in cyclic olefin copolymer (COC) thermoplastic for enriching rare liquid biopsy markers. COC devices can be mass produced by injection moulding and photo-activated using UV/O_3 irradiation to yield surface-confined carboxylic acid (-COOH) scaffolds.[22] The PC linker contains a primary amine with an

ethylene glycol spacer for EDC/NHS coupling to the surface -COOH groups, and the linker's opposing -COOH covalently anchors Abs via a second EDC/NHS reaction. Solid-phase conjugation prevents PC linker cross-linking, and identical reaction chemistry simplifies synthetic preparation and the subsequent derivatization reactions. However, EDC/NHS reaction in an aqueous buffer could yield NHS ester hydrolysis. The resulting free surface -COOH can directly attach Abs to the surface after second EDC/NHS reaction. These directly attached Abs would not be photo-released.

To mitigate NHS ester hydrolysis, we investigated the ability to perform EDC/NHS reactions in anhydrous solvent. COC is well-known for exceptional solvent resistance,[22] but the effect of anhydrous solvents on the stability of UV/O_3-activated COC has not been investigated. We tested planar COC surfaces – either unmodified or UV/O_3-activated – that were left in air, immersed in buffer (MES, pH 4.8), or immersed in anhydrous solvents – ACN or dimethylformamide (DMF) – for 2 h. Dichloromethane was also tested but was immediately rejected due to polymer swelling and degradation of the COC substrate upon exposure; no polymer degradation was observed for either ACN or DMF. After solvent exposure, the surfaces were rinsed with water, dried, and then evaluated by several surface analysis techniques (**Table 2.3**) including water contact angles (WCAs), -COOH densities via a colorimetric TBO assay, and ATR-FTIR spectroscopy.

Table 2.3. Surface analyses to evaluate the stability of UV/O_3-activated COC surfaces exposed to aqueous buffer or anhydrous solvents.

Surface treatment	WCA[f] (°)	-COOH[g] (nmol/cm^2)	ATR-FTIR (au / cm^{-1})	
			C=O[h]	O-H[i]
Unmodified[a]	94.2 ±4.7	0.2 ±0.1	0.2 ±0.1	0.0 ±0.3
Unmodified, MES	93.7 ±4.4	0.2 ±0.0	0.1 ±0.3	-0.1 ±0.4
Unmodified, DMF	86.6 ±7.6	0.1 ±0.0	0.1 ±0.3	0.0 ±0.5
Unmodified, ACN	90.6 ±5.6	0.3 ±0.1	-0.1 ±0.4	-0.2 ±0.7

UV/O_3[b]	36.5 ±2.5	1.8 ±0.3	5.6 ±0.0	3.3 ±0.4
UV/O_3, MES[c]	57.7 ±3.6	2.0 ±0.4	4.7 ±0.5	3.4 ±0.6
UV/O_3, DMF[d]	83.2 ±8.4	0.4 ±0.0	2.6 ±0.3	1.5 ±0.7
UV/O_3, ACN[e]	64.7 ±8.4	0.6 ±0.1	4.7 ±0.8	3.6 ±0.5

COC surfaces were [a] unmodified or [b] UV/O_3-activated and submersed in [c] MES (100 mM, pH 4.8), [d] DMF, or [e] ACN. [f] Water contact angles (WCA). [g] Carboxylic acid (-COOH). ATR-FTIR spectral features integrated from [h] 1650-1850 and [i] 3200-3700 cm^{-1}.

UV/O_3-activated COC surfaces not exposed to buffer or solvent, as expected, exhibited increased wettability and -COOH surface densities, which is supported by the appearance of carbonyl and hydroxyl peaks in the ATR-FTIR spectra. Treatment with MES buffer increased surface hydrophobicity and slightly decreased -COOH surface densities and ATR-FTIR peak areas. Based on previous studies, UV/O_3-activation produces a heterogenous surface containing different oxidized functionalities and scissioning of the polymer chains into smaller molecular weight fragments. While COC appeared to be more resistant to fragmentation than, for example PMMA, fragmentation is likely to occur to some extent.[22] We suspect that MES buffer immersion resulting in decreased oxidation signals may have been caused by solubilization of oxidized polymer fragments.

DMF treatment increased hydrophobicity appreciably and reduced -COOH densities to near the nonspecific limit of the TBO assay. Further, ATR-FTIR peak areas were reduced after DMF treatment compared to MES buffer. Along with the altered WCAs in the unmodified COC control, these data could indicate solvent penetration and partial solubilization of the surface even though no degradation or swelling of the bulk material was observed – only harsh solvents such as dichloromethane produced these artifacts for COC.

ACN treatment yielded a surface most comparable to the MES buffer treatment (**Figure 2.3**). The only concerning disparity between ACN and MES treatment was a 68% decrease in -COOH densities. The consequences for biomolecule immobilization are limited by the

stoichiometric ratio of smaller -COOH groups and larger biomolecules. For example, a theoretical monolayer of -COOH groups is 830 pmol/cm^2, whereas a monolayer of larger oligonucleotides or antibodies is ~13 pmol/cm^2 or 0.85 pmol/ cm^2, respectively. Thus, an approximate 3-fold decrease in -COOH densities as assessed by the TBO assay may be irrelevant for biomolecule immobilization.

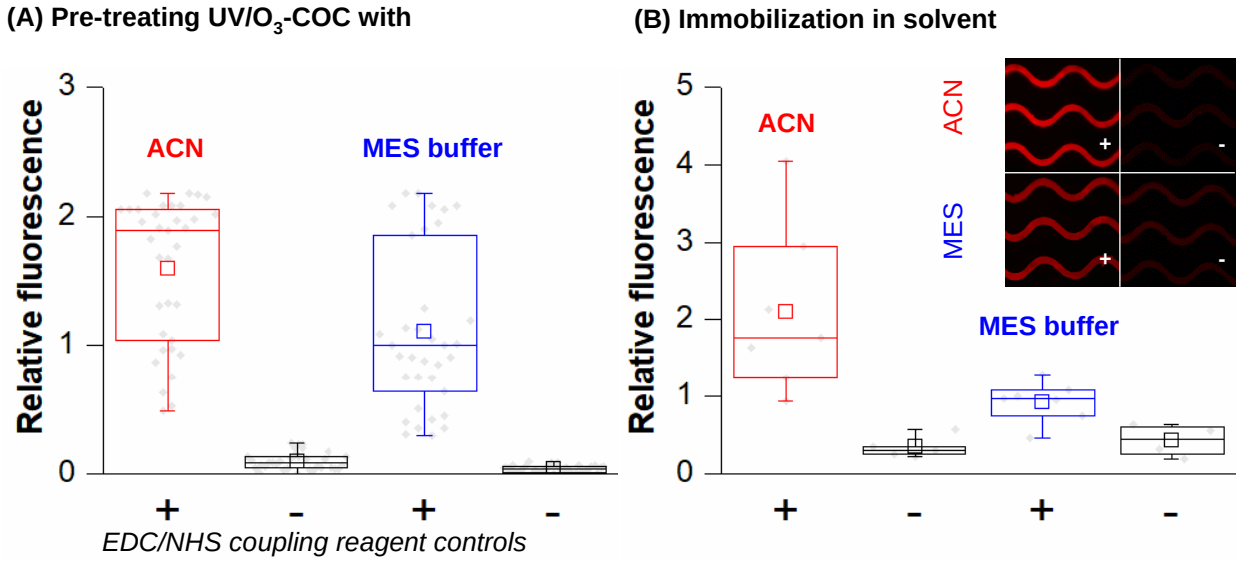

Figure 2.3. 5'-NH_2-, 3'-Cy5-oligonucleotide direct attachment to UV/O_3-COC surfaces. **(A)** ACN pre-treatment of UV/O_3-COC yielded higher loads of Cy5-oligonucleotides compared to MES (n = 33-35). **(B)** Further gains were observed in fluorescence microscopy by EDC/NHS coupling in ACN (n = 4). ((https://doi.org/10.1039/C9CC09598E) – Reproduced by permission of The Royal Society of Chemistry)

We tested immobilization efficiency using a 3' Cy5-labeled oligonucleotide reporter bearing a primary amine on its 5' end to UV/O_3-COC surfaces pre-treated with ACN or pre-treated with MES buffer (pH 4.8). EDC/NHS reaction was performed in MES buffer (pH 4.8). Cy5 oligonucleotide reporter load was slightly above in ACN pre-treated surfaces (**Figure 2.3A**). It is possible that, ACN can dissolve the short photo-fragments and remove them from the surface, which provides proper sterics to bind bio molecules. High relative fluorescence intensities were observed when EDC/NHS reaction was conducted in ACN compared to MES buffer (**Figure 2.3B**). ACN can avoid the NHS ester hydrolysis and improve the efficiency of EDC/NHS coupling

reaction. Based on these data, ACN solvent was selected for testing biomolecule coupling by EDC/NHS-activation.

2.3.3 **LED exposure chamber for PC linker cleavage**

We constructed a photo-exposure chamber using an LED outputting light from 385-470 nm (λ_{max} = 412 nm), which overlaps significantly with the PC linker's absorption spectrum (**Figure 2.4A**) and does not expose biological samples to intense UV radiation that may damage markers or their molecular cargo.[2, 34] The LED was placed 24 mm from the device surface to allow the LED's innate divergence (60°) to provide a spot diameter of 90 mm, which provided relatively homogenous illumination over the CTC or EV enrichment device's surface area (34 ±4 mW/cm^2; **Figure 2.4B**). Lastly, we note that larger or smaller devices can be accommodated without any additional optical elements by simply changing the distance between the LED light source and the device surface and elongating or shortening exposure time to achieve a consistent dose.

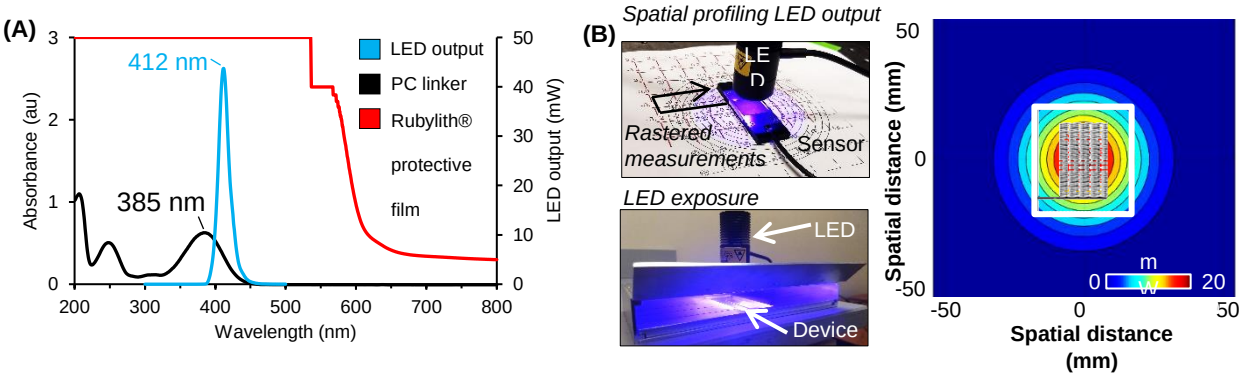

Figure 2.4. (A) The LED's spectral output, the absorbance spectra of the PC linker (measured at 0.526 µM in PBS, pH 7.4), and the Rubylith® film used to protect devices from ambient light and premature photocleavage. (**B**) For photoexposure, the Rubylith® film is removed, and devices were inserted into an aluminum exposure chamber, where the LED was centered with a 90 mm spot size over the device (shown here is the sinusoidal CTC enrichment device – 26 mm × 16 mm). The LED's spatial flux was measured by rastering a sensor underneath the LED and fitting to a 2-dimensional Gaussian (R^2 = 0.9986), which showed uniform exposure (34 ±4 mW/cm^2) over the device. ((**https://doi.org/10.1039/C9CC09598E**) – Reproduced by permission of The Royal Society of Chemistry)

2.3.4 **Cy5 reporter assay to monitor PC linker immobilization and cleavage**

We next immobilized the PC linker (in ACN and TEA) to UV/O3-activated COC microfluidic devices and measure the immobilization efficiency using Cy5 reporter. TEA was used with dry ACN to facilitate amide bond formation between the primary amine and NHS ester. We quenched unreacted NHS esters with Tris base to prevent direct attachment of Cy5-oligonucleotides. Next, we reacted the linker's -COOH terminus with EDC/NHS in ACN, and immobilized Cy5-oligonucelotides in buffer using the PC linker (**Figure 2.5A**). We then used an LED (λ_{max} = 412 nm, 32 ±4 mW/cm^2, **Figure 2.4**) to cleave the PC linker. Decreasing on-chip fluorescence of the Cy5-oligonucleotide (**Figure 2.5A and Figure 2.5B**) was confirmed as successful release. The remaining on chip fluorescence may be due to the autofluorescence of the UV/O3 activated surface and/or non- released Cy5 oligonucleotides. Note that we quantified the effects of photobleaching in the direct immobilization control, where Cy5 oligonucleotide

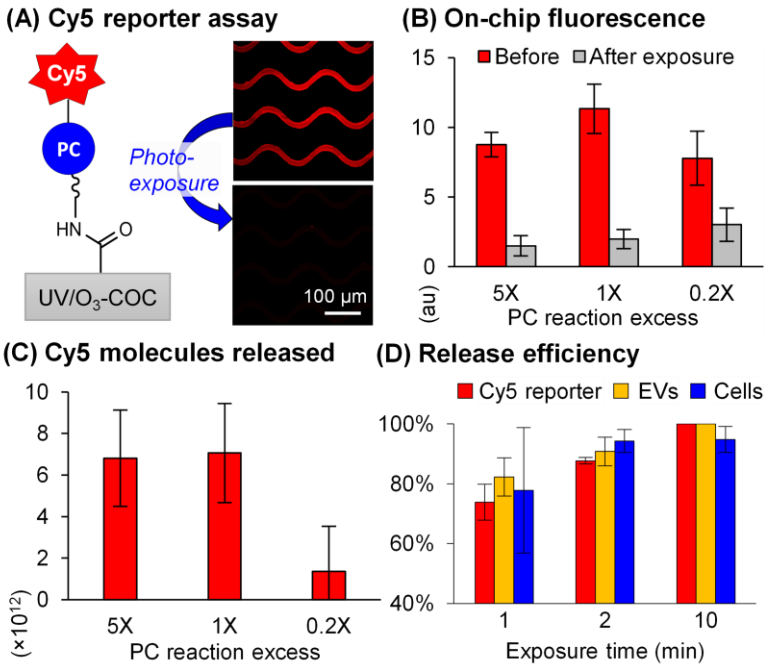

Figure 2.5. (A) Cy5-oligonucleotides were immobilized via the PC linker at 0.2-5X of the theoretical monolayer reaction excess (0.11–2.65 mM in ACN) considering the microfluidic device's surface area. **(B)** On-chip microscopy (n = 3) and **(C)** fluorescence spectroscopy of released Cy5 molecules (n = 3) show saturation at 1–5X. **(D)** Cy5- oligonucleotides (n = 3), EVs (n=5), and SKBR3 cells (n=3) were released with 88%, 91%, and 94% efficiency in 2 min, respectively. ((https://doi.org/10.1039/C9CC09598E) – Reproduced by permission of The Royal Society of Chemistry)

reporter was immobilized to the surface directly without involving the PC linker. It showed a ~20 % loss in Cy5 fluorescence after LED exposure. In separate experiments, we confirmed photobleaching occurred during fluorescence microscopy imaging (Cy5 channel), but not during LED photo exposure (data not shown). This was not unexpected as the LED output (385-470 nm) is well separated from the absorbance range of the Cy5 fluorophore (507-694 nm, λ_{max} = 649 nm).

Antibodies are much larger molecules than PC linkers. Therefore, all PC linkers immobilized on the device surface will not bind with an antibody. Hence, the minimum PC linker concentration required to bind the maximum number of antibodies is required to maximize the recovery of the required target. For that, we varied the PC linker reaction excess compared to a monolayer (considering surface area) and observed the same number of Cy5 reporter release in 1-5X PC linker excess (**Figure 2.5C**). Thus, we could saturate the device at 1X PC linker reaction excess (0.56 nmol/cm^2, 1.82 x 10^{15} molecules per device) and the PC linker concentration is sufficient to get the maximum recovery. We varied LED exposure time and released 74 ±6% Cy5 oligonucleotide reporters in 1 min and 88 ±1% reporters (6.4 ×10^{12} molecules) in 2 min (**Figure 2.5D).**

2.3.5 **Cell capture, release and propagation**

We next used the PC linker to immobilize anti-EpCAM Abs in a microfluidic device for CTC affinity-enrichment.[6] We targeted SKBR3 cells spiked into healthy blood (69-269 SKBR3 cells/mL) to evaluate the anti-interference ability of PC linker in a complexed matrix. We pre-stained SKBR3 cells with Hoechst dye and, after enrichment, stained all cells with SYTO 82, a membrane-permeable nuclear dye that is spectrally distinct from Hoechst. SKBR3 cells were dual-stained, while leukocytes were only stained with SYTO 82 enabling the determination of recovery by a self-referencing method[14] and purity of the enriched fraction (**Figure 2.6A**).

SKBR3 cells were enriched with 85 ±8% purity (16-38 leukocytes/mL) and 73 ±4% recovery (47-202 cells), slightly lower than found for the dU linker (85 ±4%)[14] and direct Ab attachment (96

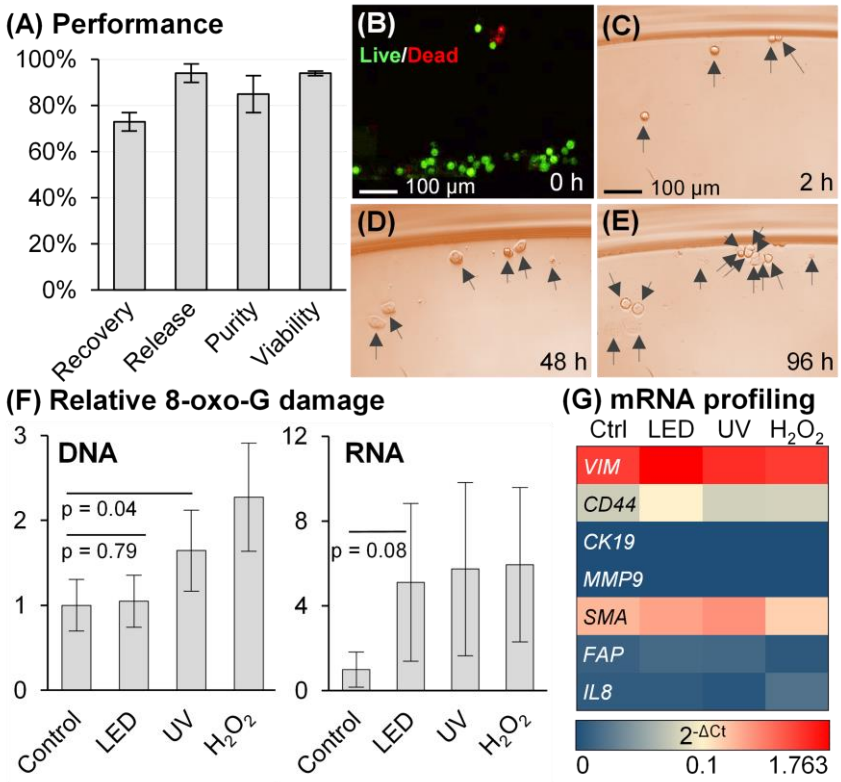

Figure 2.6. (A) Performance of sinusoidal microfluidic device using PC linker for anti-EpCAM enrichment of SKBR3 cells spiked into whole blood (n = 3). **(B)** LED release had no effect on viability, and **(C–E)** released cells in culture for 2–96 h (Scale bars = 100 µm). **(F)** DNA/RNA oxidative damage (n = 3) assessed for 2 min LED exposure, equivalent UV dose (18.5 J), and 300 µM H_2O_2 (30 min) of Hs578T cells. DNA damage is normalized to 32.2 pg 8-oxo-G per 400 ng DNA. The DNA-derived ELISA 8-oxo-G calibration curve could not quantify RNA damage absolutely. **(G)** mRNA profiling by RT-qPCR (n = 3) of Hs578T cells following no irradiation, LED or UV light exposure, or H_2O_2 treatment. ((https://doi.org/10.1039/C9CC09598E) – Reproduced by permission of The Royal Society of Chemistry)

±12%). We also observed ~40% fewer Cy5-oligonucleotide reporters immobilized through the PC linker compared to direct conjugation with the surface,[14] and we suspect that Ab load and CTC recovery may increase if the PC linker was elongated with a longer PEG spacer which would allow more access to targets. We used the PC linker to immobilize IgG 2A isotype Ab to evaluate nonspecific cell recovery (3 ±2%). The release of SKBR3 cells was rapid with 94 ±4% efficiency after 2 min of LED exposure (**Figure 2.5D**). Other breast cancer cell lines were also enriched and released with 88 ±10% and 91 ±4% release efficiency for MCF7 and Hs578T cells, respectively.

After exposure to visible LED light, released SKBR3 cells had 94 ±1% viability, the same as controls (**Figure 2.6B**), and could be propagated in culture for 96 h (**Figure 2.6C** – **E**). Similarly, exposed MCF7 and Hs578T cells had 96 ±6% and 99 ±3% cell viability, respectively. Others have also observed >90% cell viability for O-nitrobenzyl and 7-amino coumarin linkers.[20, 39, 40] However, UV irradiation can damage nucleic acids through photo-absorption and oxidation (8-oxoguanine, 8-oxo-G, production).

2.3.6 **Oxidative DNA/RNA damage**

We measured 8-oxo-G levels in RNA and DNA for Hs578T cells exposed to visible LED versus UV light (both at a dose of 18.5 J) and compared to H_2O_2, which is known to generate oxidative damage in DNA and RNA via oxygen free radicals. DNA damage was not detected for LED exposure but was present with UV irradiation (**Figure 2.6F**). Both exposures generated 8-oxo-G damage in RNA at comparable levels to that of H_2O_2 (**Figure 2.6F**). Single-stranded RNA is easily oxidized so as to protect genomic DNA from damage[41] and subsequent mutations through imperfect repair pathways.[42]

2.3.7 **Impact of RNA 8-oxo-G damage on target gene expression**

A gene panel consisting of mesenchymal and EMT markers were selected to determine the impact of mRNA oxidative damage (**Figure 2.6G**; see **Table 2.1** for primers used for the RT-qPCR). Total RNA was purified from Hs578T cells from standard culture (control) or after LED exposure (18.5 J), or after UV exposure (18.5 J) or after H_2O_2 treatment. mRNA was reverse transcribed with anchored poly(dT) primers and cDNA was amplified with gene specific primers (**Table 2.1**) by qPCR with 2-3 replicates per gene. All genes were referenced to the housekeeping gene *GAPDH* and reported as $2^{-\Delta Ct}$, where ΔC_t is $C_t^{Gene} - C_t^{GAPDH}$. No interfering amplification was observed in RT controls for all genes and samples (data not shown). However, mRNA expression was similar in all three treatments suggesting that, 8-oxo-G damage observed in total RNA, did not alter the mRNA expression of the selected gene panel. Collectively, visible LED exposure did

not affect mRNA expression or cause oxidative DNA damage, whereas UV irradiation induced DNA 8-oxo-G damage. Such DNA damage could cause false positives for clinical analysis, especially at the single cell level common to CTCs.

2.3.8 **Impact of attached Ab ligands on mRNA expression**

Molecular level changes due to the attachment of Ab ligands on cell surface after photo-release was evaluated by profiling mRNA expression of photo released cells. Total RNA was extracted from photo released cells and RT reaction was performed with primers of seven stress genes (**Table 2.1** for primer sequences). cDNA was synthesized and qPCR was conducted to analyze mRNA expression (**Figure 2.7**). All data were normalized to the house keeping gene *GADPH* as mentioned above.

We observed similar mRNA expression profiles in photo-released cells and control cells ($p = 0.1\text{-}0.9$, $r=0.99$). The results suggest that, monoclonal Ab attachment on cell surface as a ligand could not alter the mRNA expression of target genes under these experimental conditions.

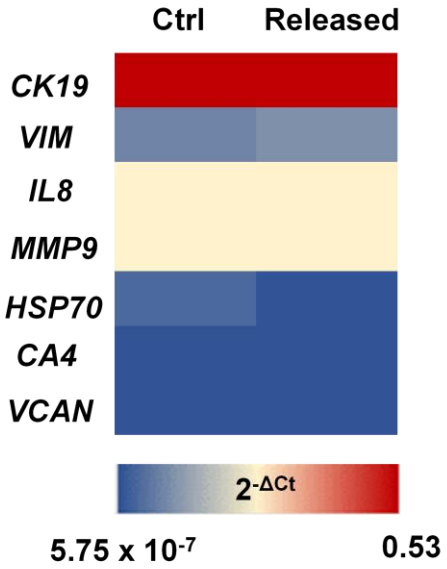

Figure 2.7. RT-qPCR was used to analyze mRNA expression changes occurred due to the presence of Ab ligands on cell surface after photo release. mRNA expression profiles of 7 genes were compared in control SKBR3 cells and photo released cells (For CK19, n=5 and for other genes n=6). The gene panel consists of stress genes and EMT markers. ((https://doi.org/10.1039/C9CC09598E) – Reproduced by permission of The Royal Society of Chemistry)

2.3.9 **Flow cytometry analysis of antigen expression in cell lines and correlation to release efficiency**

For the affinity-enriched cell lines, we analyzed antigen expression versus isotype controls by flow cytometry (**Figure 2.8A**). MCF7 had the highest expression of EpCAM (125X IgG) with lower expression of EpCAM in the SKBR3 cell line (20X). For enrichment anti-EpCAM antibodies were used for enriching MCF7 and SKBR3 cell lines, while anti-FAPα antibodies were used for enriching the Hs578T cells. Release efficiencies were 88 ±10%, 94 ±4%, and 91 ±4% for the MCF7, SKBR3, and Hs578T cell lines, respectively. We observed minimal correlation between antigen expression and release efficiency (**Figure 2.8B**). Therefore, the rate of release does not seem to depend on the number of Ab-antigen interactions. We previously encountered results which indicated that when using the enzymatically cleavable oligonucleotide linker,[14] longer incubation times with USER enzyme were required to achieve equivalent release efficiency for cells with higher antigen expression levels.[14]

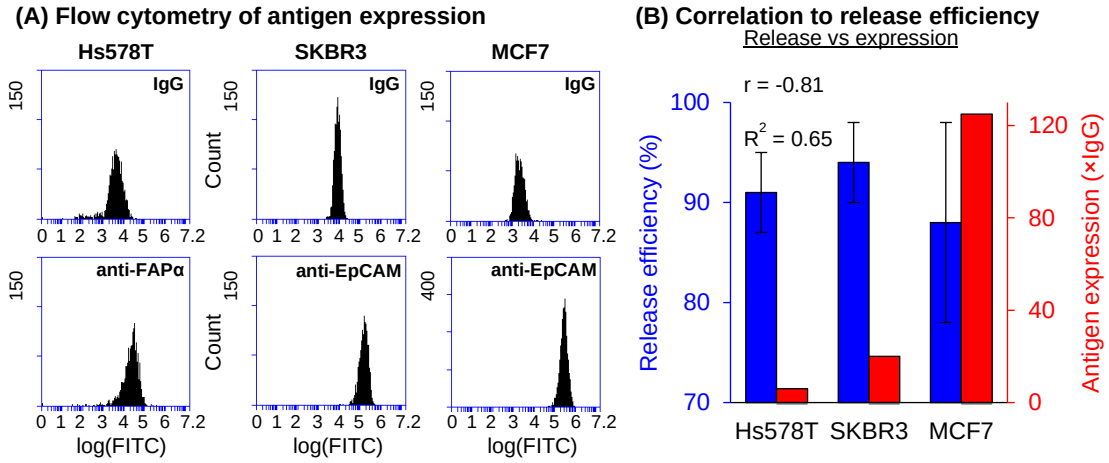

Figure 2.8. (A) Three cell lines (Hs578T, SKBR3, and MCF7) were tested for antigen expression by flow cytometry. Cells were labeled with FITC-conjugated IgG control Abs and their corresponding FITC-labeled primary Ab, anti-FAPα or anti-EpCAM. Labeled cells were analyzed with a BD Accuri C6 Plus flow cytometer. **(B)** Relative antigen expressions were obtained by flow cytometry data and correlated (r = -0.81) with release efficiency. ((https://doi.org/10.1039/C9CC09598E) – Reproduced by permission of The Royal Society of Chemistry)

2.3.10 **EV isolation and release**

Lastly, we tested the PC linker for EV catch and release. Our group recently affinity enriched CD8(+) EVs as a liquid biopsy marker to diagnose AIS. We relied on the dU linker strategy to release EVs,[43] but the 60 min enzymatic reaction increased total assay time, approaching the ~4.5 h therapeutic time window. Thus, we investigated the use of the PC linker to reduce processing time for releasing AIS-associated EVs.

We immobilized the PC linker and anti-CD8 Abs to a UV/O_3-COC microfluidic device specifically-designed to enrich EVs with high efficiency.[43] The expression of CD8 antigen in MOLT-3 cells was reported as 13.5%, thus the MOLT-3 cell line was used as model for these studies.[44] CD8(+) EVs were affinity enriched from MOLT-3 conditioned media and photo-released for NTA and TEM analysis. From the MOLT-3 conditioned media, we enriched 8.2 ±0.2 × 10^7 nanoparticles (NPs) with an EV size of ~136 nm, similar to TEM imaging (**Figure 2.9A, B**). EV release was again rapid; 82 ±6% of NPs were released after 1 min LED exposure, and 91 ±5% were released with 2 min LED exposure (**Figure 2.5D**). Thus, the PC linker is well suited to reduce the AIS assay workflow by >58 min compared to an enzymatic release strategy.

2.3.11 **RT-ddPCR of MOLT-3 derived EV-mRNA after LED exposure**

EVs from MOLT-3 cells were PEG precipitated, resuspended in PBS, and exposed to LED irradiation for 2 min or not (control). Afterwards, the EVs were lysed via Trizol, and EV-RNA was extracted and quantified. We probed a panel of 8 genes by RT-ddPCR (primer sequences in **Table 2.2**). The mRNA panel profiled in **Figure 2.9C** consists of genes whose activities are dysregulated as a result of AIS (*PLBD1*, *FOS*, *MMP9*, *CA4* and *VCAN)*. *IL8* is a stress gene and *CD81* and *CD8* genes are EV specific markers. We did not observe any effect of LED exposure on RT-ddPCR results for this EV-mRNA panel (**Figure 2.9C**).

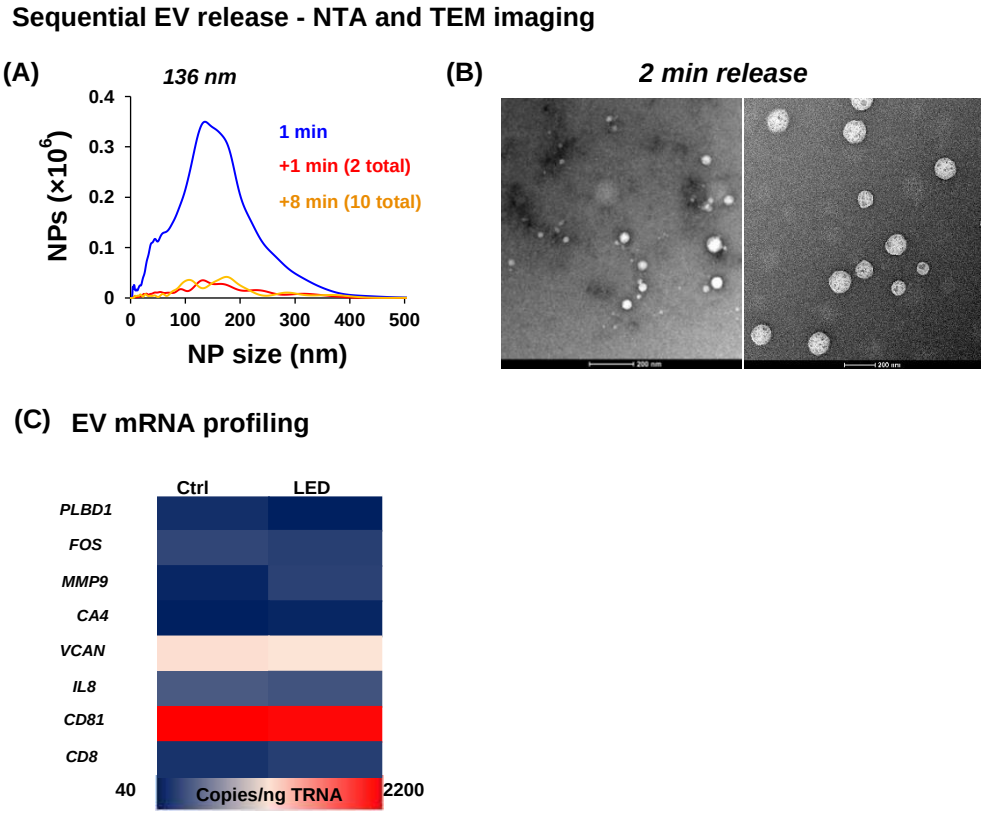

Figure 2.9. EVs affinity-enrichment (anti-CD8 mAbs). The EVs were enriched from MOLT-3 conditioned media and released by LED exposure from the EV enrichment microfluidic device. The released EVs were subjected to NTA (**A**), TEM (**B**), and ddPCR (**C**) analyses. The ddPCR was carried out on 8 genes. Among them, five genes (PLBD1, FOS, MMP9, CA4 and VCAN) are known to be dysregulated as a result of an ischemic stroke (AIS) event. See **Table S3** for the sequences of the primers used for the ddPCR. ((https://doi.org/10.1039/C9CC09598E) – Reproduced by permission of The Royal Society of Chemistry)

2.4 Conclusions

We successfully demonstrated our PC linker for the “catch and release” of clinically-relevant liquid biopsy markers (CTCs and EVs) that are affinity-enriched using two-step EDC/NHS coupling chemistry. The PC linker is easily adaptable for any affinity agent bearing a primary amine, such as antibodies and aptamers. Also, it can be adapted to different microfluidic devices and clinical applications. Most importantly, our PC linker was able to release enriched liquid biopsy markers efficiently (>90%) and rapidly (2 min) with a blue LED (400-450 nm). Targeting

AIS takes full advantage of the PC linker's rapid release to reduce assay time for diagnostic tests that possess short therapeutic time windows. This reagent-less release method is inexpensive and well suited for clinical settings because it obviates the need for thermally mediated enzymatic reactions. While ambient light can cause photocleavage, once the enrichment device has been loaded with the affinity agent using the PC linker, the device can be wrapped in a rubylith film to protect the integrity of the PC linker (see **Figure 2.4A**).

We demonstrated the anti-interference ability of PC linker by achieving a high cell recovery (>70%) from a complex matrix such as blood. We also showed a high cell viability and culturing for released CTC surrogates. Unlike UV exposure, our PC linker cleaved in response to visible light and did not affect DNA integrity (no appreciable 8-ox-G damage). The oxidative RNA damage observed due to the blue light exposure, did not alter the mRNA expression profiles of enriched biomarkers. We also showed that, remaining Ab ligand on cell surface after photo-release did not affect molecular profiling of selected gene panel. These promising results warrant future investigations to improve the PC linker performance, such as incorporating a PEG spacer to increase Ab accessibility, overall Ab loading capacity, and marker recovery.

2.5 Acknowledgment

The authors would like to thank the NIH for funding of this work (NIBIB: P41 EB020594; NCI: P30 CA168524, R01 CA211720; NIGMS: P20 GM130423, P20GM103638). We also acknowledge the KU Microscopy and Analytical Imaging Laboratory for TEM imaging (DOD-47040-2974000-908), and KU Endowment Funds (RSG).

2.6 References

1. Campos, C. D. M.; Jackson, J. M.; Witek, M. A.; Soper, S. A., Molecular Profiling of Liquid Biopsy Samples for Precision Medicine. *Cancer J.* **2018,** *24* (2), 93-103.
2. Jackson, J. M.; Witek, M. A.; Kamande, J. W.; Soper, S. A., Materials and microfluidics: enabling the efficient isolation and analysis of circulating tumour cells. *Chem Soc Rev* **2017,** *46* (14), 4245-4280.

3. Jackson, J. M.; Taylor, J. B.; Witek, M. A.; Hunsucker, S. A.; Waugh, J. P.; Fedoriw, Y.; Shea, T. C.; Soper, S. A.; Armistead, P. M., Microfluidics for the Detection of Minimal Residual Disease in Acute Myeloid Leukemia Patients using Circulating Leukemic Cells Selected from Blood. *Analyst* **2016,** *141* (2), 640-651.
4. Contreras-Naranjo, J. C.; Wu, H. J.; Ugaz, V. M., Microfluidics for exosome isolation and analysis: enabling liquid biopsy for personalized medicine. *Lab Chip* **2017,** *17* (21), 3558-3577.
5. Pullagurla, S. R.; Witek, M. A.; Jackson, J. M.; Lindell, M. A.; Hupert, M. L.; Nesterova, I. V.; Baird, A. E.; Soper, S. A., Parallel affinity-based isolation of leukocyte subsets using microfluidics: application for stroke diagnosis. *Anal Chem* **2014,** *86* (8), 4058-65.
6. Witek, M. A.; Aufforth, R. D.; Wang, H.; Kamande, J. W.; Jackson, J. M.; Pullagurla, S. R.; Hupert, M. L.; Usary, J.; Wysham, W. Z.; Hilliard, D.; Montgomery, S.; Bae-Jump, V.; Carey, L. A.; Gehrig, P. A.; Milowsky, M. I.; Perou, C. M.; Soper, J. T.; Whang, Y. E.; Yeh, J. J.; Martin, G.; Soper, S. A., Discrete microfluidics for the isolation of circulating tumor cell subpopulations targeting fibroblast activation protein alpha and epithelial cell adhesion molecule. *Nat. Prec. Onc.* **2017,** *1*, 24.
7. Ashley, E. A., Towards precision medicine. *Nat. Rev. Genet.* **2016,** *17* (9), 507-522.
8. Sheng, W.; Ogunwobi, O. O.; Chen, T.; Zhang, J.; George, T. J.; Liu, C.; Fan, Z. H., Capture, release and culture of circulating tumor cells from pancreatic cancer patients using an enhanced mixing chip. *Lab on a Chip* **2014,** *14* (1), 89-98.
9. Lotvall, J.; Hill, A. F.; Hochberg, F.; Buzas, E. I.; Di Vizio, D.; Gardiner, C.; Gho, Y. S.; Kurochkin, I. V.; Mathivanan, S.; Quesenberry, P.; Sahoo, S.; Tahara, H.; Wauben, M. H.; Witwer, K. W.; Thery, C., Minimal experimental requirements for definition of extracellular vesicles and their functions: a position statement from the International Society for Extracellular Vesicles. *J. Extracell. Vesicles* **2014,** *3*, 26913.
10. Chevillet, J. R.; Kang, Q.; Ruf, I. K.; Briggs, H. A.; Vojtech, L. N.; Hughes, S. M.; Cheng, H. H.; Arroyo, J. D.; Meredith, E. K.; Gallichotte, E. N.; Pogosova-Agadjanyan, E. L.; Morrissey, C.; Stirewalt, D. L.; Hladik, F.; Yu, E. Y.; Higano, C. S.; Tewari, M., Quantitative and stoichiometric analysis of the microRNA content of exosomes. *Proc. Natl. Acad. Sci. U. S. A.* **2014,** *111* (41), 14888-93.
11. Ao, Z.; Parasido, E.; Rawal, S.; Williams, A.; Schlegel, R.; Liu, S.; Albanese, C.; Cote, R. J.; Agarwal, A.; Datar, R. H., Thermoresponsive release of viable microfiltrated Circulating Tumor Cells (CTCs) for precision medicine applications. *Lab Chip* **2015,** *15* (22), 4277-82.
12. Hou, S.; Zhao, H.; Zhao, L.; Shen, Q.; Wei, K. S.; Suh, D. Y.; Nakao, A.; Garcia, M. A.; Song, M.; Lee, T.; Xiong, B.; Luo, S.-C.; Tseng, H.-R.; Yu, H.-h., Capture and Stimulated Release of Circulating Tumor Cells on Polymer-Grafted Silicon Nanostructures. *Advanced Materials* **2013,** *25* (11), 1547-1551.
13. Reategui, E.; Aceto, N.; Lim, E. J.; Sullivan, J. P.; Jensen, A. E.; Zeinali, M.; Martel, J. M.; Aranyosi, A. J.; Li, W.; Castleberry, S.; Bardia, A.; Sequist, L. V.; Haber, D. A.; Maheswaran, S.; Hammond, P. T.; Toner, M.; Stott, S. L., Tunable nanostructured coating for the capture and selective release of viable circulating tumor cells. *Advanced Materials* **2015,** *27* (9), 1593-9.
14. Nair, S. V.; Witek, M. A.; Jackson, J. M.; Lindell, M. A.; Hunsucker, S. A.; Sapp, T.; Perry, C. E.; Hupert, M. L.; Bae-Jump, V.; Gehrig, P. A.; Wysham, W. Z.; Armistead, P. M.; Voorhees, P.; Soper, S. A., Enzymatic cleavage of uracil-containing single-stranded DNA linkers for the efficient release of affinity-selected circulating tumor cells. *Chem. Commun.* **2015,** *51* (15), 3266-9.
15. Alison E. Baird, D. F. M., Ehud Goldin, Kory Johnson Differential Expression of Molecules Associated with Intra-Cerebral Hemorrhage. US 20100086481A1, 2010.
16. Moore, D. F.; Li, H.; Jeffries, N.; Wright, V.; Cooper, R. A.; Elkahloun, A.; Gelderman, M. P.; Zudaire, E.; Blevins, G.; Yu, H.; Goldin, E.; Baird, A. E., Using peripheral blood mononuclear cells to determine a gene expression profile of acute ischemic stroke. *Circulation*

2005, *111* (Copyright (C) 2013 American Chemical Society (ACS). All Rights Reserved.), 212-221.
17. Dong, J.; Xun, Z.; Zeng, Y.; Yu, T.; Han, Y.; Chen, J.; Li, Y. Y.; Yang, G.; Li, Y., A Versatile and Robust Vesicle Based on a Photocleavable Surfactant for Two-Photon-Tuned Release. *Chemistry–A European Journal* **2013,** *19* (24), 7931-7936.
18. Huang, Q.; Bao, C.; Ji, W.; Wang, Q.; Zhu, L., Photocleavable coumarin crosslinkers based polystyrene microgels: phototriggered swelling and release. *J. Mat. Chem.* **2012,** *22* (35), 18275-18282.
19. Lin, Q.; Bao, C.; Cheng, S.; Yang, Y.; Ji, W.; Zhu, L., Target-activated coumarin phototriggers specifically switch on fluorescence and photocleavage upon bonding to thiol-bearing protein. *J Am Chem Soc* **2012,** *134* (11), 5052-5.
20. Lv, S.-W.; Wang, J.; Xie, M.; Lu, N.-N.; Li, Z.; Yan, X.-W.; Cai, S.-L.; Zhang, P.-A.; Dong, W.-G.; Huang, W.-H., Photoresponsive immunomagnetic nanocarrier for capture and release of rare circulating tumor cells. *Chem. Sci.* **2015,** *6* (11), 6432-6438.
21. Givens, R. S.; Rubina, M.; Wirz, J., Applications of p-hydroxyphenacyl (pHP) and coumarin-4-ylmethyl photoremovable protecting groups. *Photochem Photobiol Sci* **2012,** *11* (3), 472-88.
22. Jackson, J. M.; Witek, M. A.; Hupert, M. L.; Brady, C.; Pullagurla, S.; Kamande, J.; Aufforth, R. D.; Tignanelli, C. J.; Torphy, R. J.; Yeh, J. J.; Soper, S. A., UV activation of polymeric high aspect ratio microstructures: ramifications in antibody surface loading for circulating tumor cell selection. *Lab Chip* **2014,** *14* (1), 106-117.
23. Adams, A. A.; Okagbare, P. I.; Feng, J.; Hupert, M. L.; Patterson, D.; Gottert, J.; McCarley, R. L.; Nikitopoulos, D.; Murphy, M. C.; Soper, S. A., Highly Efficient Circulating Tumor Cell Isolation from Whole Blood and Label-Free Enumeration Using Polymer-Based Microfluidics with an Integrated Conductivity Sensor. *J. Am. Chem. Soc.* **2008,** *130* (27), 8633-8641.
24. Dharmasiri, U.; Adams, A. A.; Witek, M.; Soper, S. A., Microsystems for the Capture of Low Abundant Cells. *Annu. Rev. Anal. Chem.* **2010,** *3*, 409-431.
25. Dharmasiri, U.; Balamurugan, S.; Adams, A. A.; Okagbare, P. I.; Obubuafo, A.; Soper, S. A., Highly efficient capture and enumeration of low abundance prostate cancer cells using prostate-specific membrane antigen aptamers immobilized to a polymeric microfluidic device. *Electrophoresis* **2009,** *30* (18), 3289-3300.
26. Dharmasiri, U.; Njoroge, S. K.; Witek, M.; Adebiyi, M. G.; Kamande, J. W.; Hupert, M. L.; Barany, F.; Soper, S. A., High-throughput selection, enumeration, electrokinetic manipulation and molecular profiling of low-abundance circulating tumor cells using a microfluidic system. *Anal. Chem.* **2011,** *83* (6), 2301-2309.
27. Hupert, M. L.; Jackson, J. M.; Wang, H.; Witek, M. A.; Kamande, J.; Milowsky, M. I.; Whang, Y. E.; Soper, S. A., Arrays of high-aspect ratio microchannels for high-throughput isolation of circulating tumor cells (CTCs). *Microsys. Technol.* **2014,** *20* (10), 1815-1825.
28. Kamande, J. W.; Hupert, M. L.; Witek, M. A.; Wang, H.; Torphy, R. J.; Dharmasiri, U.; Njoroge, S. K.; Jackson, J. M.; Aufforth, R. D.; Snavely, A.; Yeh, J. J.; Soper, S. A., Modular Microsystem for the Isolation, Enumeration, and Phenotyping of Circulating Tumor Cells: Managing Patients with Pancreatic Cancer. *Anal. Chem.* **2013,** *85* (19), 9092-9100.
29. Witek, M. A.; Aufforth, R. D.; Wang, H.; Kamande, J. W.; Jackson, J. M.; Pullagurla, S. R.; Hupert, M. L.; Usary, J.; Wysham, W. Z.; Hilliard, D.; Montgomery, S.; Bae-Jump, V.; Carey, L. A.; Gehrig, P. A.; Milowsky, M. I.; Perou, C. M.; Soper, J. T.; Whang, Y. E.; Yeh, J. J.; Martin, G.; Soper, S. A., Discrete microfluidics for the isolation of circulating tumor cell subpopulations targeting fibroblast activation protein alpha and epithelial cell adhesion molecule. *NPJ Precis. Oncol.* **2017,** *1*, 24.
30. Campos, C. D.; Gamage, S. S.; Jackson, J. M.; Witek, M. A.; Park, D. S.; Murphy, M. C.; Godwin, A. K.; Soper, S. A., Microfluidic-based solid phase extraction of cell free DNA. *Lab Chip* **2018,** *18* (22), 3459-3470.

31. O'Neil, C. E.; Jackson, J. M.; Shim, S. H.; Soper, S. A., Characterizing Surface Functional Group Density for O2 Plasma and UV/O3 Activated Thermoplastics using Superresolution Microscopy. *Analytical Chemistry* **2016,** *88*, 3686-3696.
32. O'Neil, C. E.; Taylor, S.; Ratnayake, K.; Pullagurla, S.; Singh, V.; Soper, S. A., Characterization of activated cyclic olefin copolymer: effects of ethylene/norbornene content on the physiochemical properties. *Analyst* **2016,** *141*, 6521-6532.
33. Runger, T. M.; Kappes, U. P., Mechanisms of mutation formation with long-wave ultraviolet light (UVA). *Photodermatol. Photoimmunol. Photomed.* **2008,** *24* (1), 2-10.
34. Sage, E.; Girard, P. M.; Francesconi, S., Unravelling UVA-induced mutagenesis. *Photochem. Photobiol. Sci.* **2012,** *11* (1), 74-80.
35. Nyaga, S. G.; Lohani, A.; Jaruga, P.; Trzeciak, A. R.; Dizdaroglu, M.; Evans, M. K., Reduced repair of 8-hydroxyguanine in the human breast cancer cell line, HCC1937. *BMC Cancer* **2006,** *6*, 297.
36. Adamski, M. G.; Li, Y.; Wagner, E.; Seales-Bailey, C.; Bennett, N.; Yu, H.; Murphy, M.; Soper, S. A.; Baird, A. E., CD15+ granulocyte and CD8+ T lymphocyte based gene expression clusters for ischemic stroke detection. *Med. Res. Arch.* **2017,** *5* (11).
37. Rider, M. A.; Hurwitz, S. N.; Meckes, D. G., Jr., ExtraPEG: A Polyethylene Glycol-Based Method for Enrichment of Extracellular Vesicles. *Sci. Rep.* **2016,** *6*, 23978.
38. Klan, P.; Solomek, T.; Bochet, C. G.; Blanc, A.; Givens, R.; Rubina, M.; Popik, V.; Kostikov, A.; Wirz, J., Photoremovable protecting groups in chemistry and biology: reaction mechanisms and efficacy. *Chem Rev* **2013,** *113* (1), 119-91.
39. LeValley, P. J.; Tibbitt, M. W.; Noren, B.; Kharkar, P.; Kloxin, A. M.; Anseth, K. S.; Toner, M.; Oakey, J., Immunofunctional photodegradable poly(ethylene glycol) hydrogel surfaces for the capture and release of rare cells. *Colloids Surf. B Biointerfaces* **2019,** *174*, 483-492.
40. Deng, Y.; Zhang, Y.; Sun, S.; Wang, Z.; Wang, M.; Yu, B.; Czajkowsky, D. M.; Liu, B.; Li, Y.; Wei, W.; Shi, Q., An integrated microfluidic chip system for single-cell secretion profiling of rare circulating tumor cells. *Sci. Rep.* **2014,** *4*, 7499.
41. Radak, Z.; Boldogh, I., 8-Oxo-7,8-dihydroguanine: links to gene expression, aging, and defense against oxidative stress. *Free Radic. Biol. Med.* **2010,** *49* (4), 587-96.
42. Yasui, M.; Kanemaru, Y.; Kamoshita, N.; Suzuki, T.; Arakawa, T.; Honma, M., Tracing the fates of site-specifically introduced DNA adducts in the human genome. *DNA Repair* **2014,** *15*, 11-20.
43. Wijerathne, H.; Witek, M. A.; Jackson, J. M.; Brown, V.; Hupert, M. L.; Herrera, K.; Kramer, C.; Davidow, A. E.; Li, Y.; Baird, A. E.; Murphy, M. C.; Soper, S. A., Affinity enrichment of extracellular vesicles from plasma reveals mRNA changes associated with acute ischemic stroke. *Commun Biol* **2020,** *3* (1), 613.
44. Greenberg, J. M.; Gonzalez-Sarmiento, R.; Arthur, D. C.; Wilkowski, C. W.; Streifel, B.; Kersey, J., Immunophenotypic and cytogenetic analysis of Molt-3 and Molt-4: human T-lymphoid cell lines with rearrangement of chromosome 7. *Blood* **1988,** *72* (5), 1755-1760.

Chapter 3 - Integrated modular microfluidic system (SMART-Chip) for the comprehensive analysis of circulating tumor cells (CTCs)

This chapter is based on the publication:

Thilanga N. **Pahattuge**., Ian Freed., Mateusz L. Hupert., Swarnagowri Vaidyanathan., Katie Childers., Malgorzata A. Witek., Kumuditha Rathnayake., Daniel Park., Anup Kasi., Mazin F Al-Kasspooles., Michael C. Murphy and Steven A. Soper "System Modularity Chip for Analysis of Rare Targets (SMART-Chip): Liquid Biopsy Samples" (ACS Sens. 2021 May 3. doi: 10.1021/acssensors.0c02728. Epub ahead of print. PMID: 33938745.)

3.1 Introduction

Liquid biopsies are generating significant interests in the medical community due to their minimally invasive nature of acquisition and the fact that they can enable decisions on managing a variety of diseases (*i.e*., precision medicine).[1-2] Liquid biopsy markers include, but are not limited to, rare cells such as circulating tumor cells (CTCs), cell-free molecules for example cell free DNA (cfDNA) and microRNA (miRNA), and extracellular vesicles (EVs). Liquid biopsies are especially useful when anatomically inaccessible organs are diseased making it difficult to secure a solid tissue biopsy (*i.e*., brain, lungs, or pancreas). For example, we have shown that CTCs can be enriched in sufficient numbers to monitor response to therapy in patients with pancreatic ductal adenocarcinoma (PDAC) using enumeration and molecular data from epithelial and mesenchymal type CTCs.[3] Not only can liquid biopsy markers be used to monitor response to therapy, they can also be used to screen for disease recurrence, stratify patients so they receive proper therapy, and even diagnose the disease at an early stage of onset.[4-5]

Analyzing liquid biopsy markers can be challenging due to the multiple processing steps involved in the assay and the low mass of the marker that is typically isolated from a clinical sample, especially for early stages of disease onset. The analysis pipeline depends on whether one is interested in just the enumeration of the particular liquid biopsy marker and/or the

acquisition of molecular information from the markers, such as determining the mutational status of disease-associated genes. For typical liquid biopsy assays, the relevant markers must first be enriched from the sample because in most cases they are a vast minority in a mixed population. Following the enrichment, the liquid biopsy markers must be further analyzed to secure the necessary clinical information to guide patient management. For example, in the case of CTCs the enriched cells must be stained with a panel of markers (*i.e*., CD45, pan-cytokeratins and DAPI) to differentiate the CTCs from white blood cells that may appear in the enriched fraction. For molecular analysis of the enriched markers, the steps required are particular to a specific molecular assay for example sequencing, fluorescence *in situ* hybridization (FISH), mutation detection or mutation scanning. Due to the low abundance of liquid biopsy markers (CTCs in patients' blood can range from 1 – 1,000 CTCs per mL),[6-7] marker loss or contamination caused by manual handling during multiple processing steps may result in false negative/positive results and the need for well-trained operators that can hamper the transition of liquid biopsy assays into the clinic.

Several new microfluidic technologies have been reported for the enrichment of liquid biopsy markers. For example, enrichment of CTCs can utilize different techniques such as deterministic lateral displacement (DLD) or inertial focusing,[8-9] dielectrophoresis,[10] acoustic waves,[11-12] size-based filtration,[12-13] or immunoaffinity methods.[14-16] Unfortunately, the enrichment microfluidic is typically the only step that the chip performs with the requirement that the cells be off-loaded for further processing. Thus, there is a need for process step integration so that all of the necessary assay steps can be performed without requiring operator intervention to obviate issues associated with sample loss and contamination as well as minimizing the need for highly trained operators. Integration of microfluidic devices to form lab-on-a-chip systems is an attractive approach to address the aforementioned issues.

Integrated microfluidic systems can be broadly categorized into centrifugal, monolithic, and modular systems. Centrifugal systems consist of a compact disk like format with fluidic channels and chambers that uses centrifugal forces to manipulate fluids.[17-22] Potential challenges are related to complex fabrication methods,[23] and limited space that restricts the number and type of operational steps that can be integrated into the system.[24-25] In a monolithic configuration, multiple functional units are situated on a single wafer.[26-29] Therefore, modifications or changes in the processing steps require redesigning the entire system, which can increase cost and limit the application portfolio of the system.[30] A modular configuration consists of a set of task-specific modules integrated together using a fluidic motherboard.[31-38] The ability to be reconfigured along with reduced sample-processing time, low-cost, and portability have made modular microfluidic systems attractive for clinical assays, such as those targeted for liquid biopsies.[37]

We report a system modularity chip for the analysis of rare targets – SMART-Chip – which contained three task-specific modules connected to a fluidic motherboard that can be used for the comprehensive analysis of liquid biopsies secured from clinical samples using CTCs as an example. Three task-specific modules were incorporated into the system and consisted of a CTC enrichment module, impedance module, and imaging module. The SMART-Chip could perform the following steps: (i) Process a clinical sample for the surface affinity selection of CTCs, but enrichment modules for cfDNA[39]or EVs[40] can be envisioned as well; (ii) release the enriched biomarkers rapidly using a photocleavable (PC) linker;[41] (iii) count the released cells using a label-free impedance sensor that also determined cell viability; and (iv) immunophenotype the enriched CTCs.[42]

The CTC enrichment module consisted of an array of high aspect ratio sinusoidally-shaped microchannels arranged in a z-configuration.[43] Due to the sinusoidal shape of the selection channels and their dimensions, high cell recovery (>90%) has been reported with exquisite purity (>85%).[44] The impedance module counted unlabeled single cells passing through a pair of

orthogonally positioned electrodes with respect to the microfluidic channel while being able to assess their viability based on the polarity of the impedance signal. The imaging module was used to physically trap the enriched cells against pore structures, stain, and image the cells for phenotypic identification.[42] The modules were connected to a fluidic motherboard with interconnects while valving structures present on the motherboard were programmed to direct the fluids precisely through the microchannels to automate sample processing.

We previously reported a microfluidic system for the enrichment of CTCs directly from a patient's blood sample and their subsequent immunophenotyping.[45] In that example, a series of microfluidic chips were connected in series via capillary tubing, which required plugging/unplugging different units during the assay that significantly complicated system operation. This was obviated in the present report by using membrane-based valving structures on a fluidic motherboard to control fluidic operation and thus, minimize the need for operator intervention during the assay.

To establish proof-of-concept of the SMART-Chip, healthy donor blood spiked with cancer cells (SKBR3) were analyzed by the system. Clinical validation of the system was performed by processing blood samples obtained from colorectal cancer (CRC) and pancreatic ductal adenocarcinoma (PDAC) patients. The SMART-Chip enabled rapid enrichment and post-enrichment analysis in a closed environment to minimize sample loss and contamination with no operator intervention required except of sample addition to the SMART-Chip. Moreover, the SMART-Chip was made using thermoplastics via micro-replication. Thus, the system is inexpensive and can be mass produced with high compliancy,[46] making it appropriate for one-time use applications as required for *in vitro* diagnostics. An additional benefit of the modular system we report herein is that the individual modules can also be used as standalone units. Finally, different modules can be connected to the fluidic motherboard to increase the number of applications in which the SMART-Chip can be used.

3.2 Experimental

3.2.1 **Reagents and materials**

COC (cyclic olefin copolymer) substrates (6013S-04) and COC cover plates (5013S-04, 250 µm) were purchased from TOPAS advanced polymers GmbH (Germany). Poly(methyl methacrylate), PMMA, substrates were obtained from SABIC polymershapes (Raleigh, NC) and cover plates (250 µm) were purchased from Goodfellow (Oakdale, PA). Pt wires (75 µm diameter) were secured from Sigma Aldrich (St. Louis, MO) and gold-plated electrical contacts (09670008576) were purchased from Harting (Germany). PEEK tubing was obtained from IDEX Health & Science (Oak Harbor, WA). PEEK tubing interfaced to the motherboard were connected to syringe pumps (New Era, Farmingdale, NY) using Inner-Lok™ union capillary connectors (Polymicro Technologies) and barbed socket Luer Lock™ fittings (3/32″ ID, McMaster-Carr). Solenoid valves (M1533724VDC) and a 12-station manifold (150M12) were purchased from Humphrey Products (Kalamazoo, MI) and PDMS membranes (HT6240, 250 µm) were secured from Standard Rubber Products Co. (Elk Grove Village, IL).

Chemical reagents used in this study included: Micro 90® (Cole-Palmer, Vernon Hills, IL), isopropyl alcohol (IPA), 1-ethyl-3-[3- dimethylaminopropyl] carbodiimide hydrochloride (EDC), N-hydroxysuccinimide (NHS), anhydrous acetonitrile (ACN), anhydrous triethyl amine (TEA; Sigma-Aldrich), phosphate buffered saline (PBS, pH 7.4), bovine serum albumin (BSA), 2-(4-morpholino)-ethane sulfonic acid (MES), nuclease free water (Fisher Scientific), and 1 M Tris pH 7.4 (KD Medical, Inc, Columbia, MD). Tris-glycine (TG) pH 8.3 was obtained from Bio-Rad (Hercules, CA). Hoechst 33342 and LIVE/DEAD™ Cell Imaging Kit were secured from Life Technologies.

The SKBR3 cell line was obtained from the American Type Culture Collection (ATCC). Culture reagents included fetal bovine serum (FBS, Performance, Gibco), McCoy's 5A (Corning), Trypsin (Sigma-Aldrich), and 25 cm^2 tissue culture flasks (Fisher Scientific). Mouse anti-human

EpCAM/TROP-1 (clone 158210, 1 mg/mL), human EpCAM/TROP1 Alexa Fluor® 488-conjugated antibody (clone 158206), Mouse IgG 2B Alexa Fluor® 488-conjugated Isotype control (clone 133303) were from R&D Systems. Anti-CD45-FITC (Clone 2D1, 0.2 mg/mL) was purchased from eBiosciences (San Diego, CA) and Anti-Pan-Cytokeratin-Cy3 antibody (clone AE1/AE3, 0.2 mg/mL) was from Affymetrix Inc. (San Diego, CA). Blocking and washing buffers were filtered (0.2 µm, PTFE, Fisher Scientific) just prior to use.

3.2.2 **Cell culture and antigen expression analysis**

SKBR3 cells were cultured in 1×Mccoy's 5A supplemented with 10% FBS at 37°C with 5% atmospheric CO_2. The cells were detached using trypsin, centrifuged at 300 g for 5 min and resuspended in ice cold PBS before use.

Cells were washed with ice cold PBS three times and conjugated primary antibody (Alexa Fluor 488, h-EpCAM) was added (5-10 µl/10^6 cells) to the suspension. The cell suspension was incubated in the dark for 30 min at room temperature following mixing. Unbound Abs were removed by washing the cells with 0.1% BSA/PBS three times. After each washing step, the cells were centrifuged (300 g, 5 min), removal of the supernatant, and resuspended in buffer. Cells were filtered using non-sterile CellTrics® filters (30 µm, Sysmex America, Inc, Lincolnshire, IL) and analyzed by flow cytometry (BD Accuri C6). Isotype Ab (Alexa Fluor 488, IgG 2B) was used as the control.

3.2.3 **Fabrication of the modules and fluidic motherboard**

The microfluidic components were manufactured via direct milling, hot embossing, and PDMS casting. The fluidic motherboard was directly milled in PMMA using a Kern Evo high-precision micromilling machine (Kern Microtechnik GmbH, Germany) and FeatureCAM was used for the CNC programming. The CTC selection module and impedance module were prepared by hot embossing. Metal masters for hot embossing were prepared by micromilling a brass plate using

high precision micromilling (KERN 44, KERN Micro- und Feinwerktechnik GmbH & Co.KG; Murnau, Germany) with carbide bits (Performance Micro Tool) and the hot embossing was performed with a HEX03 embossing machine (Jenoptik GmbH). Hot embossing of the CTC selection module was performed in COC at 155°C with a 30 kN force applied for 120 s. Hot embossing of the impedance module in PMMA was conducted at 140°C with a force of 20 kN applied for 630 s. Embossed modules were diced with a bandsaw and cleaned by rinsing with 10% micro 90, IPA, and nano-pure water, and finally dried at 60°C for 30 min. Cover plates (254 µm) were cut, cleaned, and dried.

3.2.3.1 CTC selection module

When assembling the CTC selection module, the cleaned modules and cover plates (COC) were exposed to UV/O_3 for 13 min (22 mW·cm^{-2}, λ = 254 nm) and then, the UV/O_3 exposed surface of the cover plate was placed on top of the hot embossed substrate. This assembly was placed between two borosilicate glass plates and clipped together followed by thermal fusion bonding at 134°C for 1 h.

3.2.3.2 Impedance module

This module was assembled by placing platinum (Pt) electrodes (d = 75 µm) into electrode holding channels embossed into the substrate and UV/O_3 irradiating the cover plate and substrate (PMMA) for 10 min (22 mW·cm^{-2}, λ = 254 nm) with the electrodes in place. The module was finally assembled by placing the cover plate on top of the microchannels and thermal fusion bonding at 101°C for 15 min.

3.2.3.3 Imaging module

Reliefs for casting the imaging module consisted of an SU-8 photoresist on a Si wafer support and prepared using standard lithographic procedures. Two optical masks were used for

fabrication of the dual height relief structures.[42] An approximately 4 µm thick layer of SU-8 2005 photoresist was spun onto a Si wafer and after pre-exposure baking at 95°C for 3 min, the photoresist was exposed to UV radiation (MA6/BA6 Mask Aligner, Karl Suss; Germany) through an optical mask to produce the structures that would ultimately define the CTC retaining pores. After a post exposure bake at 95°C for 3 min, a second layer of SU-8 2050, 65 µm thick, was spun onto the top of the first photoresist layer. Following a pre-exposure bake at 95°C for 10 min, the second layer of photoresist was exposed to UV radiation using a different photomask to produce structures that would ultimately become the inlet and outlet fluidic channels. Active alignment was used during the second exposure step in order to assure proper alignment between the two SU-8 layers. A post exposure bake was performed using a temperature ramping procedure (25°C - 95°C at 7°/min, 95°C for 6 min and 95°C - 25°C at 1°/min) to minimize thermal stress in the SU-8 structures and improve adhesion to the Si wafer. Microstructures were then developed using SU-8 developer to form reliefs for PDMS casting.

Sylgard 184 (Dow Corning) was used for the imaging module. Following the manufacturer's procedure, a mixture containing 10:1 (w/w) PDMS prepolymer and curing agent was thoroughly stirred and degassed under vacuum, poured over the SU-8 microstructures, and into a custom-built retaining reservoir and cured at 75°C for 5 h in a natural convection oven on a leveled platform. After removal from the casting master, single imaging modules were diced from the cast PDMS and inlet and outlet holes were punched into the substrate. The PDMS modules were then cleaned and dried and bonded to pre-cut glass slides following a 1 min exposure to O_2 plasma (90 W, 20 sccm O_2) in a reactor (Diener Electronic, GmbH + Co KG; Germany).

3.2.4 **Surface attachment of mAbs using photo-cleavable (PC) linkers**

PC linker and mAb immobilization were recently reported by our group.[41] Briefly, COC cell selection modules were UV/O_3 activated (22 mW·cm^{-2}, 13 min) and EDC (20 mg/mL) / NHS (2

mg/mL) treated for 25 min at room temperature using dry ACN. The solution was removed from the module by passing air, and PC linker (0.53 mM) dissolved in dry ACN and TEA was infused into the modules. After 2 h of incubation at room temperature, the solution was replaced by passing air through the module. Then, 100 mM Tris (pH 7.4) was introduced into the module and incubated for 30 min at room temperature. Next, Tris buffer was replaced by passing air and the EDC/NHS reaction was performed again. After incubation, the EDC/NHS solution was replaced with mAb (anti-EpCAM, 1 mg/mL) dissolved in PBS (pH 7.4) that was introduced into the module. The module was incubated for 2 h at room temperature or overnight at 4°C. Prior to sample infusion, the module was rinsed with 2 mL of 0.5% BSA/PBS at 50 µL/min to remove any unbound mAbs and minimize non-specific binding of sample components to the module's walls.

3.2.5 **Microfabrication of the membrane valve and characterization**

Fabrication of the membrane valves was reported previously.[47] Briefly, the fluidic microchannels and pneumatic control channels (w × h, 760 µm × 180 µm) were directly milled (Nomad 883, Torrance, CA) in two different PMMA substrates. The fluidic microchannel substrate also had the valve seats (400 µm) while the pneumatic control channels contained the displacement chambers (radius = 1400 µm). The two PMMA pieces were cleaned and dried. Channel measurements were made by using a VK-X 3D laser scanning confocal microscope (Keyence). The PMMA substrate with the fluidic microchannels and PDMS membrane (HT6240, 250 µm) were UV/O_3 treated (22 mW·cm^{-2}) for 10 min. Next, the UV/O_3 exposed surfaces of the PDMS membrane was placed on top of the UV/O_3 exposed PMMA fluidic microchannel surface and they were conformally bonded together. The PMMA/PDMS assembly was again UV/O_3 activated for 10 min along with the pneumatic control PMMA layer. The pneumatic control layer was placed on top of the PDMS membrane and pressure was applied (165 psi) using a PHI Precision Press (TS-21-H-C (4A)-5, City of Industry, CA) after properly aligning the fluidic and pneumatic control layers. PEEK tubing (1/16") was attached to make the final device.

Valve characterization was accomplished by measuring the outlet flow rate by varying forward fluidic pressures at valve-open and valve-closed states. The inlet of the valve was connected to a pressure sensor (15 psi) and to a fluidic channel (dye solution), which was connected to a compressed N_2 gas tank. The flow rate was measured by weighing the amount of dye solution flowed through the device in a given time interval. Valve operation was controlled by providing a vacuum (to open the valve) or pressure (to close the valve) through the pneumatic control layer. Flow rates were measured at valve-open states (-50 kPa valve open pressure) and two valve-closed states (25 kPa or 35 kPa valve closing pressures).

3.2.6 **Relationship between impedance signal polarity and cell viability**

SKBR3 cells were suspended in 1× TG buffer and incubated for 1 h at room temperature. The cells were hydrodynamically introduced into the impedance module at 30 µl/min (200 µl) while recording the impedance signals. The cells flown through the impedance module were collected into a 96 well plate and centrifuged at 300 g for 5 min. The supernatant was removed and ice-cold PBS was added. The cells were stained using a Live/dead cell kit (Life Technologies) and incubated for 15 min at room temperature. Cells were observed using a Zeiss Axiovert 200 M microscope with a 10X objective (0.3 NA, Plan NeoFluar), an XBO 75 W lamp, FITC and Cy3 filter set (Omega Optical), a Cascade 1K EMCCD camera (Photometrics), and a MAC 5000 stage (Ludl Electronic Products). All of the microscope components were computer-controlled via Micro-Manager. Calcein and Ethidium homodimer stained cells were counted and compared with the impedance signals.

3.2.7 **Cell retention in imaging module**

SKBR3 cells were stained with Calcein and incubated at room temperature for 15 min. Imaging modules that had 7,200 pores (4, 6 and 8 µm pore size) were rinsed with 0.5%BSA/PBS at 20 µL/min (500 µL). Cells were diluted (~2 cells/µL) with PBS and hydrodynamically introduced

into the imaging module at 20 µL/min (100 µL) while collecting the effluent into a 96 well plate. The imaging module was rinsed with 0.5%BSA/PBS at 20 µL/min (100 µL) while collecting the washing buffer into the same well and observed using a Zeiss Axiovert 200 M microscope using the FITC filter cube of the epifluorescence microscope. The cells retained in the imaging module and 96 well plate were then counted.

3.2.8 **SMART-Chip assembly**

The motherboard was fabricated in three layers and consisted of a fluidic layer, pneumatic control layer (both of these layers were made in PMMA) and a membrane layer consisting of a PDMS elastomer. The fluidic layer contained the fluidic network and valve seats (11 total valves in the system) as well as conical connecting ports for the 3 modules. The pneumatic control layer also contained displacement chambers. The elastomeric PDMS membrane layer was placed between the two PMMA substrates (see **Figure 3.1A**). Conical ports (top diameter = 1.706 mm, bottom diameter = 1.444 mm, depth = 2.2 mm) were milled from the back of the PMMA fluidic layer using a 3° bit (d = 0.045”). These ports were used to connect individual modules to the motherboard. After direct milling of the required structures in the PMMA layers, the substrates were cleaned with 10% micro 90, IPA, and nanopure water and finally dried with N_2. The PMMA fluidic layer and PDMS membrane were UV/O_3 activated (22 mW·cm^{-2}) for 10 min and the activated surface of the PDMS membrane was placed across the PMMA fluidic layer. This PMMA/PDMS assembly was then UV/O_3 modified and aligned to the UV/O_3 activated PMMA pneumatic control layer. The PMMA/PDMS/PMMA assembly was then subjected to pressure (165 psi) using a PHI Precision Press (model TS-21-H-C (4A)-5, City of Industry, CA) to facilitate compression bonding between the three layers (**Figure 3.1B**).

The CTC selection module, impedance module, and imaging module were connected to the motherboard (see **Figure 3.1C**) using semi-rigid Tefzel™ tubing.[35] PEEK tubing (OD = 1/32” and

1/16") was then connected to the motherboard as fluidic and pneumatic inputs, respectively. PEEK tubing (OD 1/16") from the motherboard was connected to a solenoid control system (SCS) using polyethylene tubing. The SCS contained 11 solenoids (3/2way, Humphrey, M1533724VDC) connected to a manifold (Humphrey, 150M12) and the manifold was connected to a pressure and vacuum source. Individual solenoids were connected to controller hardware (Instrumental Design Lab, KU) using 2-pin Molex C-GRID connectors. The controller hardware was interfaced to controlling software using a virtual serial port connected to a computer via a USB cable. Valve operation was controlled by graphical user interface software developed via Visual studio.

3.2.9 **Device validation using SKBR3 cells as CTC surrogates**

Healthy blood samples were provided by the Biospecimen Repository Core Facility (BRCF) at KU Cancer Center under an IRB approved protocol (HSC #5929). SKBR3 cells were stained with a nuclear stain, Hoechst 33342 (DAPI, 40 µg/mL), and incubated for 15 min at room temperature. Modules were connected to the motherboard and the SMART-Chip was washed with 0.5% BSA/PBS (0.1 mL, 20 µL/min) prior to blood infusion. Stained cells were spiked into healthy blood and hydrodynamically introduced (1 mL, 25 µL/min) into the CTC selection module that was surface decorated with anti-EpCAM monoclonal antibodies via a photocleavable (PC) linker.[41] Following blood infusion, the module was rinsed with 1 mL of 0.5% BSA/PBS (50 µL/min) to remove any non-specifically bound material. Next, 1× Tris Glycine (TG) buffer (pH 8.3, 0.1 mL) was infused into the cell selection module at 20 µL/min. Blood and the wash buffers were directed to waste using the appropriate open/closed status of the PDMS membrane valves. The CTC selection module was exposed to blue light (34 ±4 mW/cm^2, 400 – 450 nm) for 2 min (18.5 J) to release the affinity selected SKBR3 cells and swept into subsequent modules using the appropriate open/closed status of the on-system membrane valves.

Following blue-light exposure, released cells were swept through the impedance module generating an electrical signal based on cell membrane integrity. Impedance signatures were counted when the signal-to-noise ratio exceeded 7 and cell viability was determined by the polarity of the impedance signal. The data was acquired and processed using in-house built electronics.[44]

After the impedance module, the enriched cells were directed into the imaging module where they were physically trapped against pore structures. Trapped cells were stained using different fluorescently labeled markers as reported previously.[45] Briefly, the imaging module was flooded (20 µL/ min) with 0.5% BSA/PBS (0.1 mL) to replace the TG buffer used for impedance counting of the enriched cells. Anti-human CD45-FITC (2.5 µg/mL, 0.1 mL) was introduced into the device (10 µL/min) and incubated for 15 min. After washing with 0.5% BSA/PBS, 2% PFA/PBS (0.1 mL) was infused (15 µL/min) through the device and incubated for 10 min to allow for cell fixation. Then, the cells were permeabilized by introducing 0.1 mL of 0.1% Triton X-100/PBS (15 µL/min). The imaging module was then rinsed with 0.5% BSA/PBS (0.1 mL, 20 µL/min). Anti-pan-cytokeratin-Cy3 antibodies (5 µg/mL, 0.1 mL) were infused (10 µL/min) into the imaging module and incubated for 30 min. The module was finally rinsed with 0.5% BSA/PBS (0.1 mL, 20 µL/min) prior to imaging.

The stained cells were imaged using a Keyence BZ-X710 microscope (Keyence Corporation, Itasca, IL, USA) equipped with BZ-X filters. Images were collected with 20X and 40X objectives using exposure times of 50 ms for DAPI (nuclear stain), 500 ms for FITC (CD45) and 1500 ms for Cy3 (cytokeratins). Images were analyzed using a BZ-X analyzer (Keyence Corporation).

3.2.10 **Processing patients blood samples**

Patient samples were secured from KUMC according to the institution's IRB protocol. Written informed consent was obtained from the patient before enrollment. Blood samples were

collected into Vacuette® K3EDTA (Greiner) tubes containing the anticoagulant EDTA and 50 µg/mL eptifibatide[48] and processed in the SMART-Chip on the second day after blood withdrawal.

3.3 Results and Discussion

A picture of the SMART-Chip is shown in **Figure 3.1**. It contains three task-specific modules that affinity selected CTCs using antibodies attached to the walls of the sinusoidal channels via a PC linker and their subsequent release from the capture surface using blue light, single-cell impedance sensing, and immunophenotyping. The imaging module was made from PDMS via soft lithography and covered with a thin glass plate. The other two modules were made from a thermoplastic. The CTC selection module was made from COC, because COC offers high loading of antibodies following UV/O_3 activation of the COC that results in high target cell recovery.[43] The impedance module was made from PMMA, but could have been made from any thermoplastic. Both modules were produced via hot embossing. The fluidic motherboard was made from PMMA by direct high precision micro-milling the fluidic and pneumatic control channels into the substrate. In the following sections, a description of the design and performance of the fluidic motherboard and task-specific modules are provided.

3.3.1 **Fluidic motherboard**

The fluidic motherboard performed the following functions: (i) Serve as a structural element to which all task-specific modules were connected; (ii) a path for transferring fluidic information to the task-specific modules; (iii) ports for sample and reagent introduction; and (iv) valving for precise directional fluid flow through the integrated system during the assay.

The fluidic motherboard consisted of three layers (**Figure 3.1A**). The fluidic network layer (i) was made from PMMA (3 mm thick) and also contained the valve seats. The pneumatic layer (iii), which was also made from PMMA, contained control lines and displacement chambers for valve

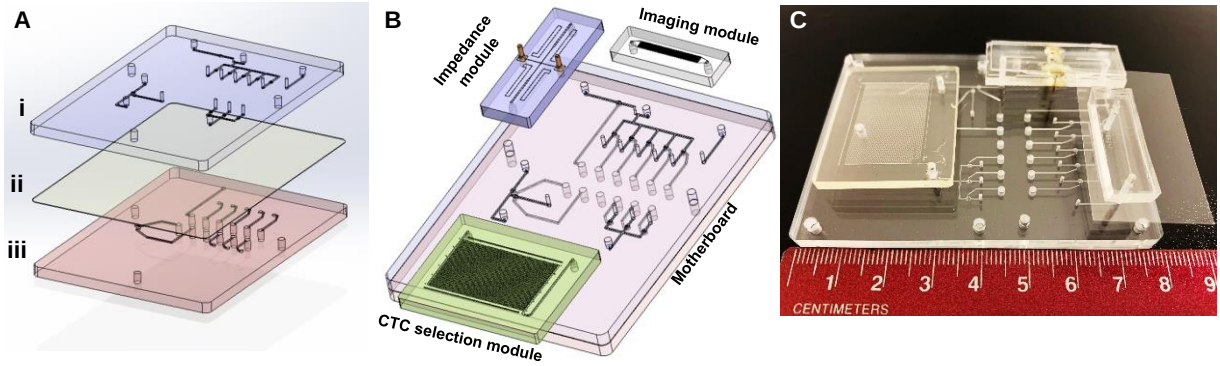

Figure 3.1. The design and assembly of the SMART-Chip. (**A**) Both sides of a PDMS membrane layer (ii) and PMMA layers that contained micro-features (i – fluidic layer and iii – pneumatic control layer) were UV/O_3 treated for 10 min (22 mW/cm^2). The PDMS membrane was sandwiched between the two PMMA layers. The micro-features (valve seats and displacement chambers) were aligned, and pressure (165 psi) was applied to conformally seal the three layers that comprised the motherboard. (**B**) 3D image of three task specific modules (CTC selection module, impedance module and imaging module) interfaced to the fluidic motherboard. (**C**) Picture of the fully assembled SMART-Chip including the 3 task-specific modules that were integrated to the motherboard using Tefzel™ tubing. (Reprinted with permission from (https://doi.org/10.1021/acssensors.0c02728). Copyright (2021) American Chemical Society)

actuation. Finally, the middle layer (ii) was made from a PDMS elastomer and served as the membrane (250 µm thick) for the 11 valves situated on the motherboard. The three layers were assembled after modifying their surfaces with UV/O_3.[47] The UV/O_3 activation caused photo-oxidation of the PMMA and PDMS resulting in a hydrophilic surface. Thus, the three layers were bonded together non-covalently.

Modules were connected to the fluidic motherboard (**Figure 3.1B-C**) using interconnects,[35] which consisted of conical receiving ports in the motherboard and modules (**Figure 3.2A-B**) and a small piece of Tefzel™ tubing. The receiving ports were milled into the motherboard from its top side and was hot embossed into the modules. The conical receiving ports had a top diameter of 1.70 mm, bottom diameter of 1.44 mm, and depth of 2.2 mm (**Figure 3.2B**). Assembly involved inserting the Tefzel™ tubes into the receiving ports on the motherboard, aligning the module, and pressing the two parts together (**Figure 3.2C**). During the compression step, the semi-rigid connecting tube conformed to the conically shaped ports and provided a tight seal with minimal unswept volume (measured value ~20 nL, which was <1% of the total interconnect volume).[34]

Permanent connection between the two pieces was provided by using an adhesive (**Figure 3.2D**). We successfully tested these interconnects to pressures up to 3 MPa without leakage. This type of interconnect is also self-aligning and did not require additional alignment features for proper placement of the modules on the motherboard, which simplified cartridge design and facilitated assembly.

The top side of the motherboard contained ports for connection of the motherboard to syringe

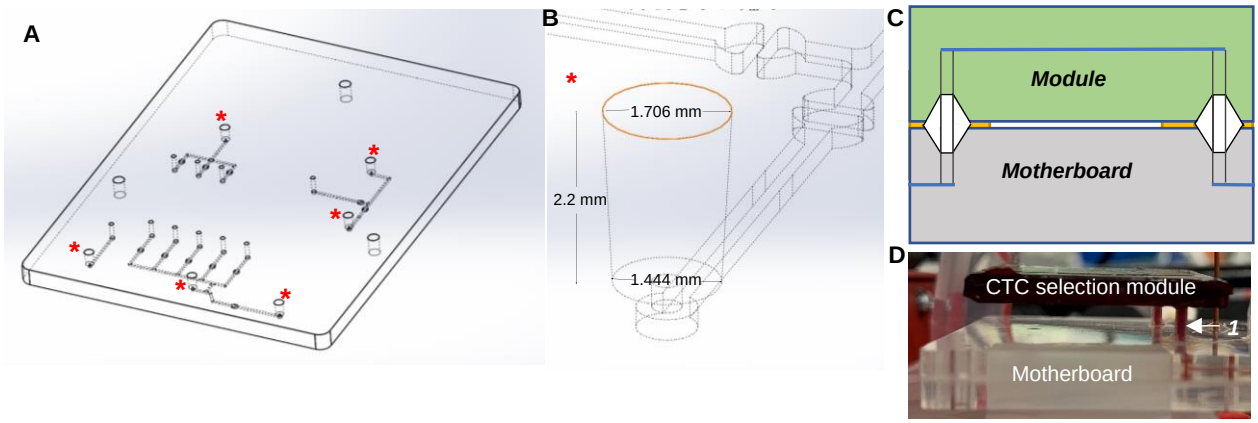

Figure 3.2. Task-specific module integration to the fluidic motherboard. (**A**) Conical receiving ports were milled from the back of the fluidic channel layer of the motherboard, where individual modules were connected (* marks the position of these ports on the motherboard). (**B**) The conical port had a top diameter of 1.706 mm and bottom diameter of 1.444 mm. Port depth was 2.2 mm for a 3.175 mm (1/8") thick substrate. (**C**) Schematic representation of fluidic interconnects for attaching modules to the motherboard. Conical receiving ports were molded into the modules. (**D**) Semi-rigid Tefzel™ tubing (1) was permanently bonded with an adhesive to make a leak-free connection with minimal unswept volume. The image was taken when processing a blood sample through the system. (Reprinted with permission from (https://doi.org/10.1021/acssensors.0c02728). Copyright (2021) American Chemical Society)

pumps for fluidic operation. The bottom side of the motherboard also contained ports for tubing that connected the motherboard to the solenoids, which served to activate the valves and used a computer-controlled solenoid system. The valves incorporated into the SMART-Chip were normally closed and we could also apply additional pneumatic closing pressure to keep the valve closed under high volume flow rates.[47] Applying vacuum to the control layer changed the position of the PDMS membrane to open the valve (**Figure 3.3A**). We prepared a single valve unit (**Figure 3.3B**) using direct milling into a PMMA substrate and evaluated its performance by measuring the outlet flow rate at different forward pressures. Different forward pressures were provided by

connecting the valve inlet to a gas tank and then monitoring flow through the valve using a dye-seeded solution (**Figure 3.3C**). The valve was operated under two different pneumatic closing pressures, 25 kPa and 35 kPa. At 25 kPa pneumatic closing pressure, the valve was able to impede the fluid passage until the forward fluidic pressure reached 40 kPa (**Figure 3.3D**). At 35 kPa pneumatic closing pressure, the valve was able to hold the forward fluidic pressure up to 60 kPa without leakage (**Figure 3.3E**).

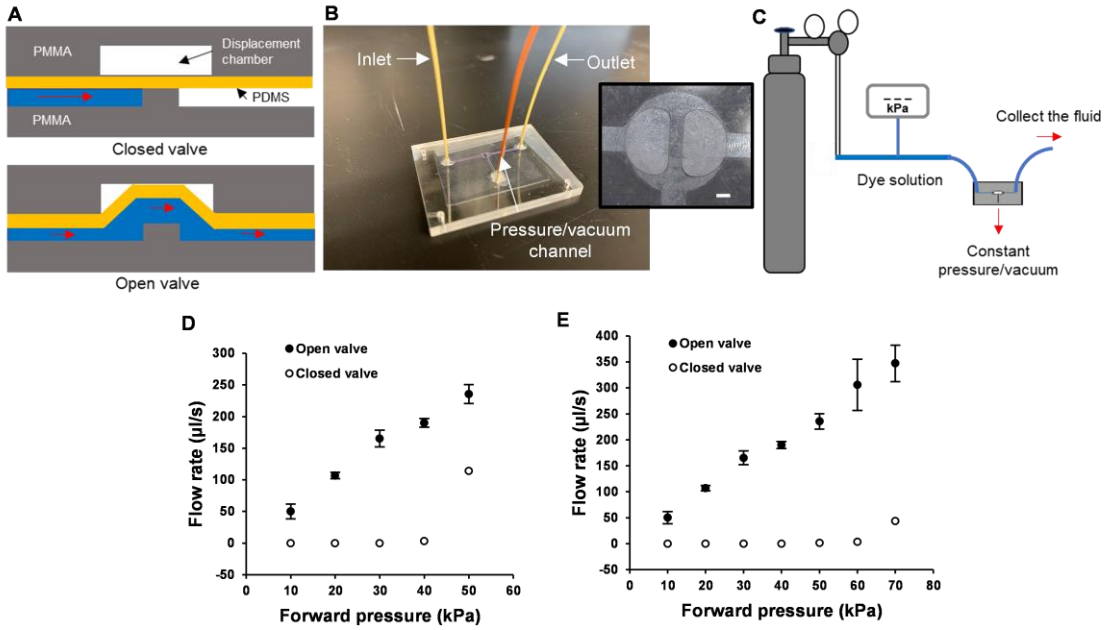

Figure 3.3. PMMA/PDMS/PMMA valve characterization. **(A)** The valve was normally closed. It was assembled by placing a UV/O_3 treated PDMS membrane (254 µm) between two UV/O_3 treated PMMA substrates that had fluidic and pneumatic channels. The valve can be opened by applying a vacuum through the pneumatic layer. **(B)** Pressure was applied to three layers to facilitate bonding and PEEK tubing was attached to make the final valve assembly. The scale bar is equivalent to 400 µm. (**C**) Schematic diagram of the valve characterization setup. The inlet of the valve was connected to a gas tank (N_2) via a dye solution filled tube and a pressure sensor. Outlet flow rate was measured by providing different forward pressures with a constant pressure (close-valve) or vacuum (open-valve) applied through the pneumatic control channels. **(D)** At 25 kPa pneumatic pressure (closed valve), the valve started leaking at 40 kPa forward pressure (n = 3). **(E)** When the pneumatic pressure was increased up to 35 kPa (closed valve), the valve started leaking at 60 kPa forward pressure (n = 3). (Reprinted with permission from (**https://doi.org/10.1021/acssensors.0c02728**). Copyright (2021) American Chemical Society)

3.3.2 **CTC selection module**

People have developed different microfluidic devices for the affinity selection of CTCs. Silicone CTC chip,[49] GEDI device,[50] herringbone chip,[51] silicone nano pillar chip[52] are few of them. Poor

purities associated with these methods are problematic especially in assays that analyzing the genomic material.

The CTC selection module that we used in this study has been reported previously by our group and consists of an array of sinusoidal microchannels (150 μm depth; 25 μm width, 30 mm length, aspect ratio = 6) that can process whole blood with a throughput of 1.5 mL/h using the 50 channel version (**Figure 3.4A**).[44] However, we have also made a 320-channel version of this device, which can process ~10 mL of whole blood in 1 h.[45] The attractive nature of this design is that it can process whole blood directly yielding high recovery of CTCs with high purity.[43] The sinusoidal channel geometry and channel width was found to maximize CTC recovery compared to a straight channel with the same effective length.[43] The selection module was hot embossed in COC because this material has excellent optical properties that enables efficient UV/O_3 activation of the high aspect ratio microchannels for high loads of antibody onto the activated channels using the PC linker[43] as well as high transmissivity in the blue region of the electromagnetic spectrum to allow for efficient CTC release.[41]

An array of 50 sinusoidal microchannels were organized in the so-called z-configuration. In this arrangement, inlet and outlet channels were positioned orthogonal to the sinusoidal microchannel array. We have demonstrated that uniform translational velocity in the sinusoidal channels is required for high CTC recovery because the cell velocity must be close to an optimal value based on the binding kinetics of the antigen/antibody pair as well as the delivery rate of CTCs to the surface-bound antibodies.[44, 53] Uniformity of the flow depends upon the proper design of the inlet/outlet channels (**Figure 3.4B**).[54] COMSOL simulations showed that tapered inlet/outlet channels provided uniform cell translational velocity within the sinusoidal channels compared to non-tapered inlet/outlet channels even for devices with >250 channels.[55]

COMSOL simulations showed that a cell travelling close to the channel wall had a reduced linear velocity as compared to distances further from the wall due to fully developed laminar flow (**Figure 3.4C**), which increased the probability of antigen-antibody interaction. The centrifugal force acting on a 16 µm diameter cell at a velocity of 3 mm/s, travelling through a curvilinear channel having a radius of curvature of 125 µm (at the midline) was calculated to be 0.162 pN.[55] Even such a small centrifugal force caused the cell to be pushed towards the wall, which would increase its interaction probability with the surface-bound capture antibodies. Moreover, as the cell travels through alternating curves, the net centrifugal force acting on the translating cell resulted in a net centrifugal force being directed toward the channel walls. However, the lift forces generated by the channel walls directed the cells away from the wall. The two opposing forces, centrifugal and lift forces, resulted in a net drift toward the sinusoidal channel wall due to the higher centrifugal force created by the sinusoidal channel geometry (**Figure 3.4D**).

CTCs are affinity selected using the appropriate antibody, such as anti-EpCAM antibodies. UV/O_3 treatment can generate surface-confined carboxylic acid groups that can be subsequently reacted with primary amine containing entities using an EDC/NHS reaction. This generates a highly stable amide bond between the surface and amine-containing entities.[56-57] We utilized EDC/NHS chemistry to covalently attach antibodies to the CTC selection module's surfaces using a Coumarin-based heterobifunctional PC linker (**Figure 3.4E**). The anti-EpCAM-PC linker strategy can select CTCs with high recovery (>95% for MCF-7 cells) and high purity (>85%).[3, 44] The affinity-selected CTCs were released for downstream analysis rapidly (2 min) and efficiently (>90%) by exposing the selection module to blue light (λ_{max} = 412 nm, 32 ±4 mW cm^{-2}).[41] Visible

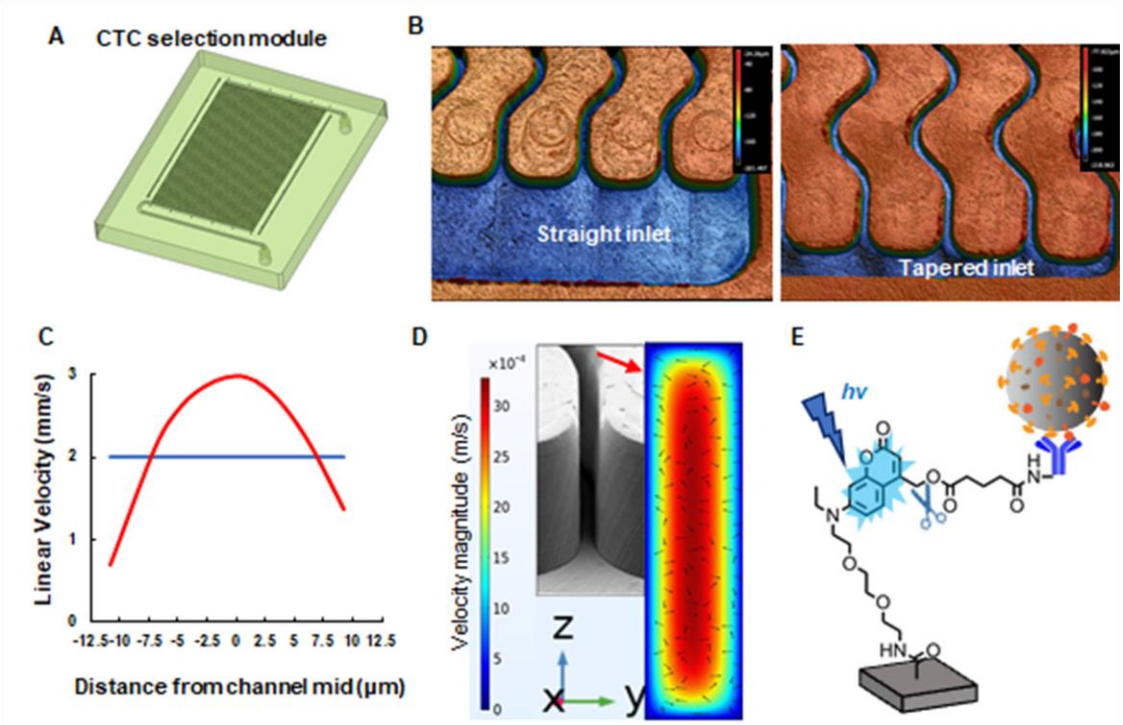

Figure 3.4. CTC selection module with high aspect ratio sinusoidal microchannels (aspect ratio = 6). **(A)** 3D design of the CTC selection module, which had 50 sinusoidal microchannels that were 150 μm deep and 25 μm wide. The effective length of the selection channels were 3 cm. (**B**) 3D images of straight and tapered geometries for the inlet/outlet channels. The inlet/outlet channels were positioned orthogonal to the sinusoidal channel array (z-configuration). These images were acquired using a rapid scanning confocal microscope (Keyence). (**C**) COMSOL simulation of the average particle velocity (n = 10) in one sinusoidal channel over a distance of 1 cm. Particles were given an initial velocity of 2 mm/s (blue line), and as they travelled through the selection channel their velocities changed with respect to the distance from the wall (red line). **(D)** COMSOL simulation with arrows indicating the direction and velocity magnitude of the fluid in the selection channel. As the fluid travels through the sinusoid apex, the fluid is directed toward both the inner and outer walls of the channel increasing the probability of antigen/antibody interaction. The arrows show the velocity profile in the yz direction. (COMSOL simulations – Swarnagowri Vaidyanathan) (**E**) Coumarin-based photocleavable linker that was used to immobilize antibodies to the cell selection module's surface. After the affinity selection of the CTCs, the PC linker was exposed to blue light (400-450 nm) to cleave the linker and release the antibody-CTC complex from the module's wall. (Reprinted with permission from (**https://doi.org/10.1021/acssensors.0c02728**). Copyright (2021) American Chemical Society)

blue light as opposed to UV-light was used to minimize any damage to the nucleic acids contained within a CTC.[58-59]

3.3.3 **Impedance sensor module**

Impedance sensing can be used as a label-free strategy for the detection of single cells with high efficiency.[44] The impedance sensor module consisted of a single fluidic channel (75 μm

depth, 50 µm width and 1 cm in length) and two Pt electrodes placed into microchannels (75 µm depth, 80 µm width and 0.8 cm length) positioned orthogonally to the fluidic channel (**Figure 3.5A**). A pair of Pt electrodes (~75 µm diameter) were inserted into the electrode microchannels and then a cover plate was thermally fusion bonded to the substrate containing the two electrodes, which allowed the plastic to seal around the electrodes resulting in no leakage. Single cells were then hydrodynamically flowed past the electrode pair that had imposed on it a voltage waveform with a characteristic frequency, in our case 40 kHz. Electrical contacts connected to the Pt electrodes shuttled the electrical signals to the detector electronics. At low waveform frequencies (<100 kHz), cells are treated as insulating particles due to high cell membrane resistance and a signal produced by the passage of an intact cell through the detector can be expressed as;[60-61]

$$\Delta R = (\rho_c\text{-}\rho_m)\frac{\pi d^3{}_c}{4A^2{}_{el}}$$

where ΔR is the change in resistance between the electrode pair, ρ_c is the resistivity of the cell, ρ_m is the resistivity of the medium, d_c is the cell diameter, and A_{el} is the area of the electrodes. The signal measured by the impedance sensor is proportional to the resistance of the medium between the pair of electrodes. When no cell was present between the electrodes, the signal was proportional to the resistance of the buffer, which defines the baseline for the measurements. Every cell that has an intact cell membrane and passing between the electrodes displaces a finite volume of the buffer solution. The volume displaced by a cell, which has an intact cell membrane, has a higher resistance than the corresponding volume of the buffer alone producing a positive impedance signal in our case. When the cell membrane was compromised, the internal

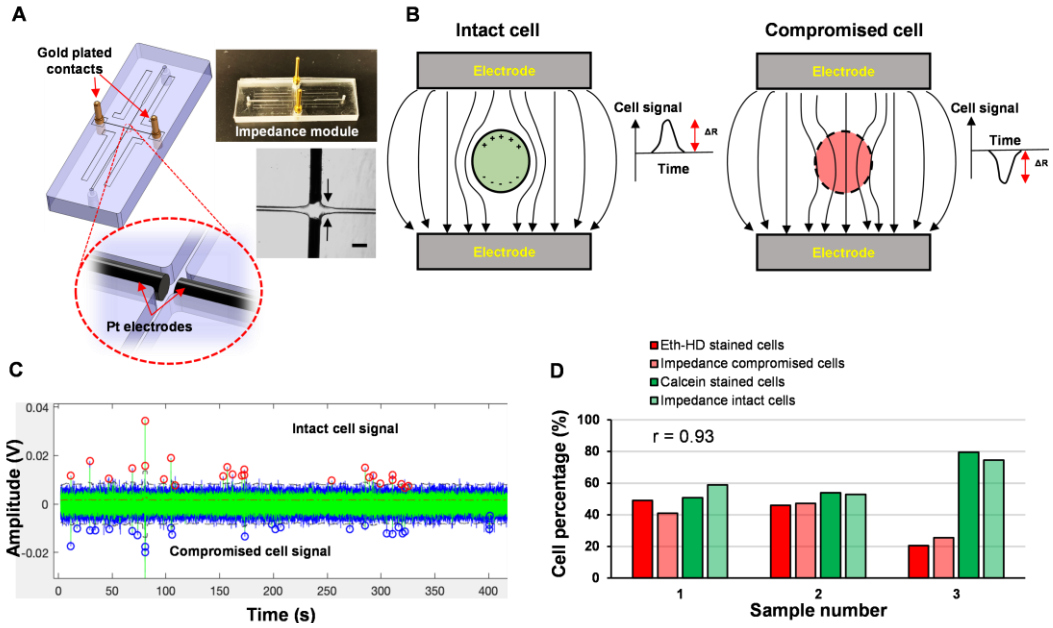

Figure 3.5. Impedance module and single cell impedance sensing. **(A)** Impedance module with Pt electrodes and gold-plated electrical contacts. Pt electrodes were situated orthogonal to the fluidic channel with an ~50 µm distance. The scale bar is equivalent to 100 µm. **(B)** Cells with an intact membrane have a higher resistance (R_{cell}) than the buffer (R_{sol}) and $\Delta R > 0$ and the detector produced a positive signal. When the membrane was compromised, $R_{cell} < R_{sol}$, making $\Delta R < 0$. This gave a negative polarity signal. **(C)** SKBR3 cells that had an intact cell membrane gave positive polarity impedance signals (red circles) while compromised cells yielded negative polarity signals (blue circles). **(D)** Cells recovered after the impedance sensing were subjected to Eth-HD1 and Calcein-AM staining. The results were compared to the impedance signals for compromised and intact cells. Strong correlation (r = 0.93) was observed between the two methods. The impedance traces were collected for cells suspended in 1× TG buffer (pH 8.3). The measurements were recorded at a voltage waveform frequency of 40 KHz. (Reprinted with permission from (https://doi.org/10.1021/acssensors.0c02728). Copyright (2021) American Chemical Society)

composition of the cell contributes to a lower resistivity than the buffer alone. Thus, the impedance signal had a negative polarity (**Figure 3.5B**).

To verify that the polarity of the impedance signal was indicative of membrane integrity, freshly harvested SKBR3 cells were suspended in 1× TG buffer. Cells were flowed through the impedance module while recording the electrical signal (**Figure 3.5C**). The cells were recovered following their passage through the impedance module and their viability was evaluated using well-known cell viability fluorescent markers, ethidium homodimer 1 (Eth-HD1) and Calcein-AM. Eth-HD1 is membrane impermeable and stains the nucleus of cells only if they have a

compromised cell membrane. Calcein-AM is a membrane permeable dye that is hydrolyzed into fluorescent calcein by intracellular active esterases, which occurs in viable cells. The results obtained from the impedance sensing and staining methods were compared with the results shown in **Figure 3.5D**. The percentage of Eth-HD1 stained cells were similar to the percentage of impedance negative signals with a Pearson correlation of 0.93 (n = 3) and the percentage of calcein stained cells were similar to the percentage of impedance positive signals with a Pearson correlation of 0.93 (n = 3). A Pearson correlation of 0.99 (n = 3) was obtained between the impedance signals and the total number of cells analyzed. Due to this strong correlation, impedance sensing can be used as a label free strategy to count individual cells while at the same time assess their viability.

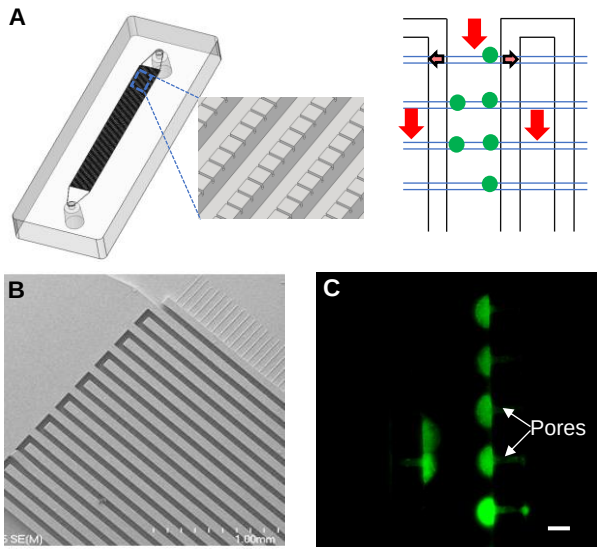

Figure 3.6. Imaging module. **(A)** 3D image of a single bed imaging module populated with cell retaining pores. Cell suspension coming from the inlet (red arrow) of the imaging module entered into the outlet channels through the pores (faded arrows) while trapping the cells at the inlet channels. **(B)** SEM image of lithographically patterned 2-level SU-8 mold for casting of PDMS to fabricate the imaging modules. **(C)** Isolation of live SKBR3 cells stained with calcein-AM with a flow rate of 20 µL/min using the imaging module with 4 µm x 3.5 µm pore structures. Cells were retained near the pore structures. The image was taken using a 40X microscope objective. Scale bar is 15 µm. (Reprinted with permission from (**https://doi.org/10.1021/acssensors.0c02728**). Copyright (2021) American Chemical Society)

3.3.4 **Imaging module**

The imaging module[42] was comprised of two interleaving feed channels interconnected using an array of smaller channels positioned orthogonal to the feed channels (**Figure 3.6A**). Once the glass cover slip was bonded to the PDMS substrate, the small cross channels and the glass cover slip produced containment pores that could "trap" cells larger than the pore size. PDMS and glass were selected to fabricate this module due to the low autofluorescence of glass and the simple O_2/plasma treatment that can be used to bond the glass cover slip to the PDMS substrate. CTCs released from the selection module travelled through the impedance sensing module and were directed into the imaging module. CTCs, which are larger than the pore sizes, were physically entrapped near the pores and could be stained (DAPI, CD45, and pan-cytokeratins) and immunophenotyped for identification of the CTCs. This unique architecture enabled simple and rapid immunophenotyping of CTCs because entrapped cells were located within a common imaging plane and found at specific locations (*i.e.,* near pore structures).

Imaging modules with 8 beds possessed 80,000 pores and has been reported previously for immunophenotyping and FISH analysis of cells enriched from leukemia and multiple myeloma diseases, but was used as a standalone unit.[42] Because the number of CTCs that can be affinity selected from an epithelial cancer is limited (1-1000 CTCs per mL), single bed imaging modules employing 2,400 and 7,200 containment pores **(Figure 3.7A)** were used in this study. Modules were produced in PDMS via casting from lithographically prepared Si wafers that had patterned on it SU-8 microstructures at two different levels (**Figure 3.6B**). After inlet/outlet holes were punched out, the PDMS substrate was permanently bonded to a glass cover slip after O_2/plasma treatment (90 W for 1 min) to form the enclosed imaging module, which could be interconnected to the fluidic motherboard.

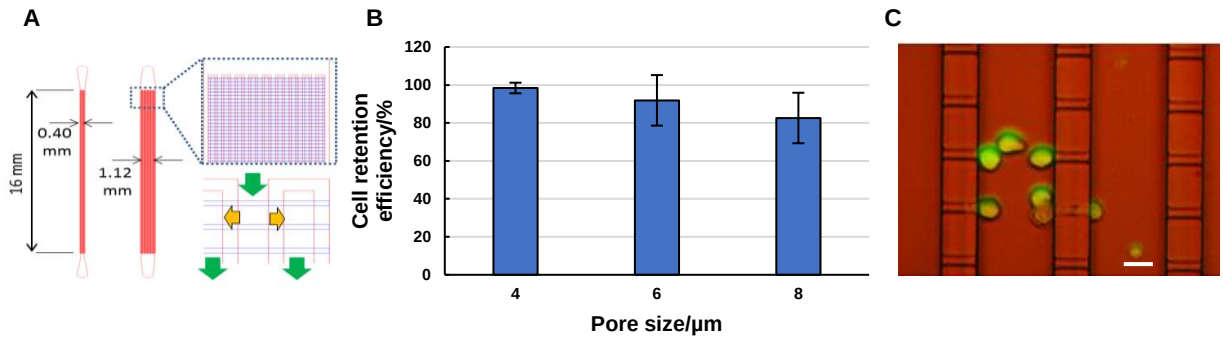

Figure 3.7. Efficiency of cell retention in the imaging module. **(A)** General design of the imaging module populated with 2,400 (narrow) and 7,200 (wide) cell retaining pores. **(B)** Cell retention efficiencies of 4, 6 and 8 μm pore sized imaging modules. Retention efficiencies were calculated using the number of cells retained in the imaging module and the number of cells in the effluent (n = 3). **(C)** SKBR3 cells passing through the 6 μm pore imaging module. The scale bar represents 15 μm. (Reprinted with permission from (https://doi.org/10.1021/acssensors.0c02728). Copyright (2021) American Chemical Society)

To establish the optimum design of the imaging module for CTC retention, we tested pore structures with 4, 6, or 8 μm widths and a fixed pore height of 3.5 μm at 20 μL/min flow rate. Live SKBR3 cells could be trapped by the pores of 4 μm width (**Figure 3.6C**) with an efficiency of 98.4 ±2.8% (n = 3). Six and 8 μm pore structures retained the live SKBR3 cells with an efficiency of 91.9 ±13.3% (n = 3) and 82.6 ±13.3 % (n = 3), respectively (**Figure 3.7B**). SKBR3 cells are ~12 μm in diameter[62] and the cells can escape from larger pores (8 and 6 μm, **Figure 3.7C**) due to the deformability of the cell caused by the fluidic pressure.[63]Due to the higher efficiency of CTC containment, we used a pore size of 4 μm for the imaging modules in this study. In our study, CTC affinity selection and CTC specific release provided highly purified CTC isolates in the imaging module (0-3 white blood cell contaminants in 2 mL of whole blood processed). Thus, the imaging module can be populated with pores of 4 μm in width to ensure retention of nearly all of the CTCs released from the CTC selection module, but at the same time eliminate possible interferences from white blood cells because they showed very poor containment at the 4 μm pore sizes (data not shown).

3.3.5 **Valve Control Steps**

Major valve control steps associated with the SMART-Chip when processing a liquid biopsy sample for CTCs are pictured in **Figure 3.8**. The liquid biopsy sample, in this case whole blood, entered into the cell isolation module with the effluent directed towards the waste reservoir (**Figure 3.8A**). BSA/PBS was then shuttled into the cell isolation module and finally towards the waste reservoir (**Figure 3.8B**). After the post selection wash, the cell isolation module was exposed to blue light, which photoreleased the enriched cells, and the released cells were directed through the impedance and imaging modules by hydrodynamically introducing Tris glycine buffer through the SMART-Chip (**Figure 3.8C**). The retained cells within the imaging module were then stained and immunophenotyped (**Figure 3.8D**). Valves were computed controlled to open/close appropriately during all of these processing steps for precise fluidic operation in an automated fashion.

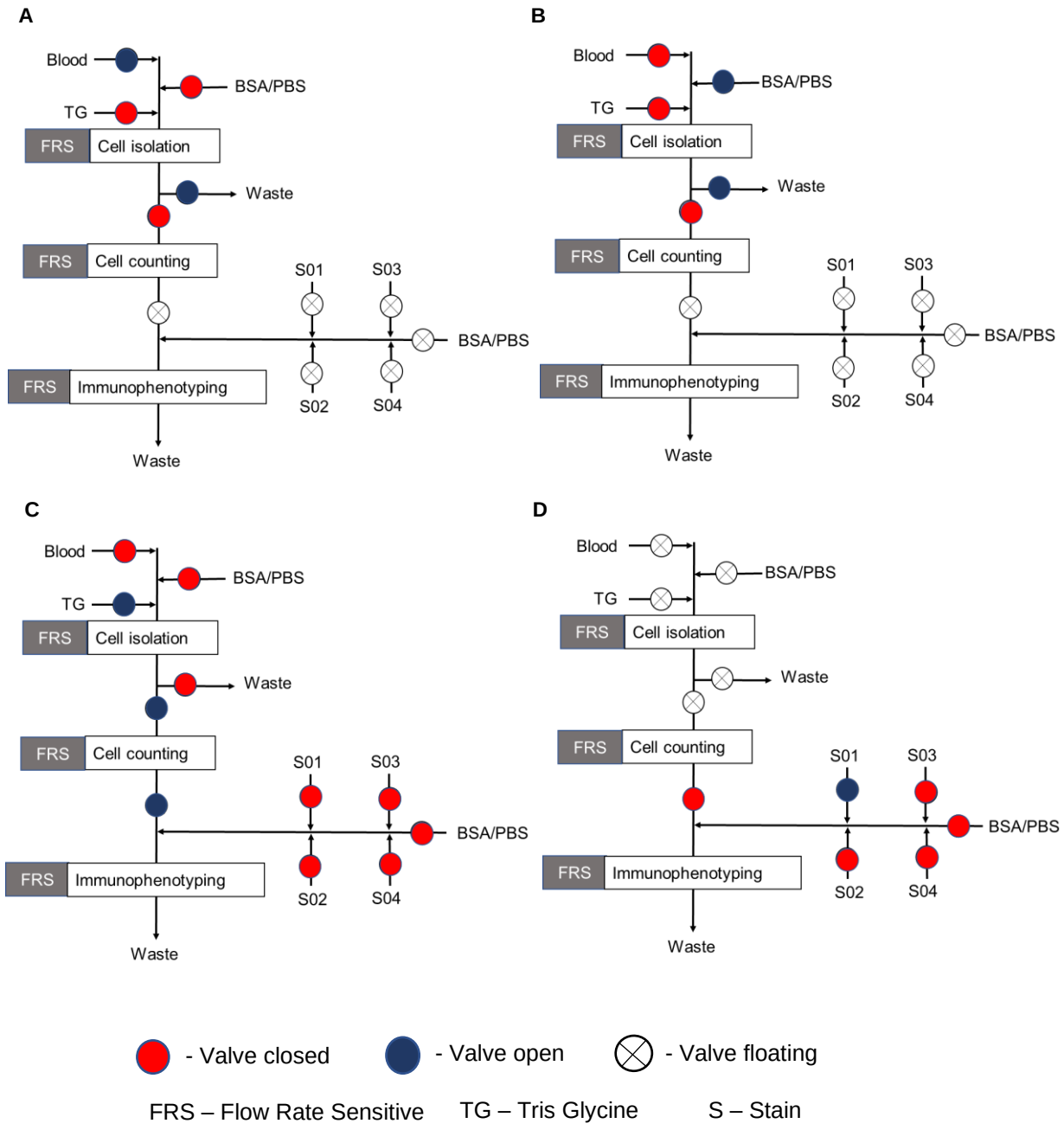

Figure 3.8. Major valve control steps of the SMART-Chip. (**A**) Whole blood processing, (**B**) post-selection wash with 0.5%BSA/PBS, (**C**) impedance cell counting and (**D**) immunophenotyping the cells trapped in the imaging module. (Reprinted with permission from (https://doi.org/10.1021/acssensors.0c02728). Copyright (2021) American Chemical Society)

3.3.6 **Operation of the SMART-Chip**

Next, we evaluated the system's ability to process whole blood spiked with CTCs. SKBR3 cells that have a high expression of cell surface EpCAM antigens (**Figure 3.9A**) were used as a model for the CTCs to initially evaluate the operational capabilities of the SMART-Chip. We quantified the cellular EpCAM expression by comparing their fluorescence signatures to Antibody Binding Capacity beads; SKBR3 cells had 1,454,052 of EpCAM receptors on their surfaces. Cells were spiked into healthy donor blood and the SMART-Chip was used to isolate, count, assess viability, and immunophenotype the cells. The PC linker was used to immobilize anti-EpCAM monoclonal antibodies to the cell selection module's surfaces to allow for enrichment of EpCAM(+) CTCs. Modules were rinsed with 0.5% BSA/PBS prior to sample infusion in order to prevent non-specific cell adsorption.

SKBR3 cells were stained with a nuclear dye (Hoechst 33342) and were spiked into a healthy donor blood sample. The blood sample was then hydrodynamically introduced into the cell selection module at 2 mm/s linear velocity. Non-specifically adsorbed materials were then removed by washing the cell selection module with 0.5% BSA/PBS at 4 mm/s. SKBR3 cell recovery (73%) was reported previously in the sinusoidal CTC selection modules that used the PC linker to immobilize anti-EpCAM antibodies (lower recovery of SKBR3 cells compared to MCF-7 is due to differences in the EpCAM expression level between these two cell lines).[41] Affinity enriched SKBR3 cells (**Figure 3.9B**) were then photoreleased by exposing the cell selection module to blue light (400 – 450 nm) for 2 min. Photoreleased cells were then directed through the impedance module and finally to the imaging module while recording the impedance signal (**Figure 3.9C**). Cells were physically trapped in the imaging module against the pore structures while the buffer solution passed to waste. Cells were then stained with anti-CD45 following fixing, permeabilizing, and staining with pan-cytokeratin. We counted 110 impedance signals in total and all of them had a positive polarity (100% viable cells). We observed 112 SKBR3 cells in the

imaging module (Hoechst 33342(+), FITC-CD45(-) and Cy3-pan-CK(+), **Figure 3.9D**). We did not observe any white blood cells (CD45(+) and pan-CK(-)) within the imaging module. In addition, we did not observe any Hoechst 33342(+) cells in the fluidic paths of the motherboard or at the

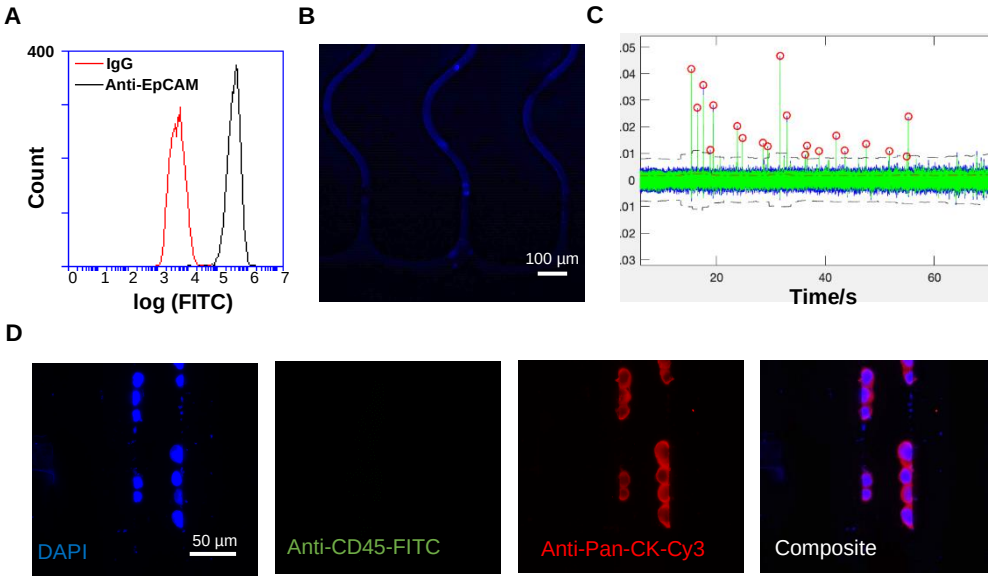

Figure 3.9. SKBR3 cells were affinity selected and photoreleased for enumeration, viability assessment, and immunophenotypic identification. (**A**) SKBR3 cells were tested for surface EpCAM expression by flow cytometry. Cells were labeled with FITC-conjugated primary antibody and comparison to the results of FITC-labeled isotype control. (**B**) Hoechst-stained SKBR3 cells were affinity selected in the CTC selection module by Anti-EpCAM monoclonal antibodies immobilized to the module's walls using the PC linker. (**C**) Photoreleased SKBR3 cells were directed towards the imaging module while recording impedance signals. Part of the impedance trace was displayed. (**D**) SKBR3 cells were physically trapped in the imaging module against the pore structures and immunostained using anti-CD45-FITC and anti-pan-CK-Cy3. Images were taken using a 40X objective. (Reprinted with permission from (https://doi.org/10.1021/acssensors.0c02728). Copyright (2021) American Chemical Society)

interconnects as well. This implied that the SKBR3 cells were not trapped in or adhered to the fluidic network of the motherboard, minimizing target cell loss during the analysis steps carried out by the SMART-Chip.

3.3.7 **CTCs from clinical samples**

We isolated and enumerated CTCs from the blood of a patient diagnosed with metastatic colorectal cancer (CRC) using the SMART-Chip. The patient's disease was confirmed via Computed Tomography (CT) a week before CTC analysis and prior to surgery and chemotherapy.

Since the first diagnosis, the patient's blood serum was tested for carcinoembryonic antigen (CEA), a tumor marker predicting treatment response and survival;[64] CEA levels in this patient's serum was normal (0.7 -1.0 ng/mL), with a value of 0.9 ng/mL. While an elevated serum CEA (>3

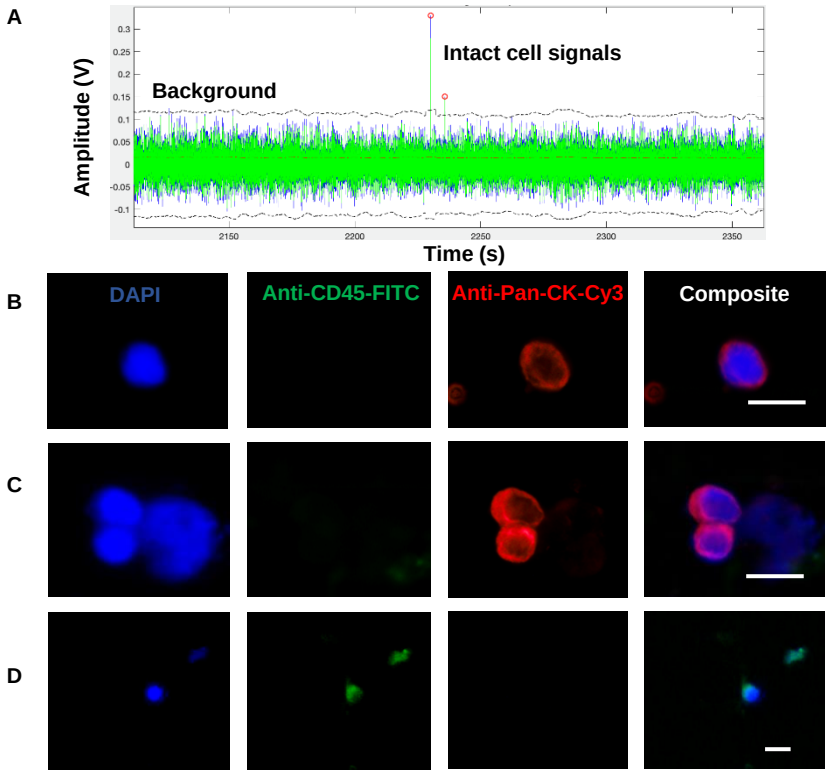

Figure 3.10. Impedance counting and identification of CTCs by immunophenotyping. The CTCs were enriched from a blood sampled secured from a metastatic colorectal cancer patient. Photoreleased CTCs were directed through the impedance module and imaging module. (**A**) A section of the impedance signal trace collected while CTCs were transported through the impedance module. Impedance signals were extracted when the signal-to-noise ratio exceeded 7. All extracted signals (7) were positive in polarity. (**B – D**) CTCs contained within the imaging module were stained on-chip with a panel of markers: Hoechst 33342-DAPI (40 µg/mL), anti-CD45-FITC (2.5 µg/mL) and anti-pan-CK-Cy3 (0.01 mg/mL). CTCs were identified as DAPI (+), CD45(-) and pan-CK(+) while white blood cells were identified as DAPI (+), CD45(+) and pan-CK(-). **(B)** Single CTC; **(C)** cluster of CTCs; and **(D)** a white blood cell. The images were taken using a 40X objective. Scale bars in the images are 15 µm. (Reprinted with permission from (**https://doi.org/10.1021/acssensors.0c02728**). Copyright (2021) American Chemical Society)

ng/mL) are found in up to 47% of CRC patients,[64] for this patient, who was a "non-secretor" of CEA, this test was not informative and unfortunately provided no predictive or diagnostic value.

The affinity enriched CTCs were photoreleased for cell counting and immunophenotypic identification. We were able to identify 7 impedance signals in total (part of the impedance signal trace is shown in **Figure 3.10A**) and 9 CTCs after immunophenotyping; this number falls within the range of CTCs we have enriched from metastatic CRC patients using anti-EpCAM mAbs.[3] All of the impedance signals were positive in polarity, which is in line with the fact that this patient had not received chemotherapy that can compromise cancer cell viability.[3] We processed 2 mL of blood in this experiment and 3 WBCs were observed following immunophenotyping. The high purity observed in this study is not surprising because we process blood at 40 dynes per cm^2 shear rates that removes most WBCs non-specifically bound to the wall of the CTC selection module and also, after photocleavage those cells would remain bound to the channel wall. The shear force applied in the post-selection wash (13 dynes per cm^2) does not affect the interaction of CTC antigens with their cognizant antibodies.[44, 55] We observed individual CTCs (**Figure 3.10B)** and micro-clusters of CTCs (**Figure 3.10C**). CTC micro-clusters are recognized as important prognostic markers in cancer because their molecular characterization offers insights into mechanisms of treatment resistance and increased metastatic potential.[65-66] We also observed only a few WBC contaminants in the imaging module (**Figure 3.10D**). A healthy blood sample was processed as a control for this experiment and no CTCs were identified.

We processed two other blood samples obtained from a CRC patient and a PDAC (Pancreatic ductal adenocarcinoma) patient to evaluate the clinical utility of the system further. In blood sample collected from CRC patient we detected 4 CTCs and all were determined non-viable based on impedance sensor. The CTC test was performed 6 months following the Hiperthermic Intraperitoneal Chemotherapy (HIPEC) procedure administered to patient following the cytoreductive surgery in order to eliminate residual cancer cells from the abdominal cavity. For the same patient before the cytoreductive surgery and HIPEC, we detected 5 times higher burden of CTC (19 cells) in blood, with 85% of CTCs being viable. Three weeks following surgery and

HIPEC, there was a significant switch in CTC viability, as 85% of detected CTCs was identified as dead. In metastatic PDAC patient, we detected 6 CTCs in the imaging module and 7 impedance signals. Among them, 4 signals were positive and three signals were negative in polarity, suggesting compromised viability of ~40% of CTCs. For this patient, CTC analysis was performed at the baseline, before enrolling patient into a clinical trial.

3.4 Conclusions

In this study, we reported on an integrated and modular microfluidic system (SMART-Chip) that could carry out the entire processing steps required for analyzing liquid biopsy samples and used CTCs as an example. The processing steps carried out by the SMART-Chip included affinity selection, photorelease, enumeration, viability assessment, and immunophenotypic identification of the enriched cells. The three task specific modules integrated into the system included: (i) CTC selection module; (ii) impedance module; and (iii) imaging module that were connected to a fluidic motherboard using interconnects that minimized unswept volumes. The fluidic motherboard contained channels that provided fluidic paths between each module as well as a valving system that was pneumatically operated so that precise control of the fluid path through the system could be achieved for each processing step. Particularly attractive with the modular nature of this integrated system is that alternative modules can be “plugged” into the fluidic motherboard to process other liquid biopsy markers, such as cfDNA[39] or EVs.[40]

Proof-of-concept was demonstrated by processing a healthy donor blood sample spiked with SKBR3 cells. The SMART-Chip was able to perform the entire assay yielding a highly pure isolate with no obervable loss of rare cells due to unswept volumes or non-specific adsorption artifacts. This was affected by using the proper material for each module and motherboard, proper design of the fluidic interconnects, and engineering surfaces to make them accommodating for the biological sample, which in this case was whole blood. We observed 112 SKBR3 cells in the imaging module and the impedance module detected 110 positive polarity signals (100% cell

viability). We also tested the clinical utility of the SMART-Chip by processing blood samples obtained from CRC and PDAC patients. We found high purity in the rare cell isolate (0-3 WBCs per mL of blood). Blood samples were processed at a throughput of 1.5 mL/h, but the throughput can be vastly improved by using a 320 channel version of the CTC selection device (10 mL/h) without sacrificing the analytical figures-of-merit.[45] Another attractive feature of the SMART-Chip is that the individual modules can be used as standalone units without requiring any modifications.

The SMART-Chip and its modular format provided several advantages compared to a non-integrated liquid biopsy processing approach: (1) The system was made from plastics using micro-replication so that all components could be produced in a high production mode and at low-cost to make it appropriate for *in vitro* diagnostics that requires disposable devices. Even the membrane valves were all plastic including the PDMS membrane, the pneumatic control layer, and the fluidic layer both of which were made from PMMA. (2) Full process automation of the assay with no requirement of transferring sample from one device to another. For example, our manual method for CTC processing of a blood-based liquid biopsy required off-loading the photoreleased cells into a microfuge tube, cytospinning the released cells onto a microscope slide, placing the microscope slide with deposited cells into an autostainer, and finally situating the slide on a microscope for fluorescence imaging. Thus, the SMART-Chip reduces sample loss and/or contamination, which is especially important for the analysis of rare targets. (3) The modular architecture of the SMART-Chip allows for reconfiguration by placing different fluidic modules onto the motherboard without requiring the need to re-engineer the entire system. As an example, the SMART-Chip can be reconfigured to isolate EVs from a liquid biopsy sample[40] and count them using a nano-coulter counter.[67-68] (4) The modular approach enables the ability to select the substrate material and fabrication modality to better suite the task requirement. As an example, we used different materials for the modules of the SMART-Chip and each utilized a different fabrication method. (5) The SMART-Chip is flexible in its operational mode. For example, following selection and enumeration, the biomarkers can be shuttled to another module for

molecular processing instead of immunophenotyping. While we performed cell processing in this example, we can add a module to the integrated system to carry out a variety of molecular assays, such as determining the presence of disease-associated DNA mutations.[35] (6) The ability to reduce the CTC assay time. In this case, manual processing of CTCs in our hands required ~8 h[45] and using the SMART-Chip the processing time was 3.5 h.

We should note that in our past work using a plastic-based modular microfluidic system, the challenge was the polycarbonate membrane layer used, which resulted in poor yield rates (process yield rate <20% for polycarbonate membrane compared to 100% using the PMMA/PDMS/PMMA valves), the need for mechanical solenoids to actuate the polycarbonate valves due to polycarbonate's higher Young's modulus compared to PDMS, and the limited number of times the polycarbonate valves could be acutated (<10 compared to 77 herein). The low process yield rate of the polycarbonate valves is that the small elongation of break of polycarbonate compared to PDMS required a very small distance placed between the valve seat and the membrane, which in many case stuck together when assemblying the system making them non-functional.

We are now directing our efforts toward employing injection molding as the micro-replication method for both the modules and motherboard due to the high-scale production capacity with reduced unit cost it offers compared to hot embossing, PDMS casting, and direct milling as used here.[69-70] We are also in the process of replacing the PDMS membrane layer for valving with an elastomeric COC (eCOC, Topas® Elastomer E-140, Topas Advanced Polymers, Germany) due to the fact that it can be injection molded and its extended hydrophilic surface characateristics compared to PDMS after UV/O_3 treatment. In addition, we are developing plastic modules that can provide molecular information from the enriched targets to not only provide phenotyping information, but also information on nucleic acids packaged into the rare cells.

3.5 Acknowledgment

The authors would like to thank the NIH for funding (NIBIB P41-EB020594; P20-GM130423). We acknowledge support from the University of Kansas (KU) Cancer Center's Biospecimen Repository Core for obtaining human specimens (NCI: P30-CA168524). We are very appreciative to patients and healthy donors for their blood donations. We acknowledge the Instrumental Design Lab at KU for making the valve control hardware and interface software. We also like to thank Physics Machine Shop at KU for micromilling the fluidic motherboard and Synthetic Chemical Biology Core Facility at KU for synthesizing the PC linker.

3.6 References

1. Macias, M.; Alegre, E.; Diaz-Lagares, A.; Patino, A.; Perez-Gracia, J. L.; Sanmamed, M.; Lopez-Lopez, R.; Varo, N.; Gonzalez, A., Liquid Biopsy: From Basic Research to Clinical Practice. In *Advances in Clinical Chemistry, Vol 83*, Makowski, G. S., Ed. 2018; Vol. 83, pp 73-119.
2. Jefferies, S. S.; Toner, M., Liquid biopsy: a perspective for probing blood for cancer. *Lab on a Chip* **2018,** *18*.
3. Witek, M. A.; Aufforth, R. D.; Wang, H.; Kamande, J. W.; Jackson, J. M.; Pullagurla, S. R.; Hupert, M. L.; Usary, J.; Wysham, W. Z.; Hilliard, D., Discrete microfluidics for the isolation of circulating tumor cell subpopulations targeting fibroblast activation protein alpha and epithelial cell adhesion molecule. *NPJ precision oncology* **2017,** *1* (1), 1-11.
4. Phallen, J.; Sausen, M.; Adleff, V.; Leal, A.; Hruban, C.; White, J.; Anagnostou, V.; Fiksel, J.; Cristiano, S.; Papp, E., Direct detection of early-stage cancers using circulating tumor DNA. *Science translational medicine* **2017,** *9* (403).
5. Beaver, J. A.; Jelovac, D.; Balukrishna, S.; Cochran, R. L.; Croessmann, S.; Zabransky, D. J.; Wong, H. Y.; Toro, P. V.; Cidado, J.; Blair, B. G., Detection of cancer DNA in plasma of patients with early-stage breast cancer. *Clinical cancer research* **2014,** *20* (10), 2643-2650.
6. Wang, S.; Thomas, A.; Lee, E.; Yang, S.; Cheng, X.; Liu, Y., Highly efficient and selective isolation of rare tumor cells using a microfluidic chip with wavy-herringbone micro-patterned surfaces. *Analyst* **2016,** *141* (7), 2228-2237.
7. Yap, T. A.; Lorente, D.; Omlin, A.; Olmos, D.; De Bono, J. S., Circulating tumor cells: a multifunctional biomarker. AACR: 2014.
8. Xiang, N.; Wang, J.; Li, Q.; Han, Y.; Huang, D.; Ni, Z., Precise size-based cell separation via the coupling of inertial microfluidics and deterministic lateral displacement. *Analytical chemistry* **2019,** *91* (15), 10328-10334.
9. Fachin, F.; Spuhler, P.; Martel-Foley, J. M.; Edd, J. F.; Barber, T. A.; Walsh, J.; Karabacak, M.; Pai, V.; Yu, M.; Smith, K., Monolithic chip for high-throughput blood cell depletion to sort rare circulating tumor cells. *Scientific reports* **2017,** *7* (1), 1-11.
10. Chiu, T.-K.; Chao, A.-C.; Chou, W.-P.; Liao, C.-J.; Wang, H.-M.; Chang, J.-H.; Chen, P.-H.; Wu, M.-H., Optically-induced-dielectrophoresis (ODEP)-based cell manipulation in a microfluidic system for high-purity isolation of integral circulating tumor cell (CTC) clusters based on their size characteristics. *Sensors and Actuators B: Chemical* **2018,** *258*, 1161-1173.

11. Wu, M.; Huang, P. H.; Zhang, R.; Mao, Z.; Chen, C.; Kemeny, G.; Li, P.; Lee, A. V.; Gyanchandani, R.; Armstrong, A. J., Circulating Tumor Cell Phenotyping via High-Throughput Acoustic Separation. *Small* **2018,** *14* (32), 1801131.
12. Yang, C.; Zhang, N.; Wang, S.; Shi, D.; Zhang, C.; Liu, K.; Xiong, B., Wedge-shaped microfluidic chip for circulating tumor cells isolation and its clinical significance in gastric cancer. *Journal of translational medicine* **2018,** *16* (1), 1-12.
13. Au, S. H.; Edd, J.; Stoddard, A. E.; Wong, K. H.; Fachin, F.; Maheswaran, S.; Haber, D. A.; Stott, S. L.; Kapur, R.; Toner, M., Microfluidic isolation of circulating tumor cell clusters by size and asymmetry. *Scientific reports* **2017,** *7* (1), 1-10.
14. Kang, Y.-T.; Kim, Y. J.; Bu, J.; Chen, S.; Cho, Y.-H.; Lee, H. M.; Ryu, C. J.; Lim, Y.; Han, S.-W., Epithelial and mesenchymal circulating tumor cell isolation and discrimination using dual-immunopatterned device with newly-developed anti-63B6 and anti-EpCAM. *Sensors and Actuators B: Chemical* **2018,** *260*, 320-330.
15. Zeinali, M.; Murlidhar, V.; Fouladdel, S.; Shao, S.; Zhao, L.; Cameron, H.; Bankhead III, A.; Shi, J.; Cuneo, K. C.; Sahai, V., Profiling heterogeneous circulating tumor cells (CTC) populations in pancreatic cancer using a serial microfluidic CTC carpet chip. *Advanced Biosystems* **2018,** *2* (12), 1800228.
16. LeValley, P. J.; Tibbitt, M. W.; Noren, B.; Kharkar, P.; Kloxin, A. M.; Anseth, K. S.; Toner, M.; Oakey, J., Immunofunctional photodegradable poly (ethylene glycol) hydrogel surfaces for the capture and release of rare cells. *Colloids and Surfaces B: Biointerfaces* **2019,** *174*, 483-492.
17. Kong, L. X.; Perebikovsky, A.; Moebius, J.; Kulinsky, L.; Madou, M., Lab-on-a-CD: A fully integrated molecular diagnostic system. *Journal of laboratory automation* **2016,** *21* (3), 323-355.
18. Brassard, D.; Geissler, M.; Descarreaux, M.; Tremblay, D.; Daoud, J.; Clime, L.; Mounier, M.; Charlebois, D.; Veres, T., Extraction of nucleic acids from blood: unveiling the potential of active pneumatic pumping in centrifugal microfluidics for integration and automation of sample preparation processes. *Lab on a Chip* **2019,** *19* (11), 1941-1952.
19. Woo, H.-K.; Sunkara, V.; Park, J.; Kim, T.-H.; Han, J.-R.; Kim, C.-J.; Choi, H.-I.; Kim, Y.-K.; Cho, Y.-K., Exodisc for rapid, size-selective, and efficient isolation and analysis of nanoscale extracellular vesicles from biological samples. *ACS nano* **2017,** *11* (2), 1360-1370.
20. Sunkara, V.; Kim, C.-J.; Park, J.; Woo, H.-K.; Kim, D.; Ha, H. K.; Kim, M.-H.; Son, Y.; Kim, J.-R.; Cho, Y.-K., Fully automated, label-free isolation of extracellular vesicles from whole blood for cancer diagnosis and monitoring. *Theranostics* **2019,** *9* (7), 1851.
21. Kim, C.-J.; Ki, D. Y.; Park, J.; Sunkara, V.; Kim, T.-H.; Min, Y.; Cho, Y.-K., Fully automated platelet isolation on a centrifugal microfluidic device for molecular diagnostics. *Lab on a Chip* **2020**.
22. Czilwik, G.; Messinger, T.; Strohmeier, O.; Wadle, S.; Von Stetten, F.; Paust, N.; Roth, G.; Zengerle, R.; Saarinen, P.; Niittymäki, J., Rapid and fully automated bacterial pathogen detection on a centrifugal-microfluidic LabDisk using highly sensitive nested PCR with integrated sample preparation. *Lab on a Chip* **2015,** *15* (18), 3749-3759.
23. Michael, I. J.; Kim, T.-H.; Sunkara, V.; Cho, Y.-K., Challenges and opportunities of centrifugal microfluidics for extreme point-of-care testing. *Micromachines* **2016,** *7* (2), 32.
24. Aeinehvand, M. M.; Ibrahim, F.; Al-Faqheri, W.; Thio, T. H. G.; Kazemzadeh, A.; Madou, M., Latex micro-balloon pumping in centrifugal microfluidic platforms. *Lab on a Chip* **2014,** *14* (5), 988-997.
25. Aeinehvand, M. M.; Weber, L.; Jiménez, M.; Palermo, A.; Bauer, M.; Loeffler, F. F.; Ibrahim, F.; Breitling, F.; Korvink, J.; Madou, M., Elastic reversible valves on centrifugal microfluidic platforms. *Lab on a Chip* **2019,** *19* (6), 1090-1100.
26. Rodriguez-Moncayo, R.; Jimenez-Valdes, R. J.; Gonzalez-Suarez, A. M.; Garcia-Cordero, J. L., Integrated Microfluidic Device for Functional Secretory Immunophenotyping of Immune Cells. *ACS sensors* **2020**.

27. Stark, A.; Shin, D. J.; Wang, T.-H., A sample-to-answer droplet magnetofluidic assay platform for quantitative methylation-specific PCR. *Biomedical microdevices* **2018,** *20* (2), 31.
28. Lai, X.; Lu, B.; Zhang, P.; Zhang, X.; Pu, Z.; Yu, H.; Li, D., Sticker Microfluidics: A Method for Fabrication of Customized Monolithic Microfluidics. *ACS Biomaterials Science & Engineering* **2019,** *5* (12), 6801-6810.
29. Huang, S.-P.; Chuang, Y.-J.; Lee, W.-B.; Tsai, Y.-C.; Lin, C.-N.; Hsu, K.-F.; Lee, G.-B., An integrated microfluidic system for rapid, automatic and high-throughput staining of clinical tissue samples for diagnosis of ovarian cancer. *Lab on a Chip* **2020**.
30. Giménez-Gómez, P.; Fernández-Sánchez, C. s.; Baldi, A., Microfluidic Modules with Integrated Solid-State Sensors for Reconfigurable Miniaturized Analysis Systems. *ACS Omega* **2019,** *4* (4), 6192-6198.
31. Zhuang, B.; Han, J.; Xiang, G.; Gan, W.; Wang, S.; Wang, D.; Wang, L.; Sun, J.; Li, C.-X.; Liu, P., A fully integrated and automated microsystem for rapid pharmacogenetic typing of multiple warfarin-related single-nucleotide polymorphisms. *Lab on a Chip* **2016,** *16* (1), 86-95.
32. Reedy, C. R.; Hagan, K. A.; Marchiarullo, D. J.; Dewald, A. H.; Barron, A.; Bienvenue, J. M.; Landers, J. P., A modular microfluidic system for deoxyribonucleic acid identification by short tandem repeat analysis. *Analytica chimica acta* **2011,** *687* (2), 150-158.
33. Sabourin, D.; Skafte-Pedersen, P.; Søe, M. J.; Hemmingsen, M.; Alberti, M.; Coman, V.; Petersen, J.; Emnéus, J.; Kutter, J. P.; Snakenborg, D., The Main STREAM Component Platform: A Holistic Approach to Microfluidic System Design. *Journal of laboratory automation* **2013,** *18* (3), 212-228.
34. Chen, Y.-W.; Wang, H.; Hupert, M.; Witek, M.; Dharmasiri, U.; Pingle, M. R.; Barany, F.; Soper, S. A., Modular microfluidic system fabricated in thermoplastics for the strain-specific detection of bacterial pathogens. *Lab on a Chip* **2012,** *12* (18), 3348-3355.
35. Wang, H.; Chen, H. W.; Hupert, M. L.; Chen, P. C.; Datta, P.; Pittman, T. L.; Goettert, J.; Murphy, M. C.; Williams, D.; Barany, F., Fully Integrated Thermoplastic Genosensor for the Highly Sensitive Detection and Identification of Multi-Drug-Resistant Tuberculosis. *Angewandte Chemie International Edition* **2012,** *51* (18), 4349-4353.
36. Millet, L. J.; Lucheon, J. D.; Standaert, R. F.; Retterer, S. T.; Doktycz, M. J., Modular microfluidics for point-of-care protein purifications. *Lab on a Chip* **2015,** *15* (8), 1799-1811.
37. Xie, X.; Maharjan, S.; Liu, S.; Zhang, Y. S.; Livermore, C., A Modular, Reconfigurable Microfabricated Assembly Platform for Microfluidic Transport and Multitype Cell Culture and Drug Testing. *Micromachines* **2020,** *11* (1), 2.
38. Chen, Y.-S.; Ma, Y.-D.; Chen, C.; Shiesh, S.-C.; Lee, G.-B., An integrated microfluidic system for on-chip enrichment and quantification of circulating extracellular vesicles from whole blood. *Lab on a Chip* **2019,** *19* (19), 3305-3315.
39. Campos, C. D.; Gamage, S. S.; Jackson, J. M.; Witek, M. A.; Park, D. S.; Murphy, M. C.; Godwin, A. K.; Soper, S. A., Microfluidic-based solid phase extraction of cell free DNA. *Lab on a Chip* **2018,** *18* (22), 3459-3470.
40. Wijerathne, H.; Witek, M. A.; Jackson, J. M.; Brown, V.; Hupert, M. L.; Herrera, K.; Kramer, C.; Davidow, A. E.; Li, Y.; Baird, A. E.; Murphy, M. C.; Soper, S. A., Affinity enrichment of extracellular vesicles from plasma reveals mRNA changes associated with acute ischemic stroke. *Communications Biology* **2020,** *3* (1).
41. Pahattuge, T. N.; Jackson, J. M.; Digamber, R.; Wijerathne, H.; Brown, V.; Witek, M. A.; Perera, C.; Givens, R. S.; Peterson, B. R.; Soper, S. A., Visible photorelease of liquid biopsy markers following microfluidic affinity-enrichment. *Chemical Communications* **2020,** *56* (29), 4098-4101.
42. M Weerakoon-Ratnayake, K.; Vaidyanathan, S.; Larkey, N.; Dathathreya, K.; Hu, M.; Jose, J.; Mog, S.; August, K.; Godwin, A. K.; L Hupert, M., Microfluidic Device for On-Chip Immunophenotyping and Cytogenetic Analysis of Rare Biological Cells. *Cells* **2020,** *9* (2), 519.

43. Hupert, M. L.; Jackson, J. M.; Wang, H.; Witek, M. A.; Kamande, J.; Milowsky, M. I.; Whang, Y. E.; Soper, S. A., Arrays of high-aspect ratio microchannels for high-throughput isolation of circulating tumor cells (CTCs). *Microsystem technologies* **2014,** *20* (10-11), 1815-1825.
44. Adams, A. A.; Okagbare, P. I.; Feng, J.; Hupert, M. L.; Patterson, D.; Goettert, J.; McCarley, R. L.; Nikitopoulos, D.; Murphy, M. C.; Soper, S. A., Highly efficient circulating tumor cell isolation from whole blood and label-free enumeration using polymer-based microfluidics with an integrated conductivity sensor. *Journal of the American Chemical Society* **2008,** *130* (27), 8633-8641.
45. Kamande, J. W.; Hupert, M. L.; Witek, M. A.; Wang, H.; Torphy, R.; Dharmasiri, U.; Njoroge, S. K.; Jackson, J. M.; Aufforth, R.; Snavely, A., Modular microsystem for the isolation, enumeration, and phenotyping of circulating tumor cells in patients with pancreatic cancer. *Analytical chemistry* **2013,** *85* (19), 9092-9100.
46. Tsao, C. W., Polymer Microfluidics: Simple, Low-Cost Fabrication Process Bridging Academic Lab Research to Commercialized Production. *Micromachines (Basel)* **2016,** *7* (12).
47. Zhang, W.; Lin, S.; Wang, C.; Hu, J.; Li, C.; Zhuang, Z.; Zhou, Y.; Mathies, R. A.; Yang, C. J., PMMA/PDMS valves and pumps for disposable microfluidics. *Lab on a Chip* **2009,** *9* (21), 3088-3094.
48. Wong, K. H.; Tessier, S. N.; Miyamoto, D. T.; Miller, K. L.; Bookstaver, L. D.; Carey, T. R.; Stannard, C. J.; Thapar, V.; Tai, E. C.; Vo, K. D., Whole blood stabilization for the microfluidic isolation and molecular characterization of circulating tumor cells. *Nature communications* **2017,** *8* (1), 1-11.
49. Nagrath, S.; Sequist, L. V.; Maheswaran, S.; Bell, D. W.; Irimia, D.; Ulkus, L.; Smith, M. R.; Kwak, E. L.; Digumarthy, S.; Muzikansky, A., Isolation of rare circulating tumour cells in cancer patients by microchip technology. *Nature* **2007,** *450* (7173), 1235-1239.
50. Gleghorn, J. P.; Pratt, E. D.; Denning, D.; Liu, H.; Bander, N. H.; Tagawa, S. T.; Nanus, D. M.; Giannakakou, P. A.; Kirby, B. J., Capture of circulating tumor cells from whole blood of prostate cancer patients using geometrically enhanced differential immunocapture (GEDI) and a prostate-specific antibody. *Lab on a Chip* **2010,** *10* (1), 27-29.
51. Stott, S. L.; Hsu, C.-H.; Tsukrov, D. I.; Yu, M.; Miyamoto, D. T.; Waltman, B. A.; Rothenberg, S. M.; Shah, A. M.; Smas, M. E.; Korir, G. K., Isolation of circulating tumor cells using a microvortex-generating herringbone-chip. *Proceedings of the National Academy of Sciences* **2010,** *107* (43), 18392-18397.
52. Wang, S.; Liu, K.; Liu, J.; Yu, Z. T. F.; Xu, X.; Zhao, L.; Lee, T.; Lee, E. K.; Reiss, J.; Lee, Y. K., Highly efficient capture of circulating tumor cells by using nanostructured silicon substrates with integrated chaotic micromixers. *Angewandte Chemie* **2011,** *123* (13), 3140-3144.
53. Chang, K.-C.; Hammer, D. A., The forward rate of binding of surface-tethered reactants: effect of relative motion between two surfaces. *Biophysical Journal* **1999,** *76* (3), 1280-1292.
54. Jackson, J. M.; Hupert, M. L.; Soper, S. A., Discrete geometry optimization for reducing flow non-uniformity, asymmetry, and parasitic minor loss pressure drops in Z-type configurations of fuel cells. *Journal of Power Sources* **2014,** *269*, 274-283.
55. Jackson, J. M.; Witek, M. A.; Soper, S. A., Sinusoidal microchannels with high aspect ratios for CTC selection and analysis. *Circulating Tumor Cells: Isolation and Analysis* **2016**, 85-126.
56. McCarley, R. L.; Vaidya, B.; Wei, S. Y.; Smith, A. F.; Patel, A. B.; Feng, J.; Murphy, M. C.; Soper, S. A., Resist-free patterning of surface architectures in polymer-based microanalytical devices. *Journal of the American Chemical Society* **2005,** *127* (3), 842-843.
57. Wei, S. Y.; Vaidya, B.; Patel, A. B.; Soper, S. A.; McCarley, R. L., Photochemically patterned poly(methyl methacrylate) surfaces used in the fabrication of microanalytical devices. *Journal Of Physical Chemistry B* **2005,** *109* (35), 16988-16996.

58. Rünger, T. M.; Kappes, U. P., Mechanisms of mutation formation with long-wave ultraviolet light (UVA). *Photodermatology, photoimmunology & photomedicine* **2008,** *24* (1), 2-10.
59. Sage, E.; Girard, P.-M.; Francesconi, S., Unravelling UVA-induced mutagenesis. *Photochemical & Photobiological Sciences* **2012,** *11* (1), 74-80.
60. Sun, T.; Morgan, H., Single-cell microfluidic impedance cytometry: a review. *Microfluidics and Nanofluidics* **2010,** *8* (4), 423-443.
61. Gawad, S.; Schild, L.; Renaud, P., Micromachined impedance spectroscopy flow cytometer for cell analysis and particle sizing. *Lab on a Chip* **2001,** *1* (1), 76-82.
62. Liu, Z.; Lee, Y.; hee Jang, J.; Li, Y.; Han, X.; Yokoi, K.; Ferrari, M.; Zhou, L.; Qin, L., Microfluidic cytometric analysis of cancer cell transportability and invasiveness. *Scientific reports* **2015,** *5*, 14272.
63. Kuo, J. S.; Zhao, Y.; Schiro, P. G.; Ng, L.; Lim, D. S.; Shelby, J. P.; Chiu, D. T., Deformability considerations in filtration of biological cells. *Lab Chip* **2010,** *10* (7), 837-42.
64. Cho, W. K.; Choi, D. H.; Park, H. C.; Park, W.; Yu, J. I.; Park, Y. S.; Park, J. O.; Lim, H. Y.; Kang, W. K.; Kim, H. C., Elevated CEA is associated with worse survival in recurrent rectal cancer. *Oncotarget* **2017,** *8* (62), 105936.
65. Amintas, S.; Bedel, A.; Moreau-Gaudry, F.; Boutin, J.; Buscail, L.; Merlio, J.-P.; Vendrely, V.; Dabernat, S.; Buscail, E., Circulating Tumor Cell Clusters: United We Stand Divided We Fall. *International Journal of Molecular Sciences* **2020,** *21* (7), 2653.
66. Hong, Y.; Fang, F.; Zhang, Q., Circulating tumor cell clusters: What we know and what we expect. *International journal of oncology* **2016,** *49* (6), 2206-2216.
67. Anderson, W.; Lane, R.; Korbie, D.; Trau, M., Observations of Tunable Resistive Pulse Sensing for Exosome Analysis: Improving System Sensitivity and Stability. *Langmuir* **2015,** *31* (23), 6577-87.
68. Maas, S. L.; Broekman, M. L.; de Vrij, J., Tunable resistive pulse sensing for the characterization of extracellular vesicles. In *Exosomes and Microvesicles*, Springer: 2017; pp 21-33.
69. Piotter, V.; Hanemann, T.; Ruprecht, R.; Hausselt, J., Injection molding and related techniques for fabrication of microstructures. *Microsystem Technologies* **1997,** *3* (3), 129-133.
70. Heckele, M.; Schomburg, W., Review on micro molding of thermoplastic polymers. *Journal of Micromechanics and Microengineering* **2003,** *14* (3), R1.

Chapter 4 – Affinity selection and enumeration of SARS-CoV-2 viral particles from saliva using microfluidics for COVID-19 detection

4.1 Introduction

Since its emergence in December 2019, Severe Acute Respiratory Syndrome Coronavirus 2 (SARS-CoV-2) remains uncontrollable with an increase of approximately 400,000 diagnosed patients globally per day.[2] The disease has a basic reproductive number (R_0) of 2.2-2.5 and can spread rapidly through direct person-to-person contact resulting in high infectivity.[4-5] The major symptoms include severe pneumonia, fever, cough, fatigue, and pain in the digestive system.[6] By the end of February 2021, the pandemic has caused more than 119 million confirmed cases and 2.6 million deaths worldwide.

Coronaviruses are a family of enveloped viruses with the size of ~125 nm in diameter [7-9] and consist of a single, positive-stranded RNA (26-32 kb) as the genetic material.[10-11] Six human coronaviruses have been identified previously (HCoV-NL63, HCoV-229E, HCoV-OC43, HCoV-HKU1, SARS-CoV-1, and MERS-CoV), and SARS-CoV-2 is the seventh coronavirus known to cause infections in humans.[12] The RNA genome encodes ten genes to produce 26 proteins,[13] including four structural proteins; spike (S), nucleocapsid (N), envelope (E), and membrane (M).[14] The S protein plays a vital role in binding to ACE2 (angiotensin-converting enzyme 2) receptors and subsequent viral entry into a host cell. N protein is essential for RNA synthesis, and E and M proteins are transmembrane proteins and necessary for the assembly, budding, and envelope formation of the virus.[15-16]

Testing has been viewed as an important tool for the control of disease spreading. Common tests for COVID-19 include molecular tests that interrogate the RNA genome of SARS-CoV-2, which requires RNA extraction and purification, reverse transcription (RT) to generate complementary DNA (cDNA) from target genes (viral N, E, and S with human RNA dependent RNA polymerase (RdRp) as a control), amplification by the polymerase chain reaction (PCR), and

reading a fluorescent signal. The lower threshold values (Ct) indicate a positive diagnostic result. RT-qPCR is the current gold standard for the etiological detection of SARS-CoV-2 [17] but requires highly trained operators, 2-3 h of assay turnaround time, and multiple reagents to carry out the test.

Rapid testing is vital for disease management since it enables the ability to screen many patients, begin the treatments immediately, and identify asymptomatic carriers to prevent further disease spread by encouraging them to isolate. The Food and Drug Administration (FDA) has approved six PCR-based tests with some appropriate for POCT.[18-21] The temperature cycling typically required in PCR can be replaced by loop-mediated isothermal amplification using a strand displacement DNA polymerase.[2, 22] The CRISPR/Cas system has recently been deployed for virus detection[23]. The combination of CRISPR/Cas13a with isothermal amplification was recently reported to detect SARS-CoV-2 through an FDA emergency use authorization (EUA).[2, 24] RT-qPCR requires sensitive and, in some cases costly reagents, such as enzymes and fluorescent reporters.[25] Other challenges include errors in sample collection, variability between different commercially-available extraction kits of RNA, and PCR inhibitors in the sample.[25]

To address some of the challenges associated with RT-qPCR, rapid serological tests, either antibody- or antigen-based, have appeared. These tests can target the S or N proteins.[26-28] Cartridge-based lateral flow assays have received FDA approval through a EUA.[25, 29-31] As of November 13, 2020, FDA has approved more than 50 antibody tests.[32] However, antibody tests have inferior limits-of-detection compared to RT-qPCR and increased false-negative results.[33-34] Besides, these tests require sensitive reagents, such as antibodies and/or fluorescent reporters.

Identifying infected individuals, even those that are asymptomatic is necessary to prevent disease spreading, especially within vulnerable populations.[35] Different types of testing needs (*i.e.*, screening versus clinical) are being recognized for monitoring COVID-19 in communities. A screening test, especially those that are simple enough to be carried out at home, would allow for

early detection of individuals so that prompt quarantine procedures could be implemented to facilitate containment (**Figure 4.1**). Whether screening or clinical testing, no test currently available can distinguish between infectious and non-infectious individuals. Those that are infectious are considered to be “active” spreaders of viral particles (VPs). As seen in **Figure 4.1**, there are certain times during the viral load profile where individuals are infectious, and PCR-based tests may provide a positive result on even post-infectious individuals because it cannot distinguish between genomic RNA encapsulated within the VP and free RNA resulting from RNA shedding. Also, serological tests only inform the individual that infection did occur. To provide some numbers with the temporal dynamics of viral load for SARS-CoV-2, He *et al.* determined that in 94 patients, infectivity started 12.3 days (mean) before symptom onset but declined rapidly 7 days after symptom onset and peaked 2 days before and 1 day after symptom onset.[36]

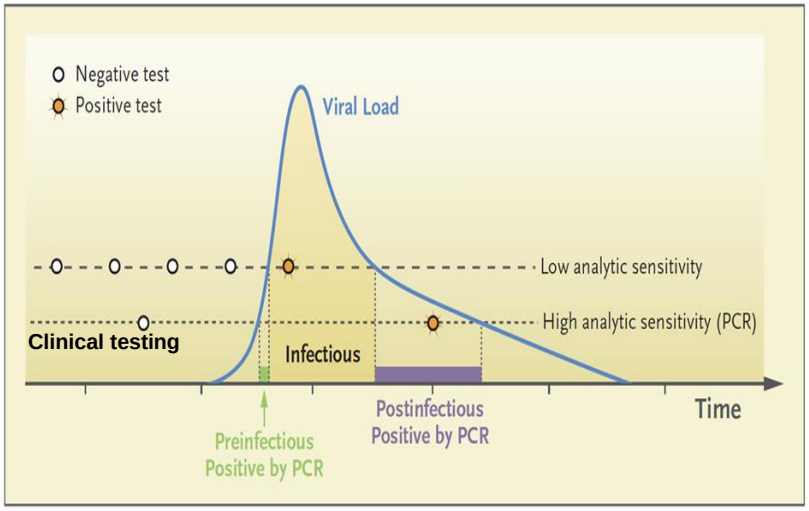

Figure 4.1. Hypothetical viral load as a function of disease progression and different testing strategies. (Reproduced with permission from Ref 35 (DOI: 10.1056/NEJMp2025631). Copyright Massachusetts Medical Society)

Affinity selection of biologicals offers attractive operational characteristics, including the ability to precisely select targets with high purity from various biological samples. Monoclonal antibodies are most often used for affinity selection of targets. However, some antibodies generated for SARS-CoV (*i.e.*, mAb CR3022 and pAb) bind SARS-CoV-2 with moderate affinity

resulting in low specificity.[37] Other antibody clones directed against the SARS-CoV receptor-binding domain (RBD) do not bind SARS-CoV-2 at all, despite relatively high degrees of structural RBD homology.[38] Aptamers are viewed as an attractive alternative to antibodies due to their ease of selection, high stability even at room temperature, and the ability to place functional groups within their structures for surface attachment. A DNA aptamer targeting the S protein in the SARS-CoV-2 viral envelope has been reported (K_d = 5.8 nM).[1] Different variant of SARS-CoV-2 were reported, B.1.1.7 (UK variant), B.1.351 (South African variant), and P.1 (Brazil variant). Some variants are more contagious and spread more quickly (ex- B.1.1.7 variant) than the wild-type. The DNA aptamer hydrogen bonds with the Thr 500, Gln 506, and Asn 437 of SARS-CoV-2 spike protein.[1] These hot spot residues were not mutated in the above variants, but the adjacent Asn 501 was mutated to Tyr (N501Y). If this mutation does not change the RBD conformation, we expect to observe the same binding affinity of the aptamer towards the variants.

This study developed a rapid and reagent-less technology that can selectively enrich SARS-CoV-2 viral particles by processing a clinical sample (saliva, throat, or nasal swab) and enumerate the viral load using a label-free technique after releasing them from the affinity-selection surface. The system contains two individual task devices, an affinity selection device and a nano coulter counter (nCC) device. The affinity selection device has seven parallel beds that comprise 1.5 million pillars providing a high surface area. This module was used for the affinity selection of extracellular vesicles (EVs) from liquid biopsy samples.[39] DNA aptamer targeting the spike protein (S protein) in the SARS-CoV-2 viral envelope was used as the affinity agent.[1] The aptamer was immobilized onto the device surface via a Coumarin-based photocleavable (PC) linker using EDC/NHS chemistry.[40] After the affinity enrichment, the isolated viral particles can be released from the device surface by exposing the device to blue light (400-450 nm). The nano coulter counter that consists of a narrow constriction (~ 350 nm) can electrically detect single particles passing through the nanopore.[41-42] Collectively, this system can be used as a rapid

screening tool to determine the number of viral particles present in a patient's sample in <20 min. Because the technology results were based on detecting VPs possessing an intact S protein, our technology can provide information on patients with *active disease* and, with frequent testing, provide early containment minimizing community spread of COVID-19. Finally, the selected and released SARS-CoV-2 VPs could also be subjected to RT-qPCR.

The devices were made from plastics and fabricated by injection molding and nanoimprinting. Low-cost device production is an essential factor in allowing them to be used as disposables. The analytical figures of merits were demonstrated by using heat-inactivated SARS-CoV-2, and Respiratory Syncytial Virus (RSV) viral particles spiked into healthy saliva specimens. The clinical utility of the system was validated by a blind study of 20 clinical samples.

4.2 Experimental

4.2.1 Materials and methods

Reagent grade IPA (isopropyl alcohol), 1-ethyl-3-[3-dimethylamino- propyl] carbodiimide hydrochloride (EDC), N-hydroxysuccinimide (NHS), anhydrous acetonitrile (ACN), anhydrous dimethylformamide (DMF), anhydrous dichloromethane (DCM), anhydrous triethylamine (TEA), nuclease-free water, (Fisher Scientific), Virkon S (Dupont), 1 M Tris pH 7.4 (KD Medical); bovine serum albumin (BSA), Polyvinylpyrrolidone, 40 kDa (PVP-40), and polyethylene glycol (PEG) were secured from Sigma-Aldrich. Phosphate buffered saline (PBS, pH = 7.4), was purchased from Gibco laboratories. Universal PCR supermix was obtained from Bio-Rad. Other reagents included TapeStation supplies (Agilent), Zymo Viral RNA isolation kit (Zymo Research), ProtoScript II First Strand cDNA Synthesis Kit (New England BioLabs). Aptamers, primers, and probes were purchased from Integrated DNA Technologies. Silicon <100> wafers were purchased from University Wafers (Boston, MA). Impact modified (IM) and non-impact modified (NIM) PMMA substrates were purchased from ePlastics (San Diego, CA) and Good Fellow

(Berwyn, PA), respectively. UV curable polyurethane (PUA) resin was purchased from Chansung Sheet Co. Ltd. (Chuncheognam-do, Korea).

Syringe pumps were purchased from New Era, and microfluidic devices were connected using inner-Lok™ union capillary connectors (Polymicro Technologies) and barbed socket Luer Lock™ fittings (3/32″ ID, McMaster-Carr).

4.2.2 **Model virus particles (VPs) for determining the assay's analytical figures-of-merits**

For determining the analytical figures-of-merit of the VP selection chip and the nCC, heat-inactivated SARS-CoV-2 (ATCC, VR-1986HK) was used. SARS-CoV-2 VPs were inactivated at 65°C for 30 min and is therefore unable to replicate. Human Respiratory Syncytial Virus (HRSV, strain A2, ATCC, VR-1540) was also used in these studies to demonstrate the programmability of the VP selection chip to isolate other VPs. An aptamer specific to HRSV has been used in these studies.[3] HCoV OC43 (ATCC, VR-1558), HCoV 229E (ATCC, VR-740), and HRSV were used for the specificity studies of SARS-CoV-2 aptamer-modified VP selection chips.

4.2.3 **VP selection chip fabrication**

The VP selection chips used in these studies were fabricated in cyclic olefin polymer (COP) via injection molding (Stratec, Austria) using a mold insert made via UV-LiGA.[43]

4.2.4 **Aptamers for SARS-CoV-2 selection**

DNA aptamers used in our assay were designed against the SARS-CoV-2 Spike (S) protein. Yanling *et al.*[44] used ACE2 competition and a machine learning screening algorithm to develop the aptamer. The most stable secondary structure of the 51 nt SARS-CoV-2 aptamer is shown in **Figure 4.2A** with thermodynamic properties shown in **Figure 4.2B**. The K_d of the aptamer has been reported to be 5.8 nM, which is smaller than the reported K_d of ACE2 and the SARS-CoV-2 S protein (34.6 nM).[38] DNA aptamers were modified with a 5' C12 amino linker and

a 3’ inverted dT (**Figure 4.2C**). All sequences of the aptamers used in this study are listed in **Table 4.1**.

Table 4.1. Sequences of the aptamers used in the study.[1, 3]

Virus Name	Aptamer Target Proteins	DNA Aptamer Sequence 5’-3’
SARS-CoV-2 (ATCC® VR-1986HK™) (heat inactivated)	S (spike)	CAGCACCGACCTTGTGCTTTGGGAGTGCTGGTCCAA G GGCGTTAATGGACA K_d =5.8 ± 0.8 nM
		ATCCAGAGTGACGCAGCATTTCATCGGGTCCAAAAGG GGCTGCTCGGGATTGCGGATATGGACACGT K_d=19.9 ± 2.6 nM
Human respiratory syncytial virus (RSV) type A2 ATCC® VR-1540™	glycoprotein (G)	TAG GGA AGA GAA GGA CAT ATG AT AGT GCG GTG AGC CGT CGG ACA TAC AAA TAC TT GAC TAG TAC ATG ACC ACT TGA K_d= 30 nM

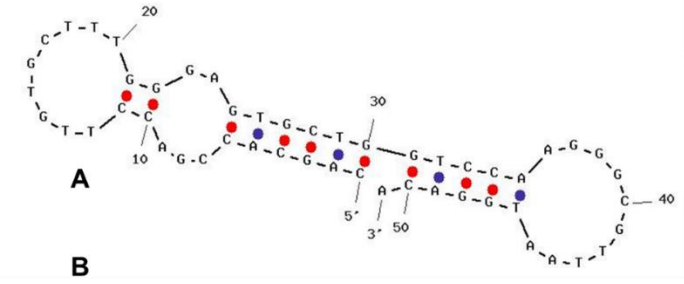

Aptamer	Length (nt)	ΔG (kcal/mole)	Tm(°C)	ΔH (kcal/mole)	ΔS (cal/K x mole)
SARS-CoV-2	51	-7.4	47.6	-104.9	-327.1

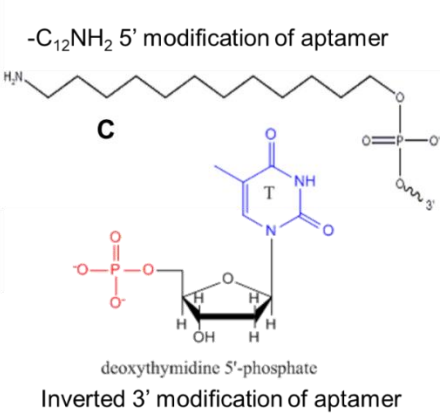

Figure 4.2. (**A**) Structure of the aptamer for SARS-CoV-2.[1] (Reproduced with permission from Ref 1 (https://doi.org/10.1021/acs.analchem.0c01394). Copyright (2020) American Chemical Society) (**B**) Thermodynamics showing the Gibbs free energy, enthalpy, and entropy for the most stable secondary structure of the 51 nt SARS-CoV-2 aptamer. (**C**) Functional groups employed within the aptamer structure to allow for covalent attachment to the activated plastic surface (5’ end with C12 linker and primary amine) and stabilization of the aptamer (3’ end with inverted dT residue).

4.2.5 **Purity and cleavage of the PC (photocleavable) linker**

Detailed synthetic routes and characterization of the PC linker are described elsewhere.[40] We verified the purity and cleavage of the PC linker before the experiments. The synthesized PC linker was dissolved in PBS (~2.0 µM) and exposed to blue light (400-450 nm, 34 ±4 mW/cm^2). Samples were collected after 0, 2, and 10 min of light irradiation and the products produced by irradiation were analyzed by UPLC/HRMS (Waters Acquity UPLC with a photodiode array UV detector and an LCT Premiere TOF mass spectrometer). Two µL of the irradiated PC linker was

injected into a Waters Acquity Atlantis T3 column (2.1 x 50 mm, 1.7 µm particle size), and the separation was performed at a flow rate of 0.6 mL/min. The gradient was run over 3.0 min and consisted of water and acetonitrile (95:5 to 0:100 with 0.05% TFA). The detection wavelength was set at 247 nm.

4.2.6 **PC linker-aptamer surface immobilization**

Immobilization of the affinity agent using the PC linker was reported previously by our group.[40] Briefly, the UV/O_3-activated and thermal fusion-bonded COP devices were wrapped in a protective Rubylith® film (Ulano) to prevent the photocleavage of the PC linker due to ambient light. EDC (20 mg/mL) and NHS (2 mg/mL) dissolved in dry ACN were infused into the device and incubated for 25 min at room temperature. Excess reagents were displaced by infusing the air, and PC linker (0.57 mM dissolved in dry ACN and 1.14 mM TEA) was introduced into the device. The devices were incubated at room temperature for 2 h. After the incubation, the excess reagents were removed from the device surface, and 100 mM Tris (pH 7.4) was introduced into the device to saturate unreacted NHS esters. After 30 min of incubation at room temperature, the air was infused into the device to remove the excess Tris buffer, and EDC/NHS reaction was performed in dry ACN to activate the -COOH group of the PC linker. Aptamer (40 µM) dissolved in PBS (pH 7.4) was infused into the device and incubated 2 h at room temperature or overnight at 4°C. Devices were rinsed with nuclease-free water (50 µL) and excess solvent or buffer before changing the infusion solvent/solution as a preventative measure against salt precipitation. The devices were washed with 0.5%BSA, 1%PVP prior to sample infusion.

4.2.7 **LED light exposure system**

LED light (M420L3, ThorLabs) producing light from 385–470 nm (λ_{max} = 412 nm) was used in these experiments as the light source for the photo-cleavage. The LED light was coupled with a 400 nm long-pass filter (Edmund Optics) to avoid the UV-A region of the emission spectrum. The LED was mounted into a polished aluminum chamber, and devices were kept beneath the

LED at a 24 mm distance. LED illuminated a 90 mm diameter spot at this distance. The light was triggered using an analog LED driver (Thorlabs) and a custom electronic timer.

4.2.8 Saliva samples

About 2 mL of saliva from consenting adults was collected to a plastic tube without stabilizer according to an approved IRB protocol. The collected saliva was then divided into 200 µL aliquots and stored at -80°C until further analysis.

4.2.9 Healthy donor and COVID-19 patient testing

Healthy donors were tested by Sinochips Diagnostics (Kansas City, KS). Two hundred µL of saliva was eluted into 50 µL using the MagMAX™ Viral/Pathogen Nucleic Acid Isolation Kit (Applied Biosystems, Cat A42352) and the KingFisher Flex system (Thermo Scientific). The eluate (5 µL) was evaluated with the COVID-19 Nucleic Acid RT-PCR Test (ZhuHai Sinochips Bioscience Co., Ltd, EUA201020) on an Applied Biosystems™ ABI 7500 Fast Dx Real-Time PCR system with SDS Software v.1.4.1. COVID-19 patients were tested in the KUMC Laboratory upon admission to the hospital. The clinical testing was performed using Cepheid Xpress SARS-CoV-2 with a sample collected via a nasopharyngeal swab, according to the manufacturer protocol under an FDA EUA. Samples were sent to the University of Kansas for testing in a blinded fashion. These samples were selected by a study coordinator and thus, do not represent the positivity rate of COVID-19 testing.

4.2.10 Sample processing

Saliva samples were hydrodynamically driven through the VP selection chip using a syringe pump (New Era Pump Systems, Inc., Farmingdale, NY USA) and a 1 mL tuberculin syringe fitted with a capillary connector (Inner-Lok™ union capillary connectors (Polymicro Technologies) and barbed socket Luer Lock™ fittings (3/32″ ID, McMaster-Carr). Samples were infused into the device at varying volumetric flow rates (20 -100 µL/min). Following sample

introduction, the VP selection chip was rinsed with PBS at 50 µL/min. All buffer solutions were filtered through a 0.45 µm polypropylene filter (Thermo Scientific) prior to use. VPs were released in PBS in ~30 µL. Approximately 1/2 of the eluent was analyzed using RT-qPCR, and the remaining portion was processed using the nCC.

4.2.11 **RT-qPCR***

**All RT-qPCR experiments were performed by Sachindra Gamage and Katie Childers in our lab.*

Table 4.2. Primer and probe sequences used in the study.

Virus Name, Gene Name		Reversed Primer 5'- 3'	Forward Primer 5'- 3'	Probe FAM-5'- 3'-BHQ1
HRSV, F gene		CTTTTGATCTTGTTCACTTCTCCTTCT	TTGGATCTGCAATCGCCA	TGGCACTGCTGTATCTAAGGTCCTGCACT
SARS-CoV-2	N1	TCTGGTTACTGCCAGTTGAATCTG	GACCCCAAAATCAGCGAAAT	ACCCCGCATTACGTTTGGTGGACC
	N2	GCGCGACATTCCGAAGAA	TTACAAACATTGGCCGCAAA	ACAATTTGCCCCCAGCGCTTCAG
	RNAse	GAGCGGCTGTCTCCACAAGT	AGATTTGGACCTGCGAGCG	TTCTGACCTGAAGGCTCTGCGCG
HCoV OC43		AATGTAAAGATGGCCGCGTATT	ATGTTAGGCCGATAATTGAGGACTAT	CATACTCTGACGGTCACAAT
HCoV 229E		CCAACACGGTTGTGACAGTGA	TTCCGACGTGCTCGAACTTT	TCCTGAGGTCAATGCA

RT-qPCR was used as the standard method for assay optimization and validation. For this, samples were first subjected to RNA extraction using a Zymo viral RNA extraction kit following the manufacturer's protocol. Purified total RNA was eluted in ~10 µL of nuclease-free water, and profiles of extracted total RNA were analyzed and quantified using gel electrophoresis (Agilent 2200 HSRNA TapeStation). Following purification, total RNA was immediately used for cDNA synthesis (5 µL for each RT(+) and RT(-) reactions in 50 µL total volume). cDNA for all viral species was synthesized via reverse transcription (RT) with random primers using ProtoScript II First Strand cDNA Synthesis Kit according to the manufacturer's instructions. RT(-) control reactions were performed in the absence of the RT enzyme. The thermal program consisted of 25°C (5 min), 42°C for 1 h followed by an enzyme inactivation step of 80°C for 5 min. qPCR consisted of 4 µL of cDNA in a 20 µL reaction volume with 0.5 µM forward and reverse primers

and 0.125 μM probe (see **Table 4.2** for the relevant sequences of primers and probes). The PCR thermal cycles for SARS-CoV-2 consisted of the CDC recommended protocol, which consisted of an initial denaturation step at 95°C for 3 min followed by 50 cycles of the following: 95°C for 3 s, 55°C for 30 s, and 72°C for 40 s.

RT-qPCR for HCoV OC43 and HCoV 229E were carried out using the following conditions: PCR activation at 95°C for 3 min and 50 cycles of amplification (15 s at 95°C and 1 min at 60°C). A summary of the qPCR figures-of-merit is shown in **Table 4.3.** Using HCoV 229E RT-qPCR, viral RNA copies ranging from 200 to 2×10^9 per reaction mixture were detected, corresponding to 10^4 to 10^{11} viral genome equivalents per mL.

Table 4.3. RT-qPCR figures of merit for the detection and quantification of different VPs.

Virus Name	Dynamic range tested (gRNA copies)	Linear regression
SARS-CoV-2	N1 and N2: $12 \times 10^0 - 0.8 \times 10^5$	N1: $y = -3.086x + 41.688$ ($R^2 = 0.997$) N2: $y = -3.069x + 40.901$ ($R^2 = 0.997$)
HRSV	$12 \times 10^0 - 1.1 \times 10^5$	$y = -3.788x + 41.048$ ($R^2 = 0.996$)
HCoV OC43	$16 \times 10^0 - 0.4 \times 10^5$	$y = -3.6048x + 41.956$ ($R^2 = 0.998$)
HCoV 229E	$16 \times 10^0 - 0.4 \times 10^5$	$y = -3.8881x + 42.865$ ($R^2 = 0.996$)

4.2.12 Nanoparticle tracking analysis (NTA)

VPs were analyzed via NTA (Nanosight NT 2.3). The samples were diluted 20× and vortexed prior to analysis. The instrument parameters used for the analysis consisted of: (i) Camera shutter 1206; (ii) camera gain 366; and (iii) capture duration 60 s. Five videos were taken for each sample at 25°C. The flow cell of the Nanosight instrument was washed 5 times with PBS in between sample analyses. During the final wash with PBS, a video was monitored to check if there were any particles left in the flow cell. If particles were detected, washing was continued until no particles were seen.

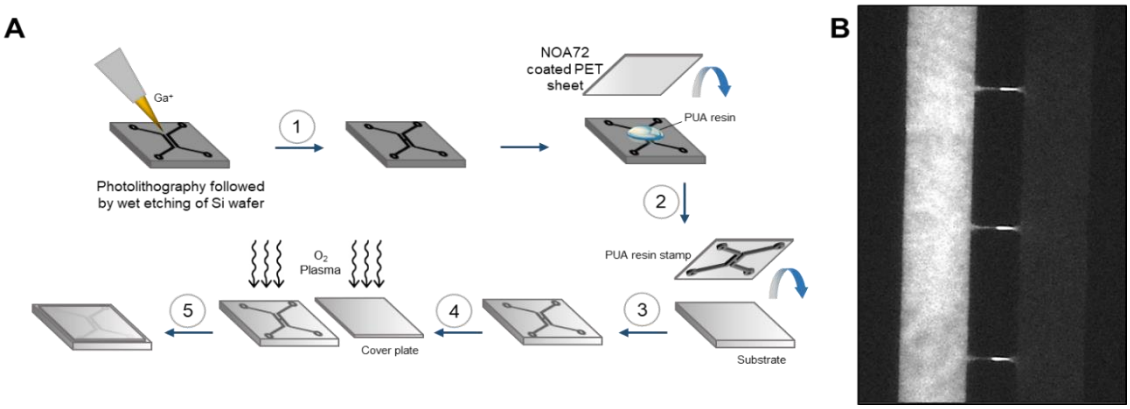

Figure 4.3. (**A**) Fabrication of nCC chip. The nCC included access microchannels fabricated via optical lithography with wet etching and nanostructures fabricated using focused-ion beam milling (step 1). Step 2 shows the resin stamp produced from the Si wafer using a UV curable polyurethane (PUA) resin that was placed on a PET sheet coated with a NOA72 adhesive. Step 3 shows the pattern of the PUA resin stamp imprinted into a plastic substrate. Step 4 presents the substrate and cover plate treated with O_2 plasma for the thermal fusion bonding step (i.e., assembly step). (**B**) Sealing test with 1 µM Rhodamine B (emission wavelength 532 nm and exposure of 100 ms) (Figure courtesy-Uditha Athapattu).

4.2.13 **Fabrication of the nano-Coulter counter (nCC)***

**Fabrication of the nCC was performed by Uditha Athapattu in our group.*

A schematic of the fabrication process for the nCC is presented in **Figure 4.3**. The access microchannels were fabricated in a Si wafer using conventional photolithography. Briefly, AZ1518 resist was spin-coated onto a Si wafer using a spin coater at 3,000 rpm for 30 s. The wafer was soft baked at 100°C for 10 min and allowed to cool until the wafer reached room temperature. A dark-field mask was placed on a mask aligner, and the wafer was exposed to UV light (365 nm) for 4 s through the mask. The wafer was then developed in MIF 300 for 20 s, rinsed with DI water, and dried with nitrogen. The wafer was inspected using an optical microscope to ensure that the patterns were transferred entirely. Wet etching of the Si wafer was done using 40% KOH with 5% IPA v/v at 70°C until the required depth (5 – 6 µm) was achieved. Then, the chromium layer was etched using a chromium etchant (step 1, **Figure 4.3A**). The cross channels and in-plane pores of the nCC were fabricated in the Si wafer using focused ion beam (FIB) milling with Ga ions. The structures were milled using a 48 pA beam current and a dwell time to achieve a 200 nm x 200 nm x 100 nm (w x d x l) in-plane nanopore. Resin stamps were produced from the Si master by

UV curing of a PUA resin for 3 min placed on a PET plate coated with a NOA72 adhesive (step 2, **Figure 4.3A**). Next, the structures on the resin stamp were thermally imprinted into PMMA or COP substrates using NIL (nanoimprint lithography; Nanonex 2500), which consisted of an air cushion thermal imprinting process (step 3, **Figure 4.3A**). nCC devices were thermally imprinted at 130°C and 300 psi for 5 min. A COC 8007 cover plate and the substrate were treated with O_2 plasma for 2 min (50 W) and then thermal fusion-bonded using NIL at 72°C and 110 psi for 15 min (steps 4 and 5, **Figure 4.3A**). Following nCC assembly, randomly selected devices were subjected to a sealing test using Rhodamine B seeding (**Figure 4.3B**).

4.2.14 **Clinical sample testing**

We received 10 saliva samples from volunteers that were asymptomatic and subsequently tested to assure they were indeed COVID-19 negative (these samples were confirmed to be COVID-19 negative by RT-qPCR). The 10 positive samples were randomly selected from symptomatic individuals that were admitted to the KU Medical Center hospital. Upon admission, a nasopharyngeal sample was collected, and the samples were subjected to RT-qPCR to confirm they were indeed COVID-19 positive. These 20 samples were blinded and shipped to the testing laboratory on the KU-Lawrence campus. All samples were stored at -80°C until required for measurements. Saliva samples were passed through the VP selection chips (200 μL), blue-light released from the chip following selection (~30 μL), and subjected either to nCC counting or RT-qPCR.

4.3 Results and Discussion

4.3.1 **VP selection chip and blue light release**

The VP selection chip contained 7 beds connected in parallel with perpendicular inlet and outlet channels arranged in a z-configuration. The device possessed ~1.5 million diamond-shaped pillars (10 µm x 10 µm, 10 µm spacing), providing a 38.6 cm^2 surface area (**Figure 4.4A-C**). **Figure 4.5A** provides a rapid scanning confocal image of a selection bed and the dimensional features of the pillars contained in one of the seven selection beds.The pillar number along with a small inter-pillar spacing allowed for high recovery of VPs and a high dynamic range, but with a small form factor. This chip was made from COP (cyclic olefin polymer) via injection molding to allow for high-scale production at low cost. Small distances between the pillars reduced diffusional distances and allowed for high recovery at high sample processing rates to keep the assay turnaround time short. Previously, this device was used for the affinity (antibody) selection of extracellular vesicles.[39]

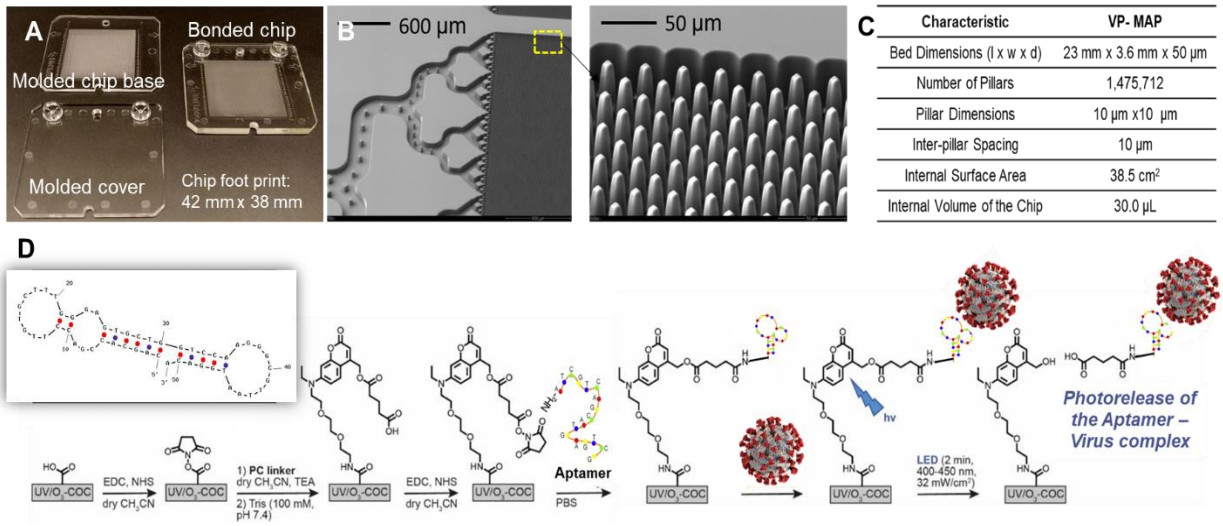

Figure 4.4. (A) Micrographs of the chip, cover plate and bonded VP selection chip. (B) SEMs of some of the beds in the VP selection device. Shown is the fluidic feed network into several beds and then, a high-resolution SEM of one bed with its micropillars. (C) Summary of the physical characteristics of the VP selection chip. (D) Scheme demonstrating covalent attachment of the aptamer via PC linker to the UV/O_3 activated surface of the plastic chip. Also shown is the stable secondary structure of the 51 nt SARS-CoV-2 aptamer.

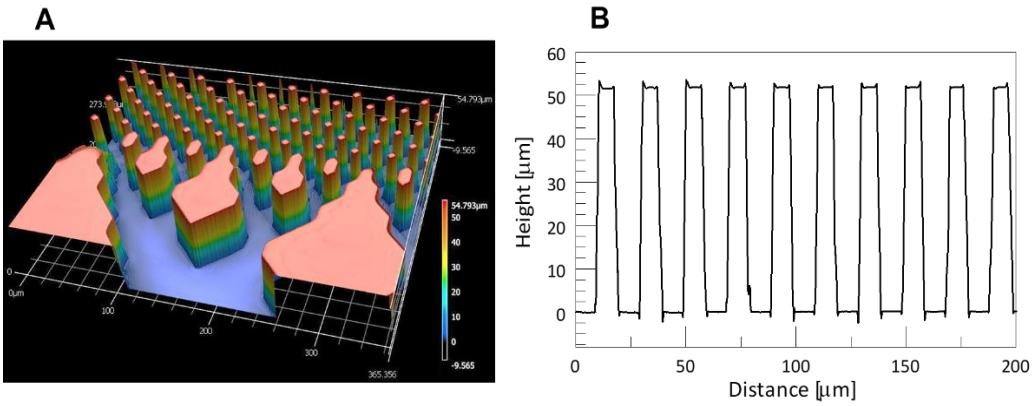

Figure 4.5. (**A**) Image of a part of the VP selection chip. (**B**) Profile of the post height and inter-post spacing in the microfluidic chip presented in (**A**).

In the current research, we employed a DNA aptamer targeting the S protein in the SARS-CoV-2 viral envelope as the affinity agent (K_d = 5.8 nM).[1] Owing to a lack of 2′-OH groups, DNAs are more resistant to endonucleases compared to an RNA aptamer, and thus, more stable in biological fluids. Because aptamers are chemically synthesized, they can be modified, and these modifications render them stable with a little batch-to-batch variation.[45] Modification of DNA aptamers (*i.e.,* 3' or 5' - internucleotide linkage, the so-called inverted dT (deoxy-thymidine),[46] phosphorothioate modified nucleotides) makes them stable in the presence of 3' exonucleases. For example, protective effects of 3'-inverted dT residues demonstrated an aptamer to the SARS-CoV/SARS-CoV-2 that could be incubated in serum for extended periods of time and showed no chemical degradation.[47-48] [44] Addition of an amino linker to the 5' or 3'-end of the aptamer and PEGylation can extend half-life in plasma.[47]

For the covalent attachment of the aptamer to the VP selection chip's surface, we used a photocleavable (PC) 7-amino coumarin linker (**Figure 4.4D**).[40] The PC linker is unique in its structure; it contains an amino and carboxy termini (*i.e*., amino acid) to allow for two EDC/NHS reactions to: (i) Covalently attach the linker to a carboxylated surface; and (ii) attach the aptamer containing a primary amine functionality at its 5' end.[40] We evaluated the purity and the photo-

cleavage of the PC linker (**Figure 4.6A**) via UPLC-MS. The intact PC linker (**1**) was present 81.2% before the light exposure and decreased with the irradiation time. After 2 min of light exposure,

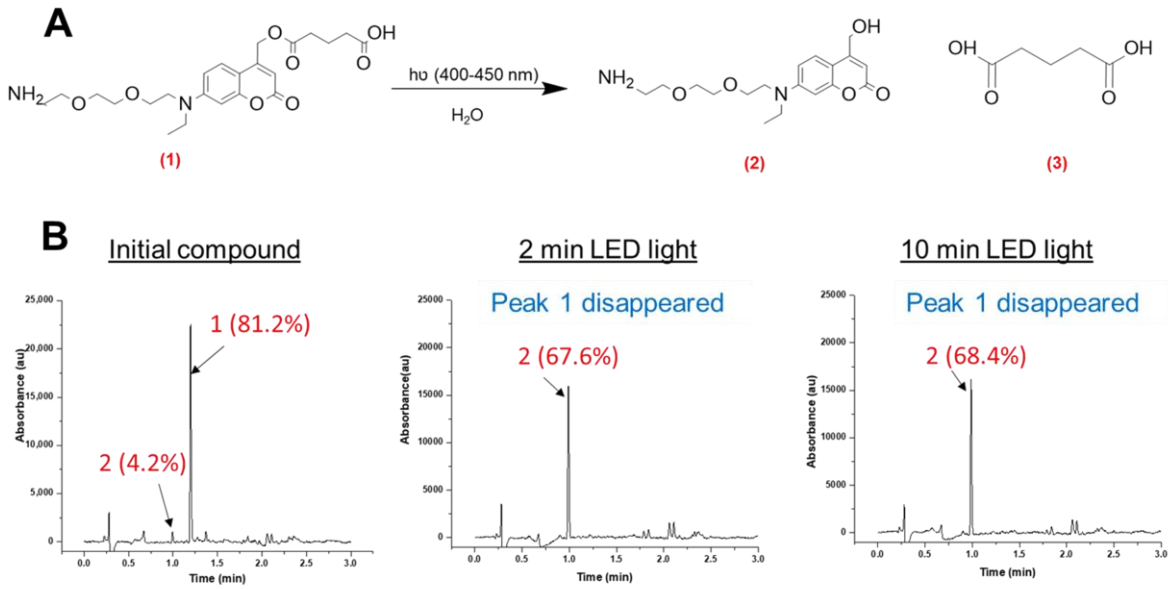

Figure 4.6. (**A**) PC linker photolysis reaction. (**B**) Ultra-high performance liquid chromatography (UPLC) signatures of the initial compound (**1**) and its photo lysis products **(2)** after exposing to 0, 2, and 10 min blue light (400-450 nm).

the chromatographic peak for the intact linker disappeared. Major photolysis product (**2**) was detected at the 4.2% level at the beginning and increased to 68% upon light irradiation (**Figure 4.6B**).

The optical transmittance of COP (cyclic olefin polymer) and COC (cyclic olefin copolymer) polymers were evaluated using UV-vis spectroscopy to ensure that sufficient amounts of blue light penetrated the microfluidic cover plate and substrate to provide sufficient levels of photolysis of the PC linker to release the VPs efficiently. **Figures 4.7A** and **4.7B** show the absorbance and transmittance spectra of COP and COC polymers. The COC and COP transmittance was ~90% at the peak LED emission wavelength. The spectral distribution of the LED used in these experiments was 400 – 450 nm (λ_{max} = 412 nm), and overlapped with the PC linker's absorption minimum. While the 1% PVP/0.5% BSA solution used to block the microfluidic

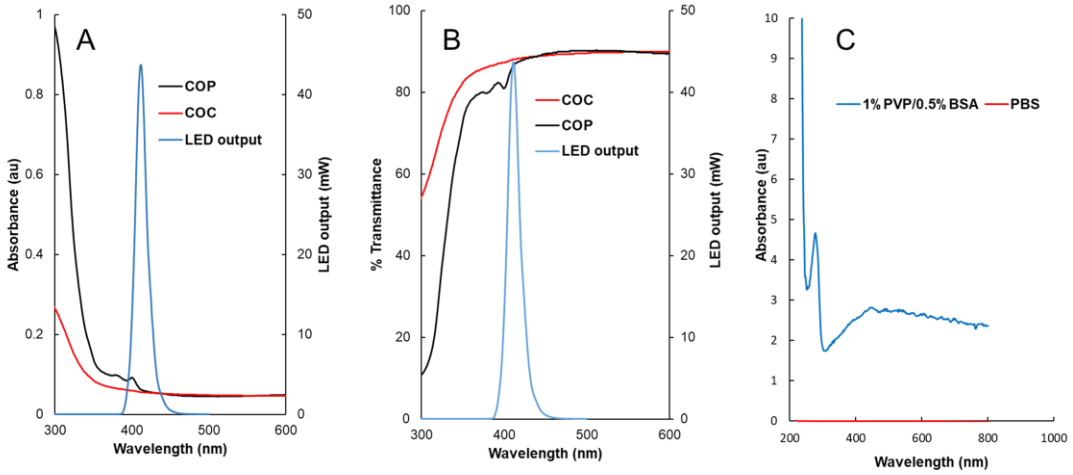

Figure 4.7. (A) UV-Vis absorption spectra for typical COC and COP plates (2 mm thick) and **(B)** the corresponding transmittance spectra. LED output light range is shown as a reference. **(C)** Absorbance of a 1% PVP/0.5% BSA solution and PBS buffer in the UV-Vis range. In this case, the PVP/BSA solution was placed in a 1 cm length cuvette to obtain the absorption spectrum.

chip surface to prevent non-specific adsorption showed some absorption over the spectral distribution of the blue-LED (**Figure 4.7C**), it was not used for the wash and release of VPs and the amount of absorption anticipated for a monolayer of PVP/BSA on the chip surface would be negligible compared to the conditions used to acquire the spectrum shown in **Figure 4.7C**.

We evaluated different blocking agents to minimize non-specific VP adsorption to the surface of the VP selection chip that was activated with UV/O_3 light (see **Figure 4.8A**). A 1% polyvinylpyrrolidone (PVP) and 0.5% bovine serum albumin (BSA) mixture added to PBS showed the lowest levels of non-specific adsorption; 1.4% of VPs non-specifically binding to the VP selection chip's surface, which was similar to the 2% PEG solution. However, we noticed that the 2% PEG solution was more viscous than the PVP/BSA solution, which can affect the recovery of the VPs because the recovery is dependent on diffusion. Based on these results, we chose PVP/BSA as a blocking agent for the aptamer-modified surface prior to VP infusion.

A

	UV/O_3 activated device passivated with blocking agents			
	Bare surface	1% BSA in PBS (n=3)	1% PVP/0.5% BSA in PBS (n=4)	2% PEG in PBS (n=4)
VPs non-specific adsorption (%)	17.3 ±10.9 (n=3)	5.3 ±0.4 (n=3)	1.4 ±0.1 (n=3)	1.4 ±1.6 (n=3)

C

Virus name	VP recovery SARS-CoV-2 aptamer (51 nt)	VP Recovery Non-specific aptamer (random)
Heat Inactivated SARS-CoV-2	39.4 ±12.4 (n=5)	1.9 ± 0.9 (n=6)
Active HCoV-OC43	3.5 ±1.3% (n=3)	-
Active HCoV-229E	0.7 ±0.8% (n=3)	-
Active HRSV	1.5 ±1.6% (n=7)	

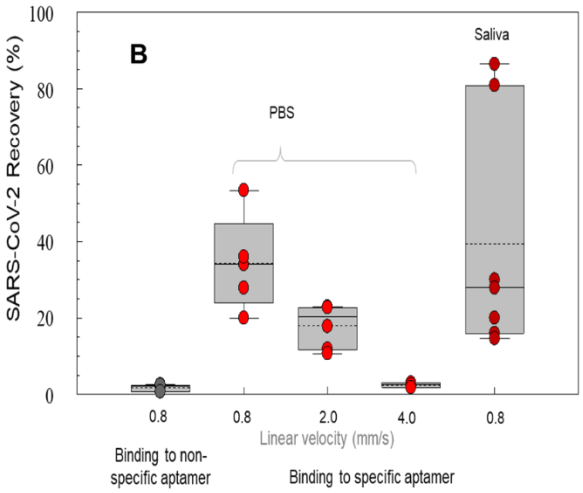

Figure 4.8. (**A**) summary of the evaluation of the efficiency of blocking agents in prevention of non-specific adsorption of VP to the surface. (**B**) Box plots presenting SARS-CoV-2 and HRSV non-specific binding to HRSV and SARS-CoV-2 aptamers, respectively and efficiency of the isolation of VPs from buffer and saliva at their specific aptamers bound to the affinity bed, at different linear velocities of sample processing. (**C**) Summary of the recovery of different VPs to the VP selection chip using different aptamers.

SARS-CoV-2 VPs, which were heat-inactivated, were seeded into PBS buffer and healthy donor saliva and infused through the VP selection chip. VPs were quantified via RT-qPCR from the starting solution and the chip eluent following VP photo-release. Primer sequences are listed in **Table 4.2,** and RT-qPCR figures-of-merit are shown in **Table 4.3**). We determined the efficiency for samples processed at different volumetric flow rates (5-20 µL/min; see **Figure 4.8B**). The seeding levels varied between 1 x 10^3 copies/mL and 1 x 10^6 copies/mL to represent VP load in clinical samples.[49] Non-specific binding (*i.e.*, VP cross-reactivity) was tested with the HRSV, human coronavirus 229E (HCoC 229E), and Betacoronavirus 1 (HCoV OC43). Non-specific binding as evaluated by recovery was determined to be 1.9 ± 0.9 (n = 6) for SARS-CoV-2 on the HRSV aptamer and 1.5 ±1.6 (n = 7) for HRSV on the SARS-CoV-2 aptamer chip (**Figure 4.8C**). Recovery of HCoC 229E and HCoV OC43 using the SARS-CoV-2 aptamer was found to be 0.7% and 3.5%, respectively. We should note that these human coronaviruses were not heat-inactivated, as was the case for the SARS-CoV-2 VPs.

The highest average recovery of VPs was observed at 0.8 mm/s (20 µL/min) linear velocity. We observed that as the linear velocity of the infused sample increased, the recovery of the VPs decreased, which is predictable due to the diffusion-controlled process that determines recovery. The recovery from saliva at 20 µL/min volumetric rates was determined to be 39.4% for heat-inactivated SARS-CoV-2. The recovery of the VPs from saliva was not statistically different from that found when the heat-inactivated SARS-CoV-2 was suspended in PBS (**Figure 4.8B**). We suspect that heat inactivation of SARS-CoV-2 could have changed the aptamer binding affinity to the epitope it was directed against in the S protein and thus affect the recovery.

We performed an experiment to determine the recovery of SARS-CoV-2 particles using our VP selection chip that was not subjected to heat inactivation. This was accomplished using a saliva sample that was positive for COVID-19 and found to have SARS-CoV-2 particles present within it. Because the number of VPs was not known in the sample, we used a self-referencing method that has been reported by our group.[50] For this determination, three VP selection chips were connected in series, and a positive COVID-19 saliva sample was flowed through the chips at 20 µL/min. Then, each chip in the series was quantified using RT-qPCR. For these

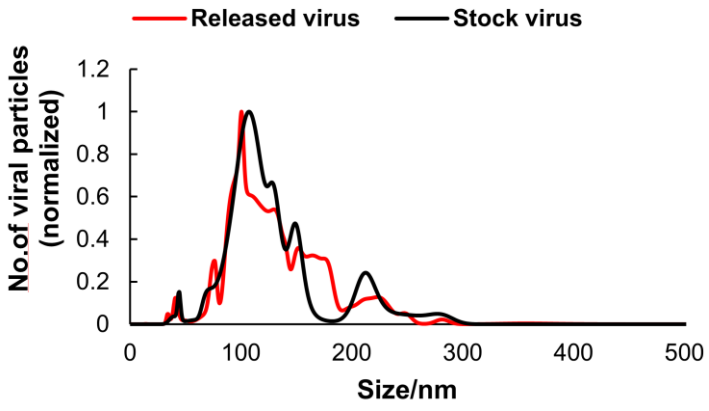

Figure 4.9. NTA of SARS-CoV-2 heat inactivated virus before and after selection using the pillared VP selection microchip. The mean diameter of the VPs in the stock and following release were 133.1 ±16.2 nm and 138.1 ±27.16 nm, respectively.

determinations, we found that the recovery of non-heat inactivated SARS-CoV-2 using our aptamer chip was 94.3% (n = 2).

We next evaluated the PC-release efficiency of the aptamer selected VPs. Release efficiency was calculated as the ratio of released VPs at 2 min with respect to all VPs released after 8 min of blue light exposure. The release efficiency was determined to be 87.9 ±9.1 (n = 8) for SARS-CoV-2 after 2 min exposure to the blue light with an energy of 18.5 J (412 nm, 32 ±4 mW/cm^2). The size distribution of the photo-released SARS-CoV-2 viral particles was compared with the stock viral particles and observed a similar size distribution (**Figure 4.9**).

4.3.2 **Nano coulter counter device**

The in-plane nCC device (**Figure 4.10A**) utilized some unique characteristics that made it appropriate for high throughput counting of single VPs including (i) Five nCC sensors placed in parallel to increase counting throughput; (ii) the device was fabricated in plastic using a top-down replication process making each pore of the sensor adopt an in-plane configuration (*i.e*., each pore was in the same plane as the fluidic network of the chip). In addition, RPS was used for label-free counting of the selected and released VPs. **Figure 4.10B** shows the equivalent RPS circuit for a single nCC sensor, where R_{mc} is the resistance of the access microchannel, R_{cc} is the resistance of the connecting channel, R_{np} is the resistance of the in-plane nanopore, and R_{np} is the resistance of the nanoparticle. The resistance of the electrolyte in the device is considered as a series connection in the circuit. Whenever the VP is traveling through the in-plane nanopore, the particle forms a parallel resistor with the nanopore resistance. We modeled via COMSOL a nanopore as a fluidic constriction through which VPs can pass and produce unique electrical signatures. When a VP occupies the nanopore, buffer ions are displaced, and the nanopore's resistivity transiently changes and causes a detectable current transient event.[51-53] Simulations aimed to gauge the feasibility (SNR) for enumerating 30-150 nm VPs within 50-200 nm nanopores were carried out. Detectable current transient events were generated for all VPs if nanopores

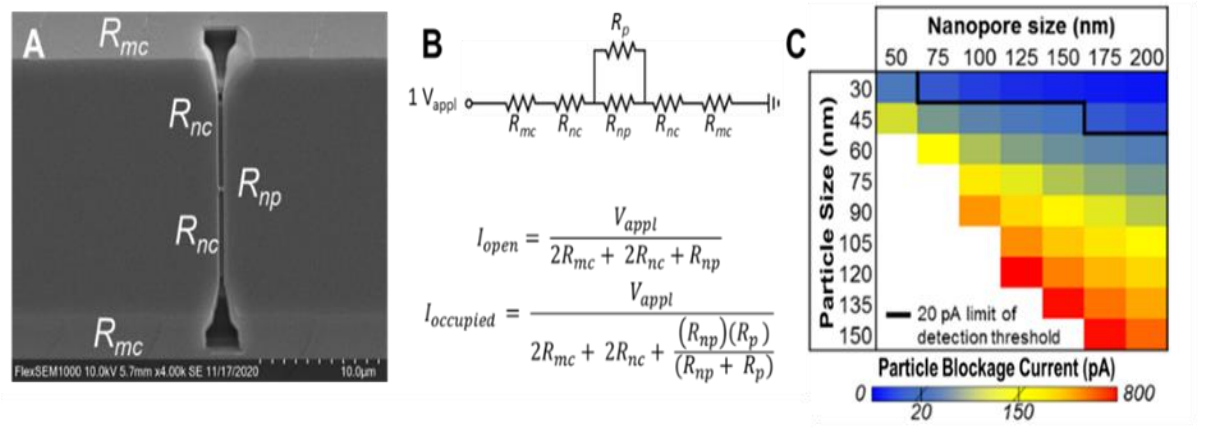

Figure 4.10. Nanopores for resistive pulse sensing of VPs**.** (A) SEM image of the nCC (200 nm effective diameter. (B) Equivalent sensing circuit for the nano-coulter counter, where R_{mc} is the resistance of the microchannel, R_{nc} is the resistance of nanochannel, R_{np} is the resistance of the in-plane nanopore, and R_{np} is the resistance of the nanoparticle. (C) Simulations of nanopore-based VPs sensing. (Figure courtesy – Zheng Zhao)

were appropriately sized, and current spikes scaled cubically with VP size (**Figure 4.10C**). Recorded peak amplitudes and widths can be used to determine the transit time of the VPs within the sensing element. The pore size (~350 nm effective diameter) was predicated on optimizing the amplitude of the RPS signal with respect to the SARS-CoV-2 particle size as determined using nanoparticle tracking analysis (NTA), which indicated an average diameter of ~138 nm with a mode of 128 nm (see **Figure 4.9** for NTA analysis).

4.3.3 **nCC calibration curve***

**Zheng Zhao in our group performed this experiment.*

Heat inactivated SARS-CoV-2 VPs at a concentration of 3×10^6 particles/ mL were serially diluted in PBS to establish a calibration curve (**Figure 4.11**). Five µl of each sample was introduced into the nCC chip. **Figure 4.11A** shows transient current responses for the heat-inactivated SARS-CoV-2 particles suspended in 1× PBS. Based on 5× standard deviation in the open pore trace, we established a threshold level for enumeration of the VPs at >99.99% confidence level. Current transient traces for heat-inactivated SARS-CoV-2 VPs traveling through

the pores are shown in **Figure 4.11B** (concentrated) and **Figure 4.11C** (diluted). **Figure 4.11D** is shown the calibration plot for the SARS-CoV-2 particles and yielded an adjusted R^2 of 0.979 over a VP concentration range of 1 x 10^3 to 3 x 10^6 VPs per mL. From this calibration plot, we estimated a concentration limit-of-detection of 1 x 10^3 VPs per mL.

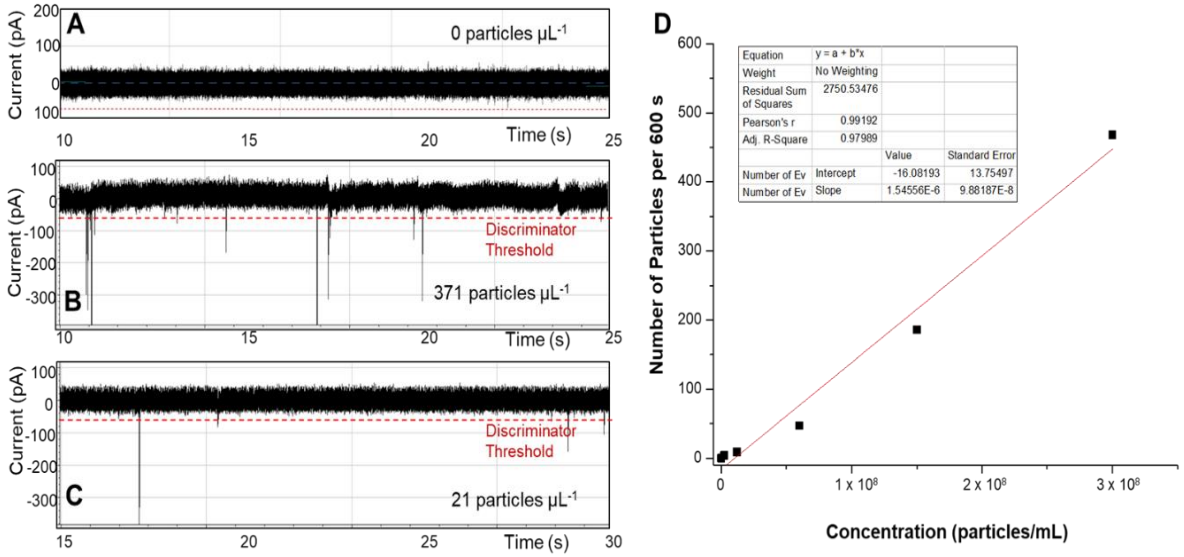

Figure 4.11. nCC transient current traces for (A) no particles (background) (B) concentrated particles, and (C) diluted particle concentrations. (D) Calibration of the nCC for the concentrations of SARS-CoV-2 particles ranging between 1.2× 10^6 /mL and 3× 10^8 /mL (Figure courtesy – Zheng Zhao).

4.3.4 **SARS-CoV-2 analysis from saliva samples**

We collected 20 saliva samples through an IRB-approved protocol at the University of Kansas Medical Center. Each sample was tested in an approved COVID-19 testing center using RT-qPCR (CDC-approved protocol). The remaining sample was then shipped to the University of Kansas and stored at -80°C until required for testing. To evaluate the ability to distinguish between those with active disease versus non-active disease (active disease is defined here as a sample containing VPs with intact S proteins), we followed the scheme shown in **Figure 4.12**. The saliva samples were processed using the VP selection chip (total sample volume = 200 µL), and the flow-through of the VP selection chip was subjected to RT-qPCR analysis. Following washing of

the VP selection chip with buffer, the chip was subjected to blue-light release of the selected VPs, the effluent was then used for nCC counting as well as subjected to RT-qPCR. The results are summarized in **Table 4.4**.

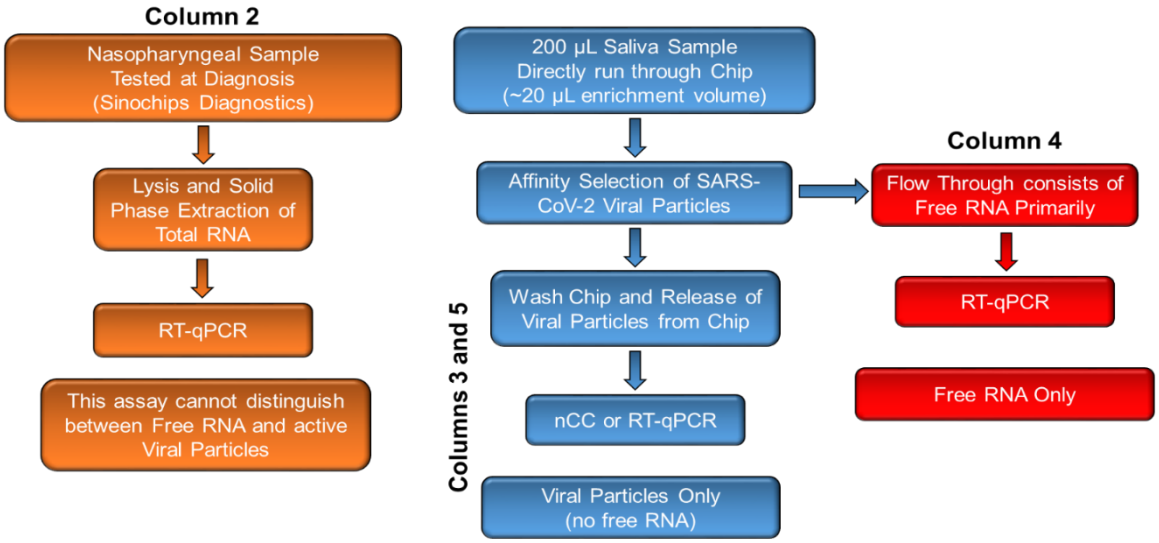

Figure 4.12. Experimental design for testing the 20 clinical samples received for this study. Matched nasopharyngeal and saliva samples were secured for each of the 20 patients through an IRB-approved protocol at the University of Kansas Medical Center.

As seen in **Table 4.4**, the samples deemed "not detected" by RT-qPCR in the approved testing laboratory agreed 100% with our results secured following chip selection of the SARS-CoV-2 VPs and testing of either the effluent or flow-through by RT-qPCR (clinical specificity = 100%). In the case of the 10 positive COVID-19 samples (as determined by the certified laboratory), only 5 samples were detected to be positive by released fraction RT-qPCR. Nine out of 10 samples were detected as positive by flow-through RT-qPCR. These results suggest that, the photo-cleavable fraction contains active viral particles and flow-through samples contains free gRNA. A positive RT-qPCR result here would indicate patients with no-active disease (*i.e.*, non-infectious).

To assure that no residual RNA fragments were present in the photocleavable fraction containing active viral particles, we did a control experiment in which gRNA from SARS-CoV-2 particles were sent through the VP selection chip, washed the chip with PBS and then subjected to blue-light photocleavage. This fraction was subjected to RT-qPCR. The gRNA contamination was <0.3% in the fraction.

Table 4.4. Summary of results for 20 saliva samples secured from anonymous donors. The first column of RT-qPCR results was performed in an approved COVID-19 testing laboratory. The second column of RT-qPCR results were secured using 5 µL of the photo-released fraction (35 µL total released volume) from the selection chip. The third column of RT-qPCR data were obtained from flowthrough samples. nCC data is not obtained yet.

Sample ID	Sinochips Diagnostics: SARS-CoV-2 gRNA presence in saliva (real time RT-PCR)*	SARS-CoV-2 g*RNA of Viral Particles*** following microfluidic affinity selection and release (via real time RT-PCR)**	Flow Through from microfluidic affinity selection chip (via real time RT-PCR)**	SARS-CoV-2 Affinity Selection, Release and nCC
1	Not detected	Not detected	Not detected	
4	Not detected	Not detected	Not detected	
5	Not detected	Not detected	Not detected	
7	Not detected	Not detected	Not detected	
8	Not detected	Not detected	Not detected	
10	Not detected	Not detected	Not detected	
13	Not detected	Not detected	Not detected	
14	Not detected	Not detected	Not detected	
16	Not detected	Not detected	Not detected	
19	Not detected	Not detected	Not detected	
2	Positive	Positive, 2.6 x10^2	Positive	
3	Positive	Positive, 8.7 x10^4	Positive	
11	Positive	Positive, 2.4 x10^3	Positive	
12	Positive	Positive, 6.3 x10^6	Positive	
15	Positive	Positive, 1.5 x10^2	Positive	
9	Positive	Not detected	Not detected	Not Detected
6	Positive	Not detected	Positive (8.4x10^2 gRNA/mL)	
17	Positive	Not detected	Positive (2.6x10^2 gRNA/mL)	
18	Positive	Not detected	Positive (6.8x10^2 gRNA/mL)	
20	Positive	Not detected	Positive (4.9x10^2 gRNA/mL)	
6 + 2	Positive	Positive	Positive	
11 + 18	Positive	Positive	Positive	

*Healthy donors test performed by Sinochips diagnostics with 0.2 mL saliva sample. COVID-19 positive individual's status confirmed using Cepheid Xpress SARS-CoV-2 test from a nasopharyngeal swab.
** ~200 µL of saliva processed on an aptamer modified microfluidic device for SARS-CoV-2 VP selection. VP releases and tested in real-time RT-qPCR.
*** RT-qPCR: N1 and/or N2: virus nucleocapsid (N) gene fragments targeted for specific detection of SARS-CoV-2.

4.4 Discussion

A recent survey of the general public, scientists, engineers, and health professionals (83-person study) highlighted several important high-level needs for new COVID-19 sensor technologies:[54] (i) Development of a point-of-care (instant) screening test for COVID-19; (ii) detect how infectious a person with the virus is; (iii) develop a non-invasive, quick, cheap, and effective

test that people can do themselves; and (iv) identify who needs COVID-19 testing in people with chronic conditions.

While RT-qPCR and serological tests have been the cornerstone of COVID-19 testing, they are challenged by some prevailing issues, the most notable of which are the sensitive reagents that require a cold-storage chain, the need for fluorescence detection in most cases, and the inability to distinguish between those with active disease and those without. Recent reports have suggested that RT-qPCR might overestimate the number of people actively spreading disease.[55] The inability to distinguish between these active and non-active spreaders results from the fact that RNA extraction procedures do not differentiate between RNA derived from active virus particles or from viral genomic fragments resulting from continuous viral RNA shedding.

The importance of the ability to discriminate between active and non-active individuals is paramount because it can determine the length of time in isolation (defined as separating those diagnosed with COVID-19 from those not infected) or planning mass quarantines (defined as separating or restricting the movement of those who have the potential to be exposed). For example, current recommendations for length of isolation for those diagnosed via RT-qPCR is 10-14 days after symptom onset or 72 h symptom-free, whichever is longer. In either case, extended isolation and/or quarantine by individuals can have dramatic socio-economic consequences, such as post-traumatic stress symptoms arising from financial loss, stigma, suicide, boredom, and infection fears.[56] In addition, extended isolation/quarantine can have detrimental effects on non-COVID-19 related diseases, such as cardiovascular disease due to changes in lifestyle.[57] Also, a population-based study performed in the UK indicated that due to delayed diagnostics, four cancer type deaths (breast, colorectal, lung, and esophageal) over a 5-y period would increase up to 9.6%, 16.6%, 5.3%, and 6.0% for breast, colorectal, lung and esophageal cancers, respectively.[58] Clearly, reducing isolation or quarantine times would improve the outcome for non-COVID-19 mortalities as well as reduce socio-economic issues.

Patients can show long-term positive RT-qPCR results due to persistent viral RNA shedding long after infectivity has ceased.[59-62] For example, of 378 patients diagnosed with COVID-19, many showed that the median duration of SARS-CoV-2 RNA appearance was 53.5 d with the longest duration determined to be 83 d.[5] This same study determined that SARS-CoV-2 IgM and IgG antibodies were persistently high 56 d post-infection. Persistent occurrence of SARS-CoV-2 RNA has also been associated with reverse transcribed and subsequent integration into the human genome.[55] A recent report on the temporal dynamics of viral shedding and transmissibility of COVID-19 indicated that 44% of transmission occurred in a pre-symptomatic stage of the viral load profile (see **Figure 4.1**).[36]

While viral infectivity can be deduced from culturing, its extensive workflow and long result turnaround time as well as the need for BSL-3 facilities makes this approach intractable for determining infectivity. A recent report indicated that the use of RT-qPCR with Ct <24 and symptom onset <8 d indicated a correlation with infectivity as determined by viral culture (odds ratio = 0.64),[63] but issues with this approach is that the test still depends on the use of sensitive reagents and the fact that determining exact symptom onset would be difficult to determine in many patients, especially those that are asymptomatic.

We outlined a unique technology that addresses the aforementioned challenges and is based on the ability to affinity select SARS CoV-2 particles from clinical samples and enumerate them in a label-free manner. The technology consisted of two fluidic devices, including an affinity selection microfluidic and nCC chips. The design and performance criteria of the VP selection and nCC chips were: (i) short processing time (<20 min); (ii) large dynamic range to accommodate the range of VPs that can be found in samples (500 – 10^8 VPs per mL);[27] (iii) manufactured at high production rates, low cost, and with tight compliance for screening applications that demand disposable devices; (iv) small form factor to fit into a handheld instrument for potential at-home testing (38 x 42 mm); and (v) reagent-free operation with a stable affinity agent for long term storage that can allow for stockpiling the disposable for future pandemics to allow for rapid

mobilization. The important attributes of our sensor technology satisfy 3/4 needs highlighted from the 83-person survey noted above.[54]

While antibodies have been widely used for the affinity selection of biological targets, aptamers as recognition elements offer several valuable qualities. For example, aptamer selection from DNA libraries is a controlled *in vitro* process designed to select sequences that bind to a target of interest while discarding sequences that bind to negative targets**.** Indeed, the aptamer used in our sensor technology showed a recovery value for non-heat inactivated SARS-CoV-2 of 94.3% with minimal binding affinity to other human coronaviruses (see **Figure 4.8C**). In addition, monoclonal antibody development can take up to a year, while aptamers can be developed in a much shorter time period due to the *in vitro* selection process, meaning that for new pandemics, new aptamers can be selected quickly for rapid wide-scale testing. Aptamers exhibit notable affinity to their targets with K_d ranging from the high pM to low nM range.[64] Finally, DNA aptamers are exceptionally stable and can be stored for extended periods of time without cold storage. In our case, once the aptamer was covalently attached to the surface of the VP selection chip, no reagents were required to carry out the selection phase of the assay, except for common buffers, such as PBS. This was facilitated by the fact that blue-light from an LED was used to release the selected VPs from the chip eliminating the need for an additional reagent.[40]

The data in **Table 4** offers some interesting results and conclusions when compared to RT-qPCR, which is currently the gold-standard for COVID-19 testing. For example, of the 10 samples that were positive by conventional RT-qPCR, only 5 were found to be positive when the photo-cleaved fraction was analyzed by RT-qPCR due to the fact that only active viral particles were present in this effluent (see the experimental design in **Figure 4.12**), while inspection of the results from the flow-through of this chip showed 9 samples to be positive by RT-qPCR. This indicated that 5 of the 10 positive samples actually contained “active” VPs with an intact S protein and viral capsid containing gRNA. The flow-through will contain primarily free RNA fragments, and the photo-released fraction consists of intact viral particles and practically no free RNA (<0.3%). While

we have demonstrated the ability to differentiate between those COVID-19 patients with and without active VPs, we need to perform culturing experiments on the selected VPs to make sure that we are actually detecting those that are infectious; this work is currently underway.

For COVID-19 testing, the CDC and WHO recommend collecting upper respiratory specimens including nasopharyngeal (NP), oropharyngeal (OP), nasopharyngeal wash (NW), or anterior nares (nasal swab). NP, OP, NW, and nasal swabs must be collected by healthcare personnel, which carries a risk of potential healthcare worker infection.[65] However, self-collected samples, such as saliva, can be performed with no or minimal supervision.[66-67] Saliva samples for COVID-19 testing have demonstrated comparable results to NP and OP samples.[65-66, 68] For example, in studies, which used RT-qPCR to determine viral load from saliva, a median viral load for first testing was found to be 3.6×10^6 VPs per mL (range of $9.9 \times 10^2 – 1.8 \times 10^8$ particles per mL).[69] Recently published work[70] reports a 3.4% (n=7,332 paired samples) increase in positivity rate using NP vs saliva specimens.

Compared to other designs, our nCC chip has several advantages: (i) Due to the positioning of the nanopore sensing element within a fluidic network, the sample volume requirement is small (5-10 µL); (ii) high-resolution electronic signal recordings can provide reliable and accurate information of particle size (peak amplitude) and particle travel time (peak width) as well as particle concentration (current transient peak frequency); (iii) dynamic range of 10^2 to 10^8 particles/mL based on 100,000 Hz sampling frequency with 600 s recording time; (iv) the sensing mechanism allows the nCC to be used for VP counting, but other nanoparticles such as extracellular vesicles can be counted as well; (v) 5 pores in parallel allows for high throughput counting and improve the limit-of-detection.

4.5 Conclusion

Screening tests, such as those geared for at-home use, for SARS-CoV-2 infections can be an essential tool for effective containment of COVID-19 because it allows for more frequent testing

and provides rapid results as opposed to clinical testing that is performed less frequently because it requires a centralized laboratory or other sites that can conduct POCT (see **Figure 1**). While new at-home technologies that are based on PCR or antibodies are evolving, they are some challenges such as the need for cold storage due to the use of sensitive reagents, which creates problems with rolling out tests quickly to meet testing demands. An additional challenge with PCR and antibody-based technologies is that they detect those that have COVID-19, but most likely will not report on the active state of the disease-causing excessive isolation and/or quarantine.

To address these challenges, we presented a technology to identify those that have been infected with SARS-CoV-2. Unique to our technology is the ability to select intact SARS-CoV-2 VPs from the sample and perform label-free counting of the VPs following selection and blue-light release of the intact VPs. We envision our technology for immediate use by first-contact

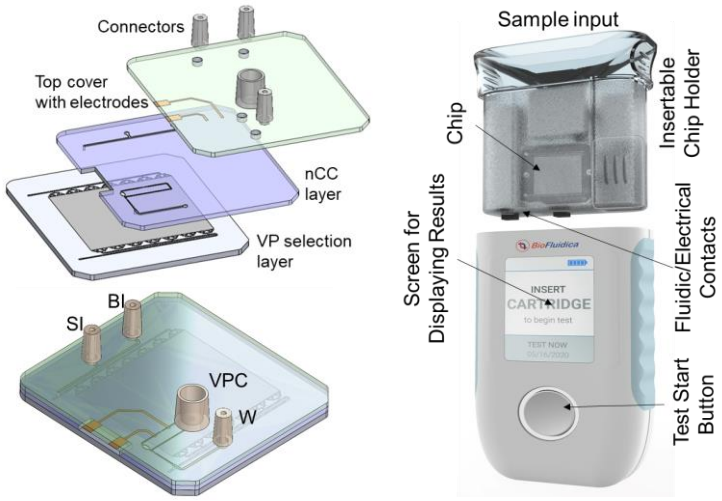

Figure 4.13. Conceptual drawings of SARS-CoV-2 chip (**A**) and handheld instrument (**B**) for at-home testing. The integrated chip is comprised of 3 layers containing the VP selection chip, the nCC chip, and the cover plate with electrical connectors. All three layers are made from a thermoplastic to allow for injection molding. Shown in the lower panel is the integrated chip with connectors for sample input (SI), buffer input for priming and washing the chip (BI), waste (W) and viral particle collector chamber (VPC). The handheld instrument contains pumps and microprocessor for fluid handling and data control and acquisition for the nCC including a transient current amplifier circuitry. The handheld also contains a blue LED for selected VP release. The size of the handheld is 120 mm (long) x 80 mm (wide).

healthcare professionals at the POC and then, due to the simplicity of the instrumentation and ease of use, home-based testing. The microfluidic devices, which were made from thermoplastics,

can be fabricated by injection molding, which is conducive to high-scale production at a low cost appropriate for large-scale screening tests.

Our assay's analytical figures-of-merit provided high VP recovery, high throughput processing capabilities for VP selection directly from a saliva sample, and an affinity agent that was appropriate for selection with high specificity and appropriate for room temperature storage. This was enabled by the high stability of nucleic acids compared to biological reagents required for PCR and serological tests. In addition, we could rapidly detect single VPs using a nCC that possessed 5 counters in parallel but could be further scaled. Taken together, these microfluidic chips could process saliva samples to test for COVID-19 in <20 min.

To envision at-home testing using our SARS-CoV-2 assay, the chip operation and supporting equipment need to be packaged into a handheld instrument with full sample processing automation. To realize this, our team is currently working on a new integrated chip design and handheld instrument as shown in **Figures 4.13A** and **B**, respectively. The chip measures 38 x 42 mm in size and consists of 3 layers, including a cover plate with electrical connections for the nCC, a layer containing the VP selection step, and the final layer consisting of the fluidic network for nCC enumeration of selected and subsequently released VPs via blue light. The integrated chip, which is made entirely from plastics to allow for injection molding, fits into the handheld instrument and contains a port that allows for sample introduction, which consists of saliva. However, other samples can be inserted into the instrument as well.

Finally, what about the ability of our technology to detect variants of SARS-CoV-2, especially because the aptamer being used for selection is directed against the receptor-binding domain (RBD) of the spike protein?[1] These variants include the UK (B.1.1.7), South African (501Y.V2), and Brazilian (B.1.1.28) lineages.[71-73] For example, the B.1.1.7 variant consists of 17 mutations, of which 8 appear in the spike protein. In particular, the N501Y mutation affects the binding of the spike protein to the ACE2 receptor. We are currently evaluating the ability of the 51-nt aptamer to

recover variants from clinical samples. If they show poor binding affinity to these or other variants, new aptamers can be explicitly selected for the variants in short time periods.

4.6 Acknowledgements

The authors thank the NIH for financial support of this work via (NIH RADx program; NIBIB P41-EB020594; P20-GM130423). The authors also acknowledge the KU Nanofabrication Facility (KUNF) and the University of Kansas Cancer Center's Biospecimen Repository (NCI: P30-CA168524). We would also like to thank Dr. Steve Wolpe, Dr. Bill Turpin, and Dr. Jaya Ghosh for helpful discussions during the course of this work.

4.7 References

1. Song, Y.; Song, J.; Wei, X.; Huang, M.; Sun, M.; Zhu, L.; Lin, B.; Shen, H.; Zhu, Z.; Yang, C., Discovery of Aptamers Targeting Receptor-Binding Domain of the SARS-CoV-2 Spike Glycoprotein. **2020**.
2. Yuan, X.; Yang, C.; He, Q.; Chen, J.; Yu, D.; Li, J.; Zhai, S.; Qin, Z.; Du, K.; Chu, Z., Current and Perspective Diagnostic Techniques for COVID-19. *ACS infectious diseases* **2020,** *6* (8), 1998-2016.
3. Percze, K.; Szakács, Z.; Scholz, É.; András, J.; Szeitner, Z.; Kieboom, C. H. v. d.; Ferwerda, G.; Jonge, M. I. d.; Gyurcsányi, R. E.; Mészáros, T., Aptamers for respiratory syncytial virus detection. *Scientific Reports* **2017,** *7* (1), 42794.
4. Chu, D. K.; Pan, Y.; Cheng, S. M.; Hui, K. P.; Krishnan, P.; Liu, Y.; Ng, D. Y.; Wan, C. K.; Yang, P.; Wang, Q., Molecular diagnosis of a novel coronavirus (2019-nCoV) causing an outbreak of pneumonia. *Clinical chemistry* **2020,** *66* (4), 549-555.
5. Li, N.; Wang, X.; Lv, T., Prolonged SARS-CoV-2 RNA shedding: Not a rare phenomenon. *Journal of Medical Virology* **2020,** *92*, 2286-2287.
6. Xu, Z.; Shi, L.; Wang, Y.; Zhang, J.; Huang, L.; Zhang, C.; Liu, S.; Zhao, P.; Liu, H.; Zhu, L., Pathological findings of COVID-19 associated with acute respiratory distress syndrome. Lancet Respir Med. 2020. *DOI: https://doi. org/10.1016/S2213-2600 (20)* **2020**.
7. Cui, J.; Li, F.; Shi, Z. L., Origin and evolution of pathogenic coronaviruses. *Nat Rev Microbiol* **2019,** *17* (3), 181-192.
8. Bárcena, M.; Oostergetel, G. T.; Bartelink, W.; Faas, F. G.; Verkleij, A.; Rottier, P. J.; Koster, A. J.; Bosch, B. J., Cryo-electron tomography of mouse hepatitis virus: insights into the structure of the coronavirion. *Proceedings of the National Academy of Sciences* **2009,** *106* (2), 582-587.
9. Neuman, B. W.; Adair, B. D.; Yoshioka, C.; Quispe, J. D.; Orca, G.; Kuhn, P.; Milligan, R. A.; Yeager, M.; Buchmeier, M. J., Supramolecular architecture of severe acute respiratory syndrome coronavirus revealed by electron cryomicroscopy. *Journal of virology* **2006,** *80* (16), 7918-7928.
10. Wang, Y.; Sun, J.; Zhu, A.; Zhao, J.; Zhao, J., Current understanding of middle east respiratory syndrome coronavirus infection in human and animal models. *Journal of thoracic disease* **2018,** *10* (Suppl 19), S2260.

11. Chen, B.; Tian, E. K.; He, B.; Tian, L.; Han, R.; Wang, S.; Xiang, Q.; Zhang, S.; El Arnaout, T.; Cheng, W., Overview of lethal human coronaviruses. *Signal Transduct Target Ther* **2020,** *5* (1), 89.
12. Ye, Z.-W.; Yuan, S.; Yuen, K.-S.; Fung, S.-Y.; Chan, C.-P.; Jin, D.-Y., Zoonotic origins of human coronaviruses. *International journal of biological sciences* **2020,** *16* (10), 1686.
13. Cheng, M. P.; Papenburg, J.; Desjardins, M.; Kanjilal, S.; Quach, C.; Libman, M.; Dittrich, S.; Yansouni, C. P., Diagnostic testing for severe acute respiratory syndrome–related coronavirus-2: A narrative review. *Annals of internal medicine* **2020**.
14. Malik, Y. A., Properties of Coronavirus and SARS-CoV-2. *The Malaysian Journal of Pathology* **2020,** *42* (1), 3-11.
15. Weiss, S. R.; Leibowitz, J. L., Coronavirus pathogenesis. In *Advances in virus research*, Elsevier: 2011; Vol. 81, pp 85-164.
16. Schoeman, D.; Fielding, B. C., Coronavirus envelope protein: current knowledge. *Virology journal* **2019,** *16* (1), 1-22.
17. Jin, Y.-H.; Cai, L.; Cheng, Z.-S.; Cheng, H.; Deng, T.; Fan, Y.-P.; Fang, C.; Huang, D.; Huang, L.-Q.; Huang, Q., A rapid advice guideline for the diagnosis and treatment of 2019 novel coronavirus (2019-nCoV) infected pneumonia (standard version). *Military Medical Research* **2020,** *7* (1), 4.
18. Hogan, C. A.; Garamani, N.; Lee, A. S.; Tung, J. K.; Sahoo, M. K.; Huang, C.; Stevens, B.; Zehnder, J.; Pinsky, B. A., Comparison of the Accula SARS-CoV-2 test with a laboratory-developed assay for detection of SARS-CoV-2 RNA in clinical nasopharyngeal specimens. *Journal of Clinical Microbiology* **2020**.
19. Creager, H. M.; Cabrera, B.; Schnaubelt, A.; Cox, J. L.; Cushman-Vokoun, A. M.; Shakir, S. M.; Tardif, K. D.; Huang, M.-L.; Jerome, K. R.; Greninger, A. L., Clinical evaluation of the BioFire® Respiratory Panel 2.1 and detection of SARS-CoV-2. *Journal of Clinical Virology* **2020,** *129*, 104538.
20. Visseaux, B.; Le Hingrat, Q.; Collin, G.; Bouzid, D.; Lebourgeois, S.; Le Pluart, D.; Deconinck, L.; Lescure, F.-X.; Lucet, J.-C.; Bouadma, L., Evaluation of the QIAstat-Dx Respiratory SARS-CoV-2 Panel, the first rapid multiplex PCR commercial assay for SARS-CoV-2 detection. *Journal of clinical microbiology* **2020**.
21. Noerz, D.; Fischer, N.; Schultze, A.; Kluge, S.; Mayer-Runge, U.; Aepfelbacher, M.; Pfefferle, S.; Luetgehetmann, M., Clinical evaluation of a SARS-CoV-2 RT-PCR assay on a fully automated system for rapid on-demand testing in the hospital setting. *Journal of Clinical Virology* **2020**, 104390.
22. Zanoli, L. M.; Spoto, G., Isothermal amplification methods for the detection of nucleic acids in microfluidic devices. *Biosensors* **2013,** *3* (1), 18-43.
23. Broughton, J. P.; Deng, X.; Yu, G.; Fasching, C. L.; Servellita, V.; Singh, J.; Miao, X.; Streithorst, J. A.; Granados, A.; Sotomayor-Gonzalez, A., CRISPR–Cas12-based detection of SARS-CoV-2. *Nature Biotechnology* **2020**, 1-5.
24. Zhang, F.; Abudayyeh, O. O.; Gootenberg, J. S., A protocol for detection of COVID-19 using CRISPR diagnostics. *A protocol for detection of COVID-19 using CRISPR diagnostics* **2020,** *8*.
25. Hosseini, A.; Pandey, R.; Osman, E.; Victorious, A.; Li, F.; Didar, T.; Soleymani, L., Roadmap to the Bioanalytical Testing of COVID-19: From Sample Collection to Disease Surveillance. *ACS sensors* **2020**.
26. Lambert-Niclot, S.; Cuffel, A.; Le Pape, S.; Vauloup-Fellous, C.; Morand-Joubert, L.; Roque-Afonso, A.-M.; Le Goff, J.; Delaugerre, C., Evaluation of a rapid diagnostic assay for detection of SARS CoV-2 antigen in nasopharyngeal swab. *Journal of clinical microbiology* **2020**.
27. Nagura-Ikeda, M.; Imai, K.; Tabata, S.; Miyoshi, K.; Murahara, N.; Mizuno, T.; Horiuchi, M.; Kato, K.; Imoto, Y.; Iwata, M., Clinical evaluation of self-collected saliva by RT-qPCR, direct

RT-qPCR, RT-LAMP, and a rapid antigen test to diagnose COVID-19. *Journal of Clinical Microbiology* **2020**.
28. Grant, B. D.; Anderson, C. E.; Williford, J. R.; Alonzo, L. F.; Glukhova, V. A.; Boyle, D. S.; Weigl, B. H.; Nichols, K. P., SARS-CoV-2 coronavirus nucleocapsid antigen-detecting half-strip lateral flow assay toward the development of point of care tests using commercially available reagents. *Analytical chemistry* **2020,** *92* (16), 11305-11309.
29. Matthews, Q.; da Silva, S. J. R.; Norouzi, M.; Pena, L. J.; Pardee, K., Adaptive, diverse and de-centralized diagnostics are key to the future of outbreak response. *BMC biology* **2020,** *18* (1), 1-5.
30. Liu, Y.; Liu, Y.; Diao, B.; Ren, F.; Wang, Y.; Ding, J.; Huang, Q., Diagnostic Indexes of a Rapid IgG/IgM Combined Antibody Test for SARS-CoV-2. *medRxiv* **2020**.
31. Chen, Z.; Zhang, Z.; Zhai, X.; Li, Y.; Lin, L.; Zhao, H.; Bian, L.; Li, P.; Yu, L.; Wu, Y., Rapid and Sensitive Detection of anti-SARS-CoV-2 IgG, Using Lanthanide-Doped Nanoparticles-Based Lateral Flow Immunoassay. *Analytical chemistry* **2020,** *92* (10), 7226-7231.
32. https://www.fda.gov/medical-devices/coronavirus-disease-2019-covid-19-emergency-use-authorizations-medical-devices/vitro-diagnostics-euas#individual-serological (accessed 11.15.20).
33. Mertens, P.; De Vos, N.; Martiny, D.; Jassoy, C.; Mirazimi, A.; Cuypers, L.; Van den Wijngaert, S.; Monteil, V.; Melin, P.; Stoffels, K., Development and potential usefulness of the COVID-19 Ag Respi-Strip diagnostic assay in a pandemic context. *Frontiers in Medicine* **2020,** *7*, 225.
34. Mak, G. C.; Cheng, P. K.; Lau, S. S.; Wong, K. K.; Lau, C.; Lam, E. T.; Chan, R. C.; Tsang, D. N., Evaluation of rapid antigen test for detection of SARS-CoV-2 virus. *Journal of Clinical Virology* **2020**, 104500.
35. Mina, M. J.; Parker, R.; Larremore, D. B., Perspective: Rethinking Covid-19 Test Sensitivity — A Strategy for Containment. *New England Journal of Medicine* **2020,** *382*, 1-3.
36. He, X.; Lau, E. H. Y.; Wu, P.; Deng, X.; Wang, J.; Hao, X.; Lau, Y. C.; Wong, J. Y.; Guan, Y.; Tan, X.; Mo, X.; Chen, Y.; Liao, B.; Chen, W.; Hu, F.; Zhang, Q.; Zhong, M.; Wu, Y.; Zhao, L.; Zhang, F.; Cowling, B. J.; Li, F.; Leung, G. M., Temporal dynamics in viral shedding and transmissibility of COVID-19. *Nature Medicine* **2020,** *26*, 672-675.
37. Jiang, S.; Hillyer, C.; Du, L., Neutralizing Antibodies against SARS-CoV-2 and Other Human Coronaviruses. *Trends in Immunology* **2020**.
38. Wrapp, D.; Wang, N.; Corbett, K. S.; Goldsmith, J. A.; Hsieh, C.-L.; Abiona, O.; Graham, B. S.; McLellan, J. S., Cryo-EM structure of the 2019-nCoV spike in the prefusion conformation. *Science* **2020,** *367* (6483), 1260-1263.
39. Wijerathne, H.; Witek, M. A.; Jackson, J. M.; Brown, V.; Hupert, M. L.; Herrera, K.; Kramer, C.; Davidow, A. E.; Li, Y.; Baird, A. E.; Murphy, M. C.; Soper, S. A., Affinity enrichment of extracellular vesicles from plasma reveals mRNA changes associated with acute ischemic stroke. *Communications Biology* **2020,** *3* (1), 613.
40. Pahattuge, T. N.; Jackson, J. M.; Digamber, R.; Wijerathne, H.; Brown, V.; Witek, M. A.; Perera, C.; Givens, R. S.; Peterson, B. R.; Soper, S. A., Visible photorelease of liquid biopsy markers following microfluidic affinity-enrichment. *Chemical Communications* **2020,** *56* (29), 4098-4101.
41. Maas, S. L.; Broekman, M. L.; de Vrij, J., Tunable resistive pulse sensing for the characterization of extracellular vesicles. In *Exosomes and Microvesicles*, Springer: 2017; pp 21-33.
42. Anderson, W.; Lane, R.; Korbie, D.; Trau, M., Observations of tunable resistive pulse sensing for exosome analysis: improving system sensitivity and stability. *Langmuir* **2015,** *31* (23), 6577-6587.
43. Soper, S. A.; Ford, S. M.; Qi, S.; McCarley, R. L.; Kelly, K.; Murphy, M. C., Polymeric microelectromechanical systems. *Analytical Chemistry* **2000,** *72* (19), 642A-651A.

44. Yanling, S.; Jia, S.; Xinyu, W.; Mengjiao, H.; Miao, S.; Lin, Z.; Bingqian, L.; Haicong, S.; Zhi, Z.; Chaoyong, Y., *Discovery of Aptamers Targeting Receptor-Binding Domain of the SARS-CoV-2 Spike Glycoprotein*. 2020.
45. Yang, S.; Li, H.; Xu, L.; Deng, Z.; Han, W.; Liu, Y.; Jiang, W.; Zu, Y., Oligonucleotide Aptamer-Mediated Precision Therapy of Hematological Malignancies. *Molecular Therapy - Nucleic Acids* **2018,** *13*, 164-175.
46. Chai, Z.; Guo, L.; Jin, H.; Li, Y.; Du, S.; Shi, Y.; Wang, C.; Shi, W.; He, J., TBA loop mapping with 3′-inverted-deoxythymidine for fine-tuning of the binding affinity for α-thrombin. *Organic & Biomolecular Chemistry* **2019,** *17* (9), 2403-2412.
47. Ni, S. Y., H.; Wang, L.; Lu, J.; Jiang, F.; Lu, A.; Zhang, G. , Chemical Modifications of Nucleic Acid Aptamers for Therapeutic Purposes. *Int. J. Mol. Sci.* **2017,** *18*, 1683.
48. Shum, K. T.; Tanner, J. A., Differential Inhibitory Activities and Stabilisation of DNA Aptamers against the SARS Coronavirus Helicase. *ChemBioChem* **2008,** *9* (18), 3037-3045.
49. Pan, Y.; Zhang, D.; Yang, P.; Poon, L. L. M.; Wang, Q., Viral load of SARS-CoV-2 in clinical samples. *The Lancet Infectious Diseases* **2020,** *20* (4), 411-412.
50. Witek, M. A.; Aufforth, R. D.; Wang, H.; Kamande, J. W.; Jackson, J. M.; Pullagurla, S. R.; Hupert, M. L.; Usary, J.; Wysham, W. Z.; Hilliard, D.; Montgomery, S.; Bae-Jump, V.; Carey, L. A.; Gehrig, P. A.; Milowsky, M. I.; Perou, C. M.; Soper, J. T.; Whang, Y. E.; Yeh, J. J.; Martin, G.; Soper, S. A., Discrete Microfluidics for the Isolation of Circulating Tumor Cell Subpopulations Targeting Fibroblast Activation Protein alpha and Epithelial Cell Adhesion Molecule *Nature Precision Oncology* **2018**, 1.
51. Anderson, W.; Lane, R.; Korbie, D.; Trau, M., Observations of Tunable Resistive Pulse Sensing for Exosome Analysis: Improving System Sensitivity and Stability. *Langmuir : the ACS journal of surfaces and colloids* **2015,** *31* (23), 6577-87.
52. Zhou, K.; Li, L.; Tan, Z.; Zlotnick, A.; Jacobson, S. C., Characterization of hepatitis B virus capsids by resistive-pulse sensing. *J Am Chem Soc* **2011,** *133* (6), 1618-21.
53. Yang, L.; Yamamoto, T., Quantification of Virus Particles Using Nanopore-Based Resistive-Pulse Sensing Techniques. *Frontiers in Microbiology* **2016,** *7* (1500).
54. Tong, A.; Sorrell, T. C.; Black, A. J.; Caillaud, C.; Chrzanowski, W.; Li, E.; Martinez-Martin, D.; McEwan, A.; Wang, R.; Motion, A.; Bedoya, A. C.; Huang, J.; Azizi, L.; Eggleton, B. J., Reasearch priorities for COVID-19 sensor technology. *Nature Biotechnology* **2021,** *(Published online: January 18, 2021)*.
55. Zhang, L.; Richards, A.; Khalil, A.; Wogram, E.; Ma, H.; Young, R. A.; Jaenisch, R., SARS-CoV-2 RNA reverse-transcribed and 1 integrated into the human genome. *bioRxiv* **2020**, 1-37.
56. Brooks, S. K.; Webster, R. K.; Smith, L. E.; Woodland, L.; Wessely, S.; Greenberg, N.; Rubin, G. J., The psychological impact of quarantine and how to reduce it: rapid review of the evidence. *Lancet* **2020,** *395*, 912-920.
57. Mattioli, A. V.; Puviani, M. B.; Nasi, M.; Farinetti, A., COVID-19 pandemic: the effects of quarantine on cardiovascular risk. *European Journal of Clinical Nutrition* **2020,** *74*, 852-855.
58. Maringe, C.; Spicer, J.; Morris, M.; Purushotham, A.; Nolte, E.; Sullivan, R.; Rachet, B.; Aggarwal, A., The impact of the COVID-19 pandemic on cancer deaths due to delays in diagnosis in England, UK: a national, population-based, modelling study. *Lancet* **2020,** *21*, 1023-1034.
59. Katz, M. H., Challenges in Testing for SARS-CoV-2 Among Patients Who Recovered From COVID-19. *JAMA Internal Medicine* **2020**.
60. Kang, H.; Wang, Y.; Tong, Z.; Liu, X., Retest positive for SARS-CoV-2 RNA of “recovered” patients with COVID-19: Persistence, sampling issues, or re-infection? *Journal of Medical Virology* **2020,** *92* (11), 2263-2265.
61. Liotti, F. M.; Menchinelli, G.; Marchetti, S.; Posteraro, B.; Landi, F.; Sanguinetti, M.; Cattani, P., Assessment of SARS-CoV-2 RNA Test Results Among Patients Who Recovered From COVID-19 With Prior Negative Results. *JAMA Internal Medicine* **2020**.

62. CDC Isolate If You Are Sick. https://www.cdc.gov/coronavirus/2019-ncov/if-you-are-sick/isolation.html (accessed January).
63. Bullard, J.; Dust, K.; Funk, D.; Strong, J. E.; Alexander, D.; Garnett, L.; Boodman, C.; Bello, A.; Hedley, A.; Schiffman, Z.; Doan, K.; Bastien, N.; Li, Y.; Caeseele, P. G. V.; Poliquin, G., Predicting Infectious Severe Acute Respiratory Syndrome Coronavirus 2 From Diagnostic Samples. *Clinical Infectious Diseases* **2020,** *71*, 2663-2666.
64. Kalra, P.; Dhiman, A.; Cho, W. C.; Bruno, J. G.; Sharma, T. K., Simple Methods and Rational Design for Enhancing Aptamer Sensitivity and Specificity. *Front Mol Biosci* **2018,** *5*, 41-41.
65. Kim, Y. G.; Yun, S. G.; Kim, M. Y.; Park, K.; Cho, C. H.; Yoon, S. Y.; Nam, M. H.; Lee, C. K.; Cho, Y. J.; Lim, C. S., Comparison between Saliva and Nasopharyngeal Swab Specimens for Detection of Respiratory Viruses by Multiplex Reverse Transcription-PCR. *J Clin Microbiol* **2017,** *55* (1), 226-233.
66. Pasomsub, E.; Watcharananan, S. P.; Boonyawat, K.; Janchompoo, P.; Wongtabtim, G.; Suksuwan, W.; Sungkanuparph, S.; Phuphuakrat, A., Saliva sample as a non-invasive specimen for the diagnosis of coronavirus disease 2019: a cross-sectional study. *Clin Microbiol Infect* **2020**.
67. Czumbel, L. M.; Kiss, S.; Farkas, N.; Mandel, I.; Hegyi, A. E.; Nagy, A. K.; Lohinai, Z.; Szakacs, Z.; Hegyi, P.; Steward, M. C., Saliva as a Candidate for COVID-19 Diagnostic Testing: A Meta-Analysis. *medRxiv* **2020**.
68. Kojima, N.; Turner, F.; Slepnev, V.; Bacelar, A.; Deming, L.; Kodeboyina, S.; Klausner, J. D., Self-Collected Oral Fluid and Nasal Swabs Demonstrate Comparable Sensitivity to Clinician Collected Nasopharyngeal Swabs for Covid-19 Detection. *medRxiv* **2020**.
69. To, K. K.-W.; Tsang, O. T.-Y.; Yip, C. C.-Y.; Chan, K.-H.; Wu, T.-C.; Chan, J. M.-C.; Leung, W.-S.; Chik, T. S.-H.; Choi, C. Y.-C.; Kandamby, D. H.; Lung, D. C.; Tam, A. R.; Poon, R. W.-S.; Fung, A. Y.-F.; Hung, I. F.-N.; Cheng, V. C.-C.; Chan, J. F.-W.; Yuen, K.-Y., Consistent Detection of 2019 Novel Coronavirus in Saliva. *Clinical Infectious Diseases* **2020,** *on-line*, 1-3.
70. Bastos, M. L.; Perlman-Arrow, S.; Menzies, D.; Campbell, J. R., The Sensitivity and Costs of Testing for SARS-CoV-2 Infection With Saliva Versus Nasopharyngeal Swabs. *Annals of Internal Medicine* **2021**.
71. Voloch, C. M.; Jr, R. d. S. F.; Almeida, L. G. P. d.; Cardoso, C. C.; Brustolini, O. J.; Gerber, A. L.; Guimarães, A. P. d. C.; Mariani, D.; Costa, R. M. d.; Jr, O. C. F.; Cavalcanti, A. C.; Frauches, T. S.; Mello, C. M. B. d.; Galliez, R. M.; Faffe, D. S.; Castiñeiras, T. M. P. P.; Tanuri, A.; Vasconcelos, A. T. R. d., A novel Brazilian SARS-CoV-2 lineage. *medRxiv* **2020**.
72. Tegally, H.; Wilkinson, E.; Giovanetti, M.; Iranzadeh, A.; Fonseca, V.; Giandhari, J.; Doolabh, D.; Pillay, S.; San, E. J.; Msomi, N.; Mlisana, K.; Gottberg, A. v.; Walaza, S.; Allam, M.; Ismail, A.; Mohale, T.; Glass, A. J.; Engelbrecht, S.; Zyl, G. V.; Preiser, W.; Petruccione, F.; Sigal, A.; Hardie, D.; Marais, G.; Hsiao, M.; Korsman, S.; Davies, M.-A.; Tyers, L.; Mudau, I.; York, D.; Maslo, C.; Goedhals, D.; Abrahams, S.; Laguda-Akingba, O.; Alisoltani-Dehkordi, A.; Godzik, A.; Wibmer, C. K.; Sewell, B. T.; Lourenço, J.; Carlos, L.; Alcantara, J.; Pond, S. L. K.; Weaver, S.; Martin, D.; Lessells, R. J.; Bhiman, J. N.; Williamson, C.; Oliveira, T. d., Emergence and rapid spread of a new severe acute respiratory syndrome-related coronavirus 2 (SARS-CoV-2) lineage with multiple spike mutations in South Africa. *medRxiv* **2020**.
73. Volz, E.; Mishra, s.; Chand, M.; Barrett, J. C.; Johnson, R.; Geidelberg, L.; Hinsley, W. R.; Laydon, D. J.; Dabrera, G.; O'Toole, A.; Amato, R.; Ragonnet-Cronin, M.; Harrison, I.; Jackson, B.; Ariani, C. V.; Boyd, O.; Loman, N.; McCrone, J. T.; Goncalves, S.; Jorgensen, D.; Myers, R.; Hill, V.; David K, J.; Gaythorpe, K.; Groves, N.; Sillitoe, J.; Kwiatkawski, D. P.; Flaxman, S.; Ratmann, O.; Bhatt, S.; Hopkins, S.; Gandy, A.; Rambaut, A.; Gerguson, N. M., Transmission of SARS-CoV-2 Lineage B.1.1.7 in England: Insight fron a linking epidemiological and genetic data. *medRxiv* **2021**.

Chapter 5 - Future Directions

5.1 Integrated modular microfluidic system for the diagnosis of acute ischemic stroke (AIS)

5.1.1 Introduction

Stroke is the second-leading cause of death globally and the third leading cause of death in the US.[1] Stroke accounts for 16% of all cardiovascular diseases, 2-4% of the healthcare costs worldwide.[2] There are two types of strokes, acuteischemic stroke (AIS) (80-85%) and hemorrhagic stroke (15-20%). In the current global COVID-19 pandemic, stroke onset can be a consequence of infection; cases of large-vessel stroke were reported in patients diagnosed with COVID-19.[3]

Acute ischemic stroke (AIS) is currently diagnosed by computed tomography (CT; clinical sensitivity = 26%) or magnetic resonance imaging (MRI; clinical sensitivity = 83%), which typically performs at the emergency center of the hospital. Recombinant tissue plasminogen activator (rt-PA) is given to the patient as the treatment after the diagnosis. AIS treatment has a narrow therapeutic time window (<4.5 h from AIS onset), and imaging techniques are challenging since they cannot provide timely diagnosis essential for the AIS treatment. Due to this limitation, the recombinant tissue plasminogen activator currently reaches <7% of AIS patients only. Therefore, it is essential to have a rapid diagnostic assay platform that can use in Point-of-Care Testing (POCT) for AIS diagnosis.

CD8 (+) and CD15 (+) leukocytes contain specific mRNAs with altered expression in AIS patients.[4] We have recently shown that mRNA expression changes in CD8 (+) extracellular vesicles (EVs) can be used for AIS diagnosis.[5] Single-molecule laser-induced fluorescence was used to achieve the required turnaround time for stroke diagnosis,[2, 6] but the hardware was not accommodating highly multiplexed operation or potential POCT that would allow for more timely diagnosis of stroke patients.

Taking advantage of our previous modular systems, we are currently working on a fully automated and modular fluidic microsystem to permit rapid AIS diagnosis. The fluidic cartridge contains a module (EV-MAP) to affinity select CD8 (+) and CD15 (+) EVs (**Figure 5.1**), count the EVs using a nano-Coulter Counter, lyse the EVs, reverse transcribe the mRNA into cDNAs using biotinylated poly(dT) primers, a module for the solid-phase extraction of the biotinylated cDNA, perform an spLDR (solid-phase ligase detection reaction), and evaluate the product identity and quantity directly using TOF (time of flight) sensing. Modular integration will be performed by introducing interconnects and alignment structures that provide high process yield rates (>90%).

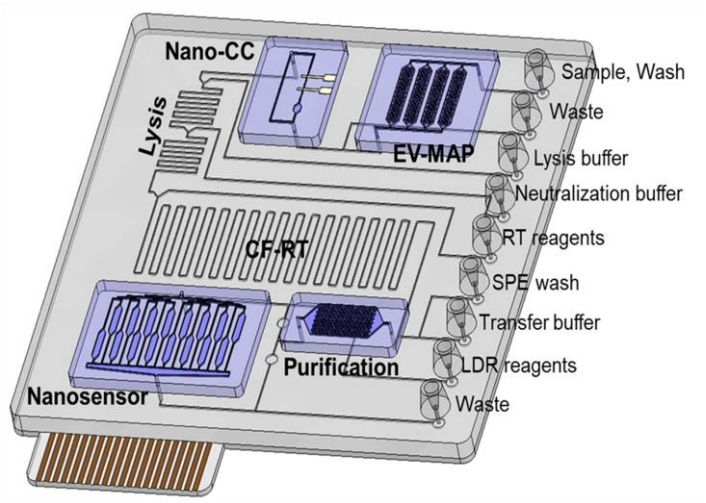

Figure 5.1. Integrated modular microsystem for the mRNA expression profiling of EVs. Four task specific modules, EV selection chip, n-CC chip, cDNA purification chip and a nano sensor chip were integrated with a continuous flow thermal reactor to form the cartridge.

5.1.2 **RNA markers for stroke**

Biomarkers based on mRNA expression, especially in peripheral blood, are emerging classes of stroke biomarkers with several advantages compared to protein biomarkers. When compared to proteins, mRNA changes are induced more rapidly in response to an injury. Microarrays were used to identify 22 genes that can be used to distinguish AIS from controls.[7-8]

Stroke-related mRNA expression changes in whole blood were verified in subsequent studies.[9-11] mRNAs expression changes were observed in AIS patients with 66%, 87%, and 100% clinical sensitivity after 2.4 h, 5 h and, 24 h of stroke onset, respectively.[11] Sensitivity of the assay increased with the higher appearance of stroke-related mRNAs in circulation.

Table 5.8. Transcript clusters for ischemic stroke in CD15 (+) and CD8 (+) cells. The clusters in the red box are gene panels that will be used for the testing.

Source	Transcripts	Adjusted p value *
CD15 Neutrophils	*IQGAP1, SLC16A6, NPL, CD93, PYGL,PLBD1*	4.41×10^{-4}
	ADM, CKAP4, FOS, BST1	1.38×10^{-3}
	ENTPD1, IL13RA1, LTA4H, S100P	4.56×10^{-3}
	DUSP1, HIST2H2AA3, BCL6, PILRA, FCGR1A, TLR2	3.62×10^{-3}
	LY96, S100A9, FPR1, S100A12, RNASE2, CCR7	85.7×10^{-3}
	CA4, MMP9, NAIP	2.9×10^{-5}
CD8 T-cells	*IL13, APLP2, ENTPD1, ETS2, PYGL, DUSP1, KIAA, ADM, S100P, CD36*	1.71×10^{-5}
	CYBB, BST1, CD93, NPL, IQGAP1	9.87×10^{-3}
	FOS, VCAN, PLBD1, MMP9, CA4	6.67×10^{-4}
	BCL6, SLC16, LTA4H, CKAP4, FPR1, FCGR1A	1.21×10^{-3}

Stroke-related mRNA expression changes can be derived from particular leukocyte subsets that are activated due to an inflammatory response occurring during a stroke event.[12] We quantified mRNA expression in multiple leukocyte subsets for differentiating between stroke and controls.[13] The absolute expression of 41 stroke-related mRNA transcripts was measured in 6 major leukocyte subsets using HT RT-qPCR and hierarchical cluster analyses. $CD15^+$ neutrophils and $CD8^+$ T lymphocytes were recognized as the major sources of mRNA expression changes in AIS with 14 and 16 genes up-regulated, respectively. Multiple clusters of transcripts were identified that discriminated between AIS and controls, most notably in $CD15^+$ neutrophils and $CD8^+$ T lymphocytes (**Table 5.1)**.

RT-qPCR is used in mRNA expression analysis, and it has a turnaround time (TAT) of ≤2 h.[14] However, RT-qPCR's analytical sensitivity is subjected to change in the low transcript copy number regime. Additionally, sample preparation, variation in reagents, primer design, and operator skill affect the result accuracy.[13] Droplet digital PCR (ddPCR) is used as a variant of RT-qPCR for mRNA expression profiling.[15] Compared to RT-qPCR, ddPCR has excellent analytical sensitivity in the low copy number regime. However, the limited multiplexing capabilities (~4 transcripts) and the complicated workflow in ddPCR and qPCR are challenging.

PCR-free techniques have been introduced to improve the analytical utility of mRNA expression profiling.[16-17] Some methods are based on single-molecule detection, SMD.[18-19] We have reported an SMD assay combined with reverse transcription and the ligase detection reaction (LDR) to count and quantify mRNA transcripts using single-pair FRET (spFRET).[6] These PCR-free systems utilize fluorescence for readout. This requires multi-color excitation and detection systems that can limit their multiplexing capacity. This project will develop a label-free nanosensor that possesses high multiplexing capabilities with the near-real-time readout of cDNA transcripts by obviating the previous limitations.

5.1.3 Integrated modular system for AIS diagnosis

An integrated modular microfluidic cartridge will be developed for the analysis of an EV mRNA marker panel for the diagnosis of stroke in ~31 min. The modular design contains 4 task-specific modules for EV isolation, label-free enumeration, spLDR, and counting and identification of cDNA products. The fluidic motherboard has structures for cell lysis and continuous flow reverse transcription (CF-RT). The fluidic cartridge is comprised of mixed-scale (nm → μm structures) modules that can accept clinical samples and provide single-molecule sensitivity for expression profiling mRNA transcripts sourced from EVs. The modules and motherboard are made from thermoplastics allowing high-rate production using replication-based techniques,[20-22]

essential for *in vitro* diagnostics that require disposables. We use injection molding and nanoimprint lithography (NIL) to fabricate micro and nanostructures, respectively.[23]

5.1.3.1 Selection of CD8 and CD15 EVs

We hypothesized that EVs released by CD8(+) T-cells and CD15 (+) leukocytes contain a gene profile similar to the host cell after an inflammatory response and thus can be used to diagnose AIS. We used EV micro-affinity purification (EV-MAP) device (**Figure 5.2A**) to isolate EVs derived from activated CD8(+) T-cells via affinity enrichment.[5] EV-MAP device possesses a high-density array of micropillars (~1.5 million) decorated with monoclonal antibodies (mAbs) to target CD8(+) and CD15(+) EVs and could operate at high flow rates (20 µL/min). Each pillar is 10 µm in height, 10 µm in diameter, and 10 µm inter-pillar spacing. The channel bed can accommodate $>10^{11}$ EV-like particles. Inlet and outlet channels have a Z-configuration and contain baffle structures to prevent large particles enter into the channel bed. Disease-associated EVs were recovered with high efficiency (~70%). Antibodies will be immobilized to the device surface using the PC linker, and EVs will be photo-released from the affinity surface for particle counting.[24]

5.1.3.2 Counting EVs

Housekeeping genes will not be used for the analysis because they can be dysregulated as a result of a stroke event.[25] Therefore, mRNA expression levels will be normalized to enriched EV numbers. n-CC chip (**Figure 5.2B**) will be used for the label-free counting of photo-released EVs. The device is made from thermoplastic via molding to allow for high-rate production. The n-CC consists of two microchannels connected by a sub-micron bridge channel and a nanopore. When a particle passes through the nanopore, it changes the resistance between the two electrodes, and the resistance change gives a signal. Each electrical pulse corresponds to a single EV passing

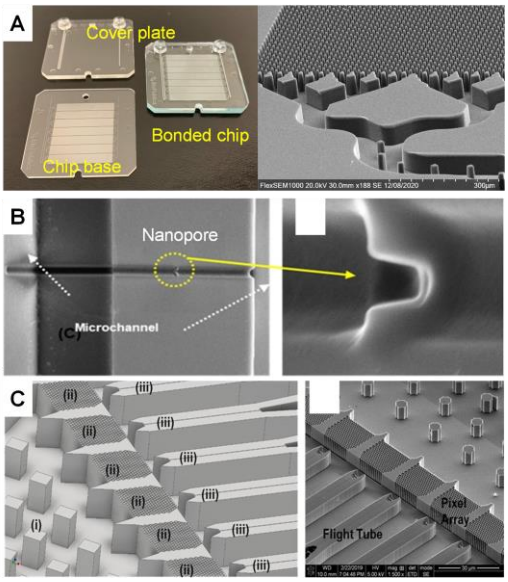

Figure 5.2. EV selection module, n-CC module and nano-sensor module. **(A)** EV selection module consists of 7 parallel beds that have ~1.5 million pillars. Inlet and outlet channels of the chip contains baffle structures to prevent large particles enter into the channel bed. (B) n-CC module contains a nano-pore bridging two microchannels. (C) Nano sensor module containing three parts, (i) Baffle structures to deliver evenly distributed fluid flow, (ii) pillar array for spLDR, and (iii) nano flight tubes for TOF measurements.

through the nanopore. The magnitude of the signal proportional to the EV size. The n-CC contains a nanopore of 200 nm x 200 nm to achieve 100% detection efficiency.

5.1.3.3 Reverse transcription (RT) in a continuous flow (CF) reactor

CF reactor was employed in the motherboard for the RT reaction. The poly(dT) primer will hybridize to the polyadenylated mRNA tail to generate cDNA with a biotin label at its 5' end. The reverse transcriptase hydrolyzes the mRNA template after the reverse transcription releasing the ss cDNA. The biotinylated cDNA is sent to the purification chip to purify from excess biotinylated poly(dT) primers. The purification chip contains pillar structures and surface-bound stroke-specific gene recognition sequences (called probes). Gene-specific cDNA will hybridize with the specific probe while other biotinylated primers and RT reagents washed away. Thus, components that may interfere with downstream processing will be removed. Hybridized cDNA targets will be released from the probes by thermal melting.

5.1.3.4 Nanosensor

Biotinylated cDNA targets are then be shuttled to the spLDR reactor in the nanosensor and bound to the streptavidin-modified pillars (1 μm diameter and 250 μm interpillar space). The nanosensor module consists of a fluid disperser with baffle structures for the uniform distribution of the sample, pillar array for the spLDR reaction, and finally, nano-flight tubes for TOF measurements (**Figure 5.2C**). spLDR reaction is performed using different length spLDR primers for each transcript. There are 8 pillar arrays for the high throughput sample processing. The spLDR products are thermally released and electrokinetically swept towards the nanopore (50 nm x 50 nm) for identification and quantification based on their molecular-dependent TOF signatures.

5.1.3.5 eCOC valves

For the SMART-Chip modular system, we used PMMA/PDMS/PMMA valving system for the fluidic manipulation. While PDMS has been shown to be effective in these microfluidics valves, PDMS has two major drawbacks that impede its use in future integrated systems. First, PDMS requires casting. While the PDMS casting process is applicable within academic laboratories for rapid, low-cost prototyping, the process is time consuming and requires hands-on manipulation of materials.[26-27] Ultimately, this does not lend itself well to transition to industrial, large scale, low-cost manufacturing of point of care diagnostic tools. Second, the group has shown that PDMS does not bond to materials with adequate glass transition temperatures necessary for running PCR assays. For example, the valves made from PC/PDMS/PC and COC/PDMS/COC were incapable of actuating effectively (data were not shown). In order to improve the valves' manufacturability, alternative materials such as elastomeric COC (Topas® Elastomer E-140, Topas Advanced Polymers, Germany) will be investigated. Elastomeric COC or eCOC is flexible and inert with a Young's Modulus of 68 MPa, >500% tensile strain at break, and a melting temperature of 84°C. Most importantly, eCOC is capable of being injection molded with a series of processing temperatures as specified by the manufacturer. Injection molding is low-cost,

efficient, and allows for large-scale production in comparison to PDMS casting.[28-29] Initial studies have found eCOC to have successful bonding with several thermoplastics. eCOC bonded to PMMA, PC, and COC-6013 after 10 min UV/O_3 exposure and to PMMA and PC after 1 min Oxygen plasma treatment. Future efforts will focus on injection molding a 250 µm membrane from eCOC to create and characterize novel valves made from the combination of the eCOC and various thermoplastics.

5.2 Integrated modular microfluidic system for the fast detection of SARS-CoV-2 from saliva specimens

The virus isolation module and n-CC module will be integrated using superhydrophobic seals. Superhydrophobic fluid interconnects use capillary forces to seal a connection between two aligned through-holes with superhydrophobic surfaces separated by a fixed gap defined by alignment structures.[30-32] We will use an n-CC molded substrate as a cover plate for the viral particle selection module, as shown in **Figure 5.3**. The fluidic network of the n-CC will be enclosed by a cover plate with patterned thin-film electrodes for electrical signal generation and data collection. All pieces will be bonded together using an aligned, UV facilitated thermal fusion bonding process. Micro-scale reservoirs and connectors made using CNC machining will be bonded to the top cover to complete the fluidic cartridge.

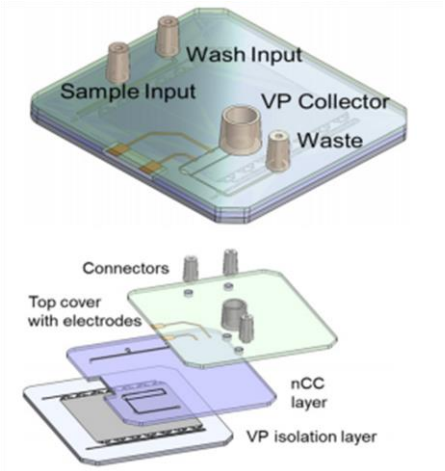

Figure 5.3. Construction of the integrated chip for viral particle isolation and label-free counting. n-CC molded substrate will be used as the cover plate for the µSPE chip. The n-CC fluidic network will be enclosed using a cover plate with patterned thin film electrodes.

5.3 References

1. Feigin, V. L.; Lawes, C. M.; Bennett, D. A.; Barker-Collo, S. L.; Parag, V., Worldwide stroke incidence and early case fatality reported in 56 population-based studies: a systematic review. *The Lancet Neurology* **2009,** *8* (4), 355-369.
2. Pullagurla, S. R.; Witek, M. A.; Jackson, J. M.; Lindell, M. A.; Hupert, M. L.; Nesterova, I. V.; Baird, A. E.; Soper, S. A., Parallel affinity-based isolation of leukocyte subsets using microfluidics: application for stroke diagnosis. *Analytical chemistry* **2014,** *86* (8), 4058-4065.
3. Oxley, T. J.; Mocco, J.; Majidi, S.; Kellner, C. P.; Shoirah, H.; Singh, I. P.; De Leacy, R. A.; Shigematsu, T.; Ladner, T. R.; Yaeger, K. A., Large-vessel stroke as a presenting feature of Covid-19 in the young. *New England Journal of Medicine* **2020,** *382* (20), e60.
4. Adamsk, M.; Li, Y.; Wagner, E.; Seales-Bailey, C.; Yu, H.; Bennett, N.; Murphy, M.; Soper, S. A.; Baird, A. E., CD15+ granulocyte and CD8+ T lymphocyte based gene expression clusters for ischemic stroke detection. *Med Res Archives* **2017,** *(in press)*.
5. Wijerathne, H.; Witek, M. A.; Jackson, J. M.; Brown, V.; Hupert, M. L.; Herrera, K.; Kramer, C.; Davidow, A. E.; Li, Y.; Baird, A. E., Affinity enrichment of extracellular vesicles from plasma reveals mRNA changes associated with acute ischemic stroke. *Communications biology* **2020,** *3* (1), 1-11.
6. Peng, Z. Y.; Young, B.; Baird, A. E.; Soper, S. A., Single-Pair Fluorescence Resonance Energy Transfer Analysis of mRNA Transcripts for Highly Sensitive Gene Expression Profiling in Near Real Time. *Analytical Chemistry* **2013,** *85* (16), 7851-7858.
7. Moore, D. F.; Li, H.; Jeffries, N.; Wright, V.; Cooper, R. A.; Elkahloun, A.; Gelderman, M. P.; Zudaire, E.; Blevins, G.; Yu, H.; Goldin, E.; Baird, A. E., Using peripheral blood mononuclear cells to determine a gene expression profile of acute ischemic stroke. *Circulation* **2005,** *111* (Copyright (C) 2013 American Chemical Society (ACS). All Rights Reserved.), 212-221.
8. Adamski, M. G.; Li, Y.; Wagner, E.; Yu, H.; Seales-Bailey, C.; Soper, S. A.; Murphy, M.; Baird, A. E., Expression profile based gene clusters for ischemic stroke detection. *Genomics* **2014,** *104* (3), 163-169.
9. Tang, Y.; Xu, H.; Du, X.; Lit, L.; Walker, W.; Lu, A.; Ran, R.; Gregg, J. P.; Reilly, M.; Pancioli, A., Genomic biomarkers and cellular pathways of ischemic stroke by RNA gene expression profiling. . *Neurology* **2010,** *75*, 1009-1014.
10. Barr, T. L.; Conley, Y.; Ding, J., Genomic biomarkers and cellular pathways of ischemic stroke by RNA gene expression profiling. . *Neurology* **2010,** *75*, 1009-1014.
11. Tang, Y.; Xu, H.; Du, X.; Lit, L.; Walker, W.; Lu, A.; Ran, R.; Gregg, J. P.; Reilly, M.; Pancioli, A.; Khoury, J. C.; Sauerbeck, L. R.; Carrozzella, J. A.; Spilker, J.; Clark, J.; Wagner, K. R.; Jauch, E. C.; Chang, D. J.; Verro, P.; Broderick, J. P.; Sharp, F. R., Gene expression in blood changes rapidly in neutrophils and monocytes after ischemic stroke in humans: a microarray study. *J. Cereb. Blood Flow Metab.* **2006,** *26* (8), 1089-1102.
12. Du, X.; Tang, Y.; Xu, H.; Lit, L.; Walker, W.; Ashwood, P.; Gregg, J. P.; Sharp, F. R., Genomic profiles for human peripheral blood T cells, B cells, natural killer cells, monocytes, and polymorphonuclear cells: Comparisons to ischemic stroke, migraine, and Tourette syndrome. *Genomics* **2006,** *87* (6), 693-703.
13. Adamski, M. G.; Li, Y.; Wagner, E.; Yu, H.; Seales-Bailey, C.; Soper, S. A.; Murphy, M.; Baird, A. E., Next-generation qPCR for the high-throughput measurement of gene expression in multiple leukocyte subsets. . *J Biomol Screen* **2013,** *18*, 1008-1017.
14. Palmer, S.; Wiegand, A. P.; Maldarelli, F.; Bazmi, H.; Mican, J. M.; Polis, M.; Dewar, R. L.; Planta, A.; Liu, S.; Metcalf, J. A.; Mellors, J. W.; Coffin, J. M., New real-time reverse transcriptase-initiated PCR assay with single-copy sensitivity for human immunodeficiency virus type 1 RNA in plasma. *J Clin Microbiol* **2003,** *41* (10), 4531-6.

15. Hayden, R. T.; Gu, Z.; Ingersoll, J.; Abdul-Ali, D.; Shi, L.; Pounds, S.; Caliendo, A. M., Comparison of Droplet Digital PCR to Real-Time PCR for Quantitative Detection of Cytomegalovirus. *Journal of Clinical Microbiology* **2013,** *51* (2), 540-546.
16. Medley, C. D.; Drake, T. J.; Tomasini, J. M.; Rogers, R. J.; Tan, W. H., Simultaneous monitoring of the expression of multiple genes inside of single breast carcinoma cells. *Analytical Chemistry* **2005,** *77* (15), 4713-4718.
17. Chen, X. J.; Roy, S.; Peng, Y. F.; Gao, Z. Q., Electrical Sensor Array for Polymerase Chain Reaction-Free Messenger RNA Expression Profiling. *Analytical Chemistry* **2010,** *82* (14), 5958-5964.
18. Neely, L. A.; Patel, S.; Garver, J.; Gallo, M.; Hackett, M.; McLaughlin, S.; Nadel, M.; Harris, J.; Gullans, S.; Rooke, J., A single-molecule method for the quantitation of microRNA gene expression. *Nature Methods* **2006,** *3* (1), 41-46.
19. Korn, K.; Gardellin, P.; Liao, B.; Amacker, M.; Bergstrom, A.; Bjorkman, H.; Camacho, A.; Dorhofer, S.; Dorre, K.; Enstrom, J.; Ericson, T.; Favez, T.; Gosch, M.; Honegger, A.; Jaccoud, S.; Lapczyna, M.; Litborn, E.; Thyberg, P.; Winter, H.; Rigler, R., Gene expression analysis using single molecule detection. *Nucleic Acids Research* **2003,** *31* (16).
20. Uba, F. I.; Pullagurla, S. R.; Sirasunthorn, N.; Wu, J.; Park, S.; Chantiwas, R.; Cho, Y.; Shin, H.; Soper, S. A., Surface Charge, Electroosmotic Flow and DNA Extension in Chemically Modified Thermoplastic Nanoslits and Nanochannels. *Analyst* **2015,** *140*, 113-126.
21. Jackson, J. M.; Witek, M. A.; Kamande, J. W.; Sope, S. A., Materials and microfluidics: enabling the efficient isolation and analysis of circulating tumour cells. *Chemical Society Reviews* **2017,** *46*, 4245-4280.
22. Weerakoon-Ratnayake, K. M.; O'Neil, C. E.; Uba, F. I.; Soper, S. A., Thermoplastic nanofluidic devices for biomedical applications. *Lab on a Chip* **2017,** *17*, 362-381.
23. Wu, J.; Chantiwas, R.; Amirsadeghi, A.; Soper, S. A.; Park, S., Complete plastic nanofluidic devices for DNA analysis via direct imprinting with polymer stamps. *Lab on a Chip* **2011,** *11* (17), 2984-2989.
24. Pahattuge, T. N.; Jackson, J. M.; Digamber, R.; Wijerathne, H.; Brown, V.; Witek, M. A.; Perera, C.; Givens, R. S.; Peterson, B. R.; Soper, S. A., Visible photorelease of liquid biopsy markers following microfluidic affinity-enrichment. *Chemical Communications* **2020,** *56* (29), 4098-4101.
25. Adamski, M. G.; Gumann, P.; Baird, A. E., A Method for Quantitative Analysis of Standard and High-Throughput qPCR Expression Data Based on Input Sample Quantity. *PLoS One* **2014,** *9*, e103917.
26. Berthier, E.; Young, E. W.; Beebe, D., Engineers are from PDMS-land, Biologists are from Polystyrenia. *Lab on a Chip* **2012,** *12* (7), 1224-1237.
27. Friend, J.; Yeo, L., Fabrication of microfluidic devices using polydimethylsiloxane. *Biomicrofluidics* **2010,** *4* (2), 026502.
28. Fiorini, G. S.; Chiu, D. T., Disposable microfluidic devices: fabrication, function, and application. *BioTechniques* **2005,** *38* (3), 429-446.
29. Mair, D. A.; Geiger, E.; Pisano, A. P.; Fréchet, J. M.; Svec, F., Injection molded microfluidic chips featuring integrated interconnects. *Lab on a Chip* **2006,** *6* (10), 1346-1354.
30. You, B.-H.; Chen, P.-C.; Park, D. S.; Park, S.; Nikitopoulos, D. E.; Soper, S. A.; Murphy, M. C., Passive micro-assembly modular, hot embossed, polymer microfluidic devices using exact constraint design. *J. Micromechanics Microeng.* **2009,** *19* (12), 125025.
31. Lee, T. Y.; Han, K.; Barrett, D. O.; Park, S.; Soper, S. A.; Murphy, M. C., Accurate, predictable, repeatable micro-assembly technology for polymer, microfluidic modules. *Sensors & Actuators B* **2018,** *254* (1), 1249-1258.
32. You, B.-H.; Park, D. S.; Rani, S.; Murphy, M. C., Assembly of polymer microfluidic components and modules: Validating models of passive alignment accuracy. *JMEMS* **2015,** *24* (3), 634-650.